

**MAGNETOHYDRODYNAMIC ENERGY GENERATION AND FLOW  
CONTROL FOR PLANETARY ENTRY VEHICLES**

A Dissertation  
Presented to  
The Academic Faculty

By

Hisham K. Ali

In Partial Fulfillment  
of the Requirements for the Degree  
Doctor of Philosophy in the  
Daniel Guggenheim School of Aerospace Engineering

Georgia Institute of Technology

August 2019

Copyright © Hisham K. Ali 2019

**MAGNETOHYDRODYNAMIC ENERGY GENERATION AND FLOW  
CONTROL FOR PLANETARY ENTRY VEHICLES**

Approved by:

Dr. Robert D. Braun, Advisor  
Daniel Guggenheim School of  
Aerospace Engineering  
*Georgia Institute of Technology*

Dr. Mitchell L.R. Walker, Co-  
Advisor  
Daniel Guggenheim School of  
Aerospace Engineering  
*Georgia Institute of Technology*

Dr. Stephen M. Ruffin  
Daniel Guggenheim School of  
Aerospace Engineering  
*Georgia Institute of Technology*

Dr. Robert W. Moses  
Atmospheric Flight and Entry  
Systems Branch  
*NASA Langley Research Center*

Dr. James E. Polk  
Propulsion and Materials Engineer-  
ing Section  
*NASA Jet Propulsion Laboratory*

Date Approved: April 29 2019

“Progress, not perfection, is the mantra of all successful scientific research”

*To my wife, Shaquia Idlett-Ali, for her everlasting love and support.*

*To my parents, Kamaleldin and Salwa Ali, for everything they have given to and for me.*

## **ACKNOWLEDGEMENTS**

This research was funded in part through a NASA Space Technology Research Fellowship, Grant Number NNX13AL82H, an Alfred P. Sloan Minority Ph.D. Fellowship, and the Georgia Space Grant Consortium. In addition, this effort would not have been possible if it were not for numerous and fruitful discussions with researchers in the Georgia Institute of Technology Space Systems Design Lab, Georgia Institute of Technology High-Power Electric Propulsion Laboratory, NASA Langley Research Center, NASA Marshall Space Flight Center, NASA Jet Propulsion Laboratory, and NASA Ames Research Center.

## TABLE OF CONTENTS

<b>Acknowledgments</b> . . . . .	v
<b>List of Tables</b> . . . . .	xi
<b>List of Figures</b> . . . . .	xiii
<b>Chapter 1: Introduction</b> . . . . .	1
1.1 Introduction: Planetary Entry, Descent, and Landing . . . . .	1
1.2 Motivation: Mars, Entry, Descent, and Landing . . . . .	2
1.3 Previous Mars EDL System Architectures . . . . .	4
1.3.1 High-Mass Mars EDL Challenges . . . . .	8
1.4 Magnetohydrodynamics for Planetary Entry . . . . .	10
1.5 Plasma Physics . . . . .	12
1.5.1 What is a Plasma? . . . . .	12
1.5.2 Governing Forces . . . . .	14
1.5.3 Characteristic Length Scales: The Debye Length . . . . .	18
1.5.4 Definition of a Plasma . . . . .	19
1.5.5 Types of Plasmas . . . . .	21
1.5.6 Plasma Modeling . . . . .	24
1.5.7 Magnetohydrodynamics . . . . .	28

1.6	Applications of Magnetohydrodynamics: Energy Generation . . . . .	31
1.6.1	Physical Considerations and Principles for MHD Energy Generation	33
1.6.2	Application of MHD Energy Generation Technologies . . . . .	37
1.7	Magnetohydrodynamics and Planetary Entry: A History . . . . .	38
1.7.1	MHD and Planetary Entry: Early History . . . . .	39
1.7.2	MHD and Planetary Entry: Modern Numerical Investigations . . . . .	44
1.7.3	MHD and Planetary Entry: Energy Generation . . . . .	48
1.8	MHD and Planetary Entry: Modern Experimental Investigation . . . . .	52
1.8.1	State of the Art: Experimental MHD Drag . . . . .	52
1.8.2	State of the Art: Experimental MHD Energy Generation . . . . .	55
1.9	MHD Applications to Mars Entry . . . . .	55
1.9.1	MHD Energy Generation for Mars Entry . . . . .	58
1.9.2	MHD Lorentz Force Drag Augmentation at Mars . . . . .	60
1.10	Gap Analysis and Thesis Statement . . . . .	62
1.11	Research Goals and Summary of Contributions . . . . .	63
1.11.1	Contribution I: Magnetohydrodynamic Energy Generation and Lorentz Force Drag Augmentation Performance Characterization and Im- pact on Planetary Entry Architectures . . . . .	63
1.11.2	Contribution II: Experimental Design and Investigation for Magne- tohydrodynamic Energy Generation in Conditions and Configura- tions Relevant to Planetary Entry . . . . .	65
1.11.3	Summary of Contributions . . . . .	67
 <b>Chapter 2: Magnetohydrodynamic Energy Generation and Lorentz Force Drag Augmentation Performance Characterization and Impact on Plan- etary Entry Architectures . . . . .</b>		 <b>68</b>

2.1	Magnetohydrodynamic Energy Generation and Lorentz Force Drag Augmentation Performance Characterization . . . . .	68
2.1.1	Modeling and Computation of Post-Shock Properties . . . . .	68
2.1.2	Magnetohydrodynamic Energy Generation Performance Model for Conceptual Design . . . . .	73
2.1.3	Magnetohydrodynamic Lorentz Force Drag Augmentation Performance Model for Conceptual Design . . . . .	79
2.2	Case Study for Impact of Magnetohydrodynamic Energy Generation on Planetary Entry Architectures . . . . .	82
2.2.1	Introduction to Electrical Energy Storage Systems . . . . .	82
2.2.2	Electrical Energy Storage System Performance Modeling . . . . .	85
2.2.3	Magnetohydrodynamic Energy Generation and Storage Case Studies Definition . . . . .	89
2.2.4	Simulated Trajectories . . . . .	89
2.2.5	Power Available for MHD Energy Generation . . . . .	91
2.2.6	Electrical Energy Storage System Performance . . . . .	93
2.3	Case Study for Impact of Magnetohydrodynamic Lorentz Force Drag Augmentation on Planetary Entry Systems . . . . .	95
<b>Chapter 3: Experimental Design for Magnetohydrodynamic Energy Generation in Conditions and Configurations Relevant to Planetary Entry .</b>		<b>100</b>
3.1	Test Chamber Experimental Design . . . . .	101
3.1.1	Gas Exhaust System . . . . .	104
3.1.2	Gas Supply System . . . . .	110
3.1.3	Quartz Nozzle Design . . . . .	113
3.1.4	Radio-Frequency (RF) Ionization System . . . . .	118
3.1.5	Experimental Instrumentation, Control, and Data Acquisition . . . . .	129

3.1.6	Test Section Model Mount Assembly . . . . .	134
3.2	Test Section Demonstration of Supersonic Flowing Plasma . . . . .	144
3.3	Test Section Aerothermal Characterization . . . . .	147
3.3.1	Choked Flow Testing . . . . .	150
3.3.2	Supersonic Flow Characterization . . . . .	155
3.4	Experimental Test Conditions and Relevance to Planetary Entry . . . . .	162
<b>Chapter 4: Experimental Investigation for Magnetohydrodynamic Energy Generation in Conditions and Configurations Relevant to Planetary Entry 165</b>		
4.1	Research Questions . . . . .	166
4.2	MHD Energy Generator Model Development . . . . .	166
4.2.1	MHD Model Design: Theory . . . . .	166
4.2.2	MHD Model Design: Sizing . . . . .	169
4.2.3	MHD Model Design: Design Variations and Final Drawings . . . . .	174
4.2.4	MHD Model Manufacturing: Materials and Process . . . . .	177
4.2.5	MHD Model Manufacturing: Assembly . . . . .	181
4.2.6	MHD Model Manufacturing: Completed Models . . . . .	185
4.3	Experimental Design . . . . .	188
4.3.1	Experimental Design: Theory and Measurement Objectives . . . . .	188
4.3.2	Experimental Design: Test Matrix and Methodology . . . . .	190
4.3.3	Experimental Design: Testing Protocol . . . . .	193
4.4	Experimental Results . . . . .	196
<b>Chapter 5: Summary, Conclusions, and Future Work . . . . . 205</b>		

5.1	Summary of Contributions . . . . .	205
5.1.1	Magnetohydrodynamic Energy Generation and Lorentz Force Drag Augmentation Performance Characterization and Impact on Planetary Entry Architectures . . . . .	205
5.1.2	Experimental Design and Investigation for Magnetohydrodynamic Energy Generation in Conditions and Configurations Relevant to Planetary Entry . . . . .	207
5.2	Suggestions for Future Work . . . . .	209
5.2.1	Suggested future work: Magnetohydrodynamic Energy Generation and Lorentz Force Drag Augmentation Performance Characterization	209
5.2.2	Suggested Future Work: Experimental Design and Investigation for MHD Energy Generation in Conditions and Configurations Relevant to Planetary Entry . . . . .	210
<b>Appendix A: List of Publications by the Author . . . . .</b>		<b>213</b>
<b>References . . . . .</b>		<b>219</b>
<b>Vita . . . . .</b>		<b>220</b>

## LIST OF TABLES

1.1	Previous Successful Mars Entry Parameters [2] [5]	8
1.2	Approximate Plasma Parameters [12]	24
2.1	Martian Atmospheric Composition	69
2.2	Earth Atmospheric Composition	69
2.3	Electrical Energy Storage System Performance Data by Technology Type	84
2.4	Electrical Energy Storage System Performance Data by Technology Type	85
2.5	Moses Test Vehicle Direct Entry Electrical Energy Storage System Mass	88
2.6	Case Study Entry Vehicle Configurations	91
2.7	Initial Conditions for Case Studies at 120 km Altitude	91
2.8	Parameter Study Names and Values	91
2.9	Initial Conditions for Case Studies at 120 km Altitude	94
2.10	TRL of EES System Required at 5% Mass Constraint for Each Case	97
2.11	Lorentz Force MHD Drag Augmentation Parameter Study Names and Values	98
2.12	Unseeded Case Peak Decelerations as a Function of B-field and Vehicle Configuration	98
2.13	1% K Seeded Case Peak Decelerations as a Function of B-field and Vehicle Configuration	98
3.1	RF Power System	127

3.2	Test Section Instrumentation Measurement Data . . . . .	156
3.3	Table of nozzle shock location dimensions . . . . .	159
3.4	Test Section Flow Characterization Results . . . . .	161
4.1	Table of nozzle shock location dimensions . . . . .	169
4.2	Completed MHD Energy Generator Model Inventory . . . . .	185
4.3	MHD Energy Generation Experiment Plasma Discharge Test Conditions . .	190
4.4	Summary of MHD Energy Generator Model Designs for Testing . . . . .	190
4.5	MHD Energy Generation for Planetary Entry Experimental Test Matrix, <i>N</i> = 3 Trials at Each Test Point . . . . .	191
4.6	MHD Energy Generation for Planetary Entry Experimental Test Parameters, Schematic Shown as Figure 4.20. . . . .	191
4.7	MHD Energy Generator Ceramic Model Thermal Response Testing . . . . .	193
4.8	Measured Electrode Voltage Potentials. Open Circuit Configuration. . . . .	199
4.9	Measured Electrode Voltage Potentials. Load Circuit Configuration. . . . .	199

## LIST OF FIGURES

1.1	MOLA Elevation Histogram [2] . . . . .	5
1.2	Mars Science Laboratory EDL Sequence [NASA Jet Propulsion Laboratory] . . . . .	7
1.3	HIAD Concept [NASA Langley Research Center] . . . . .	9
1.4	ADEPT Concept [NASA Ames Research Center] . . . . .	10
1.5	Artist Rendering of MHD During Planetary Entry [7] . . . . .	11
1.6	MHD drag force conceptual schematic for a representative blunt-body planetary entry vehicle. . . . .	13
1.7	Density-temperature regime for hydrogen plasma [12] . . . . .	25
1.8	MHD energy generator geometries, adapted from [19] . . . . .	32
1.9	Linear Faraday-type MHD generator and associated coordinate system . . . . .	35
1.10	Resler and Sears proposed magneto-aerodynamic decelerator device for re-entry missiles, adapted and modified from [21]. . . . .	41
1.11	Bow Shock on the sphere without (left) and with (right) magnetic field, adapted from [29] . . . . .	42
1.12	Experimental data for shock stand-off distance vs. magnetic interaction parameter overlaid on theoretical curve, adapted from [29] . . . . .	43
1.13	Computed pressure field showing bow-shock on sphere without (left) and with (right) magnetic field, adapted from [34] . . . . .	45
1.14	Comparison of numerical results for shock standoff distance vs magnetic interaction parameter, $Q$ , with 1958 analytical theory by Bush [22], adapted from [34] . . . . .	46

1.15	Computed pressure distributions and bow-shocks for various magnetic fields between 0 and 0.5 T ahead of the vehicle forebody, adapted from [35] . . .	47
1.16	Sum of aerodynamic and magnetoaerodynamic drag over the reentry trajectory for magnetic fields between 0 and 0.5T, adapted from [35] . . . . .	48
1.17	Steeves et al. non-flow through MHD generator design for planetary entry vehicles, adapted from [43] . . . . .	50
1.18	Steeves et al. magnetic field, flow and current diagram for MHD generator power panel, adapted from [43] . . . . .	51
1.19	Design for measurement of MHD drag augmentation on a cylindrical blunt body, adapted from [45] . . . . .	53
1.20	Measurements of MHD drag enhancement on a cylindrical blunt body in ionized flow, adapted from [45] . . . . .	54
1.21	Schematic of artificial supersonic discharge for measurement of MHD energy generation for reentry vehicles, adapted from [8] . . . . .	56
1.22	Design of MHD energy generator model for reentry, cylindrical forebody with two embedded permanent magnets, adapted from [8] . . . . .	56
1.23	Measurements of MHD energy generation from the artificial microwave supersonic discharge, adapted from [49] . . . . .	57
1.24	electrical conductivity as a function of temperature for the Earth and Mars atmospheres, adapted from [53] . . . . .	58
1.25	MHD power available vs. time for 1000 kg ballistic test vehicle simulation at Mars, adapted from [55] . . . . .	59
1.26	Mars Pathfinder vehicle forebody equipped with a 1.0 T electromagnet for simulation, adapted from [53] . . . . .	61
1.27	Mars pathfinder forebody drag with and without a 1.0 T magnetic field. Inflow velocity $V_\infty = 7431.3 \text{ m/s}$ and atmospheric conditions for 70 km MOLA altitude, adapted from [53] . . . . .	61
2.1	Conceptual design tool framework for MHD interaction during planetary entry. . . . .	70

2.2	Post-shock scalar electrical conductivity $\frac{1}{\Omega m}$ as a function of Mars altitude and vehicle velocity . . . . .	72
2.3	Post-shock scalar electrical conductivity $\frac{1}{\Omega m}$ as a function of Earth altitude and vehicle velocity . . . . .	72
2.4	$C_{power}$ example correlation based on MHD power available vs. time profile results presented in [55]. Reconstructed trajectory altitude-velocity history is input into the developed thermochemical model to calculate electrical conductivity. Magnetic field strength is fixed at $B = 0.2 T$ . . . . .	78
2.5	Ragone plot for electrical energy storage systems under consideration. Example MHD energy generation minimum performance requirement calculation result shown. . . . .	84
2.6	Electrical energy storage system model flowchart . . . . .	86
2.7	Direct entry power generation profile for Moses test vehicle . . . . .	87
2.8	Percent available energy stored for Moses test vehicle direct entry case, mass constrained to 100 kg . . . . .	89
2.9	Simulated ballistic entry trajectories for Mars 7 km/s entry condition . . . . .	90
2.10	Power available for extraction via MHD energy generation for Mars 7km/s Entry Condition . . . . .	92
2.11	Sensitivity of percent energy stored to EES mass constraint for the 7 km/s Mars entry condition . . . . .	94
2.12	1% K seed Mars Pathfinder altitude versus velocity curves for various B field magnitudes. . . . .	96
2.13	1% K seed Mars Pathfinder total deceleration versus altitude for various B field magnitudes . . . . .	97
3.1	MHD energy generation for planetary entry vehicles experimental design schematic . . . . .	102
3.2	MHD energy generation for planetary entry vehicles solid model design implementation . . . . .	102
3.3	Actual final experimental assembly. Gas flow is from left to right as pictured.	103

3.4	High-Power Electric Propulsion Laboratory Vacuum Test Facility-1. . . . .	104
3.5	HPEPL VTF-1 Twin dual-stage mechanical pumping systems. . . . .	105
3.6	HPEPL VTF-1 pump manifold ISO-K 250 end flange with a custom adapter to KF40 flange installed. . . . .	106
3.7	Experiment 2-inch stainless-steel vacuum gas exhaust line, with right angle isolation valve connection to VTF-1 manifold end-flange. . . . .	109
3.9	Experiment MKS 1162B MFM/MFC calibration. Calibration date is Au- gust 2016. Calibration range is 0 - 500 <i>sccm Ar</i> . . . . .	112
3.10	Experiment quartz converging-diverging nozzle sizing process . . . . .	115
3.11	Required mass flow rate in <i>sccm Ar</i> vs. exit Mach number, $M$ , for 34.1 <i>mm</i> exit diameter and 5.6 <i>Torr</i> upstream $P_t$ at $T_t = 300 K$ . . . . .	116
3.12	Quartz nozzle design submitted for glassblowing, dimensions in inches . . .	117
3.13	Physical quartz tube-nozzle assembly implementation. RF antenna coil is shown upstream of nozzle inlet. Distance between quartz tube vacuum compression fittings is approximately 9 <i>in.</i> . . . . .	117
3.14	Schematic of final delivered quartz nozzle, updated with actual dimensions.	118
3.15	RF generator (left) and variable capacitance impedance matching network (right). . . . .	119
3.16	Top view of 4-turn coil constructed of 1/4-inch water-cooled copper tubing. Antenna placement is upstream of nozzle throat. Gas flow from left to right as pictured . . . . .	119
3.17	‘Gamma’ and ‘L’ RF matching network topologies . . . . .	121
3.18	Advanced Energy model VM2715AW impedance matching network con- figuration with water-cooled 6-turn tune-coil connected for 6 active coils in L-match topology. . . . .	123
3.19	Thin copper strap connection between the matching network output and water-cooled copper RF antenna coil. . . . .	124
3.20	Stainless-steel mesh custom Faraday cage implementation surrounding RF antenna and experimental test-section. . . . .	126

3.21	RF test pulse side view, gas flow from left to right. . . . .	128
3.22	RF test pulse top view . . . . .	128
3.23	Test chamber instrumentation. . . . .	129
3.24	Test chamber gauge readouts. Upstream pressure is $0.75 \text{ Torr}$ , downstream pressure is $0.518 \text{ Torr}$ , and mass-flow rate readout is $0.241 \text{ V}$ , as described in section 3.1.2. . . . .	131
3.26	Oscilloscope data acquisition system. Channel 2 (blue) shows forward RF power $5000 \text{ ms}$ pulse output with maximum of $8 \text{ VDC}$ ( $800 \text{ W}$ ). Test-section thermocouple readout shown at right. . . . .	133
3.28	MMA Side view, with the thermocouple probe (white) installed in the model mount block. Also pictured is model mount extension tube (bottom left) . . . . .	135
3.29	MMA top view with precision linear feedthrough adjustment (bottom cylinder). . . . .	136
3.30	Model mount block front view. $0.257 \text{ in}$ center model mount hole, and $0.128 \text{ in}$ probe mount holes shown at each corner. Type0K thermocouple interface (bottom) and model electrode interface (top) connections shown . . . . .	137
3.31	Model mount assembly BNC interface. Passes signal from model electrodes (red-green, black-green) and Type-K thermocouple (red, yellow) Only BNC center pins are used, as outer pins are chamber ground. . . . .	138
3.32	MMA in lubricated sliding track for test section insertion alignment. . . . .	140
3.33	MMA laser-leveling process to ensure model centering in test-section. . . . .	141
3.34	Model fully extended, with front of model coincident with nozzle throat. . . . .	142
3.35	Linear micrometer feedthrough in fully extended position. . . . .	143
3.36	Test schematic to visualize and confirm supersonic flowing plasma shock wave. . . . .	145
3.37	Test implementation to visualize and confirm supersonic flowing plasma shock wave. . . . .	145
3.38	Shock wave for model located $1.000 \text{ in}$ from the throat, $600 \text{ W}$ forward RF power, and $15,380 \text{ sccm Ar}$ mass flow rate. Side view. . . . .	146

3.39	Shock wave for model located 1.000 <i>in</i> from the throat, 600 <i>W</i> forward RF power, and 15,380 <i>sccm Ar</i> mass flow rate. Top view. . . . .	146
3.40	Shock wave for model located 2.000 <i>in</i> from the throat, 800 <i>W</i> forward RF power, and 9,300 <i>sccm Ar</i> mass flow rate. Side view. . . . .	147
3.41	Experimental schematic to characterize test section aerothermal environment.	148
3.43	MEDTHERM thermocouple in supersonic plasma discharge. 800 <i>W</i> forward RF power, 9,300 <i>sccm Ar</i> (3 <i>V</i> ) gas mass flow rate. Measured temperature is approximately 1215 <i>K</i> . . . . .	149
3.44	Adiabatic choked flow check value for test section, ratio of measured upstream pressure to mass flow rate. No added RF power upstream of nozzle throat. . . . .	151
3.45	Choked flow check value for test section, ratio of measured upstream pressure to mass flow rate. RF power deposition of 400 <i>W</i> upstream of nozzle throat. . . . .	152
3.46	Choked flow check value for test section, ratio of measured upstream pressure to mass flow rate. RF power deposition of 600 <i>W</i> upstream of nozzle throat. . . . .	153
3.47	Choked flow check value for test section, ratio of measured upstream pressure to mass flow rate. RF power deposition of 800 <i>W</i> upstream of nozzle throat. . . . .	154
3.48	Nozzle shock location computation schematic. . . . .	158
4.1	Representative blunt-body MHD energy generator model design, dimensions in inches (front view). Cylindrical ceramic model body with rare-earth permanent magnets and 90-degree arc length sheet metal electrodes. .	167
4.2	Finite element simulation results of parallel (left) and Anti-parallel (right) magnetic dipole orientations. Top view. . . . .	168
4.3	Side view of MHD energy generator model design, showing dimensions in inches and magnet offset from forebody surface . . . . .	170
4.4	Back view of MHD energy generator model design, showing dimensions in inches and locations of the magnet and mounting holes . . . . .	172

4.5	Selected model permanent magnet geometry front(left) and side(right views). Diameter dimension $D = 4 \text{ mm}$ (0.158 <i>in</i> ), thickness dimension $T = 3 \text{ mm}$ (0.118 <i>in</i> ). Magnetic dipole moment aligned with the cylinder axis. . . . .	173
4.6	90 Degree final MHD energy generator model drawing for manufacturing. All dimensions in inches. . . . .	174
4.7	45 Degree final MHD energy generator model drawing for manufacturing. All dimensions in inches. . . . .	175
4.8	0 Degree final MHD energy generator model drawing for manufacturing. All dimensions in inches. . . . .	176
4.9	CNC milling process for MHD energy generator models. Material is 0.375 <i>in</i> thick Boron-Nitride ceramic plate. . . . .	177
4.10	Example MHD model after machining with hole for electrode wire. 45 Degree variation, as shown in Figure 4.7, back view. . . . .	178
4.11	Tantalum foil electrode water-jet process. Design dimensions of 0.375 <i>in</i> x 0.375 <i>in</i> manufactured to a tolerance of 0.001 <i>in</i> . . . . .	179
4.12	Tantalum foil electrode spot-welding to 0.010 <i>in</i> diameter Nickel-Chromium wire. . . . .	180
4.13	MHD model components. MHD model body, electrodes, and permanent magnets shown at left, and 6 <i>in</i> length 1/8 <i>in</i> diameter double-bore ceramic model mount tube shown at right. Also pictured is 1/4" model mount structural support tube, right. . . . .	181
4.14	MHD model sub-assemblies on a plate for oven-curing. . . . .	183
4.15	MHD model electrode wire solder extension to sliver-coated, Teflon insulated 24- <i>AWG</i> hookup wire for reduced lead resistance and model placement flexibility. . . . .	183
4.16	Example fully-assembled MHD model. 90-degree model type, parallel magnetic dipole alignment. . . . .	184
4.17	Type-K spot-welded thermocouple junctions and 90, 45, and 0-degree MHD model variations sub-assemblies. Assembled and cemented with ceramic paste to facilitate MHD model thermal response characterization . . . . .	184

4.18	Full set of assembled 0 degree and 90 degree MHD energy generator model variations. $N = 3$ each for versions with embedded magnets and two control models without magnets. Total of 14 assembled models. . . . .	186
4.19	Thermocouple embedded inert MHD model bodies for thermal response characterization. One of each of 90, 45, and 0-degree model variations respectively. . . . .	187
4.20	MHD energy generation for planetary entry experimental schematic. . . . .	188
4.21	Model thermal response characterization test. Condition 1, $P_{RF} = 400 W$ , MFC set-point voltage of 3 V or approximately 9,300 <i>sccm</i> Ar test gas mass flow rate. 0-degree based MHD model body variation with embedded thermocouple. . . . .	192
4.22	Model thermal response characterization test. Condition 4, $P_{RF} = 800 W$ , MFC set-point voltage of 5 V or approximately 15,300 <i>sccm</i> Ar test gas mass flow rate. 90-degree based MHD model body variation with embedded thermocouple. . . . .	193
4.23	Condition 2, trial 2 voltage across model 1 electrodes with no load (open) circuit configuration and average steady-state value. Also shown is generator RF power output reaching steady-state of 400 W in less than 1 s. . . . .	195
4.24	Condition 2, trial 2 voltage across model 1 electrodes with load circuit configuration and average steady-state value. Also shown is generator RF power output reaching steady-state of 400 W in less than 1 s. . . . .	195
4.25	Test condition 1 photo, test gas mass flow rate set-point of 3 V and forward RF power level of 400 W. Model 5, open circuit configuration. . . . .	196
4.26	Test condition 2 photo, test gas mass flow rate set-point of 5 V and forward RF power level of 400 W. Model 5, open circuit configuration. . . . .	196
4.27	Test condition 3 photo, test gas mass flow rate set-point of 3 V and forward RF power level of 800 W. Model 5, open circuit configuration. . . . .	197
4.28	Test condition 4 photo, test gas mass flow rate set-point of 5 V and forward RF power level of 800 W. Model 5, open circuit configuration. . . . .	197
4.29	Calculated resistive load dissipated power, $P_{MHD}$ , for all models and test conditions. . . . .	198
4.30	Calculated generator load factor, $K_{MHD}$ , for all models and test conditions. . . . .	200

4.31	Calculated dissipated power in resistive load, $P_{MHD}$ , for test condition 2. 5 V ( 15,300 sccm Ar mass-flow rate set-point, 400 W RF power) . . . . .	201
4.32	Calculated dissipated power in resistive load, $P_{MHD}$ , for test condition 3. 3 V ( 9,300 sccm Ar mass-flow rate set-point, 800 W RF power) . . . . .	201
4.33	Calculated generator load factor, $K_{MHD}$ , for test condition 2. 5 V ( 15,300 sccm Ar mass-flow rate set-point, 400 W RF power) . . . . .	202
4.34	Calculated generator load factor, $K_{MHD}$ , for test condition 3. 3 V ( 9,300 sccm Ar mass-flow rate set-point, 800 W RF power) . . . . .	202

## SUMMARY

Proposed missions such as a Mars sample return mission and a human mission to Mars require landed payload masses in excess of any previous Mars mission. Whether human or robotic, these missions present numerous engineering challenges due to their increased mass and complexity. To overcome these challenges, new technologies must be developed, and existing technologies advanced. Resource utilization technologies are particularly critical in this effort. This thesis aims to study the reclamation and harnessing of vehicle kinetic energy through magnetohydrodynamic (MHD) interaction with the high temperature entry plasma. Potential mission designs, power generation and power storage configurations are explored, as well as uses for the reclaimed energy. Furthermore, the impact and utility of MHD flow interaction for vehicle control is assessed. The state of the art for analysis of MHD equipped planetary entry systems is advanced, with the specific goals including: development of performance analysis capabilities for potential MHD equipped systems, identification of systems or configurations that show promise as effective uses of MHD power generation, experimental designs for developing technologies applicable to MHD power generation systems, assessment of MHD flow interaction and beneficial use for entry vehicle control through drag modulation, and increasing the technology readiness level of MHD power generation architectures for entry, descent and landing

# CHAPTER 1

## INTRODUCTION

### 1.1 Introduction: Planetary Entry, Descent, and Landing

When a spacecraft makes an initial approach to a planetary body, it must reduce its relative velocity to that body from orbital or super-orbital speeds of multiple kilometers per second to zero in order to ensure a safe landing on the surface of that body. This sequence of events is called planetary entry, descent, and landing (EDL), which refers to the sequence of maneuvers, operations, and events that bring a spacecraft or probe from an initial encounter with a planetary body to a final resting state on the surface of that body. Though usually only representing a small fraction of the overall mission, lasting minutes or hours in comparison to a total of months or years for most interplanetary missions, EDL operations are absolutely critical to mission success and are the subject of much of the engineering challenges associated with interplanetary spaceflight, driving requirements for the entire mission in many cases.

In the 2015 National Aeronautics and Space Administration’s (NASA) technology roadmap: “Entry, descent and landing (EDL) is defined to encompass the components, systems, qualification, and operations to safely and usefully bring a vehicle from approach conditions to contact with the surface of a solar system body, or to transit the atmosphere of the body.” [1].

Though this definition technically includes planetary bodies without an atmosphere such as the Moon, this thesis focuses on planetary bodies with an atmosphere such as the Earth or Mars. The addition of an atmosphere provides a useful tool for deceleration through aerodynamic drag; however, this high-speed aerodynamic interaction produces numerous additional engineering challenges not present with airless bodies. In particular,

these differences are most apparent during the entry phase, in which the vehicle transitions from an initial orbital or super-orbital hypersonic speed to the lower supersonic or subsonic speeds during which the descent phase is initiated.

During this largely hypersonic vehicle entry phase, the gas flow in the shock layer around the vehicle is highly heated, and is usually heated to such a degree that ionization is present. Engineering challenges during this phase include adequate thermal protection of the vehicle from significant convective and / or radiative heat transfer, as well as structural considerations due to peak decelerations and aerodynamic pressures within this regime. Other engineering challenges can also arise due to the presence of the ionized gas in the shock layer, such as partially or totally impeded radio communications, or ‘blackout.’ The complex engineering challenges during this phase of spaceflight have been the subject of many studies, research, and development since the dawn of the space-age in the early 1950s, and remain a subject of intense interest and engineering development today.

In this thesis, the ‘entry’ phase of EDL is the primary subject of interest. The engineering challenges during this mission phase are significant, and in the case of Mars entry, are so significant that they drive system requirements and capabilities for the entire mission. The gap between current system capabilities for Mars EDL such as landed mass, landing accuracy, and landed elevation and required future system capabilities for planned robotic and human exploration is measured by multiple orders of magnitude [2]. As a result, future exploration of Mars will require significant technology investment and development in the entry system, and is the motivation for the investigation presented by this thesis.

## **1.2 Motivation: Mars, Entry, Descent, and Landing**

Though EDL operations have been successfully conducted by the United States and others on various planetary bodies with an atmosphere including Earth, Mars, Venus, and Titan, Mars EDL presents unique and complex engineering challenges that have driven Mars planetary exploration mission design since the 1970s. [2]

Although Mars has an atmosphere, the atmospheric pressure and density are less than 1% of the surface values for Earth [3], while the surface gravity is a significant fraction of that at Earth,  $3.71 \text{ m/s}^2$  for Mars vs.  $9.81 \text{ m/s}^2$  for Earth, or approximately 38% of Earth's surface gravity. Thus, for Mars, a situation is present in which the gravitational interaction is a significant relative to Earth, pulling a spacecraft or probe towards the surface, but with significantly impaired aerodynamic deceleration capability relative to Earth. Typical planetary entry velocities at Mars range from  $5 - 7 \text{ km/s}$ , while planetary reentry velocities at Earth typically range from  $7 - 12 \text{ km/s}$ . [2]

Though Mars entry velocities, surface gravity, and atmospheric density are lower than those for Earth, the speeds are still well into the hypersonic regime, and there is significant aerodynamic heating that is present. The high speeds make propulsive deceleration extremely cost-prohibitive, and the aerodynamic heating makes hypersonic retro-propulsion infeasible from an engineering standpoint, leading to aerodynamic drag being used for deceleration in the hypersonic entry phase for all previous Mars missions. Thus, there is a situation in which the atmosphere is too “thin” to provide good deceleration, but is thick enough to require a thermal protection system during the hypersonic phase of entry to deal with aerodynamic heating.

Due to the limited Mars atmospheric density, Mars entry vehicles require a high hypersonic drag area,  $C_D A$ , to achieve sufficient aerodynamic drag as well as a blunt vehicle forebody to deal with the intense aerodynamic heating loads. The entry vehicle mass is limited by the aerodynamic drag capability, subject to the square-cube mass scaling law, with drag area being proportional to the linear dimension squared, and vehicle mass being proportional to the linear dimension cubed. This relation of aerodynamic deceleration to gravitational acceleration is captured by the ballistic coefficient  $\beta$ , defined below as

$$\beta = \frac{m}{C_D A} \quad (1.1)$$

where  $m$  is the vehicle mass,  $C_D$  is the vehicle's hypersonic drag coefficient, and  $A$

is the vehicle's characteristic drag area. High mass planetary entry systems tend to have high ballistic coefficients, which are unfavorable for planetary entry, due to their reduced capability to decelerate effectively through aerodynamic drag alone. At Mars, this effect is one of the primary reasons for the difficulty in landing high-mass systems, with the highest ever delivered payload mass being approximately 1 *MT* with the landing of the Mars Science Laboratory (MSL) Curiosity Rover in 2012. [4]

### 1.3 Previous Mars EDL System Architectures

Landing on Mars is fraught with engineering challenges, and there have been many failures. Landings have been attempted by the United States, the former Soviet Union (USSR), and the European Space Agency (ESA). Of these three entities, only the United States has been completely successful in delivering spacecraft to the Martian surface.

Landing on Mars is also challenging due in part to the significant variability in atmospheric and landing site conditions. The Martian atmosphere is approximately 95% carbon-dioxide [3], and the atmospheric density can change by as much as 40% over a Martian year, or about two Earth years, due to sublimation of carbon-dioxide trapped as dry-ice at the Martian poles. Moreover, Mars Orbiter Laser Altimeter (MOLA) measurements of surface elevation reveal tremendous variability in the altitude and thus the density of the Martian surface, covering a range of nearly 16 *km* from the lowest to the highest point [2]. Many scientifically interesting landing sites are located above +2 *km* MOLA elevation, and have been out of reach for all Mars landers prior to 2012 due to the reduced time for terminal descent and lower atmospheric density.

Despite the complex engineering challenges, there have been seven successful Mars landings by the United States. The first two were the result of a pioneering effort in the 1970s, the Viking I and II landers, both landing in 1976. Afterward, there was a more than 20 year-gap in the next successful landing attempt, the Mars Pathfinder Mission in 1997. The success of Mars Pathfinder followed by the successful landing of the two Mars

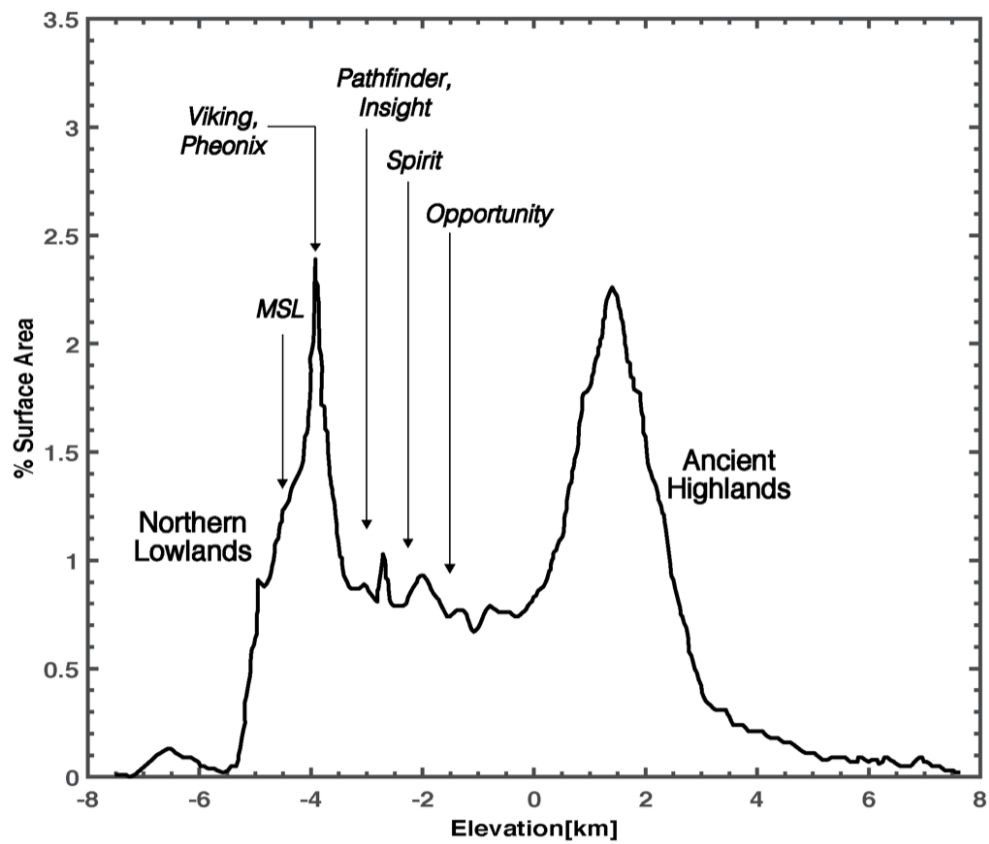


Figure 1.1: MOLA Elevation Histogram [2]

Exploration Rovers (MER), Spirit and Opportunity, in 2004. The Phoenix lander followed in 2008, and another successful Mars landing followed with the delivery of the Mars Science Laboratory (MSL) Curiosity Rover in 2012. Finally, the Mars Insight Lander, based on the Phoenix Lander EDL system, had a successful Mars Landing in November 2018, making the total number of successful Mars landings by the United States eight at the time of writing this thesis.

Each successful Mars landing to date has heavily leveraged technology originally developed for the Viking missions [2]. Technology development for the Viking missions spanned several years, leveraging lunar lander heritage for terminal descent and landing, and was not constrained by the relatively smaller budgets allocated to planetary exploration missions today. No single technology satisfied the mission requirements of a rigid aeroshell and thermal protection system for hypersonic entry combined with the large drag areas necessary for supersonic descent and terminal landing. As a result, a novel mission architecture was proposed that has largely been left intact in every subsequent Mars landing. The portion of this architecture that has been repeated for every Mars landing consists of a rigid 70-degree sphere-cone aeroshell forebody geometry for hypersonic entry and a supersonic disk-gap-band parachute for supersonic and subsonic descent.

The material and structural constraints on parachute size and deployment conditions, combined with the difficulty in reaching those deployment conditions with sufficient time for terminal descent and landing in the thin Martian atmosphere after hypersonic entry, constitute a limit in the payload mass that can be delivered to the surface. This limit may have been reached with the 1 *MT* payload mass delivered during the MSL landing in 2012, and may actually only be 2 *MT* in ideal landing conditions such as the season for peak Martian atmospheric density and a low Martian elevation landing site. [2] This number is an order of magnitude lower than the higher landed masses of 20 *MT* expected for future Mars exploration, and illustrates a clear need for additional EDL technology development effort to meet these future requirements.

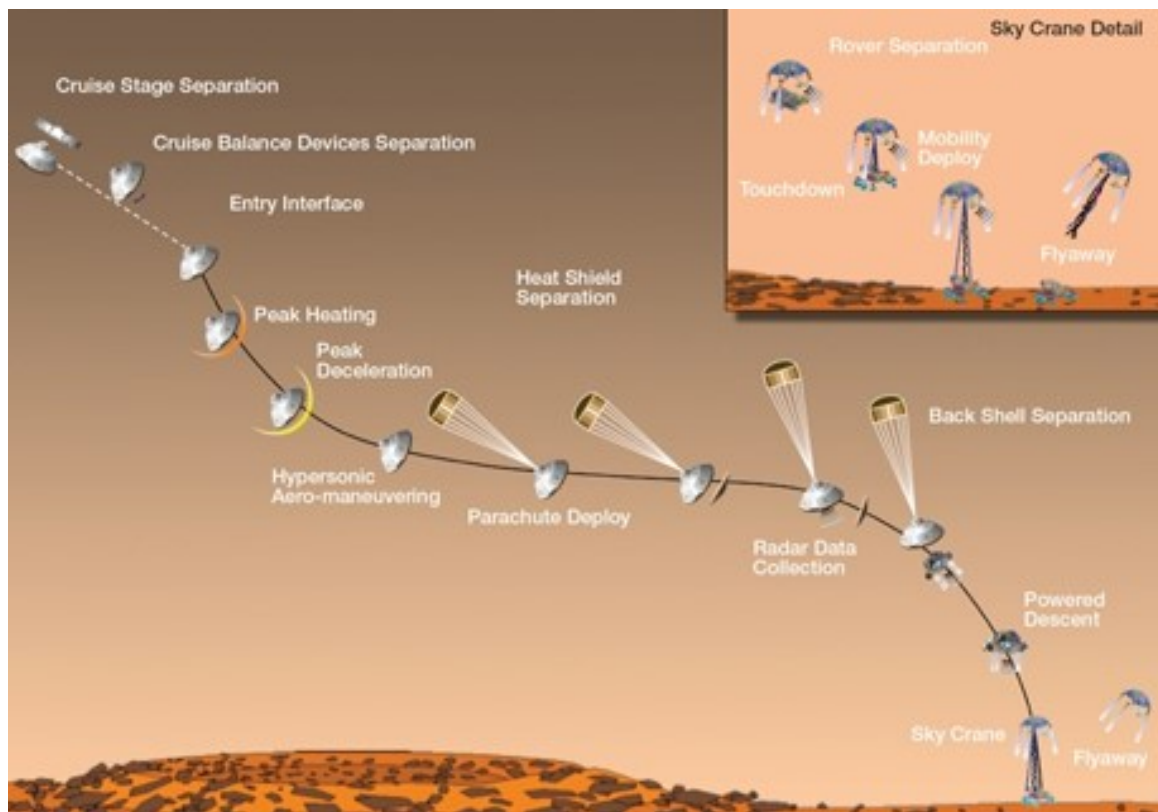


Figure 1.2: Mars Science Laboratory EDL Sequence [NASA Jet Propulsion Laboratory]

Table 1.1: Previous Successful Mars Entry Parameters [2] [5]

Mars Entry System	Entry Mass ( $MT$ )	Aeroshell Diameter ( $m$ )	$\beta(\frac{kg}{m^2})$
Mars Pathfinder	0.58	2.65	63
Mars Exploration Rover (MER)	0.83	2.65	94
Mars Phoenix Lander	0.60	2.65	70
Mars Science Laboratory	3.15	4.50	145

### 1.3.1 High-Mass Mars EDL Challenges

Future missions to Mars such as a Mars sample return mission and potential human mission will require much higher masses than have ever been delivered to the Mars surface. Previous Mars missions have relied primarily on Viking era technologies for entry descent and landing.[2] As mentioned previously, the limit of these technologies may have been reached with the MSL mission, with a landed mass capability of approximately 1  $MT$ . The maximum feasible limit for these technologies is expected to reach approximately 2  $MT$  in ideal conditions. However, even this ideal limit is dwarfed by the 40-80  $MT$  projected landed masses required for Human exploration at Mars.

Landing such large masses at Mars requires a simultaneous improvement in several different phases of EDL. For hypersonic entry, the two most important parameters which govern performance are the ballistic coefficient,  $\beta$ , which is ideally as low as possible, and increased vertical lift without significant reduction in drag, or a high  $L/D$  ratio.

Hypersonic drag coefficient  $C_D$  only varies from approximately 1 - 2 through selection of variation of the fore-body geometry. The 70-degree sphere-cone shape has a hypersonic drag coefficient of approximately 1.67, and cannot be significantly improved upon through selection of a different geometry. Thus, the only feasible option to reduce the ballistic coefficient  $\beta$  is to increase the aeroshell diameter. Projected maximum launch fairing diameters through the middle of the 21st century give a maximum rigid aeroshell diameter of approximately 10  $m$ . [1] This constraint leaves inflatable technologies such as the hy-

personic inflatable aerodynamic decelerator (HIAD) and deployable technologies such as the Adaptable, Deployable Entry Placement Technology (ADEPT) as the only options for increasing aeroshell diameters beyond 10 *m* without in-space assembly. [1]

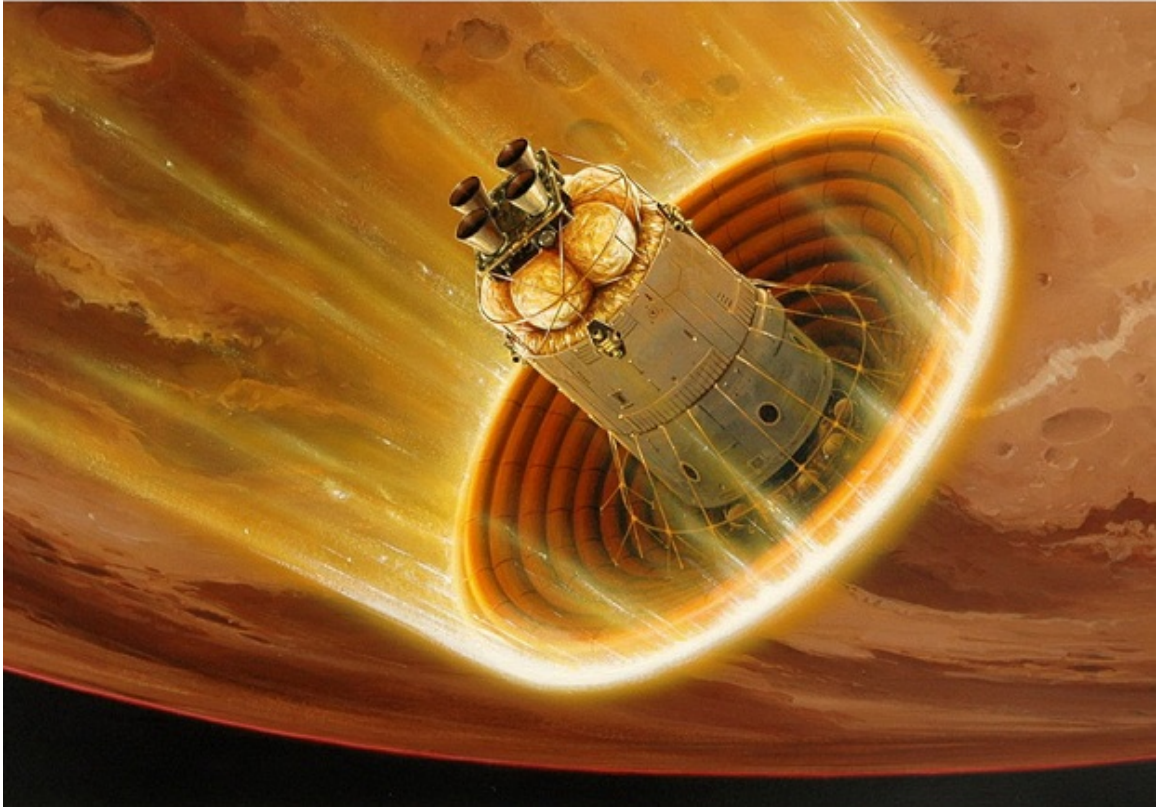


Figure 1.3: HIAD Concept [NASA Langley Research Center]

For hypersonic planetary entry at Mars for a 100 *MT* entry mass and 15 *m* diameter aeroshell,  $L/D > 0.3$  with most of the aerodynamic drag retained is sufficient to achieve mission requirements. [2] Currently this  $L/D$  ratio can only be achieved through angle-of-attack modulation to 20 degrees for the 70-degree sphere-cone geometry, which comes at a penalty to the hypersonic drag coefficient. Moreover, this trim angle of attack is typically achieved via center of gravity offset for the symmetrical 70-degree sphere-cone geometry, which is more difficult for the larger entry masses and aeroshell diameters required of human-scale Mars missions. In addition, for inflatable and deployable aeroshell technologies such as HIAD and ADEPT, this relatively high  $L/D$  is only achievable through hypersonic trim-tabs or shape augmentation, which can result in undesirable localized aero-

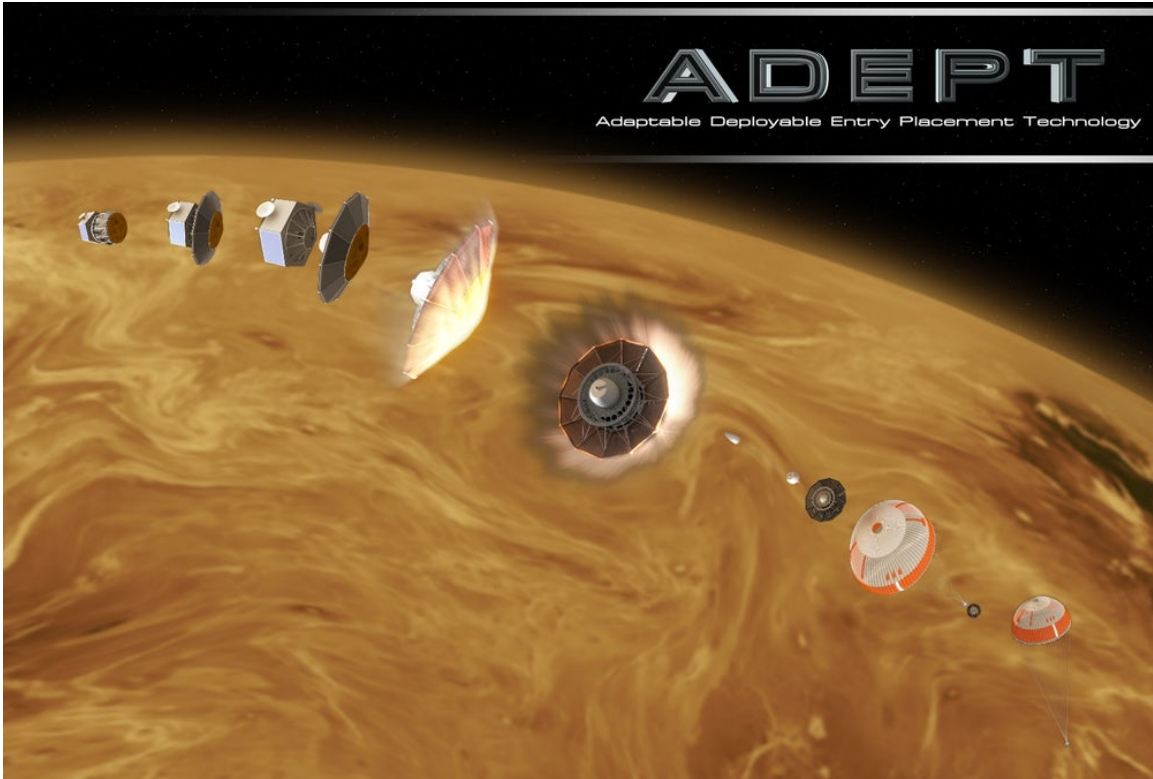


Figure 1.4: ADEPT Concept [NASA Ames Research Center]

dynamic heating in addition to the aerodynamic drag penalty.

For both parameters, there is difficulty in meeting the technical performance requirements necessitated for future Mars exploration, and there are limited options for doing so with the current state-of-the-art for EDL technologies. Thus, additional technology development in innovative concepts such as magnetohydrodynamic assisted planetary entry is necessary in order to enable future Mars exploration.

#### 1.4 Magnetohydrodynamics for Planetary Entry

To achieve humanity's goals for Mars exploration, significant technology development is required. Previous Mars missions have shown that greater than 90% of the vehicle's initial kinetic energy is dissipated during the hypersonic phase of entry, about 92.5% in the case of Mars Pathfinder.[6] During this hypersonic phase of entry, there exists a highly heated, ionized flow around the vehicle driven by the conversion of kinetic energy to thermal en-

ergy. The free electrons in the flow can be harnessed to create a sustained, usable electric current via magnetohydrodynamic (MHD) energy generation, reclaiming some of the vehicle's dissipated kinetic energy as well as increasing the decelerating body-force on the vehicle through the Lorentz force.

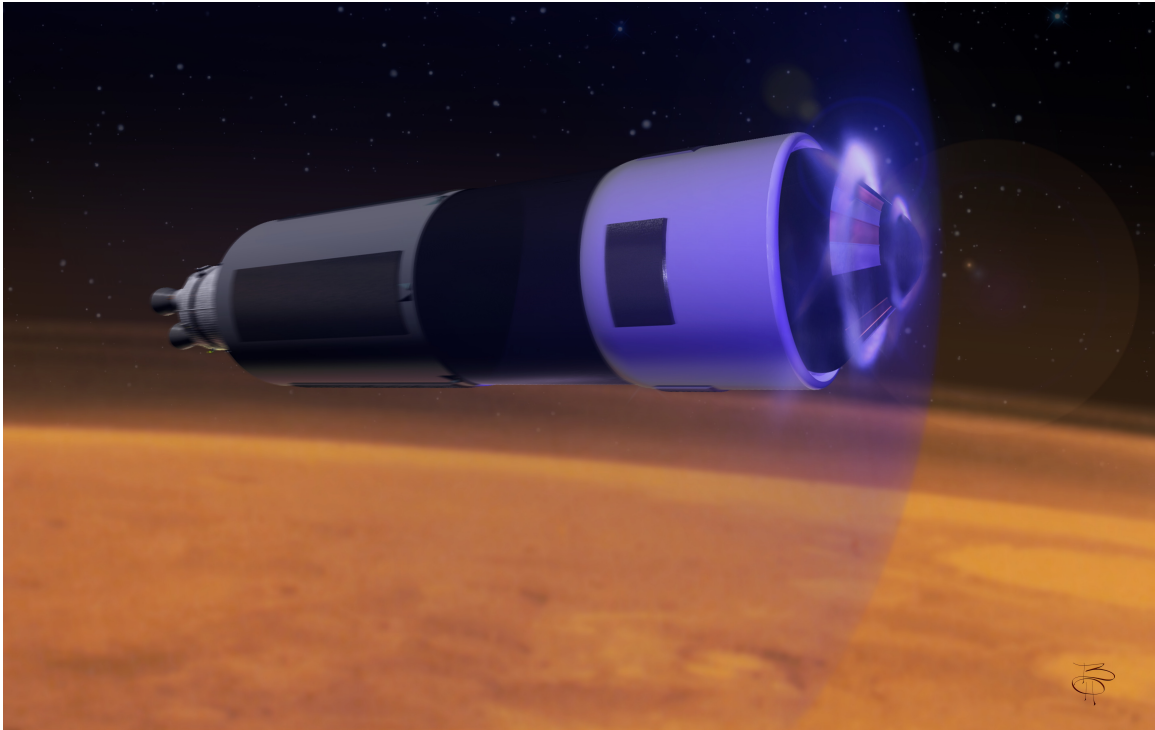


Figure 1.5: Artist Rendering of MHD During Planetary Entry [7]

The benefits of MHD energy generation for planetary entry vehicle are numerous. There are many potential uses of this electrical energy, including communications blackout mitigation, aiding ingestion of the atmosphere for resource utilization, and active thermal control of entry vehicle components.[8] Moreover, this energy could also be used to run key vehicle systems used during EDL at greater power levels, such as more powerful computers for image processing or more capable radar systems. In addition, this energy could be used to ingest and store the atmosphere for use as an oxidizer for retro-propulsion during the descent phase. [9][7]

When a magnetic field is applied to the ionized gas flow-field that exists around the vehicle during hypersonic entry, the charged particles tend to avoid crossing magnetic field

lines due to the Lorentz force, which acts as an additional body force to aerodynamic pressure on the flow-field. An example of this 'plasma drag' is shown as Figure 1.6. This force reacts in an equal and opposite manner through the on-board magnet embedded in the vehicle. Thus, a magnetohydrodynamic flow interaction is created which has the potential to increase the total drag force, lift force, and / or control moments acting on the vehicle in comparison to aerodynamic interaction alone. This control mechanism could increase the total hypersonic lift acting on the entry vehicle without significantly reducing the drag, a key technology requirement outlined for successful human-scale Mars missions. Moreover, increasing the drag through MHD interaction could result in a lower effective ballistic coefficient without increasing the aeroshell diameter, also a key technology requirement for human-scale mars missions.

In this thesis, the goal is to advance the state of the art for the performance analysis of planetary entry systems equipped with MHD energy generator and flow control devices. In particular, this investigation is motivated by the critical engineering challenges presented by Mars EDL operations, and presents results geared towards those applications. An overview of relevant background followed by a statement of research goals is presented in the remainder of this Chapter, which is followed by results and discussion pursuant to those goals as Chapters 2 - 4 and concluded with a summary of contributions and suggestions for future work as Chapter 5.

## **1.5 Plasma Physics**

### 1.5.1 What is a Plasma?

A plasma is an ionized, gaseous substance consisting of free positive and negative charges such that the substance becomes significantly electrically conductive. Because of this significant electrical conductivity coupled with free movement of charge carriers, long-range electromagnetic interactions can have a commensurate and greater significance to the particle dynamics than traditional gas kinetics. For this reason, a plasma is distinct from the

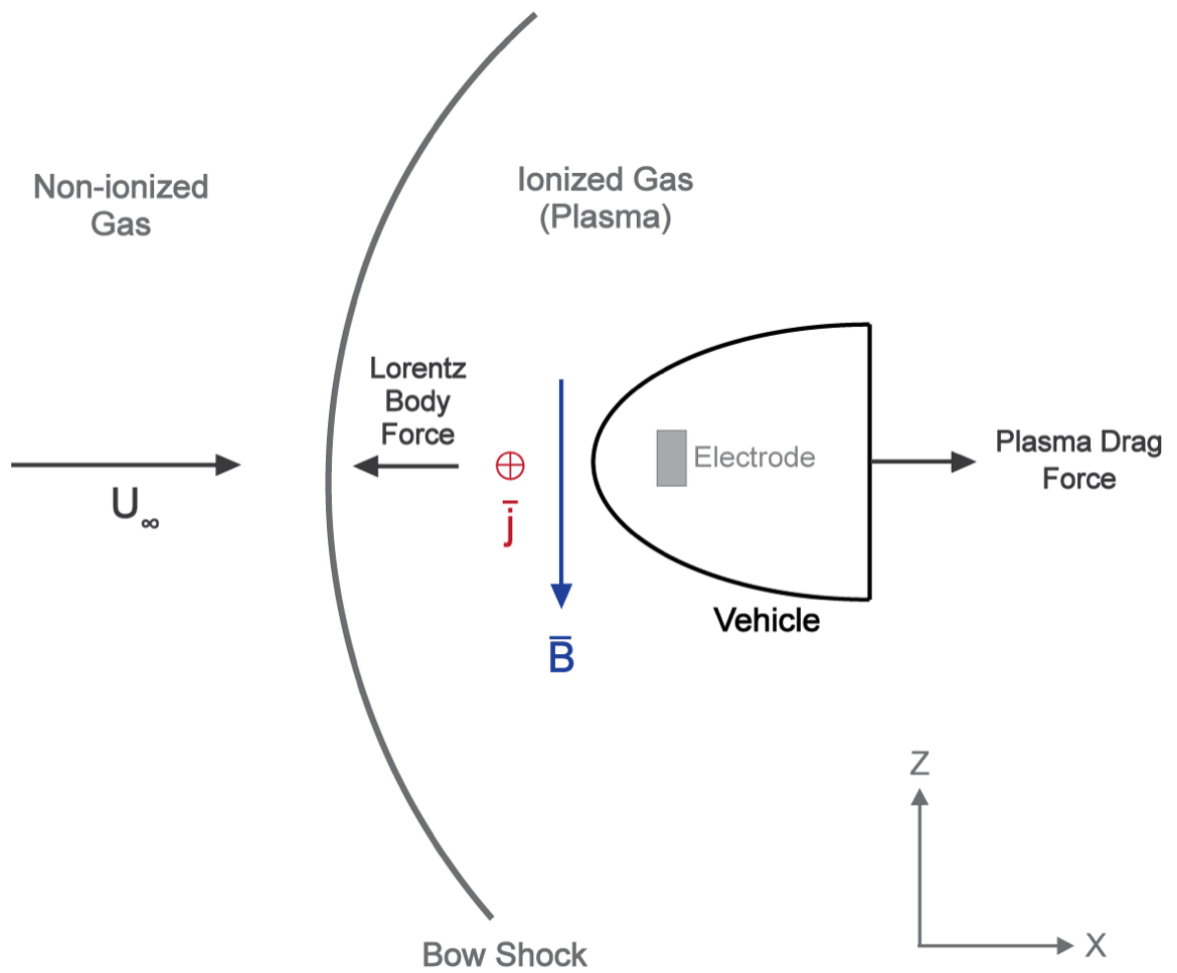


Figure 1.6: MHD drag force conceptual schematic for a representative blunt-body planetary entry vehicle.

traditional three states of matter, solid, liquid, and gas, and is known as the “fourth state of matter.”

The term plasma was first applied to this state of matter in the 1920s by Nobel Laureate Chemist and Physicist Irving Langmuir and comes from the Ancient Greek  $\pi\lambda\alpha\sigma\mu\alpha$ , meaning 'mold-able substance' or 'jelly', and describes the behavior of the fluid-like substance with floating positive and negative charges. [10]

### 1.5.2 Governing Forces

Because of the unbound nature of electrical charges in a plasma, it is not electrically neutral on a localized level. The mobility of charges combined with this potential for localized electrical non-neutrality makes plasmas also subject to long-range electrostatic and electromagnetic forces. These dynamics are in contrast to traditional gas kinetics in which the particles are subject to gravity only, and interact with their environment solely through collisions with either each other or fixed boundaries such as container walls.

The two additional forces that are of relevance to plasmas are the electrostatic, or *Coulomb* force, and the electromagnetic, or *Lorentz* force. These forces represent the electric and magnetic field influences, respectively.

The electrostatic, or Coulomb force, is part of the electromagnetic force, one of the traditional four fundamental forces of the universe, amongst gravity and the weak and strong nuclear forces. This force defines the interaction between two charged particles. Opposite charges experience an attractive force towards one another, and like charges experience a repulsive force away from each other. Consider a test particle with charge  $q$ , in the presence of another charged particle, with charge  $Q$ . The electrostatic force exerted on the test charge due to the charged particle can be stated as a mathematical equation. This equation, known as Coulomb's law after French Physicist Charles-Augustin de Coulomb, is given as follows:

$$\vec{F}_{coulomb} = k_e \frac{qQ}{r^2} \hat{r} \quad (1.2)$$

where  $q$  and  $Q$  are the signed charge magnitudes, the standard unit for which is the *Coulomb* (C),  $k_e$  is a constant of proportionality, known as Coulomb's Constant, and  $\vec{r}$  is a position vector pointing from charge  $Q$  to  $q$ . In standard meters-kilograms-seconds (mks) units, Coulomb's constant is given as:

$$k_e = \frac{1}{4\pi\epsilon_0} \quad (1.3)$$

where  $\epsilon_0$  is the absolute permittivity of free space, a physical constant given as  $\epsilon_0 = 8.987551787368 \times 10^9 \frac{N \cdot m^2}{C^2}$ .

The Coulomb force on a test charge can be generalized and expressed in terms of the electric field  $\vec{E}$ , a vector field that maps the net electrostatic force imparted on the test charge to each point in space. The expression for the electrostatic Coulomb interaction then becomes

$$\vec{F}_{coulomb} = q\vec{E} \quad (1.4)$$

In the simplest case of force due to only one other charged particle with charge  $Q$  as in 1.2, the electric field is simply:

$$\vec{E} = k_e \frac{Q}{r^2} \hat{r} \quad (1.5)$$

In reality, the electrostatic interaction is usually due to a collection of charged particles, whose effects linearly superimpose upon one another to create a net electric field effect. Though simple in theory, the sheer scale of the interactions in a typical plasma can lead to complex and often non-analytical expressions for  $\vec{E}$  that require additional theories or numerical approximations to solve.

In addition, because the Coulomb force is a force like any other, there is an associated potential,  $\phi$ , which can be calculated through integration through a length, such as the radial distance  $r$  from the charged particle. In its most basic form, for a single charged particle of charge  $Q$ , it is known as the bare Coulomb potential, and is given as:

$$\phi_r = \frac{Q}{4\pi\epsilon r} \quad (1.6)$$

The electrostatic forces and potentials given above only account for the forces due to the mere presence of electrical charges in the vicinity of one another. However, in reality, charged particles can move as well. In contrast to electrostatics, which only accounts for forces due to the presence of electrical charges, electrodynamics accounts for the motion of charged particles as well.

A moving charged particle or group of particles constitutes an electrical current, with areal density  $\vec{j}$ , which in turn induces a magnetic field,  $\vec{B}$ , through a relation known as Ampere's law, one of Maxwell's four relations. Making the assumption that the currents and displacements are of relatively low frequency compared to that associated with the speed of light,  $c$ , Ampere's Law is given in its differential form as:

$$\nabla \times \vec{B} = \mu_0 \vec{j} \quad (1.7)$$

Solving this differential equation gives the magnetic field  $\vec{B}$ . Analytical solutions exist for a series of classical geometries and boundary conditions. The *magnetic Lorentz force* that is exerted on a test particle of charge  $q$  moving through a magnetic field  $\vec{B}$  with velocity  $\vec{v}$  is:

$$\vec{F}_{magnetic} = q\vec{v} \times \vec{B} \quad (1.8)$$

The form of 1.8 also has another interesting consequence. Since the magnetic force  $\vec{F}_{magnetic}$  is everywhere mutually perpendicular to the velocity  $\vec{v}$ , it does no work on a

moving charge. This conclusion can be found through a simple derivation from the definition of work  $W$  defined in equation 1.9 as follows:

$$dW = \bar{F} \cdot d\bar{S} \quad (1.9)$$

From this definition, noting that the displacement  $d\bar{S}$  can also be expressed as  $d\bar{S} = \bar{v} \cdot dt$ , and letting  $\bar{F}_{magnetic}$  be the force we have:

$$dW_{magnetic} = q\bar{v} \times \bar{B} \cdot \bar{v}dt \quad (1.10)$$

Since by the definition of the cross-product, the vector  $\bar{v} \times \bar{B}$  is everywhere mutually perpendicular to the vector  $\bar{v}$ , the dot-product of these two vectors is zero, and we have:

$$dW_{magnetic} = 0 \quad (1.11)$$

Although no net work is done by the magnetic force, it does have an influence on charged particles by changing, or curling their trajectories, in a ‘gyrating’ motion. Magnetic fields do not create or destroy energy, but do prove very useful in converting energy from one form to another, for example as is done in an electrical motor, where electrical energy is converted to mechanical energy through interaction with a magnetic field. Of most interest to this thesis, another useful property of magnetic fields is that this process can be done in reverse, with mechanical energy converted into electrical energy through interaction with a magnetic field, as is done in conventional electrical power generation.

Thus, the electric field  $\bar{E}$  and the magnetic field  $\bar{B}$  are of great significance to the motion of particles with charge  $q$ . The forces imparted by these fields on a moving test particle with charge  $q$  and velocity  $\bar{v}$  can be combined into one empirical electromagnetic force, as is stated in the *Lorentz Force Law*, given below in equation 1.12

$$\bar{F}_{Lorentz} = q(\bar{E} + \bar{v} \times \bar{B}) \quad (1.12)$$

As plasmas consist of free, moving positive and negative charges, the Lorentz force plays a critical role in the behavior, dynamics, and physics of plasmas.

### 1.5.3 Characteristic Length Scales: The Debye Length

The presence of free positive and negative charges alone does not technically guarantee that a substance is a plasma. A plasma must also generally be quasi-neutral and exhibit bulk, or collective, behavior based on characteristic length scales such as the Debye length,  $\lambda_D$ .

The Debye length, named after chemist Peter Debye, describes the range of a charge carriers' electrostatic effect in a solution of other charge carriers. When a positive or negative 'test-charge' is introduced into a sea of other unbound charge carriers, electrostatic forces attract species of the opposite charge to surround the test charge. However, this effect also weakens the range and impact of the test charge by enhancing the local concentration of the opposite charge, or 'screening' the charge. Eventually, at a large enough radial distance away from the test charge, there is no net impact from the test charge's presence, and it has been fully screened. This 'screening' effect causes the electrostatic potential of the test charge to diminish with distance more rapidly than it otherwise would. The Debye length is a characteristic length scale that quantifies this 'screening' effect, and is defined such that the electrostatic potential from a test charge in a quasi-neutral solution of charge carriers is diminished by  $1/e$  for every Debye length,  $\lambda_D$ , in radial distance from that test charge.

Consider a particle with charge  $Q$ . The electric potential  $\phi$  due to the presence of this particle in isolation is the bare-coulomb potential reference in equation 1.6. When placed in a plasma of unbound charges and Debye length,  $\lambda_d$ , this bare-coulomb potential is 'screened' as follows:

$$\phi_{r,screened} = \frac{Q}{4\pi\epsilon r} e^{-\frac{r}{\lambda_d}} \quad (1.13)$$

The specific formulation of the Debye length  $\lambda_d$  is dependent on many different plasma

parameters, with different phenomenological factors having importance based on the validity of different simplifying assumptions. The formulation most appropriate to the type and regime of plasma must be selected to correctly calculate  $\lambda_d$  *a priori*.

#### 1.5.4 Definition of a Plasma

A useful definition of a plasma, as presented in Chen's 1984 Textbook, "*Introduction to Plasma Physics and Controlled Nuclear Fusion*" [11] states that:

*"A plasma is a quasineutral gas of charged and neutral particles which exhibits collective behavior."*

The meaning of the terms *quasineutral* and *collective behavior* are made clear through the characteristics of a plasma. As mentioned earlier, the presence of unbound positive and negative charge carriers alone does not make a substance a plasma, rather serving as only a necessary, but not sufficient condition. As an example, air at room temperature contains very small concentrations of free ions and electrons, but is not considered a plasma. Thus, there must be other characteristics that in concert, define a plasma. In practice, there are three characteristics that define a plasma: **significant bulk, or *collective behavior*, the validity of the plasma approximation, enabling *quasineutrality*, and sufficiently high plasma frequency.** These conditions are elucidated in more detail below.

**Significant bulk, or *collective behavior*:** In an ordinary gas or non-ionized substance, forces and molecular interactions are transmitted solely between direct collisions of atoms or molecules. The field of gas kinetics describes nearly all macroscopic fluid dynamics, whether they be the concept of 'pressure', sound wave propagation, viscous effects, and others as being caused or transmitted by direct collisions of particles. In this way, non-ionized gases can be said to exhibit local, or *non-collective* behavior, interacting with their environment through gravity alone and with other particles only when they approach within a few atomic radii. The unbound charged particles present in a plasma, however, can exhibit a totally different type of behavior. As mentioned in section 1.5.2, the Lorentz Force

law shows that individual charged particles can be subject to long-range interaction forces through electric and magnetic fields. These interactions enable bulk or *collective* behavior, without necessarily requiring collisions between particles. **A defining characteristic of plasmas is that this *collective behavior* is significant in comparison to the ordinary collisional gas dynamics.** In fact, for some plasmas, the long-range electromagnetic field effects are so strong that the effect of inter-particle direct collisions can be neglected entirely, and the plasma can be said to be *non-collisional*. This enables even plasmas such as those found in planetary magnetospheres like the one surrounding the Earth in outer space for several Earth radii, to exhibit *collective behavior* by forming large structures and conforming to magnetic fields, even though individual ions or electrons of the plasma do not collide frequently or at all. This criteria for *collective behavior* requires that the ionized solution be dense enough such that the Debye length, as mentioned in section 1.5.3, is smaller than the overall length scale of the problem  $\lambda_d \ll L$ .

**Validity of the plasma approximation:** As mentioned in section 1.5.3 the Debye length  $\lambda_d$  represents the length scale characteristic to the ‘screening’ of charge by other charged particles in an ionized solution. A Debye sphere is a sphere with radius equal to the Debye length. A common definition of the plasma parameter,  $N_D$ , is that it is equal to the number of unbound charge carriers, typically electrons, contained within such a Debye sphere. When the plasma parameter, is sufficiently large  $N_D \gg \gg 1$ , then a test charge, an ion for example, located in the center of the Debye sphere is effectively screened outside of the sphere. In this way, at locations outside a Debye sphere, the plasma is effectively electrically neutral, hence the term *quasineutral*. The term for this screening effect, *Debye Shielding*, makes a locally electrically non-neutral solution of charged particles globally electrically neutral, or *quasineutral*. **For this Debye shielding to be statistically valid and effective, a sufficiently high plasma parameter  $N_D \gg \gg 1$  is required and is necessary for an ionized solution to be considered a plasma.**

**Sufficiently high plasma frequency:** A third defining characteristic of plasmas in-

volves a parameter called the *plasma frequency*,  $\omega_p$ , given as equation 1.14.

$$\omega_p^2 = \frac{n_{e,i}e^2}{\epsilon_0 m_{e,i}} \quad (1.14)$$

where  $e$  is the fundamental charge,  $1.602 \times 10^{-19}C$ , and  $n_{e,i}$  and  $m_{e,i}$  are the number densities and mass of either the ions ( $i$ ) or electrons ( $e$ ). In most ionized gases, electrons are by far the more mobile charged species, due to their having the same charge magnitude as a proton, but less than 1% of the mass. In practice, one can associate a plasma frequency  $\omega_p$  with either ions or electrons, but it is the electron plasma frequency  $\omega_{pe}$  that defines the plasma dynamic response. [11] A defining characteristic of plasmas is that the plasma dynamic response occurs on a timescale faster than the other processes that may be occurring, represented by characteristic time  $\tau$ , such as

The three characteristics that define a plasma are summarized by:

$$\lambda_D \ll L \quad (1.15)$$

$$N_D \gg \gg 1 \quad (1.16)$$

$$\omega_{pe}\tau > 1 \quad (1.17)$$

### 1.5.5 Types of Plasmas

Although often seen exotic and relatively rare in daily life, hence the term '*fourth state of matter*,' plasmas are extremely common and prevalent in nature. Plasma is by far the most common state of matter in the known universe, with over 99% of matter existing as plasma, whether at the center stars such as the Sun or as part of the intergalactic or interstellar medium.[11]. On Earth, the relative scarcity of plasmas is an anomaly in comparison to the rest of the universe, and in fact, a necessary one, as life cannot coexist with the extreme

temperatures and conditions in which naturally occurring plasmas are typically found.

Examples of natural and man-made plasmas include: *laboratory gas discharges, controlled thermonuclear fusion, the ionosphere, planetary magnetospheres, solar plasmas, solar wind, the interstellar medium, the intergalactic medium,* and finally, of most relevance to this thesis, *atmospheric entry plasmas.*[12].

**Laboratory Gas Discharges:** This type of plasma involves a man-made ionized gas discharge in the laboratory. Common examples include plasmas in plasma screen televisions, arc-welding torches, plasmas in compact fluorescent lightbulbs, arc-jets, and many others. These typically exist at much higher temperatures than room temperatures, on the order of a few thousand degrees Kelvin, but usually with much lower densities than standard conditions.

**Controlled Thermonuclear Fusion Plasmas:** These plasmas exist as part of controlled thermonuclear fusion experiments, where the substance, typically isotopes of hydrogen, is heated to a level that enables significant fusion nuclear reactions to produce helium. The plasma temperatures here can reach similar magnitudes to those of the sun, on the order of  $10^8$  Kelvin, that no known material can withstand. As a result, such plasmas are typically 'magnetically confined' in specialized magnetic field geometries such as the nuclear fusion Tokamak. [13]

**Solar Plasmas** These plasmas comprise much of the known matter in the universe, and exist as, typically hydrogen, plasmas in stars such as the Sun. Compressed by gravity and heated to resulting thermonuclear temperatures, the hydrogen nuclei are stripped of their electrons and undergo nuclear fusion, producing the heat and light output from stars such as the Sun for millions or even billions of years. In addition to the high temperatures, solar plasmas can also have significant magnetic field effects or structures, such as 'loops' of solar plasma bound to magnetic field lines in the outer layers of the Sun. [14]

**Solar Wind** The solar wind is a continuous ejection of hydrogen ions and electrons from the Sun that fills the solar system. The primary source of interplanetary plasma in the Solar System, this plasma is ejected from the Sun's outer layer at velocities of up to 250 to 750  $\frac{km}{s}$ . It then goes on to interact with all the planetary bodies in the solar system, and is the original source of energy and particles for natural phenomena such as the Aurora Borealis, or 'Northern Lights.' [15]

**Planetary Magnetospheres:** These plasmas form around planetary bodies with significant internal magnetic fields such as the Earth. When the solar wind plasma impinges upon the planetary magnetic field, the typical dipole magnetic field lines are 'swept' or 'blown' back, and strong current systems and large scale plasma structures bound to the magnetic field lines on the order of several planetary radii are formed. Examples of planets with significant dipole magnetic fields are the Earth, Jupiter, and Saturn. The magnetic field of Jupiter is so strong that, its magnetosphere structure has an impact as far away as the orbit of Saturn. [15]

**The Ionosphere:** The ionosphere is a region of the Earth's upper atmosphere that has been partially ionized through photo-ionization interactions with the Sun's light. The mixture of both ionized and neutral gas molecules creates a collisional plasma that has a finite conductivity. This plasma is responsible for enhanced terrestrial radio transmission through signal reflection back to Earth as well as the natural aurora phenomena visible near the Earth's polar latitudes. [15]

**Interstellar and Intergalactic Mediums:** These types of plasmas refer to the extremely sparse particle medium that exists between stars in the galaxy and between galaxies in the universe respectively. These plasmas are affected and driven by the forces that have shaped the universe such as supernovae, radiative heating from stars, and compression by plasma shock waves, and cooling from thermal radiation. [12]

**Atmospheric Entry Plasmas:** These plasmas are created when a spacecraft or space ob-

ject such as an asteroid, moving at velocities on the order of multiple  $\frac{km}{s}$ , impinges upon the atmosphere of a planetary body such as Mars. The resulting hypersonic velocity drives rapid compression and heating of the atmosphere through a shock wave in front of the body, stripping electrons from the gas molecules and creating a partially or fully ionized plasma. These plasmas, and their impact and utility are the main focus of this dissertation and will be discussed in further detail later.

These plasmas exist in and cover a broad range of possible thermodynamic states in the known universe, with temperatures ranging from hundreds, thousands, or billions of degrees Kelvin. The region of temperature - density states in which plasmas typically exist is given as Figure 1.7.

Typical values of the plasma parameters for these various types of plasmas are given as Table 1.2.

Table 1.2: Approximate Plasma Parameters [12]

Plasma	$n_e(m^{-3})$	$T(K)$	$B(T)$	$\lambda_d(m)$	$N_D$	$\omega_p(\frac{1}{s})$
Laboratory Gas Discharge	$10^{16}$	$10^4$	–	$10^{-4}$	$10^4$	$10^{10}$
Nuclear Fusion (Tokamak)	$10^{20}$	$10^8$	10	$10^{-4}$	$10^8$	$10^{12}$
Solar (Core)	$10^{32}$	$10^7$	–	$10^{-11}$	1	$10^{18}$
Solar Wind	$10^6$	$10^5$	$10^{-9}$	10	$10^{11}$	$10^5$
Planetary Magnetosphere	$10^7$	$10^7$	$10^{-8}$	$10^2$	$10^{10}$	$10^5$
Ionosphere	$10^{12}$	$10^3$	$10^{-5}$	$10^{-3}$	$10^5$	$10^8$
Interstellar Medium	$10^5$	$10^4$	$10^{-10}$	10	$10^{10}$	$10^4$
Intergalactic Medium	1	$10^6$	–	$10^5$	$10^{15}$	$10^2$
Atmospheric Entry	$10^{18}$	$10^4$	–	$10^{-5}$	$10^4$	$10^{11}$

### 1.5.6 Plasma Modeling

Unlike the traditional fluids approach for gases, in which each species, for example oxygen is treated as a homogeneous whole with similar properties and temperatures, accurately modeling plasmas necessitate a more granular approach. The collective behavior dictated

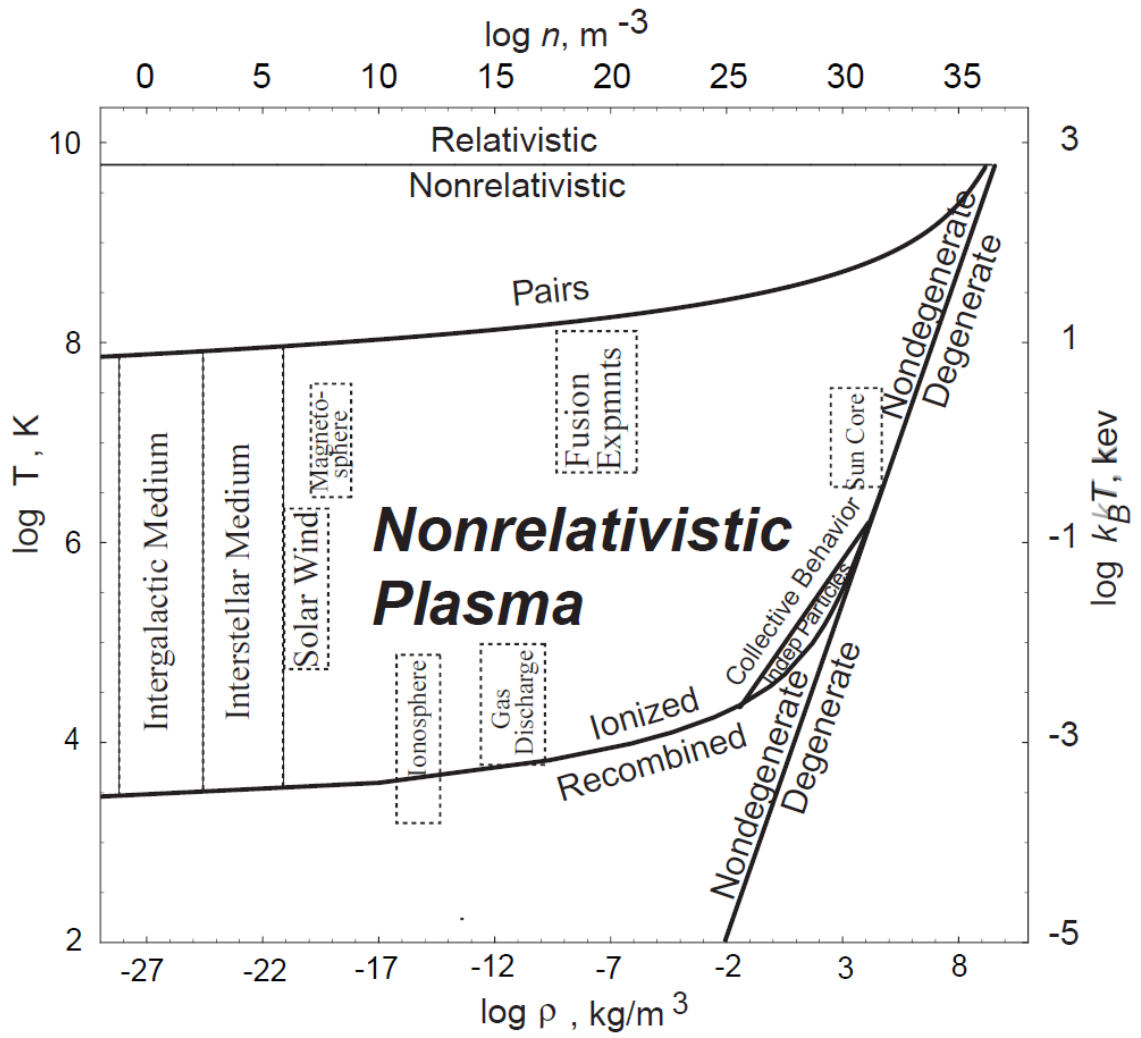


Figure 1.7: Density-temperature regime for hydrogen plasma [12]

by the electric and magnetic fields,  $\bar{E}$  and  $\bar{B}$ , is complicated by the fact that those fields themselves depend on the motion of each charged particle. Thus, the most technically accurate way to model plasma dynamics is to solve a self-consistent problem of direct numerical simulation for each particle. However, when observing typical particle number densities as given in Table 1.2, with densities of order  $10^{10} m^{-3}$ , it is clear that such an approach is infeasible for even the most powerful of computers available today. With such wide variation in plasma parameters, there does not exist one physics approximation that is appropriate for all plasmas, rather one must choose a physics model that is most appropriate for solving the problem at hand in terms of accuracy and feasibility.

Broadly, these plasma physics modeling approaches fall into three categories:

**Direct (Exact) Approach:** This approach is the most accurate, or exact technique. The position and velocity states for each particle are tracked and known. The relevant forces or interactions that each particle is subject to (gravity, electromagnetism, particle collisions) are applied in a dynamical model using Newton's second law, and the equations of motion are solved directly. This approach is the most numerically expensive, and even with modern computational resources remains unfeasible for the vast majority of plasma regimes. Even in the case of a diffuse plasma such as the Solar Wind plasma in interplanetary space, there exists over 1 million particles within one cubic meter. Modified versions of this approach can be employed for diffused plasmas, such as the *particle in cell method*, but this level of exactness is not usually required, and is impractical for denser, collisional plasmas. [11]

**Kinetic Theory Approach:** This approach involves simplifying the particle dynamics to distribution functions describing particle position and velocity based on an applied theory. In doing so, statistical mechanics techniques are employed to calculate macroscopic properties, similar to the kinetic theory of gases. Statistical techniques are also used to model particle collisions, with the probability of each collision represented by a 'collision cross-section.' [11] This approach is generally used when the plasma

cannot be treated as a single fluid with isotropic properties, but instead has disparities in values for temperature, mobility, and other properties for differing species in the plasma such as ions and electrons. This approach has more general applicability to various plasmas than the fluid approach, but is more complex and offers less insight into the fundamental physical phenomenology or behavior. [11] [13] [15]

**Fluid Theory Approach:** The fluid theory approach is a simpler treatment of plasma dynamics than kinetic theory. In this approach, the statistical distribution functions of properties from kinetic theory are replaced by a few averaged quantities. In doing so, the plasma is treated as a conducting and magnetized fluid with bulk, or averaged properties, such as temperature (thermal energy), density, and bulk velocity. In a plasma, there is an at least factor of 1836 mass difference between ions and electrons, while each has the same charge magnitude, so these bulk properties may have different values across species. This approximation is termed the multi-fluid approach. For some plasmas, however, the dynamics of the plasma are slow enough or the fields weak enough that both ions and electrons behave more or less *synchronously*, and the plasma can be treated as a single conducting fluid with consistent density, temperature, and velocity amongst species. This fluid approach is called the single-fluid, or *magnetohydrodynamic* approach. [11] [13] [15]

For the plasmas of interest to this thesis, atmospheric entry plasmas, the weakly ionized plasma has strong fluid like properties in the region of interest, with neutrals, ions, and electrons moving more or less synchronously, and thus the single-fluid approach to plasma modeling is employed. This approach is called the *magnetohydrodynamic* approach, and serves tremendous utility in understanding and predicting plasma dynamics during atmospheric entry.

### 1.5.7 Magnetohydrodynamics

As mentioned earlier, in *magnetohydrodynamics* (MHD), the plasma is represented as a single fluid with averaged properties. This requires *nearly synchronous* behavior between species, such as ions, and electrons. This *nearly synchronous* behavior is what allows for small electrical and magnetic fields and currents to exist, as if all particle motion was truly synchronous, then there would be no separation of charge and thus no electrical current. The dynamical processes must be so slow in comparison to the intrinsic response of the plasma that the electrons and ions do not strongly decouple, which is exacerbated by the 1836 times greater mass of a proton versus an electron. These conditions can be simply stated as:

- Process characteristic frequencies  $\ll$  Plasma frequencies
- Process characteristic length scales  $\gg$  Plasma length scales

The MHD equations are an amalgamation of the Navier-Stokes fluid dynamics equations and Maxwell's equations of electromagnetism. Together, they are known as the *magnetohydrodynamic* (MHD) model. In differential form they are [13]:

**Continuity:**

$$\frac{\partial \rho}{\partial t} + \nabla \cdot \rho \bar{\mathbf{u}} = 0 \quad (1.18)$$

**Momentum:**

$$\rho \frac{\partial \bar{\mathbf{u}}}{\partial t} + \nabla P = \bar{\mathbf{j}} \times \bar{\mathbf{B}} \quad (1.19)$$

**Ohm's Law:**

$$\eta \bar{\mathbf{j}} = \bar{\mathbf{E}} + \bar{\mathbf{u}} \times \bar{\mathbf{B}} \quad (1.20)$$

**Maxwell's Equations (Faraday's Law):**

$$\nabla \times \bar{\mathbf{E}} = -\frac{\partial \bar{\mathbf{B}}}{\partial t} \quad (1.21)$$

**Maxwell's Equations (Ampere's Law):**

$$\mu_0 \bar{\mathbf{j}} = \nabla \times \bar{\mathbf{B}} \quad (1.22)$$

**Maxwell's Equations (No Magnetic Monopoles):**

$$\nabla \cdot \bar{\mathbf{B}} = 0 \quad (1.23)$$

**Equation of State:**

$$\frac{d}{dt}(P \rho_m^{-\gamma}) = 0 \quad (1.24)$$

where in the MHD equations the following variables are functions of space and time:  $\rho$  represents the mass density,  $P$  represents the plasma pressure,  $\bar{u}$  represents the plasma bulk velocity,  $\bar{j}$  represents the plasma areal current density,  $\bar{E}$  represents the electric field,  $\bar{B}$  represents the magnetic field,  $\eta$  represents the plasma resistivity, or the inverse of the plasma conductivity  $\sigma$ , and  $\mu_0$  is the magnetic permeability of free space, a physical constant which has a value of  $\mu_0 = 4\pi \times 10^{-7} \frac{N}{A^2}$ .

Implicit in these equations are a few assumptions. Namely, there are no sources or sinks in the model, so ionization and recombination are assumed to either not occur or be in equilibrium. The other two aforementioned validity limits of the single-fluid approach still apply as well. [13]

Using the MHD equations, there are several physical quantities or relationships of relevance that can be revealed. For example, using the generalized adiabatic state equation 1.24, and combining with the continuity equation 1.18, an energy conservation law can be derived as:

$$\frac{1}{\mu_0} \nabla \cdot (\bar{\mathbf{E}} \times \bar{\mathbf{B}}) + \frac{\partial}{\partial t} \left( \frac{B^2}{2\mu_0} \right) + \bar{\mathbf{E}} \cdot \bar{\mathbf{j}} = 0 \quad (1.25)$$

Applying Ohm's law, equation 1.20, the momentum equation 1.19, the continuity equation 1.18, then the energy conservation law is reduced to:

$$\nabla \cdot \frac{1}{\mu_0} (\bar{\mathbf{E}} \times \bar{\mathbf{B}}) + \frac{\partial}{\partial t} \left( \frac{\rho u^2}{2} + \frac{P}{\gamma - 1} + \frac{B^2}{2\mu_0} \right) + \eta j^2 + \nabla \cdot \left( \frac{\rho u^2}{2} + \frac{P}{\gamma - 1} + P \right) \bar{\mathbf{u}} \quad (1.26)$$

Similarly, a diffusion relation for the magnetic field,  $\bar{\mathbf{B}}$ , into the plasma can be derived using Ohm's law, equation 1.20, and Faraday's law, equation 1.21.

$$\frac{\partial \bar{\mathbf{B}}}{\partial t} = \nabla \times (\bar{\mathbf{u}} \times \bar{\mathbf{B}}) + \frac{\eta}{\mu_0} \nabla^2 \bar{\mathbf{B}} \quad (1.27)$$

The quantity  $\frac{\eta}{\mu_0}$  in equation 1.27 is referred to as the magnetic viscosity  $\nu_m$ , which refers to the degree to which the magnetic field diffuses into the plasma, similar to momentum and the traditional gas dynamic kinetic viscosity term,  $\nu$ . [13]

An equation of motion for the plasma can be derived by substituting Ampere's law, equation 1.22, into the momentum equation 1.19, yielding equation 1.28:

$$\rho \frac{d\bar{\mathbf{u}}}{dt} = -\nabla \left( P + \frac{B^2}{2\mu_0} \right) + \frac{1}{\mu_0} (\bar{\mathbf{B}} \cdot \nabla) \bar{\mathbf{B}} \quad (1.28)$$

The ratio of the two terms in the magnetic diffusivity equation 1.27, given as equation 1.29, represents the ratio of the magnetic diffusion time  $\tau_r = \frac{\mu_0 L^2}{\eta}$  to the Alfven transit time,  $\tau_H = \frac{L}{\frac{B}{\sqrt{\rho \mu_0}}}$ .

$$\frac{|\nabla \times (\bar{\mathbf{u}} \times \bar{\mathbf{B}})|}{\nabla^2 \bar{\mathbf{B}} \left( \frac{\eta}{\mu_0} \right)} \approx \frac{\frac{uB}{L}}{\left( \frac{B}{L^2} \right) \left( \frac{\eta}{\mu_0} \right)} = \frac{\mu_0 u L}{\eta} \equiv R_m \quad (1.29)$$

This ratio, called the magnetic Reynolds number,  $R_m$ , is an important ratio in plasma physics and MHD and determines the degree to which the magnetic field is bound or convected with the plasma. For  $R_m \ll 1$ , the magnetic field in a plasma changes according to a diffusion equation. That is,  $\bar{\mathbf{B}}$  is not convected by particle motion, and the applied

magnetic field is uncoupled to the magnetic field induced by particle motion. **This regime is most relevant to highly collisional atmospheric entry plasmas.** For  $R_m \gg 1$ , the  $\bar{B}$  field is frozen into the plasma (ideal MHD). This is most applicable to magnetospheres and non-collisional plasmas.[13]

## 1.6 Applications of Magnetohydrodynamics: Energy Generation

An interesting practical application of the physical principles of magnetohydrodynamics is that of energy generation. An MHD generator is a device that can extract energy from a moving conducting fluid without moving parts, essentially converting thermal and kinetic energy into electricity. [16]. In order to facilitate this energy conversion, an MHD energy generator relies on moving a conductor, in this case a conducting fluid or plasma already in motion, through a magnetic field to induce an electric current, much like a conventional electric generator.

MHD energy generation was originally conceived of as a means to increase the efficiency of terrestrial electrical energy generation through use as a ‘topper’ cycle to extract energy from moving hot exhaust gases without contacting moving parts such as turbines, thereby enabling potentially higher gas temperatures than previously possible due to material limitations. MHD electrical energy generation as a practical concept was first researched in the United States by Westinghouse Corporation in 1938 under the direction of Hungarian national Bela Karlovitz. The initial patent on MHD energy conversion was awarded to B. Karlovitz on August 13th, 1940 as US Patent 2,210,918, entitled, “Process for the Conversion of Energy.” [17]. Since then, there have been numerous development efforts throughout the 20th century, with research occurring across the world in the United States, former U.S.S.R, Japan, China, and other nations. [18]

There are several possible geometries for MHD energy generators. All geometries, however, employ a magnetic field orientation which is at least to some degree not parallel to the gas velocity, such that a *Lorentz body force* is exerted on the moving fluid. Three

common types of magnetogasdynamic, or magnetohydrodynamic energy generators are the Faraday, or linear configuration, the Hall, or vortex-type configuration, and the radial outflow, or disc-type configuration. These three configurations are summarized as Figure 1.8 and described below.

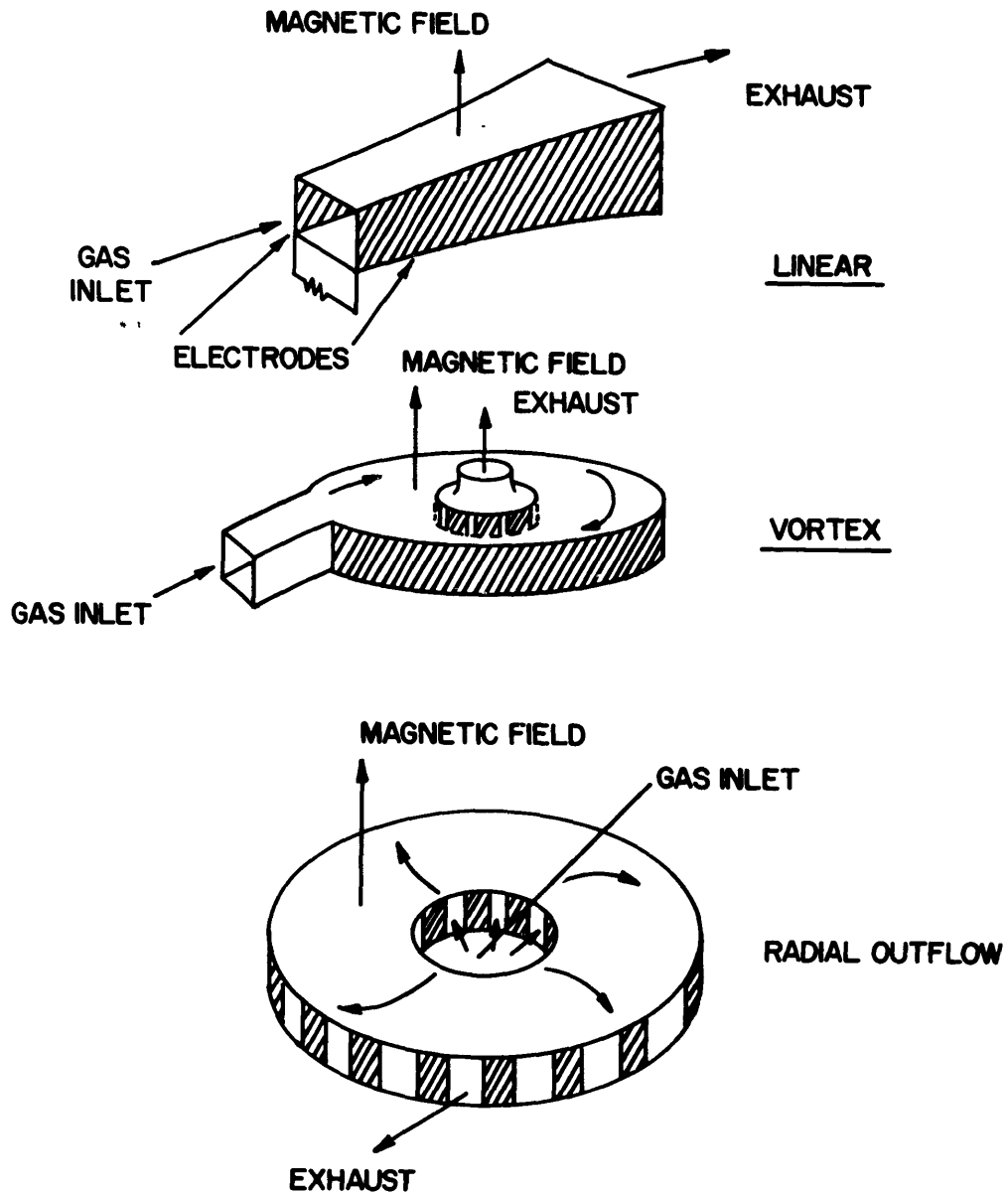


Figure 1.8: MHD energy generator geometries, adapted from [19]

The linear MHD generator geometry is the most commonly investigated, and the sim-

plest. It consists of a 'linear' design in which the plasma flows through a duct or channel with electrodes lining the sides. A magnetic field is applied such that the field orientation is mutually perpendicular to both the flow axis and the line connecting the two electrodes.

The flowing conductive plasma across the magnetic field induces an electric field along the vector cross product of the flow velocity and magnetic field vectors. The electrodes are located along this direction, and if a load is connected across them, a current will flow.

The Vortex and radial outflow generator geometries are variations of the linear generator principle designed to take advantage of secondary effects such as the Hall current or increase interaction length by forcing several revolutions of the plasma before it can exit the generator. The physical principles involved are similar to those for the linear MHD energy generator, and thus only the linear MHD generator geometry is discussed further. [19].

#### 1.6.1 Physical Considerations and Principles for MHD Energy Generation

As presented, all of the MHD generator geometries presented above generate DC power, through it is possible to generate AC power using dynamic magnetic field configuration. In addition, as a prerequisite for continuum conductive behavior, the plasma Debye length must be much smaller than the generator length scale to prevent charge separation.

Unlike in highly ionized, collisionless plasmas such as those found in planetary magnetospheres, the plasmas of typical relevance to MHD energy generation have relatively low ionization levels and high neutral gas densities, and therefore have very low magnetic Reynolds numbers. In addition, due to the relatively low ionization fraction and significant neutral density, the detailed electrical properties of gases and ionization processes become important.[16] [18]

There are typically two approaches to achieving significant ionization in the moving gas such that it becomes a plasma. The first approach, called 'thermal,' or equilibrium ionization, involves raising the overall gas temperature sufficiently such that the electrons are

ripped from the atomic nuclei from thermal excitation alone. These plasmas require nothing but the deposition of thermal energy into the gas, however, due to the high temperatures (on the order of  $10,000\text{ K}$ ) involved, pose significant or impossible material challenges. The other approach, called ‘extra-thermal’ or non-equilibrium ionization, involves directly coupling energy to the electrons in the gas through some other method, such as radio-frequency induced ionization. In this approach, the electrons are not in thermal equilibrium with the rest of the gas, existing at much higher temperatures than the rest of the gas and reducing heat transfer to equipment such as the generator walls and electrodes. Both approaches have associated technical challenges and merits, with the thermal approach being the simplest. A common variation of the thermal approach is to introduce a small amount of an easily ionizable non-gaseous substance such as an alkali metal seed fraction. Due to the relatively low ionization potentials of elements such as potassium, sodium, or cesium, they can be fully ionized and release their electrons at temperatures far below those required for significant ionization in most gases and thus enable construction of the MHD energy generator from furnace materials. The disadvantage of this approach is the highly reactive nature of most alkali metals, attacking electrode surfaces and producing potentially undesirable toxic byproducts. [16].

Once this ionization is achieved, this ionized, conductive gas is now considered a plasma, and is ready to pass through an MHD generator for energy extraction. From first principles and to first-order, expressions for the energy available can be derived. Consider a linear, or Faraday, type MHD energy generator, a schematic for which is presented as figure 1.9.

As the plasma flows through the generator, it will induce an electric field the direction mutually perpendicular to both the flow velocity and magnetic field, across which electrodes are placed in order to capture the resulting current. From Ohm’s law, given before as equation 1.20, we can calculate the resulting current as:

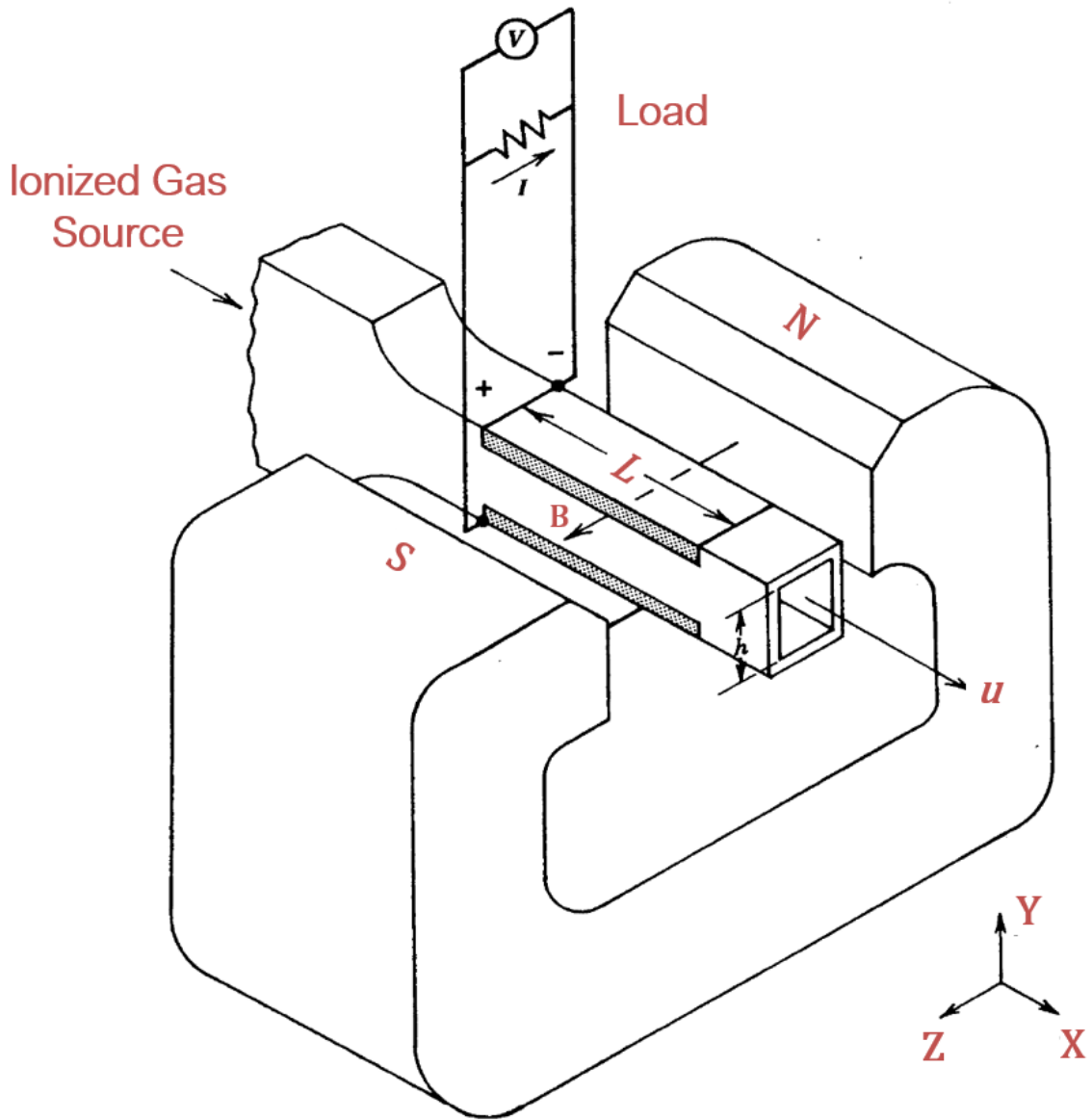


Figure 1.9: Linear Faraday-type MHD generator and associated coordinate system

$$j_y = \sigma_e(E_y + uB) \quad (1.30)$$

where  $\sigma_e$  is the scalar electrical conductivity of the ionized gas, and the vector quantities and cross-products involving current density  $\bar{\mathbf{j}}$ , flow velocity  $\bar{\mathbf{u}}$ , magnetic field  $\bar{\mathbf{B}}$ , and electric field  $\bar{\mathbf{E}}$  have been replaced with scalar values due to their mutually perpendicular orientations.

The power per-unit volume is expressed as follows:

$$P_v = \bar{\mathbf{E}} \cdot \bar{\mathbf{j}} = E_y \cdot j_y \quad (1.31)$$

The electrical load influences the electrical power extracted. Conceptually, the influence of this load is represented by considering two extremes between the electrodes: a short-circuit and open-circuit. In a short-circuit load configuration, the potential difference between the two electrodes is reduced to zero, and no power is extracted. Similarly, in an open circuit configuration, there may exist a significant potential difference across the electrodes, but no current flows, and thus no power is extracted. This effect is captured through the definition of a load factor that is qualitatively described as the ratio between the electrode potential difference under load to that of an open circuit. [19] Quantitatively, this load factor  $K$  varies between 0 (short circuit) and 1 (open circuit) and is defined in equation 1.32:

$$K \equiv \frac{E_y}{uB} \quad (1.32)$$

From equation 1.32, the expression for the electric field can be written in terms of the load factor, flow velocity, and magnetic field as  $E_y = KuB$ . Substituting this relation into equations 1.30 and 1.31, an expression for the power per-unit volume extracted from a Faraday-type MHD generator can be derived, given as equation 1.33:

$$P_{\forall} = \sigma_e u^2 B^2 K(1 - K) \quad (1.33)$$

From this equation, it can be seen that there is an optimal load factor  $K$  which results in maximum theoretical power generation. From simple mathematics, this optimal value is  $K = 1/2$ , and results in a maximum power per-unit volume of:

$$P_{\forall,Max} = \frac{1}{4} \sigma_e u^2 B^2 \quad (1.34)$$

Finally, the total maximum electrical power extracted from the generator can be calculated, assuming uniform plasma and magnetic field properties within the generator to first order, by multiplying by the product of generator cross-sectional area  $A_c$  and electrode length  $L_i$ .

$$P_{MHD,Max} = \frac{1}{4} \sigma_e u^2 B^2 A_c L_i \quad (1.35)$$

Thus, it can be seen that power available via MHD energy generation scales as follows:

$$P_{MHD} \propto \sigma_e u^2 B^2 A_c L_i \quad (1.36)$$

### 1.6.2 Application of MHD Energy Generation Technologies

The scaling law given as equation 1.36 is only accurate to first order, and neglects losses such as Hall or eddy currents due to the high magnetic field intensities, electrode sheath effects, aerodynamic drag, heat transfer, and other non-ideal behavior. [16]. These technical and practical concerns have limited significant integration of MHD generator technology for terrestrial power generation, due to problems such as electrode wear, low ionization density, and limited efficiency. [18]

However, since a planetary entry vehicle encounters a high-speed plasma during the entry process, a moving conducting fluid is present. Moreover, the phase of entry dur-

ing which ionization is significant lasts on the order of only minutes, so concerns such as electrode wear and toxic material exhaust in residential areas are of less relevance. Furthermore, there is the consideration that moving parts represent an additional, and often undesired complexity for spacecraft entry systems, due to mechanical and thermal considerations. Thus, a technology such as MHD energy generation is uniquely suited to the challenges of extracting electrical energy by converting the thermal and kinetic energy from the high-speed plasma that surrounds a planetary entry vehicle during hypersonic flight. An additional benefit is that the Lorentz body force acting on the plasma due to the magnetic field would necessarily react through the on-board magnet embedded within the reentry vehicle, thus lending an additional mechanism for vehicle control and maneuvering without external control surfaces, an important benefit for the extreme thermal challenges of hypersonic flight. The beneficial intersection of these two fields, magnetohydrodynamics and planetary entry, has not gone unnoticed, and has been the subject of many studies, described further in the sections that follow.

## **1.7 Magnetohydrodynamics and Planetary Entry: A History**

MHD vehicle interaction for high-speed aerospace applications has been studied since the dawn of the space race, with early theoretical studies dating back to late 1950's and 1960's.

These studies focused primarily on the flow control applications possible with MHD interaction for purposes such as drag augmentation and heat mitigation. At the time, such ideas were limited by available technologies, as the coils needed to produce the necessary magnetic field were mass prohibitive and inefficient, being non-superconducting, and energy storage technologies were not nearly as developed. Since that time, however, dramatic advances in energy storage and magnetic field generation have been achieved [20] and in conjunction with a pressing need to reduce interplanetary launch masses, warrants additional investigation of the topic.

### 1.7.1 MHD and Planetary Entry: Early History

In November 1957, Resler and Sears presented for publication a seminal work entitled, “The Prospects for Magneto-Aerodynamics,” in the Journal of Aerospace Sciences.[21] Published the dawn of the space race between the U.S. and former USSR, this work develops fundamental equations and expressions relating to a new, distinct extension of magnetohydrodynamics and plasma physics dubbed ‘magnetoaerodynamics.’ The term referred to a class of weakly ionized, high neutral density, relatively low-temperature plasmas such as those commonly found in high-speed aeronautics and aerospace applications. In a similar physics modeling approach to the magnetohydrodynamic approximation used in planetary magnetospheres and nuclear fusion reactors, the plasma is treated as a conducting fluid with additional body forces due to the Lorentz force interaction. However, unlike the collisionless plasmas present in relatively sparse planetary magnetospheres, or the high-temperature, fully ionized plasmas present in nuclear fusion reactors, ‘magnetoaerodynamics’ is concerned with relatively weakly ionized gases with high neutral densities. This weak ionization combined with relatively high neutral gas densities gives rise to frequent electron-neutral collision that inhibit electrical conductivity to significantly lower values than those encountered in magnetospheres or nuclear fusion. For both magnetospheric and nuclear fusion plasmas, the treatment is that of ideal MHD, in which the conductivity is assumed to be effectively infinite, such that the magnetic field is ‘frozen’ into the plasma and convected with its motion. These plasmas typically have very high magnetic Reynolds numbers,  $R_m \gg 1$ , as mentioned earlier. In contrast, the aerospace plasmas of interest to magnetoaerodynamics have much lower conductivities, and the induced magnetic field due to the motion of charged particles within the plasma is ‘diffused’ much more effectively, such that the ‘frozen’ assumption is no longer valid. Such plasmas typically have very low magnetic Reynolds numbers,  $R_m \ll 1$ . There are several consequences to this property of aerospace plasmas, namely that the applied magnetic field is effectively uncoupled to the induced magnetic field due to the motion of charged particles in the plasma, which allows

for some simplification in the modeling process. In addition, there exists an additional joule heating term in the fluid mechanics energy equation due to the finite electrical conductivity, similar to the familiar concept of electrical resistive heating.

In their work, Resler and Sears develop the equations for this non-ideal, resistive form of magnetohydrodynamics by augmenting the Navier-Stokes equations with the Lorentz body force momentum equation contribution and electrical joule heating energy equation contribution. They then present solutions for several classical fluid mechanics example problems including the effects of ionized gases in the presence of applied magnetic fields. Example problems include variations on Poiseuille flow and quasi one-dimensional acceleration of a gas through a channel such as a nozzle. Finally, they discuss potential aerospace applications, or ‘prospects’ for utilizing magnetoaerodynamic interaction, namely ballistic missile reentry. They find that for such cases of high-speed, hypersonic flight such as the regimes present during atmospheric reentry, there is potential for significant magnetoaerodynamic interaction, to be useful for vehicle drag augmentation and energy extraction from the flow. A schematic of their proposed device is reproduced as Figure 1.10. Although the work is preliminary and exploratory in nature, they conclude that the potential benefits warrant additional research and development resources through further experimental and theoretical investigations. [21]. Such investigations occurred throughout the late 1950s and 1960s, amongst numerous researchers and institutions, though ultimately limited by the non-superconducting magnetic coils available and other technological constraints of the time.[22][23][24][25][26][27][28]

In addition to early theoretical investigations of magnetoaerodynamics, there were experimental studies on the subject as well. In 1958, Ziemer and Bush presented results of an experimental investigation entitled, “Magnetic Field Effects on Bow Shock Stand-Off Distance.” [29]. This paper represents one of the first experimental studies concerning magnetoaerodynamics specifically. Ziemer and Bush conduct high-speed flow testing and imaging on hard spheres both with and without an embedded magnetic field. The shock

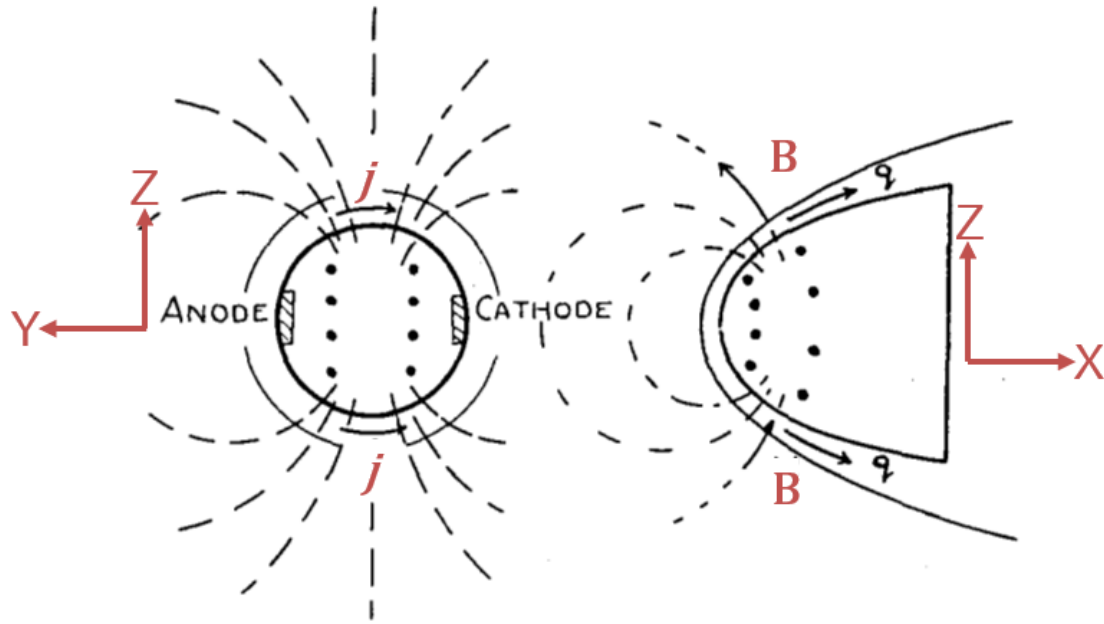


Figure 1.10: Resler and Sears proposed magneto-aerodynamic decelerator device for re-entry missiles, adapted and modified from [21].

wave produced by the spheres with an embedded magnet was offset further from the surface, thus implying a larger drag force imparted to the sphere due to the presence of the magnetic field. It was clear evidence of the postulated magnetoaerodynamic interaction in a flight regime relevant to aerospace applications. A photograph of this effect, as well as a comparison of their experimental data with developed theory are presented as Figures 1.11 and 1.12, respectively.

Other experimental investigations were conducted throughout the late 1950s and 1960s, verifying the soundness of the fundamental physics concepts and effects relevant to magnetoaerodynamics. A selection are referenced as follows: [30] [31] [32] [33].

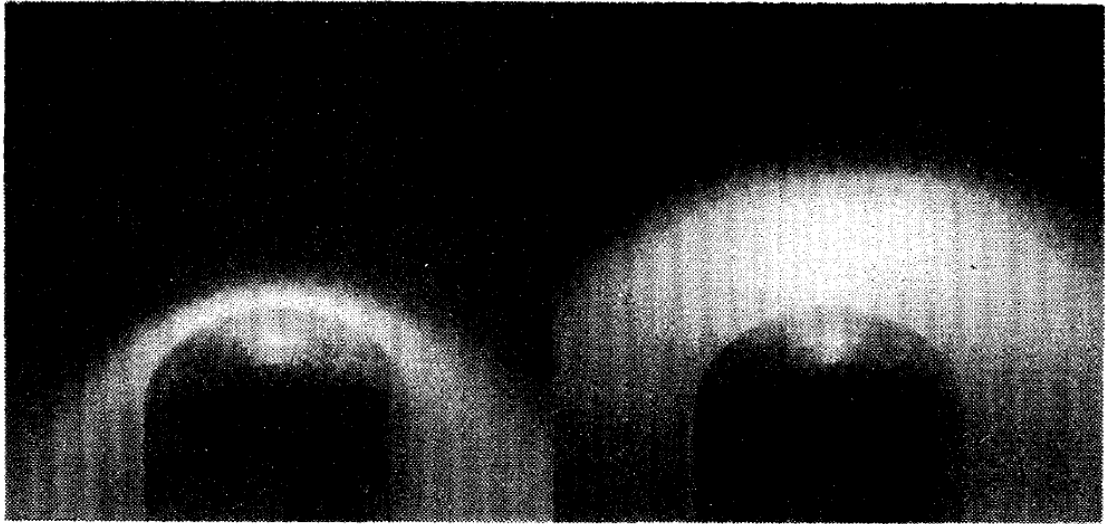


Figure 1.11: Bow Shock on the sphere without (left) and with (right) magnetic field, adapted from [29]

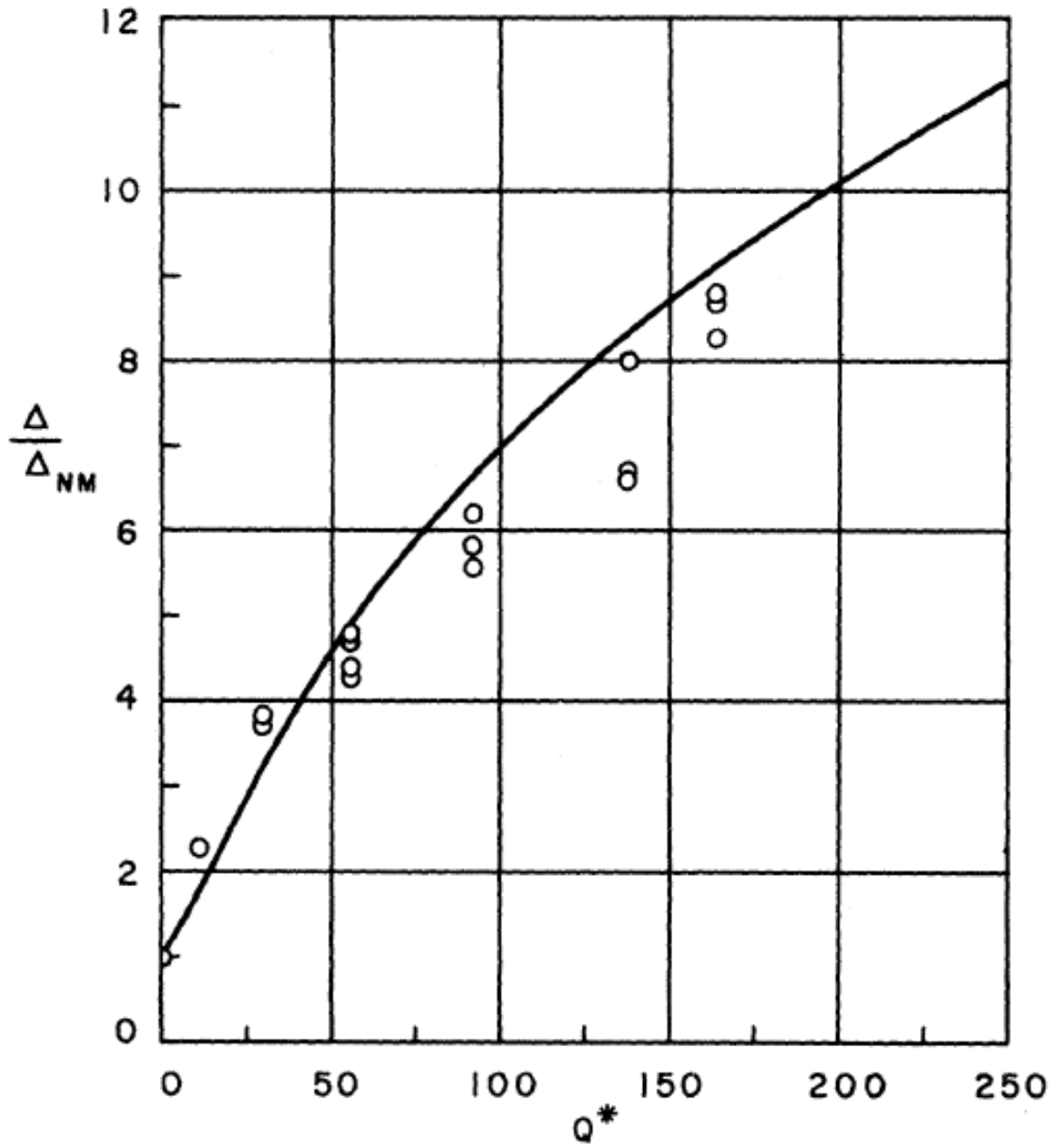


Figure 1.12: Experimental data for shock stand-off distance vs. magnetic interaction parameter overlaid on theoretical curve, adapted from [29]

### 1.7.2 MHD and Planetary Entry: Modern Numerical Investigations

In contrast with the early experimental and analytical investigations of magnetoaerodynamics in the late 1950s and early 1960s, modern computers made a numerical simulation of the full system of equations feasible. Due to a resurgence of interest in hypersonics and technical challenges associated with high-speed flight, magnetoaerodynamics was again investigated. In a 2002 work entitled, “Magnetic control of flow past a blunt body: Numerical validation and exploration,” Poggie of the United States Air Force Research Laboratory conducts detailed numerical simulations on a computer for a spherical geometry, showing similar results to those predicted and observed by Ziemer and Bush in 1958 [22] [29]. [34] This work is significant as it demonstrates these complex simulations becoming computationally feasible to carry out with minimal assumptions, allowing for design of more complex vehicle geometries. These more nuanced numerical computations with fewer simplifying assumptions emphasize the feasibility of this concept for future space missions and designs. Numerical simulation for the bow-shock standoff distance and comparisons with the 1958 theory by Bush are presented as Figures 1.13 and 1.14 respectively.

Although numerical computations and feasibility studies had been carried out for specific points in entry vehicle trajectories, there still remained the challenge of simulating the impact of magnetoaerodynamic interaction over an entire reentry trajectory. In a 2008 study entitled, “Numerical Analysis of Reentry Trajectory Coupled with Magnetohydrodynamics Flow Control,” Fujino et al. perform a full-field numerical simulation of the hypersonic flow field around a re-entry vehicle including magnetoaerodynamics at not just a single point, but along the entire trajectory, for a prototype Earth reentry vehicle design known as the OREX. [35] This work is significant in that it concludes that the magnetoaerodynamic interaction is on the order of and sometimes greater than the aerodynamic interaction alone. It also confirmed that convective heat flux to the reentry vehicle could be drastically reduced as well, lending credence to the idea of a magnetic heat shield. Interestingly, the presence of the magnetoaerodynamic effect causes a second peak in the

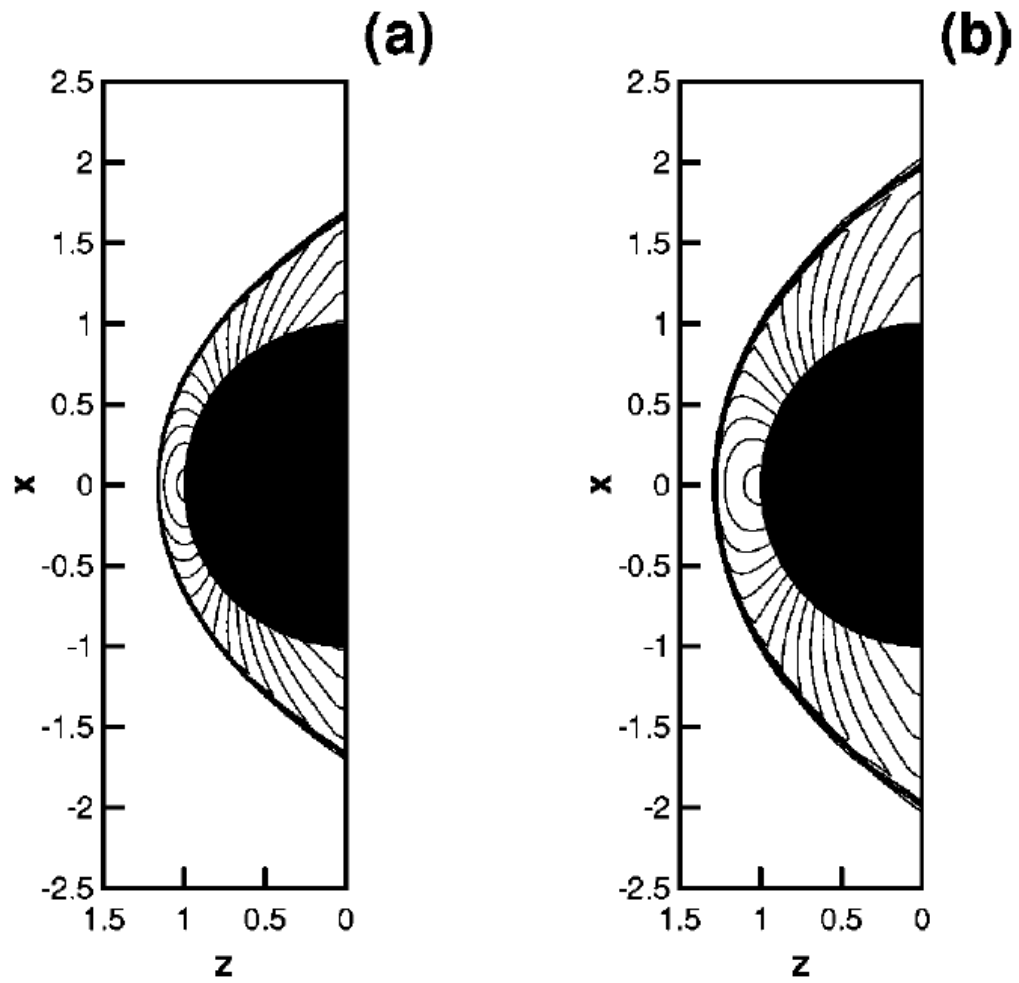


Figure 1.13: Computed pressure field showing bow-shock on sphere without (left) and with (right) magnetic field, adapted from [34]

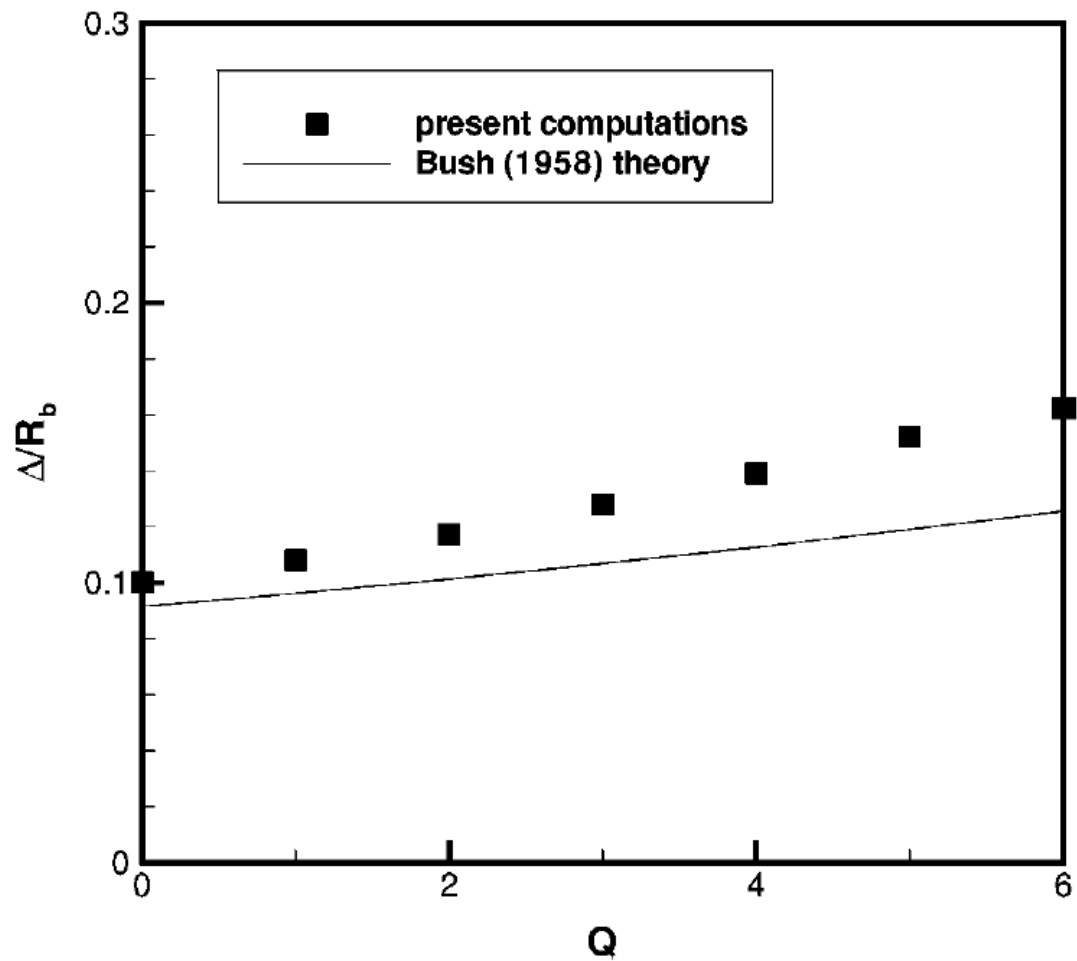


Figure 1.14: Comparison of numerical results for shock standoff distance vs magnetic interaction parameter,  $Q$ , with 1958 analytical theory by Bush [22], adapted from [34]

deceleration curve at altitudes much higher than typical for aerodynamic drag alone. This deceleration higher in the altitude is analogous to a vehicle having a lower ballistic coefficient  $\beta$ , without actually increasing the vehicle forebody area. This supports the notion that the bow-shock standoff distance makes the vehicle seem ‘larger’ to the oncoming flow than it really is due to the addition of a ‘magnetic pressure’ term from the Lorentz force, thereby increasing drag and reducing convective heat transfer. This effect is illustrated graphically in Figure 1.15, while the overall magnetoaerodynamic effect on deceleration force is shown as Figure 1.16.

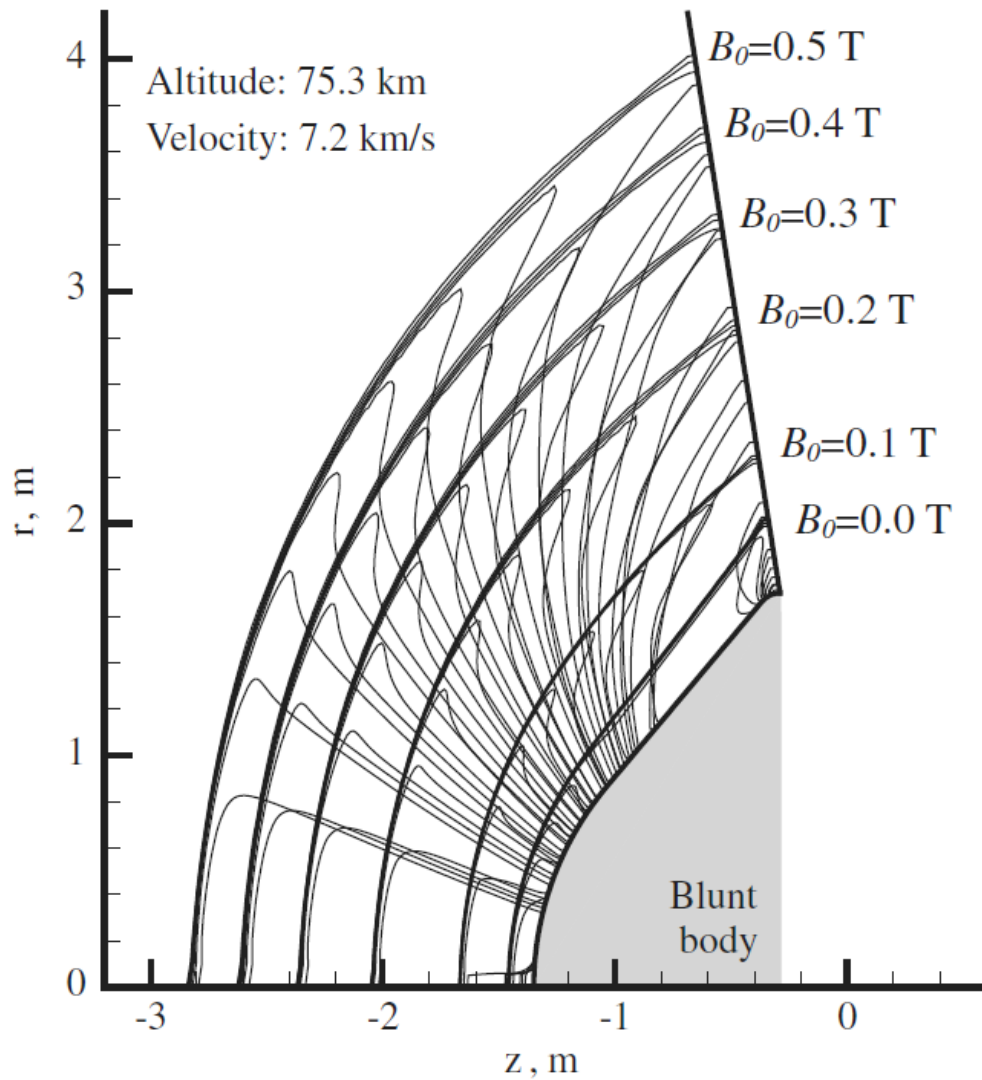
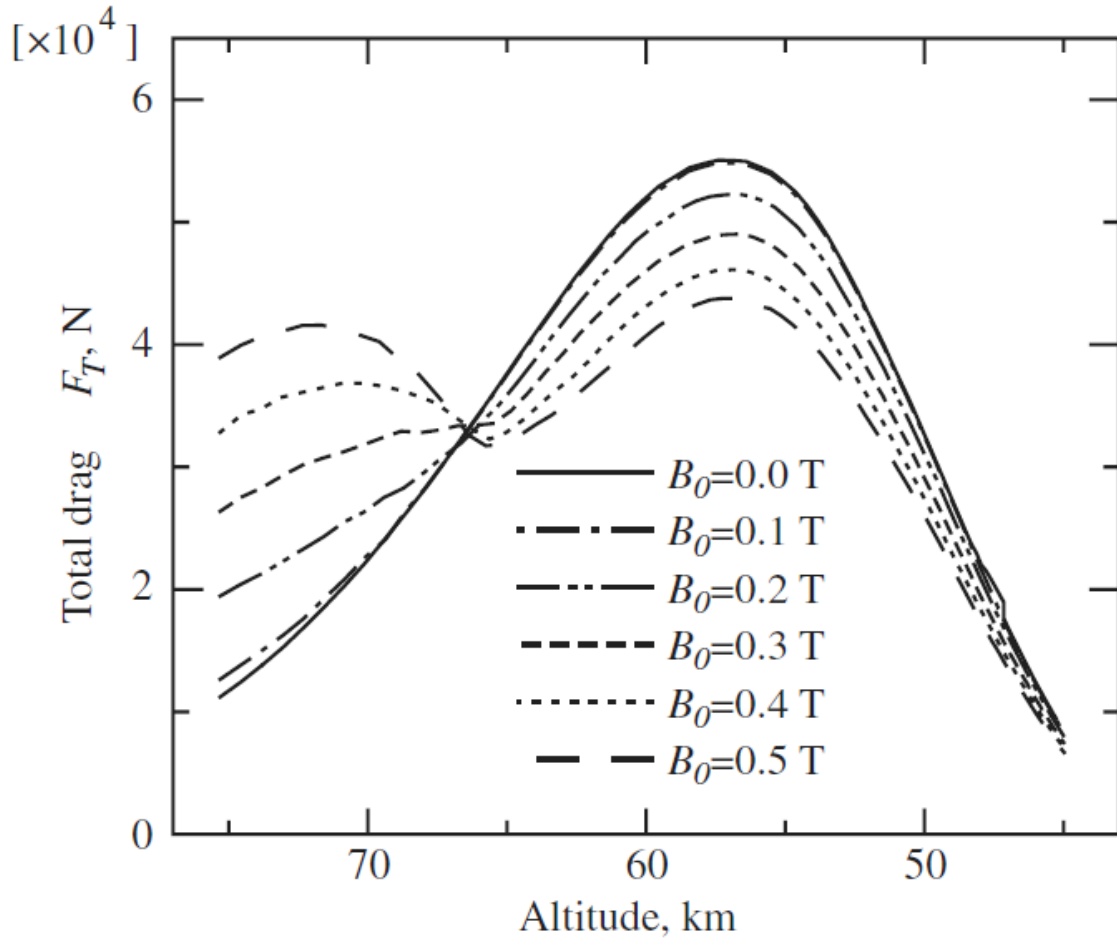


Figure 1.15: Computed pressure distributions and bow-shocks for various magnetic fields between 0 and 0.5 T ahead of the vehicle forebody, adapted from [35]



### a) Total drag $F_T$

Figure 1.16: Sum of aerodynamic and magnetoaerodynamic drag over the reentry trajectory for magnetic fields between 0 and 0.5T, adapted from [35]

These two studies highlight the potential for significant magnetoaerodynamic interaction for planetary entry vehicles. In addition, other numerical studies have been conducted with relevance to MHD and planetary entry, such as [36], [37], [38], [39], [40], and [41]. As more computational power continues to become available, the complexity and range of these studies will likely continue to increase.

### 1.7.3 MHD and Planetary Entry: Energy Generation

As mentioned earlier, the presence of a moving conducting fluid around a planetary entry vehicle lends itself to the possibility of extracting electrical energy from the flow via MHD

energy generation. MHD energy generation for planetary entry vehicles based on terrestrial magnetogasdynamic energy generation principles has been investigated since the mid-1960s [42]. In a 2007 study entitled, “A Magnetohydrodynamic Power Panel for Space Reentry Vehicles,” Steeves et al. present a design for a modular MHD energy generator for integration on the forebody of a planetary entry vehicle.[43] This work is significant in that it demonstrates and provides a feasible design for a magnetohydrodynamic power panel for energy generation through magnetoaerodynamic interaction. In contrast with traditional magnetohydrodynamic energy generators that require hot plasma to flow through an open channel, spacecraft designers specifically want to avoid plasma flowing through the spacecraft heatshield. This generator panel design is significant in that it displayed many of the same performance characteristics of a conventional magnetohydrodynamic energy generator, but in a modular, expandable design without requiring an open plasma channel. In addition, this work provides evidence that many of the same scaling laws and equations developed for conventional magnetohydrodynamic energy generators were valid for the spaceflight application of planetary reentry, namely the scaling law presented as equation 1.36. This enables these previously developed scaling laws to be applied to planetary entry problems for theoretical design trades. Illustrations of this design and its associated magnetic field are given as Figures and respectively.

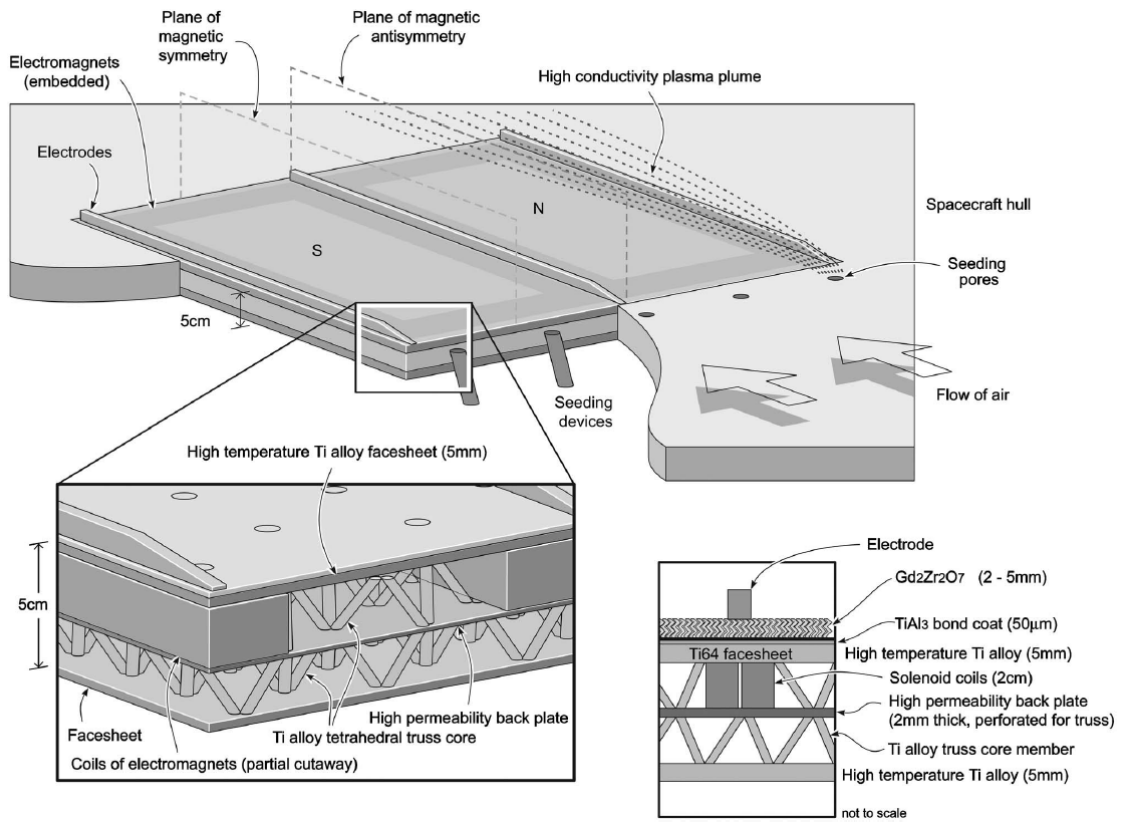


Figure 1.17: Steeves et al. non-flow through MHD generator design for planetary entry vehicles, adapted from [43]

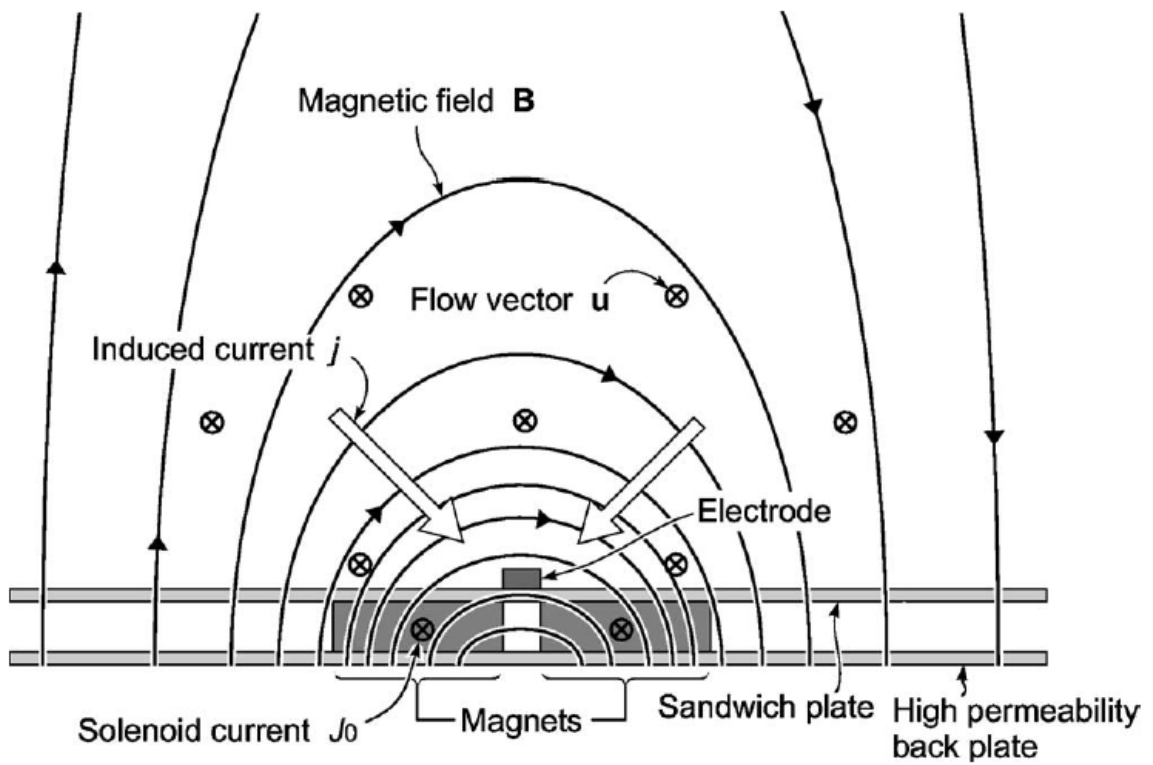


Figure 1.18: Steeves et al. magnetic field, flow and current diagram for MHD generator power panel, adapted from [43]

## 1.8 MHD and Planetary Entry: Modern Experimental Investigation

To date, including modern studies, experimental investigation of MHD interaction for planetary entry applications has been limited. From the few studies that exist, what is apparent is the technically difficult nature of designing experiments and gathering experimental data relevant to this regime of flight, as illustrated in a heat transfer experiment such as [44]. Two classes of experiments are considered, the first being modern experimental investigations of MHD drag augmentation, and the other being modern experimental investigations of MHD energy generation.

### 1.8.1 State of the Art: Experimental MHD Drag

As mentioned earlier, there have been several investigations into MHD interaction and shock standoff modification, which is expected to result in increased total drag. However, the experimental demonstration and measurement of this drag increase is more involved. In a 2009 study entitled, “Experiment on Drag Enhancement for a Blunt Body with Electrodynamic Heat Shield,” Kawamura et al. investigate MHD drag augmentation.[45] In this work, a state of the art experimental investigation of magnetoaerodynamic drag enhancement in regimes relevant to planetary entry vehicles is described, utilizing an arcjet as the plasma source and ceramic model body with permanent magnets embedded inside. The authors of the study found clear evidence of drag enhancement due to the interaction of a magnetized vehicle with the high-speed plasma, agreeing with earlier photographic, analytical, and computer predictions. though conducted with small models, and with magnetic fields up to 0.4T, this work is significant in illustrating the difficulty and scarcity of experimental measurements pertaining to magnetoaerodynamics. A diagram of the experimental design employed is given below as Figure 1.19, while results are given as Figure 1.20.

Other follow-up experiments by Kawamura in 2013 show that this MHD force need not only be limited to drag enhancement alone, but also can act in side-force directions through

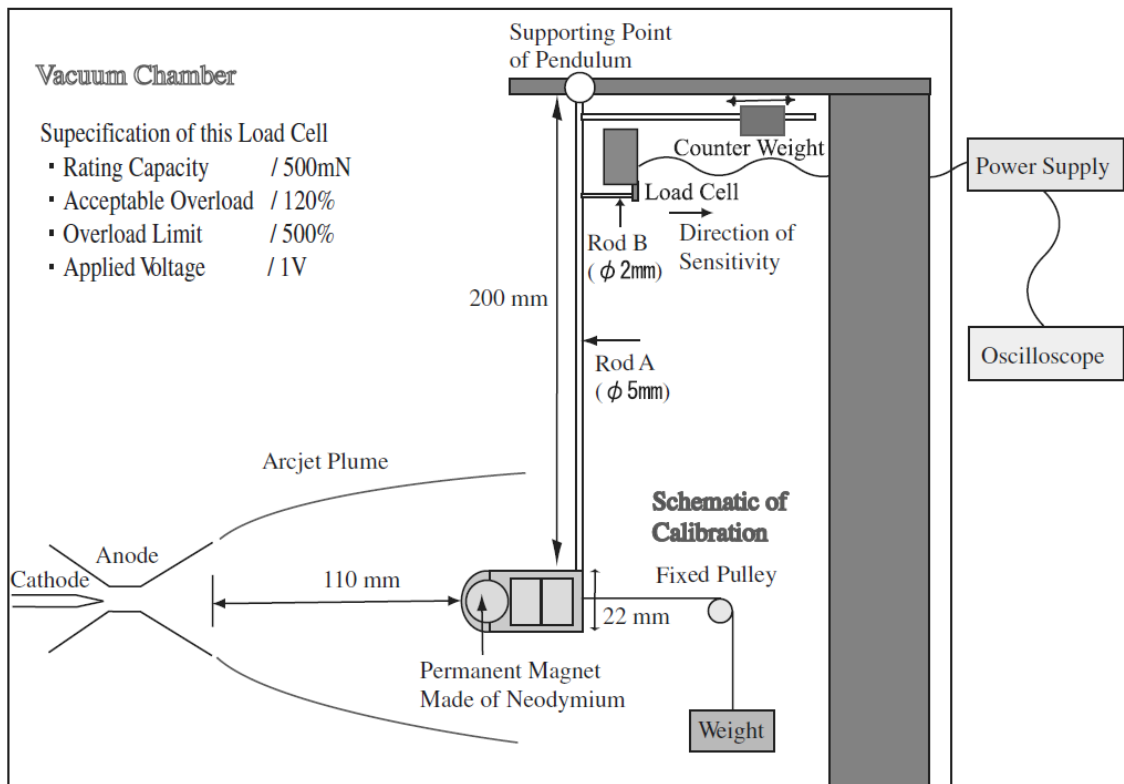


Figure 1.19: Design for measurement of MHD drag augmentation on a cylindrical blunt body, adapted from [45]

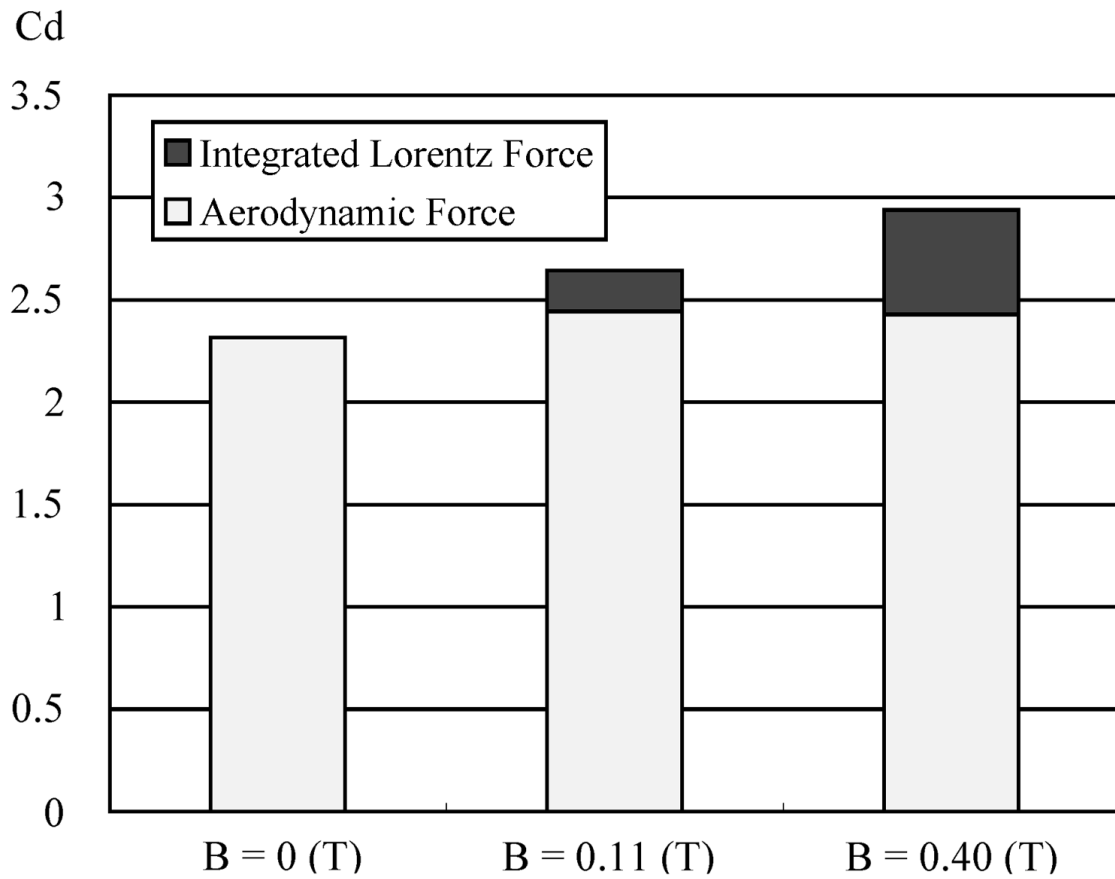


Figure 1.20: Measurements of MHD drag enhancement on a cylindrical blunt body in ionized flow, adapted from [45]

rotation of the embedded magnet's dipole axis. [46]. In addition, there recently have been additional experiments related to MHD drag augmentation during reentry, including expansion tube experiments by Gildfind et. al. at the University of Queensland Centre for Hypersonics in Australia. [47] [48]

### 1.8.2 State of the Art: Experimental MHD Energy Generation

There have also been preliminary experiments designed and constructed to test MHD energy generation concepts for planetary entry vehicles. In one such study, entitled, "System Development for Mars Entry in Situ Resource Utilization," Popovic et al. describe planetary entry MHD energy generation experiments performed by Drake as part of her doctoral thesis [49],[50],[51]. [8]. In this unique work, an artificially microwave-ionized supersonic plasma flows over a prototype MHD energy generator model suitable for planetary entry vehicles. In the only previously existing experiment of its kind, the authors appear to show a positive experimental result indicating that it is possible to extract electrical energy from a reentry plasma flow-field using an on-board MHD energy generator design. A schematic of the experimental setup, diagram of the model design, an example data showing a proof of concept are given as Figures 1.21, 1.22, and 1.23 respectively.

## **1.9 MHD Applications to Mars Entry**

Previously, most work relating to MHD and planetary entry specifically concerned Earth's atmosphere. However, MHD technology can also apply to Mars entry for both energy generation and drag augmentation. There have been a few theoretical studies relating to the topic that show much potential for energy harvesting and drag augmentation. These technologies may be useful for Mars entry in particular due to the low atmospheric density and extreme challenges associated with successfully conducting atmospheric entry at Mars versus the Earth. [2]. Though Mars has an atmosphere about 1% the density of that at Earth, there is still significant heat dissipation and ionization that occurs in the shock layer

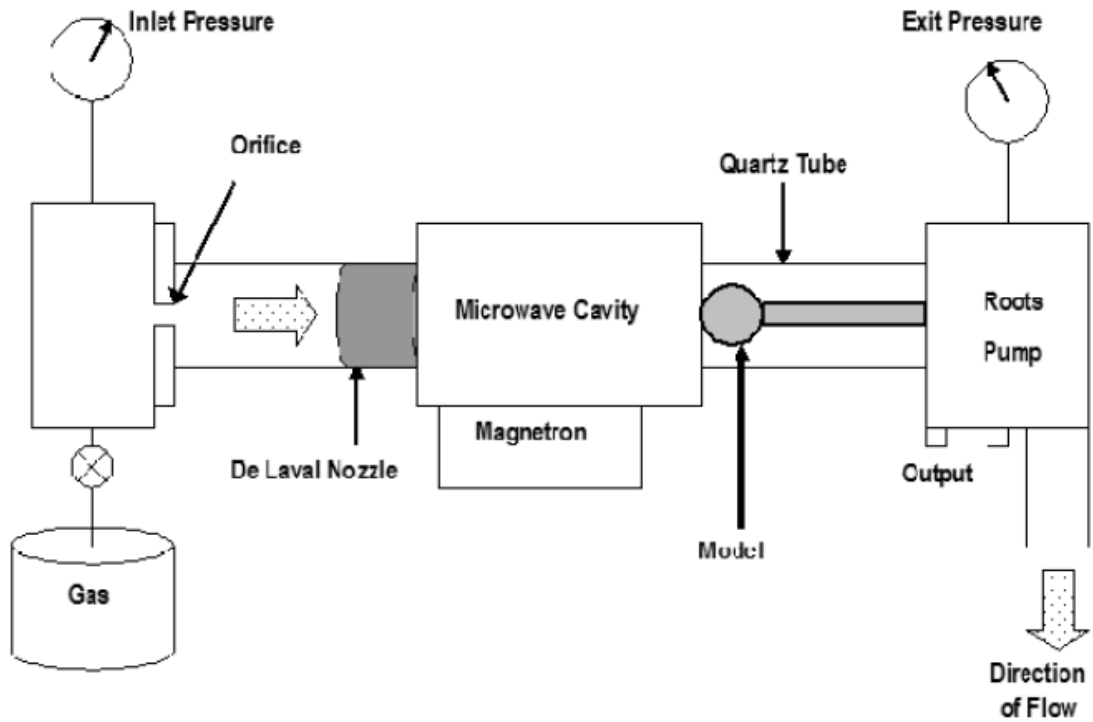


Figure 1.21: Schematic of artificial supersonic discharge for measurement of MHD energy generation for reentry vehicles, adapted from [8]

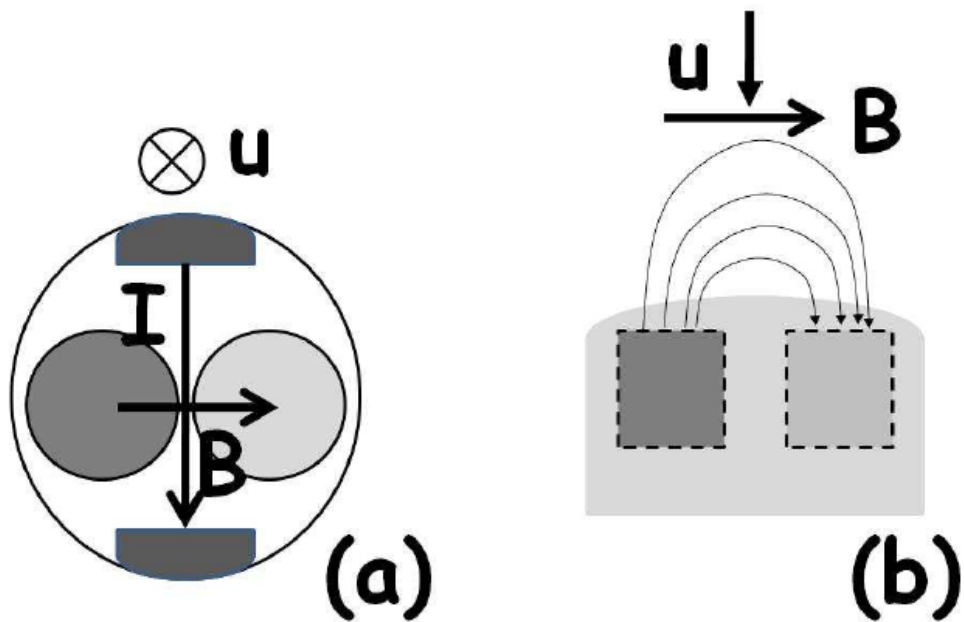
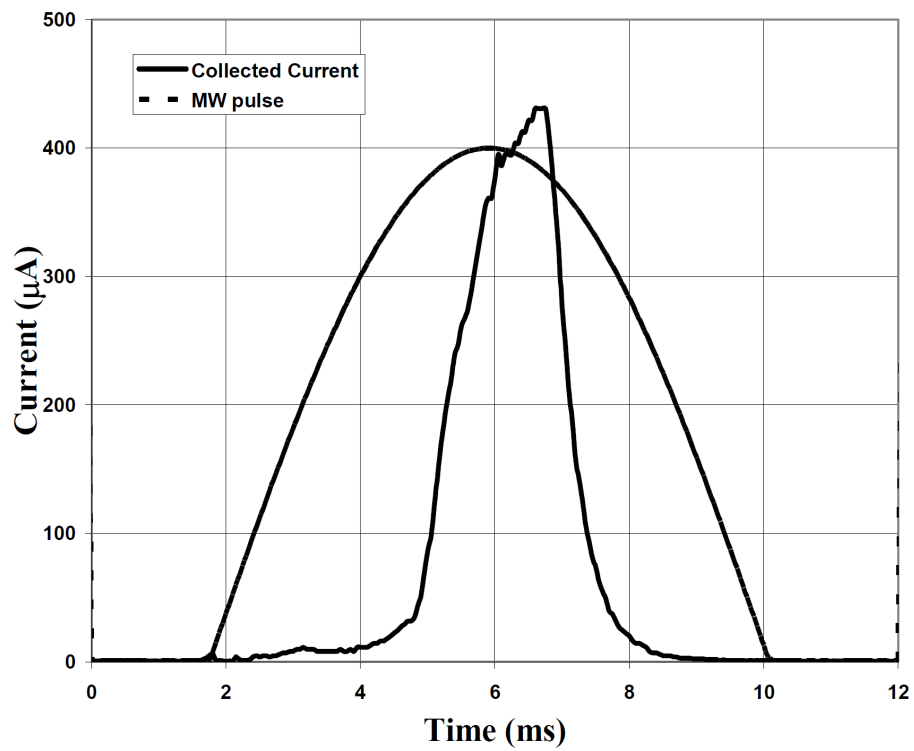


Figure 1.22: Design of MHD energy generator model for reentry, cylindrical forebody with two embedded permanent magnets, adapted from [8]



**Figure 10.** A typical MHD current pulse (unbiased) compared to an approximate MW pulse

Figure 1.23: Measurements of MHD energy generation from the artificial microwave supersonic discharge, adapted from [49]

during entry with significant electrical conductivity possible [52], and thus MHD technologies developed for Earth can be applicable. Figure 1.24 illustrates the difference between electrical conductivity for Earth and Mars atmospheric entry plasmas. [53]

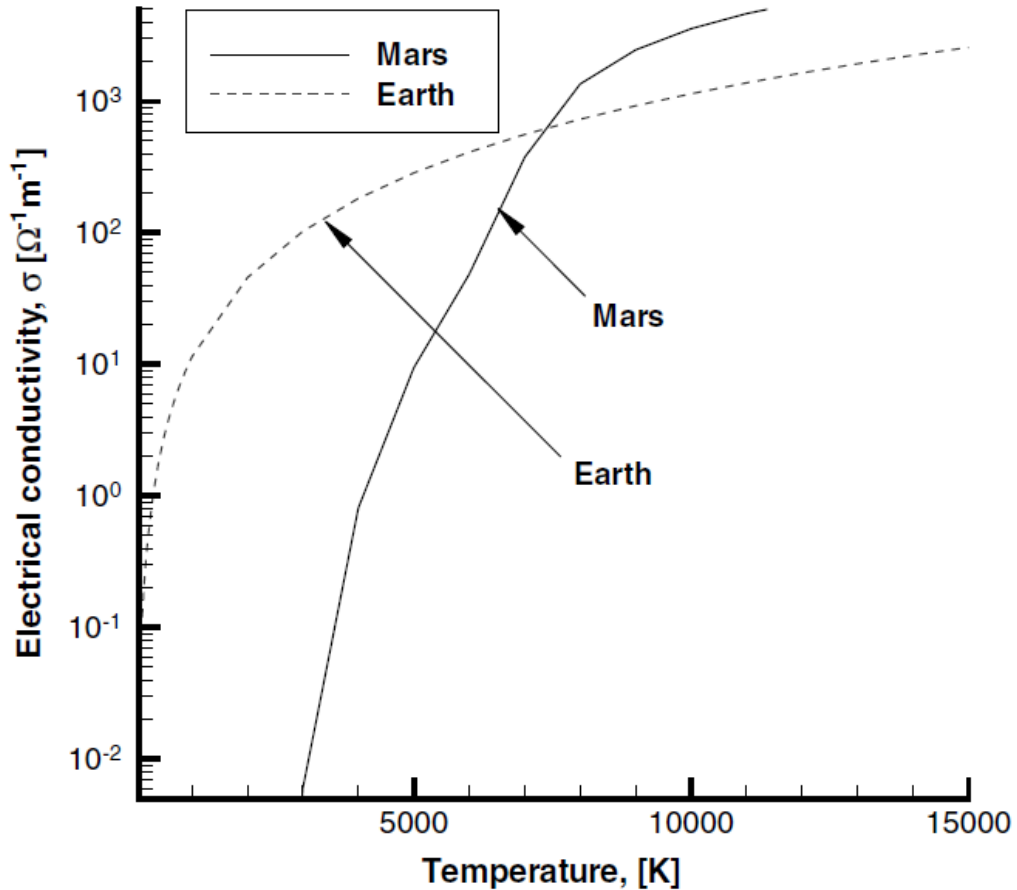


Figure 1.24: electrical conductivity as a function of temperature for the Earth and Mars atmospheres, adapted from [53]

### 1.9.1 MHD Energy Generation for Mars Entry

MHD energy generation for Mars entry is first mentioned in a study entitled, “Regenerative Aerobraking,” by Moses in 2005. [54] In it, the author investigates both the magnitude and potential uses of energy harvested via MHD energy generation at Mars. The principal use of this energy investigated is the conversion of carbon-dioxide into oxygen via the solid oxide electrolysis process. In addition, due to the magnitude of energy available,

energy storage considerations are made, leading to the investigation of ‘multi-pass’ entry trajectories, in which the deceleration pulse typically done via one atmospheric pass to the planetary surface is spread over multiple, decreasing energy orbits. Using a conceptual test vehicle with mass of  $1000\text{ kg}$ , drag area of  $7\text{ m}^2$ , drag coefficient of  $0.4$ , and entry velocity of approximately  $7.5\text{ km/s}$ , as well as a  $1\text{ m}^2$  electrode area MHD generator with magnetic field intensity of  $0.2\text{ T}$ , it is shown that up to  $750\text{ kW}$  of peak electrical power may be extracted over a period of a few minutes. The resulting energy available is approximately  $14\text{ MJ}$ , indicating that there is significant potential for MHD flow interaction and energy generation at Mars. [55]. Figure 1.25 illustrates this result.

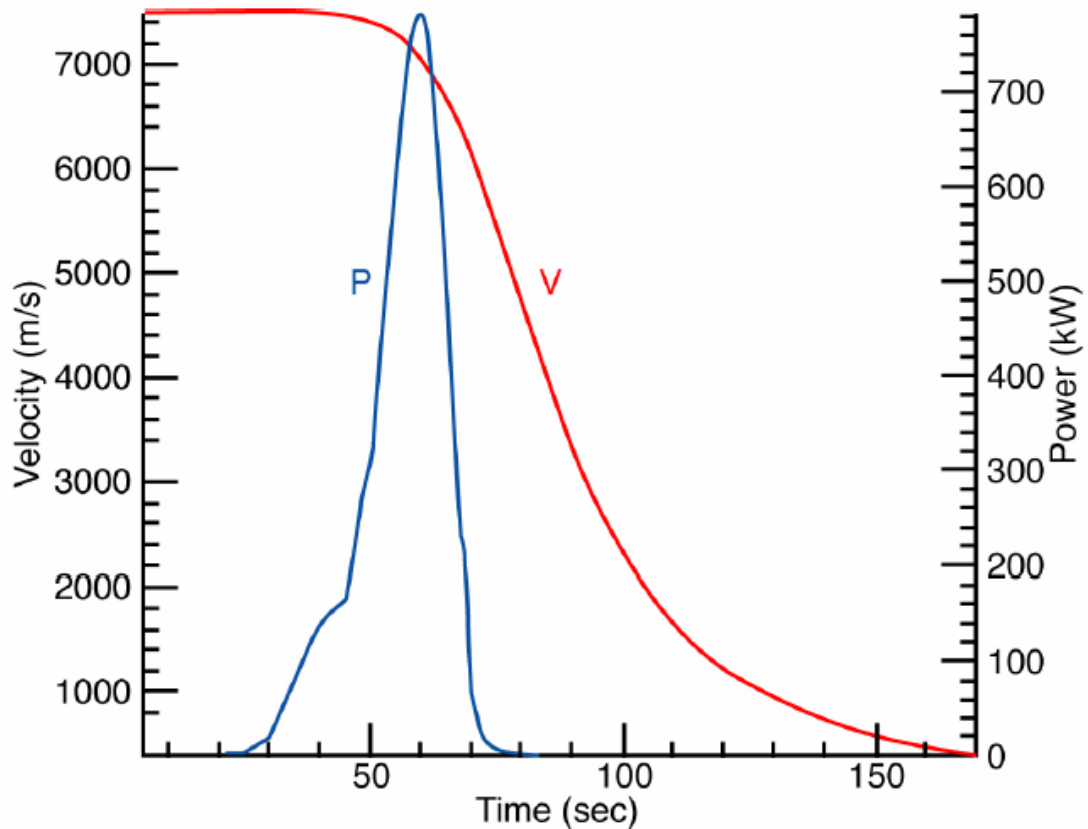


Figure 1.25: MHD power available vs. time for  $1000\text{ kg}$  ballistic test vehicle simulation at Mars, adapted from [55]

In addition to the work presented in [55], additional systems investigations of this concept have been undertaken by Moses as well as the author of this thesis, showing further

potential for MHD energy generation at Mars. [54] [56] [7] [57]

### 1.9.2 MHD Lorentz Force Drag Augmentation at Mars

MHD deceleration of reentry vehicles is also possible at Mars. In a 2012 study entitled, “Effectiveness of a Magnetohydrodynamics System for Mars Entry,” Kim and Boyd investigate MHD interaction during Mars entry for drag augmentation and convective heat flux reduction. [53] This work is significant in that it does a detailed numerical investigation of magnetoaerodynamically enhanced drag and reduced convective heat flux for Mars applications, which had not been done thus far at this fidelity. In the study, Kim and Boyd investigate MHD interaction by simulating the Mars Pathfinder entry vehicle forebody geometry with a 1.0  $T$  dipole magnet embedded within. They present computational results that show the potential for a large magnetoaerodynamic drag force of similar magnitude to the aerodynamic drag force. These results are particularly promising for the case of Mars entry because the thin atmosphere provides limited aerodynamic drag, so that the ‘magnetic parachute’ concept that MHD deceleration can provide is particularly useful. Figures 1.26 and 1.27 give a schematic of the simulated reentry vehicle and sample results at a point on the trajectory corresponding to a free-stream velocity of approximately  $7.4 \text{ km/s}$  and altitude of  $70 \text{ km}$  at Mars.

There have recently been other numerical and design investigations into MHD deceleration at Mars by the author of this thesis and others; however, it remains an area of much interest with limited studies available on the subject. [58] [59]

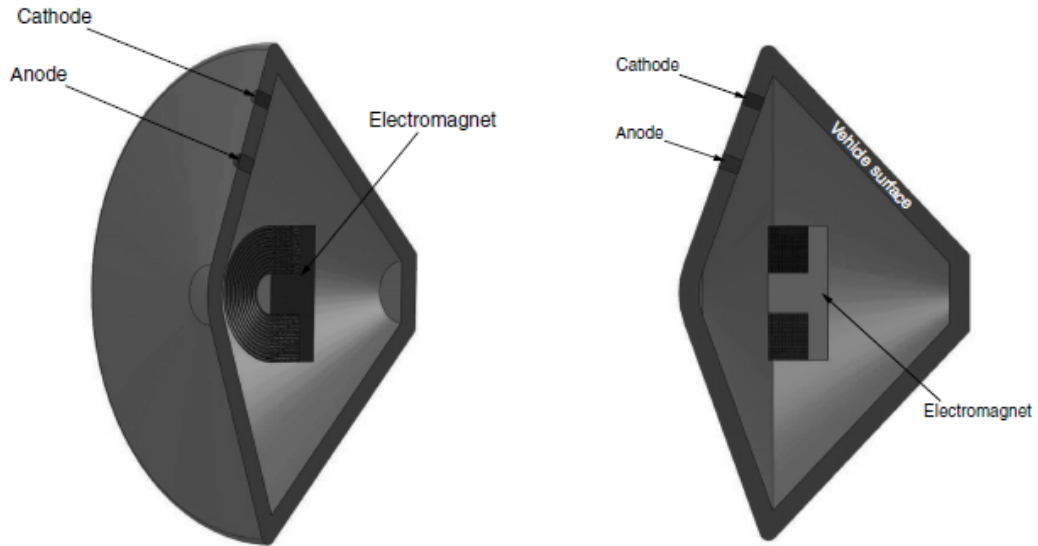


Figure 1.26: Mars Pathfinder vehicle forebody equipped with a 1.0 T electromagnet for simulation, adapted from [53]

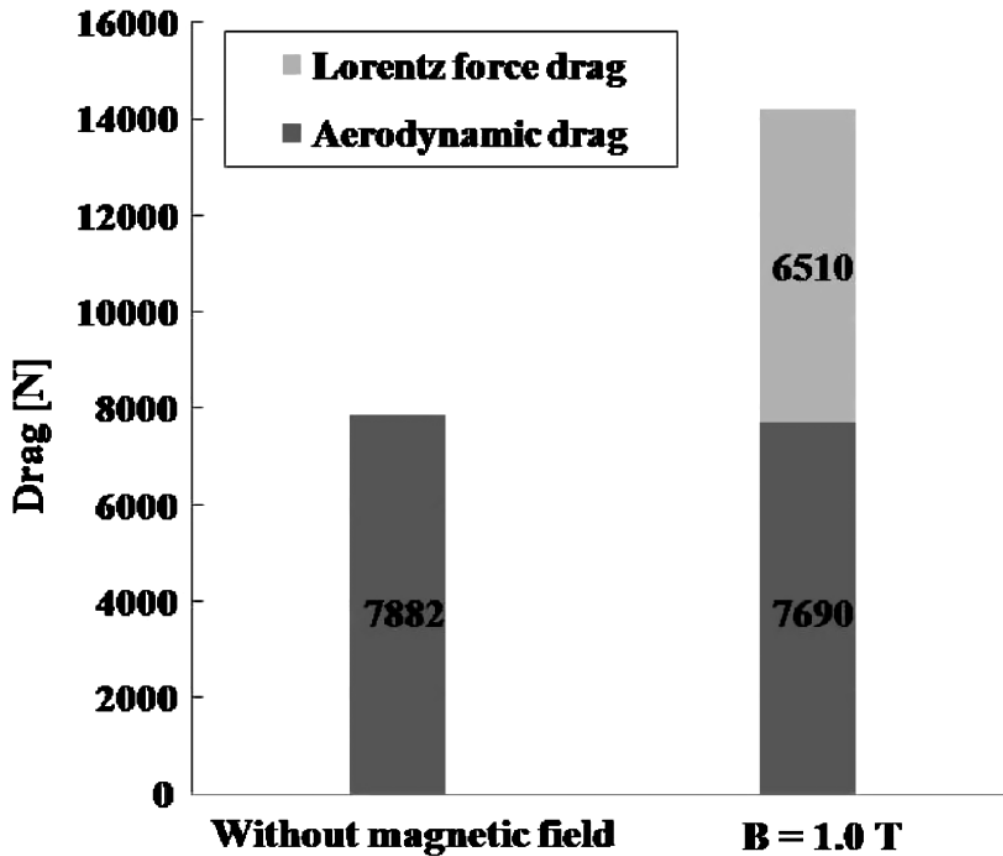


Figure 1.27: Mars pathfinder forebody drag with and without a 1.0 T magnetic field. Inflow velocity  $V_\infty = 7431.3 \text{ m/s}$  and atmospheric conditions for 70 km MOLA altitude, adapted from [53]

## 1.10 Gap Analysis and Thesis Statement

Previous research indicates that MHD energy generation can be a useful part of future Mars missions.[55] It may also be of use for control of communications blackout during entry, making it of immediate interest to Earth entry as well. Numerous MHD energy generation schemes for planetary entry vehicles have been proposed and studied.[36][43] Preliminary analysis based on an entry trajectory similar to that used for the Mars Pathfinder mission suggests that up to 100 MJ per square meter of generator area could be harvested.[8] However, strong magnetic fields on the order of 1 Tesla would be required, as well as an electrical energy storage system to store and handle the generated energy.

A potential MHD generator system for a planetary entry application would at its core consist of the following elements: MHD energy generator body, magnetic field source, electrodes, and some type of electrical energy storage system.[8] Performance of an MHD energy generation system is contingent on the electrical conductivity of the plasma involved, which for the regimes typically encountered during atmospheric entry is most dependent on ambient electron number density, which is most dependent on temperature. The ambient electron number density is driven by ionizing reactions taking place in the high-temperature post-shock region and is significant for a relatively short period of time during a traditional direct entry trajectory. For example, the aforementioned 92.5% of kinetic energy lost during the hypersonic phase of the Mars Pathfinder entry occurred in about 30 seconds, presenting difficulties in implementing an energy storage system capable of handling the electrical load. For a Mars Pathfinder class spacecraft, about 14  $MJ$  of energy per  $m^2$  of electrode area can be reclaimed during this period; however, because this energy generation occurs over about 30  $s$ , a electrical energy generation power of nearly 1  $MW$  occurs.[55] If the energy storage device cannot accept power at this rate, then not all of the energy can be stored. In addition, the ability of an energy storage device to accept energy at a high rate is coupled to its mass, exacerbating the difficulty of reclaiming all the available

energy.[60]

Previous investigations of MHD interaction for planetary entry vehicles employed full-field numerical analysis of the hypersonic flow-field, chemical and ionizing reactions, and detailed design of the MHD energy generator at specific boundary conditions to calculate the energy reclaimed through MHD energy generation.[36][43] Modeling the storage of this generated energy is also difficult due to the diversity of technologies with which electrical energy can be processed and stored.[60] During the conceptual design of a mission, these calculations are further challenged by variations and trade studies in the specific entry vehicle trajectory, geometry, and energy storage system.

## **1.11 Research Goals and Summary of Contributions**

The goal of this thesis is to advance the state of the art for the performance analysis of planetary entry systems equipped with MHD energy generator and flow control devices. This goal is advanced through two primary contributions. The first contribution relates to estimation methodologies for MHD interaction, while the second relates to experimental investigations of MHD interaction. Both contributions are developed in parallel, without coupling, with demonstrating feasibility as the primary goal of the experimental efforts. These contributions are described in more detail in sections 1.11.1 and 1.11.2, respectively.

### 1.11.1 Contribution I: Magnetohydrodynamic Energy Generation and Lorentz Force Drag Augmentation Performance Characterization and Impact on Planetary Entry Architectures

Calculating the energy reclaimed through MHD energy generation during hypersonic entry is challenging, with previous investigations employing full-field numerical analysis of the hypersonic flow-field, chemical and ionizing reactions, and detailed design of the MHD energy generator at specific boundary conditions. [36][43] The additional drag potential due to the presence of the Lorentz force is similarly challenging to compute without a full-field numerical simulation.[53] These calculations are made even more challenging during mis-

sion design, as the specific entry vehicle trajectory, geometry, and energy storage system may be unknown, and trade studies can become computationally expensive. Thus, there is a need for tools and techniques that are more applicable to conceptual design. This contribution represents methodologies by which the energy available for extraction through MHD energy generation and additional drag due to the Lorentz force can be calculated in a manner suitable for conceptual design. These methodologies do not require detailed knowledge of the MHD generator or flow control system, and depend on only on parameters such as the planetary body, entry vehicle diameter, drag coefficient, entry vehicle mass, and applied magnetic field strength, enabling rapid iterations and trades useful for identifying planetary entry mission architectures that may benefit from the inclusion of MHD energy generation and flow control.

Previous literature concerning MHD and planetary entry has usually focused on one entry vehicle configuration at one or a few entry conditions[35][39][53], limiting the analysis capability for rapid trade studies with the limited entry vehicle design and trajectory specifics available in conceptual design. In this contribution, systems analysis capabilities for entry systems equipped with MHD generators and flow control devices are developed. These capabilities aim to quantify the additional system mass required for MHD systems, as well as their potential performance for energy generation and flow control across a wide variety of vehicles.

Currently, a conceptual analysis capability for MHD generator equipped entry descent and landing systems has been developed. This methodology integrates models for flight dynamics, MHD energy generation, energy storage, atmosphere, and post-shock chemical equilibrium to compute the potential for generation and storage of energy through MHD interaction. In addition, the application of the methodology is demonstrated for various case studies in which the entry mass, entry conditions, and energy storage system technologies were varied. A benefit of this methodology for space systems conceptual design is the ability to conduct rapid iteration across many design parameters without detailed generator

and vehicle design information, thus allowing the identification of mission configurations amenable to MHD energy generation and storage. For a majority of the cases analyzed, storage of the available energy with an electrical energy storage system that had a medium or higher TRL was deemed possible. As such, MHD energy generation and storage is deemed a potential useful technology for future planetary exploration missions.

In addition, a systems analysis capability for the effect of MHD flow interaction on a planetary entry vehicle equipped with a MHD energy generation system has been developed. The analysis techniques employed and the associated results demonstrate that MHD flow interaction effects can be computed for a variety of entry vehicles using fundamental functional relationships between flow properties. The results show that MHD flow interaction for the magnetic field configuration presented causes a significant increase in overall entry vehicle deceleration and trajectory given appropriate alkali metal seed and magnetic field strength. The effect of the flow interaction is similar to a decrease in the ballistic coefficient of a particular vehicle, essentially causing the vehicle to decelerate higher in the atmosphere. In this thesis, consideration of active control of the magnetic field orientation and magnitude for inducing lift and control moments on the vehicle is left to future work. This aspect of the MHD flow interaction could prove particularly interesting because the majority of the additional drag occurs at much higher altitudes than the aerodynamic drag.

#### 1.11.2 Contribution II: Experimental Design and Investigation for Magnetohydrodynamic Energy Generation in Conditions and Configurations Relevant to Planetary Entry

The number of experimental investigations of MHD interaction for conditions relevant to planetary entry is limited. There are a few experimental investigations dating back to the late 1950s and 1960s, mainly concerned with the effects MHD interaction has on shock standoff distance.[29][31][32][33] More recent studies describe various experimental campaigns aimed at investigating drag enhancement, heat-flux mitigation, artificial ionization, and energy generation through MHD interaction. [45][44][50][8] From all of these exper-

iments, it is apparent that creating and testing MHD interaction in conditions relevant to planetary entry is a challenging task requiring specialized equipment.

The design, implementation, and characterization of a supersonic plasma discharge wind-tunnel is presented. The overall structure of the experiment is similar to that described in [8], in which a gas source was accelerated to supersonic speed using a converging-diverging nozzle, artificially ionized to create a supersonic plasma, and used to simulate atmospheric entry plasmas. In this thesis, the gas is first ionized using radio-frequency (RF) radiation instead of microwaves, passed through an optically clear quartz converging-diverging nozzle tube, and expanded to supersonic speed. The new experimental design is demonstrated to produce a highly repeatable, verified supersonic plasma wind-tunnel, with calculated free-stream Mach numbers on the order of  $M = 3.0$ . This supersonic plasma wind-tunnel is used to simulate atmospheric entry plasmas in order to study experimentally magnetohydrodynamic interaction for planetary entry vehicle geometries.

Furthermore, the design and execution of an experimental campaign to demonstrate MHD energy generation for a non-channel type MHD energy generation on a simulated blunt-body reentry vehicle is presented. A permanently magnetized ceramic model with electrodes for current generation is designed, manufactured, and inserted into the aforementioned supersonic plasma discharge. The proposed experimental design is executed for several configurations, and appears to show a positive effect for current through the MHD generator model when the supersonic plasma discharge is present. As compared to the preliminary investigation done in [8], the experimental campaign in this thesis includes additional diagnostics and higher fidelity datasets that enable correlation to real atmospheric entry flight conditions and better informed parametric dependencies for theoretical models used in conceptual design.

### 1.11.3 Summary of Contributions

To conclude, MHD flow interaction has the potential to significantly benefit planetary entry systems. Through the aforementioned contributions, this thesis advances the state of the art for planetary entry systems equipped with MHD interaction devices.

**CHAPTER 2**

**MAGNETOHYDRODYNAMIC ENERGY GENERATION AND LORENTZ  
FORCE DRAG AUGMENTATION PERFORMANCE CHARACTERIZATION  
AND IMPACT ON PLANETARY ENTRY ARCHITECTURES**

**2.1 Magnetohydrodynamic Energy Generation and Lorentz Force Drag Augmentation Performance Characterization**

In this section, analytic conceptual design models are developed in order to estimate the upper-bound performance of planetary entry systems equipped with magnetohydrodynamic (MHD) flow interaction devices. In particular, the models presented focus on characterizing the energy available for extraction for via MHD generation and Lorentz force drag augmentation impact.

2.1.1 Modeling and Computation of Post-Shock Properties

In order to calculate both the energy available via MHD energy generation and the additional Lorentz force possible through MHD interaction, the post-shock thermal properties and gas composition must be known. The scalar electrical conductivity of the ionized gas in the shock layer is of particular importance. The approach taken in this conceptual design tool is to treat the shock in front of the vehicle as a normal shock with chemistry in order to better facilitate applicability to entry vehicles with varying forebody geometry, making both the pre-shock and post-shock properties uniform. This model most closely approximates the hypersonic bow shock near the stagnation region. A schematic of the developed model is shown as Figure 2.1.

Because the model assumes that all properties in the shock layer are uniform, and that electrical conductivity can be treated as a scalar, rather than the true tensor-formulation

including Hall-effect terms, it represents idealized, upper-bound performance results. The true performance of an actual MHD interaction system is expected to be lower, represented by an efficiency knockdown factor  $\eta$ , though the exact degree will only be evident from detail numerical or experimental investigations, which is outside the scope of this conceptual design effort.

To calculate the electrical conductivity, the atmospheric properties and composition after passing through a shock wave must be calculated. Since the ambient density, pressure, and temperature can be calculated as functions of altitude, and ambient atmospheric species composition is known and assumed to be constant, the addition of velocity fully specifies the post-shock state. A chemical equilibrium solver, in this case NASA's Chemical Equilibrium and Applications (CEA) code, is then used to calculate the post-shock state by solving the equilibrium one-dimensional normal shock problem with chemistry.[61]

Table 2.1: Martian Atmospheric Composition

Constituent	Relative Abundance
CO <sub>2</sub>	96.0%
Ar	1.9%
N <sub>2</sub>	1.9%
O <sub>2</sub>	0.14%
CO	0.06%

Martian atmospheric constituents and their abundances are presented in Table 2.1 in or-

Table 2.2: Earth Atmospheric Composition

Constituent	Relative Abundance
N <sub>2</sub>	78.084%
O <sub>2</sub>	20.946%
Ar	0.934%
CO <sub>2</sub>	0.036%

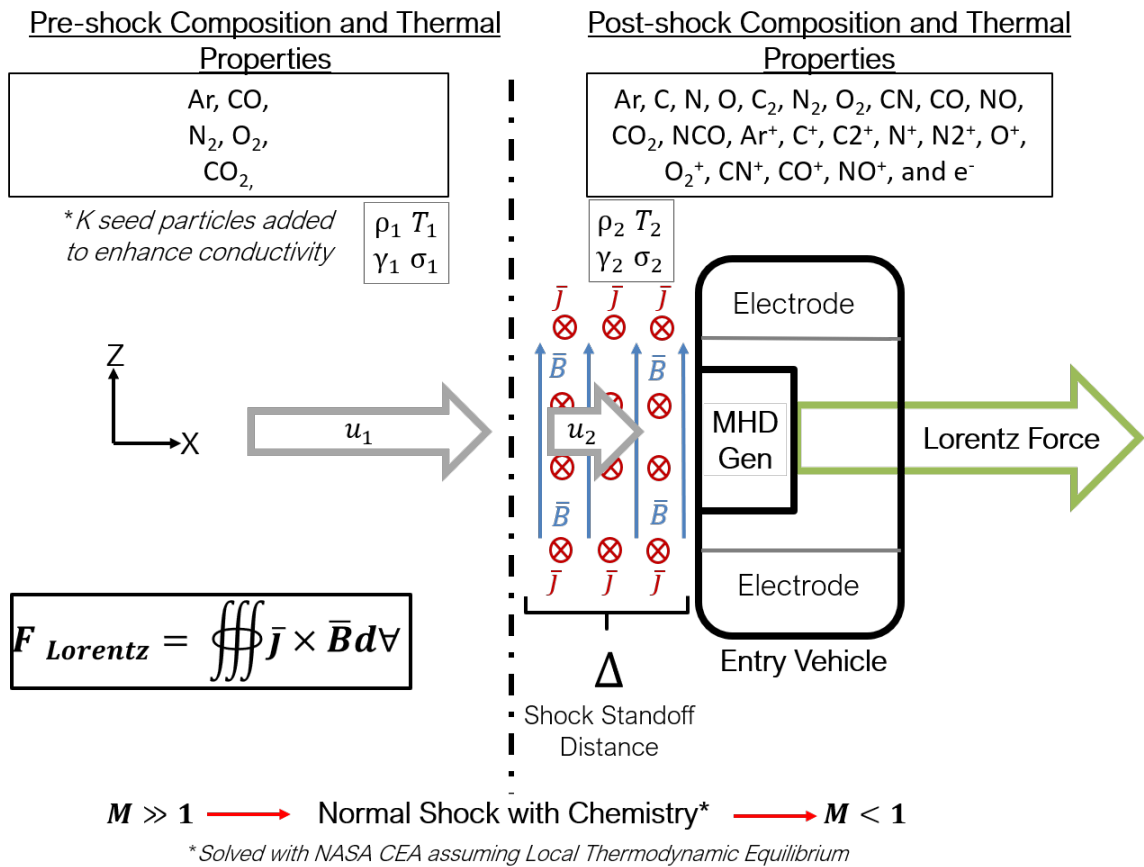


Figure 2.1: Conceptual design tool framework for MHD interaction during planetary entry.

der of relative abundance.[3] Post-shock species include: Ar, C, N, O, C2, N2, O2, CN, CO, NO, CO2, NCO, Ar+, C+, C2+, N+, N2+, O+, O2+, CN+, CO+, NO+, and e-. Similarly, the atmospheric constituents and abundances used for Earth are given in Table 2.2, with the same post shock species. Using these data in conjunction with the ambient atmospheric temperature and pressure as a function of altitude, the post-shock temperature, pressure, and species composition can be calculated as a function of altitude and free-stream velocity by solving the equilibrium one-dimensional shock problem with chemistry.

Once the species composition, temperature, and pressure are known, the scalar electrical conductivity in the shock layer can be calculated. The scalar electrical conductivity is strongly dependent on the post-shock temperature for both the Earth and Mars atmospheres, as shown in previous investigations on the topics.[53] [39] For this analysis, the conductivity models employed for both the Mars and Earth atmospheres are taken as functions of temperature. The conductivity model employed for the Mars atmosphere is shown as equation 2.1.[53]

$$\sigma = a_0 + a_1(T/T_0) + a_2(T/T_0)^2 + a_3(T/T_0)^3 + a_4(T/T_0)^4 \quad (2.1)$$

where  $T$  is the temperature in the shock layer,  $T_0 = 1000K$ ,  $a_0 = 95.369 \frac{1}{\Omega m}$ ,  $a_1 = -174.4 \frac{1}{\Omega m}$ ,  $a_2 = 81.289 \frac{1}{\Omega m}$ ,  $a_3 = -2.7945 \frac{1}{\Omega m}$ , and  $a_4 = 0.02783 \frac{1}{\Omega m}$ . For the Earth atmosphere case, the conductivity model shown as equation 2.2 is employed.[39]

$$\sigma = C_1 e^{(-C_2/T)} \quad (2.2)$$

where  $T$  is the temperature in the shock layer,  $C_1 = 8300 \frac{1}{\Omega m}$ , and  $C_2 = 36000 K$ . The results of the conductivity models using the calculated post-shock properties as functions of altitude and velocity are shown in Figures 2.2 and 2.3

The free-stream chemical composition in Table 2.1 can be altered by considering the addition of a small mass fraction of easily ionizable alkali metal seed such as potassium into

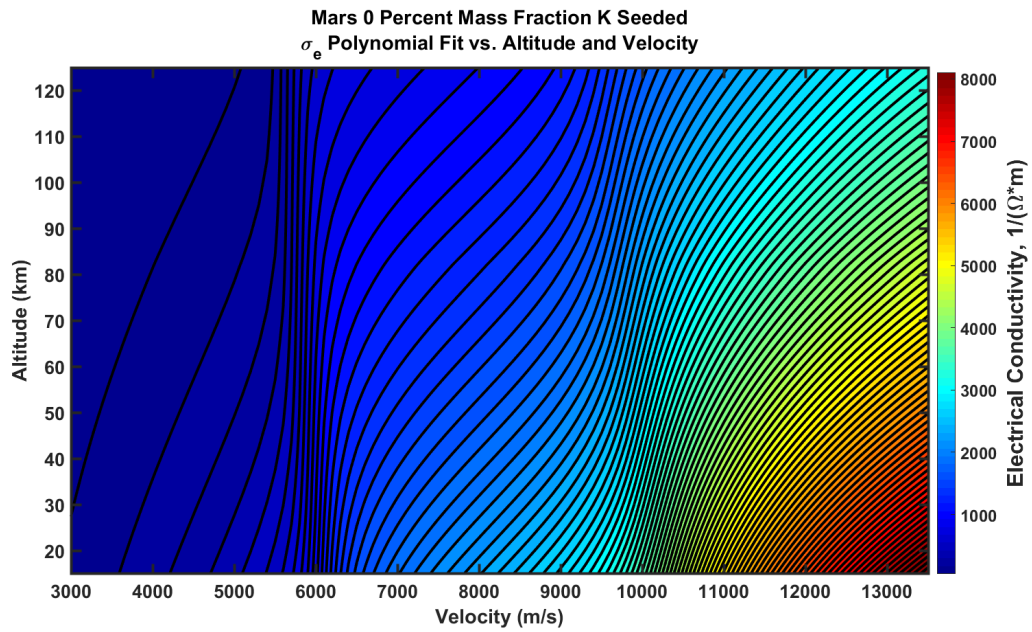


Figure 2.2: Post-shock scalar electrical conductivity  $\frac{1}{\Omega m}$  as a function of Mars altitude and vehicle velocity

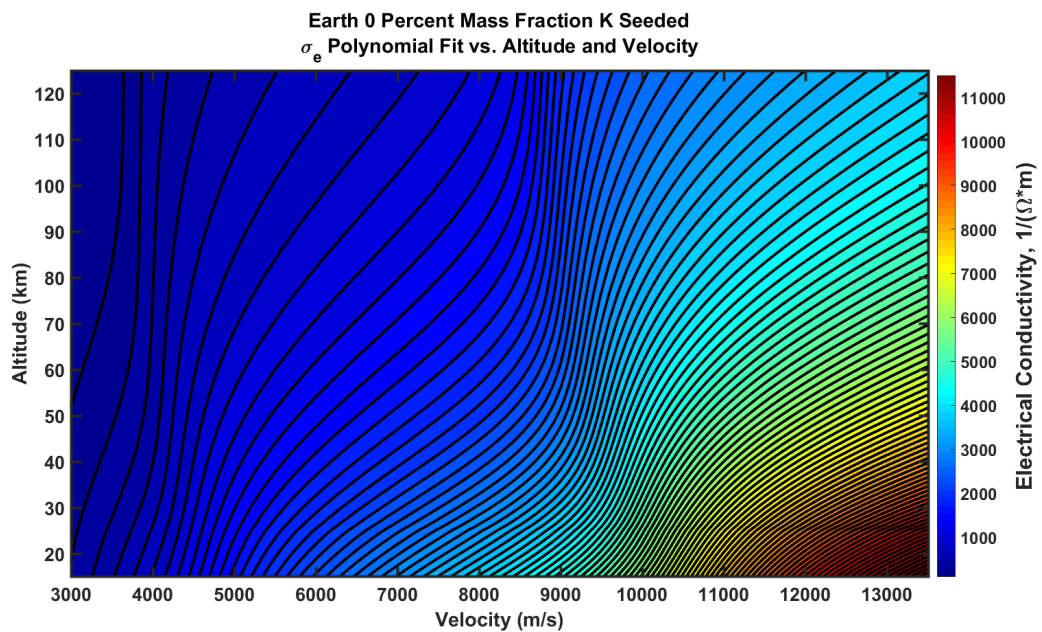


Figure 2.3: Post-shock scalar electrical conductivity  $\frac{1}{\Omega m}$  as a function of Earth altitude and vehicle velocity

the shock layer. It was found in [36] that the post-shock electron number density and thus the electrical conductivity and MHD interaction effect are significantly enhanced at even potassium seed mass fractions of less than 1%. As such, variable free-stream chemical compositions are considered for potassium seed mass fractions between 0% and 1%. So far, this functionality has only been implemented for the Martian atmosphere, and ratio electron number density for seeded to unseeded flow is used as a multiplier on the initial electrical conductivity computed based on post-shock temperature.

Once a seed mass fraction and planetary atmosphere are selected, the post-shock state is solved using NASA's Chemical Equilibrium with Applications Code [61] for altitudes between 15 and 125 km and free-stream velocities between 3000 and 13500 m/s to encompass the range of conditions relevant to hypersonic entry. The post-shock properties at each grid point are stored for efficient computation of these chemical properties via a bilinear interpolation table lookup during dynamics simulations. These properties include but are not limited to: the electron number density, shock density ratio, post-shock velocity, ionization fraction, electrical conductivity, temperature, and molecular composition. Post-shock properties of particular interest for the computation of electrical power available for extraction via MHD energy generation and additional axial Lorentz force drag on the entry vehicle are the shock layer scalar electrical conductivity and the shock density ratio.

### 2.1.2 Magnetohydrodynamic Energy Generation Performance Model for Conceptual Design

The total energy available via MHD energy generation is the integration of the power available for a MHD generator along a given trajectory. To actually calculate this power generation profile, it is necessary to identify the relevant physical interactions occurring along a given trajectory. These interactions are the gravitational interaction between planetary body and spacecraft, the aerodynamic interaction between planetary atmosphere and spacecraft, and the thermochemical interaction within the atmosphere as the spacecraft moves at hypersonic speed. The superimposed effects of these three physical interactions allow for the

definition of the position state, velocity state, and electron number density. These states define the total power that can be generated by MHD energy conversion. For a Faraday type MHD generator, the generated power behaves according to the scaling law given in equation 2.3.[55]

$$P \propto \sigma_e u^2 B^2 A_c L_i \quad (2.3)$$

where  $P$  is the generator power output,  $\sigma_e$  is the scalar electrical conductivity,  $u$  is the local flow velocity,  $B$  is the magnetic field strength,  $A_c$  is the generator interaction area, and  $L_i$  is the generator length. In reality, an open channel Faraday type MHD energy generator may be unsuitable for planetary entry applications due to the necessity of allowing the high-temperature entry plasma to flow through the vehicle. However, equation 2.3 still applies to a non-flow through MHD energy generator design applicable to planetary entry vehicles and thus be used in this design tool.[43]

For the purposes of this design tool, the magnetic field strength is assumed in all cases to be a constant  $0.2 T$  as determined in previous investigations.[36][43] The generator area is assumed to be 1 square meter in all cases as well, with a characteristic length of 1 meter, to remove the influence of  $A_c$  and  $L_i$ . As a result, the above scaling law can be reduced to a function of electrical conductivity and velocity only, given as equation 2.4.

$$P \propto \sigma_e u^2 \quad (2.4)$$

The local flow velocity is proportional to the free-stream velocity, which can be calculated by defining the system dynamics and integrating to obtain position and velocity as a function of time. Taking into account the gravitational and aerodynamic interaction, the equations of motion for the system relative to the planetary center of mass are solved, shown as equation 2.5.

$$\ddot{\bar{r}} = -\frac{\mu}{(\bar{r} \cdot \bar{r})^{\frac{3}{2}}}\bar{r} - \frac{\rho(\dot{\bar{r}} \cdot \dot{\bar{r}})\hat{\bar{r}}}{2\beta} \quad (2.5)$$

where  $\bar{r}$  is the position vector of the entry vehicle relative to the planetary body,  $\mu$  is the gravitational parameter for the planetary entry body,  $\rho$  is the ambient atmospheric density, and  $\beta$  is the ballistic coefficient of the entry vehicle, a similarity parameter that defines the influence of aerodynamic drag on the entry vehicle dynamics, defined as equation 2.6

$$\beta = \frac{m}{C_D A} \quad (2.6)$$

where  $m$  is the entry vehicle mass,  $C_D$  is the entry vehicle drag coefficient, and  $A$  is the entry vehicle area.

The aforementioned approach is implemented numerically in MATLAB. The temperature and pressure are written as simple functions of altitude based on relevant Mars and Earth atmospheric data, with temperature following a linear profile and pressure following an exponential one. The atmospheric composition is taken to be constant with altitude and in conjunction with the ideal gas law allows for the calculation of the density variation with altitude as well. The specification of the ambient temperature, pressure, composition, density complete all relevant atmospheric inputs into the model. Given initial conditions, the model calculates the position and velocity states as functions of time until the spacecraft's trajectory intersects with the planetary surface.

Each initial condition allows for the computation of the position and velocity states throughout the corresponding trajectory, giving the altitude and velocity at each point in time. The scalar electrical conductivity is calculated using equations 2.1 and 2.3 and the output of NASA's CEA solution to the post-shock thermochemistry problem. Inputs to NASA CEA are the freestream velocity, atmospheric composition, ambient atmospheric pressure, and ambient temperature. The ambient pressure and temperature can be generalized as functions of altitude for each planetary atmosphere, such that the shock layer

electrical conductivity is essentially a function of altitude and velocity only. These values then define the power available for MHD energy generation as represented by equation 2.7.

$$P = C_{power} \sigma_e u^2 B^2 \quad (2.7)$$

where  $C_{power}$  is a constant of proportionality to be determined from either detailed numerical results or previous work. Based on a reconstructed altitude velocity history from the previous literature [55] and the thermochemical model presented in this thesis, the constant  $C_{power}$  has a value of  $1.9417 \times 10^{-3}$  for power available in Watts, allowing for analysis across multiple entry vehicles, planetary bodies, and entry conditions.

An example of this sample calibration is shown as Figure 2.4. As mentioned earlier, the applied magnetic field value is fixed at  $0.2 T$ , as specified by previous literature in order to minimize diminishing returns due to induced Hall-currents.[36] The reconstructed trajectory altitude and velocity history are input into the aforementioned thermochemical model presented in this thesis, and the power output calculated from the previous detail numerical investigation is plotted against the product of free-stream velocity squared, magnetic field value squared, and scalar electrical conductivity ( $u^2 B^2 \sigma_e$ ). In this case, the model is limited to when the electrical conductivity can be treated as a scalar and increasing the ionization fraction or applied magnetic field values significantly beyond the data for which the calibration coefficient is determined requires computation of a new  $C_{power}$ . As an example of the uncertainty in the estimations produced by this model, changing the parametric model for electrical conductivity, the most variable parameter, resulted in variation by approximately an order of magnitude in the final  $C_{power}$  value. As a result, this model can be said to be an upper-bound performance estimate, with expected accuracy of within one order of magnitude.

In future work, this constant can be recomputed using a more detailed numerical simulation that accounts for the specific geometry of the generator as well as the full flow field and chemical kinetics surrounding the entry vehicle. Alternatively,  $C_{power}$  could be deter-

mined from experimental results for generator configurations and test conditions relevant to planetary entry, though they do not currently exist with enough fidelity to do so. However, for the current form of this model, this value for  $C_{power}$  is used to provide a reference demonstration for the methodology, and to determine for which planetary entry vehicle design cases MHD interaction is relevant.

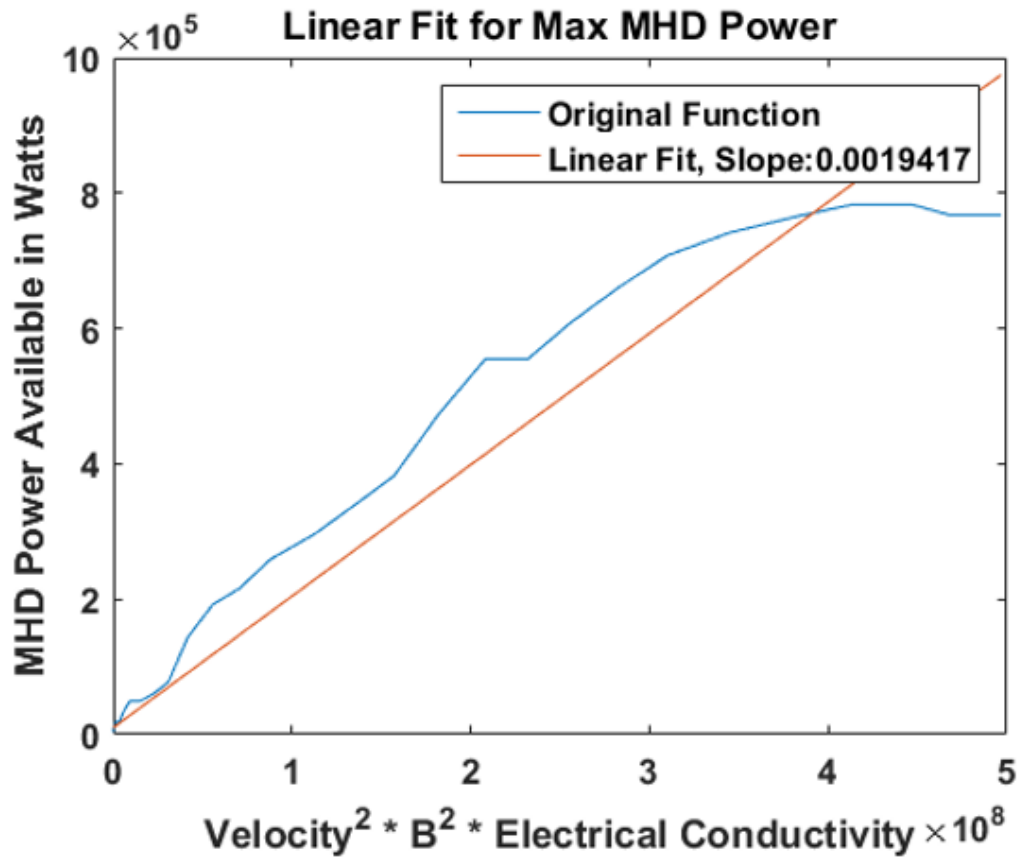


Figure 2.4:  $C_{power}$  example correlation based on MHD power available vs. time profile results presented in [55]. Reconstructed trajectory altitude-velocity history is input into the developed thermochemical model to calculate electrical conductivity. Magnetic field strength is fixed at  $B = 0.2 T$

### 2.1.3 Magnetohydrodynamic Lorentz Force Drag Augmentation Performance Model for Conceptual Design

For the ionized, hypersonic flow-field around a blunt-body entry vehicle with an applied magnetic field, there will exist an additional body force on the fluid due the MHD flow interaction, called the Lorentz force. This force, denoted as  $\bar{F}_{MHD}$ , acts on the entry vehicle through the magnetic field, and is expressed as equation 2.8. [35]

$$\bar{F}_{MHD} = \int \bar{j} \times \bar{B} dV \quad (2.8)$$

where  $\bar{j}$  represents the electric current density vector, and  $\bar{B}$  represents the applied magnetic field vector. The electrical current density can be determined through an application of Ohms law, given below as equation 2.9.

$$\bar{j} = \sigma(\bar{E} + \bar{u} \times \bar{B}) \quad (2.9)$$

where  $\sigma$  is the local electrical conductivity. In the manner of [35], the Hall effect is neglected in equation 2.9 by assuming that the entry vehicle walls are non-conductive. Furthermore, in conjunction with an assumed axisymmetric magnetic field, there is no induced electric field and the current density vector will only have an azimuthal component. In further assuming that all flow properties in the shock layer, such as electrical conductivity, velocity, and density are constant, equation 2.10 is obtained for the axial Lorentz force acting on the vehicle due to MHD flow interaction.

$$\bar{F}_{MHD} = \sigma u_{post-shock} B^2 \forall_{shock-layer} \quad (2.10)$$

where  $B$  is the magnitude of the applied magnetic field, also assumed constant throughout the shock layer and  $\forall_{shock-layer}$  is the volume of the shock layer, with the electrical conductivity and thus the current density assumed to be zero in the pre-shock environment.

The post-shock velocity is determined by applying conservation of mass across a steady, one-dimensional shock wave, and is given as equation 2.11.

$$u_{post-shock} = \frac{\rho_{\infty}}{\rho_{post-shock}} u_{\infty} \quad (2.11)$$

where  $\rho_{\infty}$  represents the free-stream density,  $\rho_{post-shock}$  represents the shock layer density, and  $u_{\infty}$  represents the free-stream velocity.

The shock layer volume is approximated as the product of the shock separation distance,  $\Delta$ , and the projected vehicle area,  $A$ , and is given as equation 2.12.

$$\forall_{shock-layer} = \Delta \times A \quad (2.12)$$

The shock separation distance for an axisymmetric blunt body in hypersonic flow has been experimentally shown to be a strong function of the shock density ratio [30], and is given below as 2.13.

$$\Delta \propto \frac{\rho_{\infty}}{\rho_{post-shock}} D \quad (2.13)$$

where  $D$  is the vehicle diameter. Since the projected area,  $A$ , is itself a function of diameter, equation 2.12 can be rewritten as equation 2.14.

$$\forall_{shock-layer} \propto \frac{\rho_{\infty}}{\rho_{post-shock}} D^3 \quad (2.14)$$

Combining equations 2.11 and 2.14 and substituting into equation 2.10 gives the relationship for the additional axial force caused by MHD flow interaction, shown as equation 2.15.

$$\bar{F}_{MHD} = C_{force} \sigma u_{\infty} \frac{\rho_{\infty}}{\rho_{post-shock}}^2 B^2 D^3 \quad (2.15)$$

where  $C_{force}$  is a constant of proportionality, determined from a survey of prior results for MHD augmented drag and is a function of the vehicle, flow field, and magnetic field ge-

ometries. Generally, it is based on previous results from a full-field numerical simulation. For example, in reference [53] a 70 degree sphere-cone blunt body with a dipole magnetic field entering the Martian atmosphere is considered. Based on the vehicle diameter, applied magnetic field strength, and computed additional axial force due to MHD interaction,  $C_{force}$  had a value of 0.0564, enabling rapid computation across a range of flight conditions and vehicle diameters, a function useful for vehicle design. In a similar fashion to the  $C_{power}$  coefficient determined for MHD energy generation, the  $C_{force}$  calibration coefficient is most accurate for the case in which it was determined, in this case Mars ballistic entry, and if there is significant deviation from this case, due to significantly higher ionization or applied magnetic field, then a new constant would be necessary, due to variation on the order of one magnitude. In this thesis, the value of  $C_{force} = 0.0564$  is used for all further investigation, due to its relevance to Mars entry and as a demonstration of the estimation methodology, again as an upper-bound. The modified equation of motion including MHD interaction is given as equation 2.16. This equation is integrated numerically to calculate the modified vehicle trajectory.

$$\ddot{\vec{r}} = -\frac{\mu}{(\vec{r} \cdot \vec{r})^{\frac{3}{2}}}\vec{r} - \left(\frac{u_{\infty}^2}{2\beta} + \frac{\bar{F}_{MHD}}{m}\right)\hat{\vec{r}} \quad (2.16)$$

where once again  $\mu$  is the planetary body's gravitational parameter,  $m$  is the entry vehicle mass,  $\beta$ , and  $\rho_{\infty}$  and  $u_{\infty}$  are the free stream density and velocity respectively. Equation 2.16 indicates that adding MHD interaction at any point along the trajectory *always* increases the total drag force, though it may reduce the peak deceleration experienced as compared to pure-aerodynamic drag alone due to reduced velocity lower in the atmosphere. This effect is captured when the entire trajectory with MHD interaction is integrated.

Given the initial conditions for planetary entry, vehicle parameters, and magnitude of the applied magnetic field, the equations of motion are numerically integrated in MATLAB, and the position and velocity states of the entry vehicle subject to gravity, aerodynamic, and

MHD interaction forces are computed. The simulation is terminated once the vehicle goes below 1 *km* altitude. In addition, an alkali metal seeding mass fraction is specified, allowing for the calculation of modified post-shock electrical conductivity for determination of the MHD interaction force. This model has currently only been applied to Mars as a planetary body, but could be extended to other planetary bodies as well.

## **2.2 Case Study for Impact of Magnetohydrodynamic Energy Generation on Planetary Entry Architectures**

In this section, the impact of magnetohydrodynamic interaction on planetary entry systems for energy generation is investigated using the performance models presented previously. The investigations consider both the Earth and Mars planetary atmospheres and present trade space explorations across a variety of planetary entry system parameters.

### 2.2.1 Introduction to Electrical Energy Storage Systems

Electrical energy storage (EES) systems are extremely diverse in their mechanisms and applications. These systems can be mechanical, chemical, and electrodynamic in mechanism, while others still are combinations of these elements. Applications for electrical energy storage systems range from mobile devices to large water retention ponds capable of powering entire cities for long periods of time.[62] With such a diversity in mechanisms and applications, appropriate performance objectives upon which to evaluate electrical energy storage systems are challenging to develop. This problem is particularly troublesome for systems under development that may have an ill-defined application profile.

Examples of common electrical energy storage system performance parameters include mass, endurance, power capacity, longevity, and heat generation. The application being presently considered is a flight application, and thus mass is expected to play an extremely important role in the suitability of an energy storage technology. In addition, although electrical energy storage system parameters such as longevity and heat generation are im-

portant, the assessment of their impact requires detailed system design information that is outside the scope of this analysis and typically not known without precise knowledge of the energy usage loads and flight system geometry. The total amount of electrical energy generated will allow for estimation of the size of energy storage device needed; however, as mentioned earlier the electrical energy generation for this application may occur at a relatively high rate that will place requirements on system power capacity as well.[62]

Thus, for the purposes of this analysis, total electrical energy storage system mass is determined to be the most important parameter. If some total amount of energy is to be generated at a certain rate, mass and energy requirements can be calculated. Both total energy storage capacity and discharge power capacity for an electrical energy storage system can be related to system mass by defining mass specific versions of each of these properties. Typical units are Watt hours per kg and Watts per kg for specific energy storage and power discharge capacity. Although electrical energy storage systems for a given type may vary in their values for the aforementioned parameters, there is typically a range for each parameter that is considered appropriate for a given technology. These values are determined experimentally and continually evolve as new developments in energy storage techniques come to fruition. These ranges can be used to define a best, average, and worst case scenario for a given technology.

The electrical energy storage systems categories that will be considered in this analysis are batteries, capacitors, and miscellaneous devices such as flywheels and super conducting magnetic energy storage. For the present application of power generation and energy storage, charge power capacity and discharge power capacity are assumed to be roughly equal, simplifying the analysis. One way in which to visualize the performance of these systems is to plot the specific power versus the specific energy storage capacity. Such a plot is termed a Ragone plot, and such a plot generated using the values employed for this analysis is given as Figure 2.5. For the application being considered, good choices generally lie to the top right of the chart, while poorer choices lie to the bottom left.

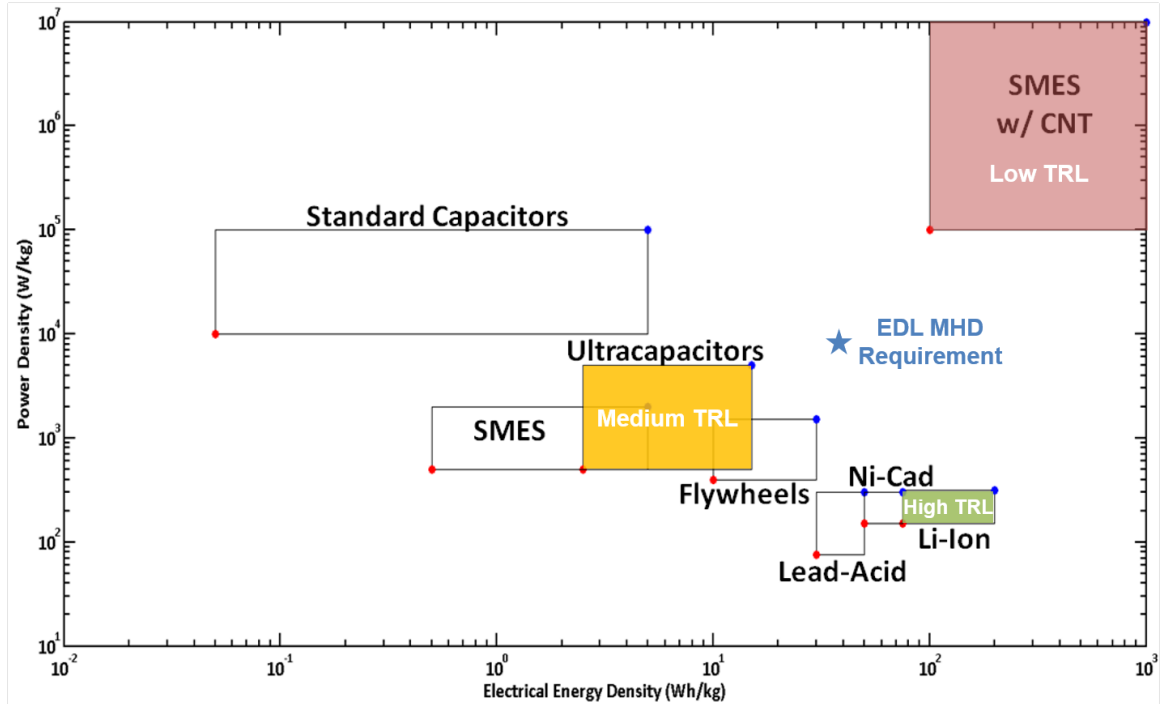


Figure 2.5: Ragone plot for electrical energy storage systems under consideration. Example MHD energy generation minimum performance requirement calculation result shown.

The plot presented as Figure 2.5 includes highlights of best and worst case scenarios, as represented by the red and blue dots, respectively. Numerically, they are summarized along with an estimate of their technology readiness level (TRL) below in Table 2.3.

Table 2.3: Electrical Energy Storage System Performance Data by Technology Type

EES System	Min $Wh/kg$	Max $Wh/kg$	Min $W/kg$	Max $W/kg$	TRL
Lead Acid	30	50	75	300	High
Nickel Cadmium	50	75	150	300	High
Lithium Ion	75	200	150	315	High
Capacitors	0.05	5	10,000	100,000	Medium
Ultracapacitors	2.5	15	500	5,000	Medium
SMES	0.5	5	500	2,000	Low
SMES w/ CNT	100	1,000	100,000	10,000,000	Low
Flywheels	10	30	400	1,500	Low

The values illustrated by Table 2.3 give all necessary information to calculate the electrical energy storage system mass for a power versus time profile for a given technology. In

addition, it may prove useful to characterize electrical energy storage system performance by TRL alone. This characterization is done by taking the best overall performer in each of the three TRL categories as representative of that category. The minimum and maximum values for the best performer within each TRL are then used to generate an average case that is used for analysis. The resulting average values for each TRL are presented as Table 2.4 .

Table 2.4: Electrical Energy Storage System Performance Data by Technology Type

EES System TRL	Avg. Specific Energy $Wh/kg$	Avg. $W/kg$
High (Lithium-Ion)	137.5	232.5
Medium(Ultracapacitors)	8.75	2,750
Low (SMES w/ CNT)	550	5,050,000

### 2.2.2 Electrical Energy Storage System Performance Modeling

A model has been created that calculates the electrical energy storage system mass for a given power generation profile and energy storage system type. It does so by integrating the power generation versus time profile curve to calculate the total energy available for storage while also noting the peak energy generation power. As shown in Figure 2.5 and Table 2.3, both power and energy requirements define energy storage system mass. Thus, there are two possibilities, power capacity driven mass, and energy generation driven mass. Both approaches must be taken, and the final stored energy is assessed relative to the initial amount of energy. From the system mass and relative energy conversion metrics, an educated assessment can be made with regards to what energy storage system mass is most advantageous for a given technology.

The minimum and maximum pairs for specific energy and power in Table 2.3 define worst and best cases, respectively. In addition, an average case for specific energy and power is generated for each technology. Thus, three distinct performance cases for each

technology are selectable within the model by the user. The end result is to generate specific values for power and energy density given selections for energy storage system type and performance scenario. The process for doing so is described in Figure 2.6.

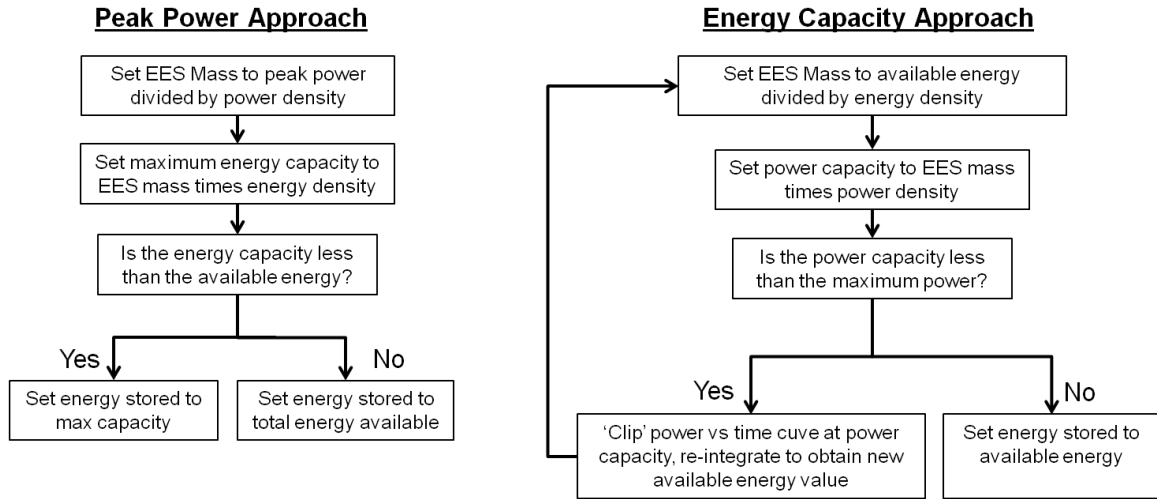


Figure 2.6: Electrical energy storage system model flowchart

As shown in Figure 2.6, there are two approaches to finding energy storage system mass. The reason for taking both approaches is to find an energy storage system mass that is capable of storing all available energy at the rate it is generated. The first approach, termed the Peak Power Approach, involves defining system power capacity as equal to the maximum energy generation rate from the given power profile. Dividing this system power capacity by the specific power capacity for the technology under consideration results in the system mass. Total stored energy is calculated by multiplying this mass by the specific energy capacity of the technology under consideration, and this value is compared with the total energy available. Depending on the technology, this approach may generate a very high or very low mass and very high or very low percent available energy stored.

The second approach, termed the Energy Capacity Approach, involves using the total available energy to drive system mass. An initial guess for the system mass is set by dividing total available energy by specific energy capacity for the technology in question. This initial guess for system mass is then used to calculate the power density of this

system. If the power capacity is above the maximum power for the power profile, no further action is taken, otherwise, the power generation profile must be clipped at the maximum power capacity rate for the system. Thus, a new power profile curve and associated total energy is generated, requiring that the initial guess for the mass be modified. This process must be completed iteratively until a converged value for energy storage mass is found. At the completion of the process, the final mass determines the amount of energy stored, and it can be compared with the original amount of energy available from the power generation profile.

At the conclusion of this process, the model outputs the system mass and converted energy using both approaches in addition to the total energy available for conversion. Different technologies may result in one or the other sizing approach being better than the other. For this analysis, the highest percent energy available retained is chosen. Finally, there is an option to limit the total energy storage system mass to some predefined value, which is also useful in assessing energy storage technological requirements. A digitized power generation profile for a 1000 kg test vehicle direct entry case from previous work is presented as Figure 2.7.[55]

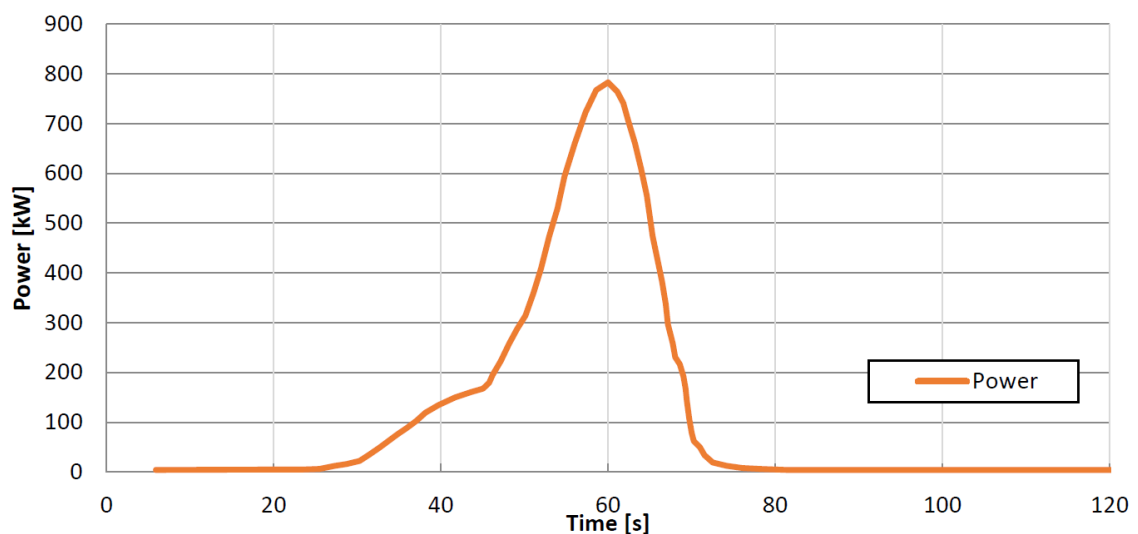


Figure 2.7: Direct entry power generation profile for Moses test vehicle

Analysis of the aforementioned power profile assuming no constraints on energy stor-

age mass, each energy storage technology’s average performance case for specific energy and power, and requiring that all available energy be stored yields the energy storage system masses presented in Table 2.5.

Table 2.5: Moses Test Vehicle Direct Entry Electrical Energy Storage System Mass

EES Technology	Mass ( <i>kg</i> )	Calculation Method
Li-Ion	3368	Peak Power
Lead Acid	4176	Peak Power
NiCad	3480	Peak Power
Capacitor	1551	Max Energy
Ultracapacitor	447.5	Max Energy
SMES	1424	Max Energy
SMES w/ CNT	7.120	Max Energy
Flywheel	824.2	Peak Power

Many of the energy storage system masses in Table 2.5 are above the original vehicle mass of 1000kg. In many cases, the mass is very high due to the limited input power capacity in comparison to the total energy stored capacity or vice versa. Since the energy storage system mass is a function of only two parameters, power density and energy density, a surface plot of the total energy stored while constraining total energy storage system mass to 10% of overall vehicle mass can be generated, given as Figure 2.8

As can be seen in Figure 2.8, the energy storage system is incapable of storing all the available energy up to a certain performance point, marked with a data cursor highlighting a required specific energy of 40.95 *Wh/kg* and specific power 8685 *W/kg*, shown as a blue star in Figure 2.5. This point is of interest because it defines the minimum performance characteristics necessary for an energy storage system to satisfy a certain mass constraint and store all of the available energy at the rate that it is generated.

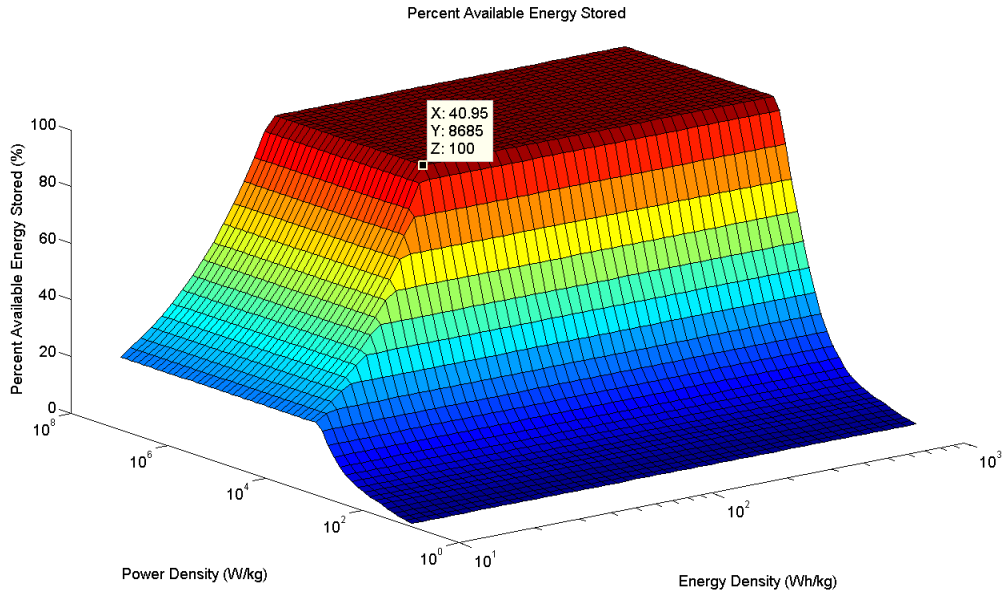


Figure 2.8: Percent available energy stored for Moses test vehicle direct entry case, mass constrained to 100 kg

### 2.2.3 Magnetohydrodynamic Energy Generation and Storage Case Studies Definition

Using the techniques and methodology discussed in this thesis, a suite of case studies was analyzed to demonstrate the systems analysis capability for conceptual design. This suite spans three possible mission classes defined in Table 2.6, five possible trajectories defined in Table 2.7, and five possible electrical energy storage system mass constraints. At each of the 75 possible sample points, the power available was calculated, and the total energy available and maximum power determined. Then, the performance of various electrical energy storage systems was assessed. Selected results from this study are presented in this section, and the parameters are summarized as Table 2.8.

### 2.2.4 Simulated Trajectories

Simulated ballistic entry trajectories for the 7 km/s Mars entry condition are shown in Figure 2.9.

As expected, the principal factor in determining the altitude velocity history for a

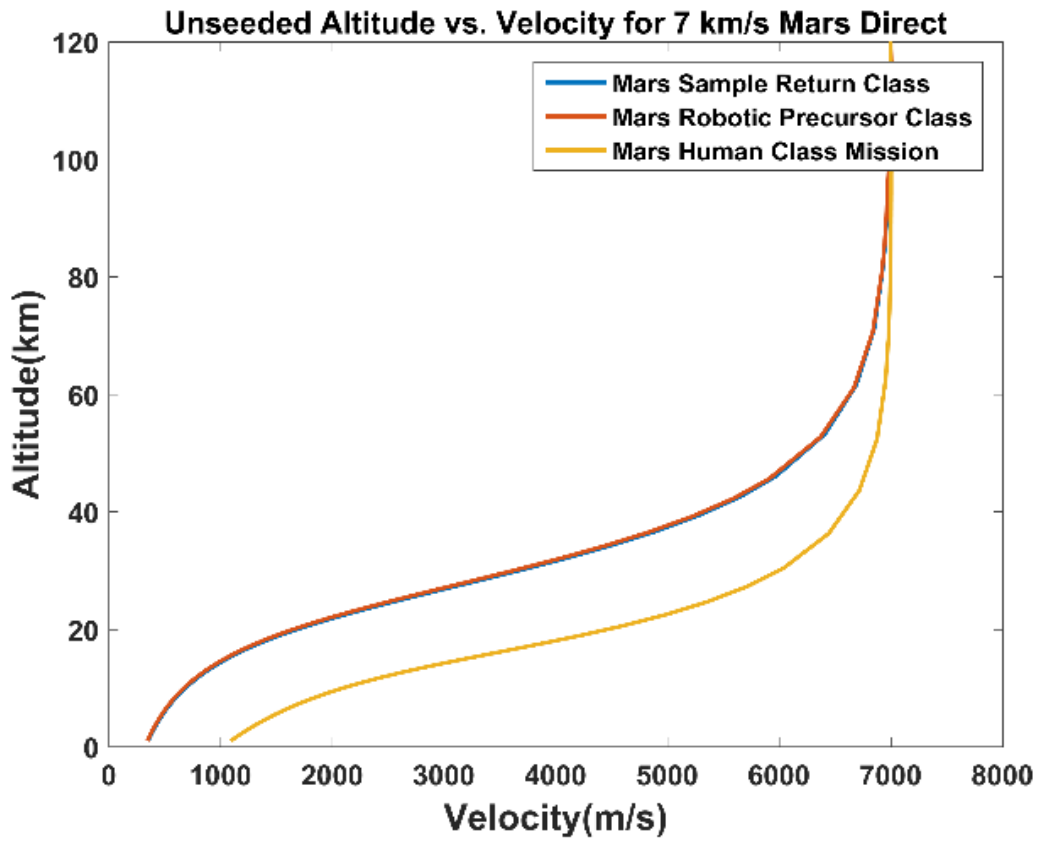


Figure 2.9: Simulated ballistic entry trajectories for Mars  $7 \text{ km/s}$  entry condition

Table 2.6: Case Study Entry Vehicle Configurations

Vehicle Name	Mass ( $MT$ )	Diameter ( $m$ )	$C_D$	Vehicle $\beta(kg/m^2)$
Mars Sample Return Class	4	5.0	1.6	127
Mars Robotic Precursor	10	7.0	1.6	162
Mars Human Mission Class	70	10.0	1.6	557

Table 2.7: Initial Conditions for Case Studies at 120 km Altitude

Trajectory	Entry Altitude (km)	Entry Velocity (km/s)	Entry FPA (degrees)
5.5 km/s Mars	120	5.5	-12.0
7 km/s Mars	120	7.0	-12.0
7.5 km/s Earth	120	7.5	-10.0
11 km/s Earth	120	11.0	-10.0
13 km/s Earth	120	13.0	-10.0

Table 2.8: Parameter Study Names and Values

Vehicle Configurations	Trajectory Types	EES Mass Constraint
Mars Sample Return Class (MSR)	5.5 km/s Mars	5% of Vehicle Mass
Mars Robotic Precursor Class (MRP)	7 km/s Mars	10% of Vehicle Mass
Mars Human Mission Class (MHMN)	8 km/s Earth	15% of Vehicle Mass
	11.5 km/s Earth	20% of Vehicle Mass
	13 km/s Earth	25% of Vehicle Mass

given entry condition is the vehicles ballistic coefficient, with the Mars Sample Return and Robotic Precursor classes overlapping. These trajectories serve as the input into the MHD energy generation model.

### 2.2.5 Power Available for MHD Energy Generation

For each simulated trajectory, the power available for MHD energy generation was calculated at each point in simulated time. The results from this analysis are shown as Figure

2.10.

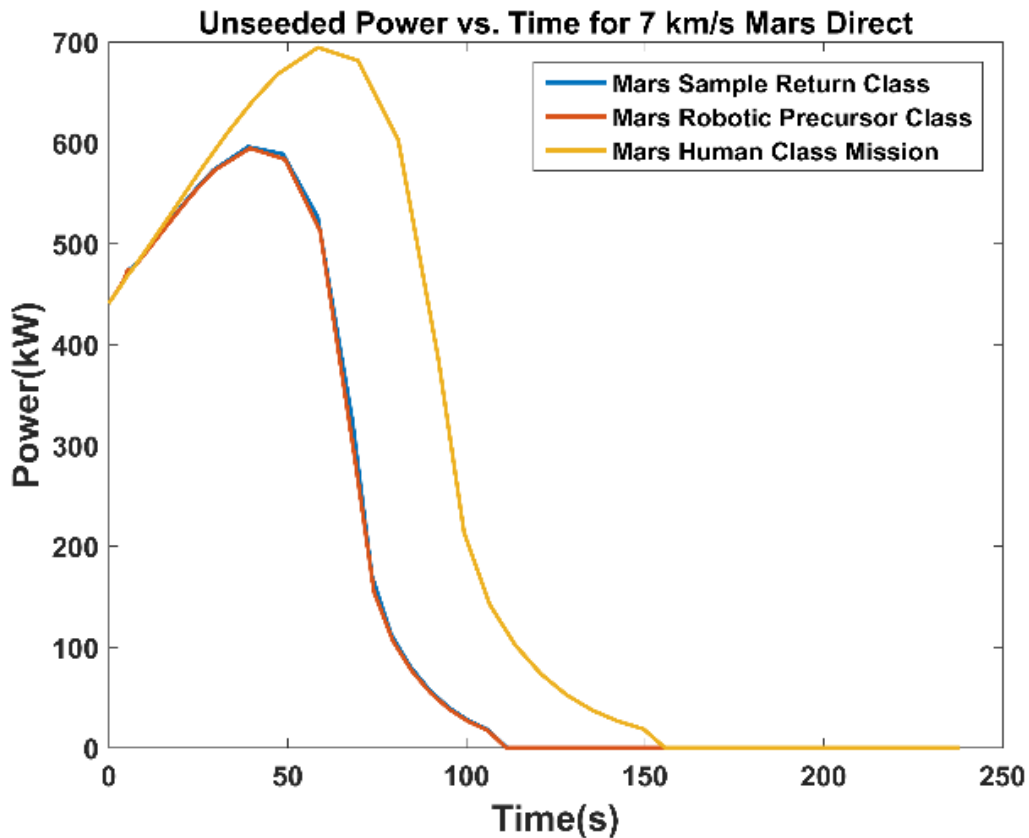


Figure 2.10: Power available for extraction via MHD energy generation for Mars 7km/s Entry Condition

Similar to the results for simulated trajectories, the amount of power that can be generated with the same MHD energy generator depends on vehicle ballistic coefficient and entry conditions. This design methodology confirms that higher ballistic coefficient vehicles produce more power for a given MHD generator than lower ballistic coefficient vehicles, and the near overlapping of the Mars Robotic Precursor and Sample Return class vehicles is consistent with ballistic coefficient as the determining factor for the power available through MHD energy generation. To obtain the total amount of energy available for each case, the curves shown in Figure 2.10, must be integrated. Tabulated values showing the results of this integration for all cases are given as Table 2.9.

The tabulated results indicate that for Mars entry, the peak power available for MHD

energy generation is lower than that for Earth entry, but that the total energy available is generally higher for equivalent entry conditions. It can thus be concluded that for a Mars entry, energy storage systems that excel in energy storage capacity will be favored, whereas for Earth entry, energy storage systems that excel in power input capacity will be favored.

#### 2.2.6 Electrical Energy Storage System Performance

For each entry condition and vehicle configuration combination, an energy storage analysis was conducted for a high, medium, and low TRL representative energy storage system, using the parameters given in Table 2.4. For each energy storage technology, the total mass of the energy storage system was constrained to a certain percentage of the original entry vehicle mass, identified in Table 2.8. Thus, the sensitivity of the percent available energy stored to the energy storage system mass could be assessed. An example of a plot produced by this analysis is given as Figure 2.11.

The output of the analysis methodology illustrated in Figure 2.11 indicates that the lower the mass of a given entry vehicle, the more sensitive the percent stored energy is to a vehicle mass-based electrical energy storage mass constraint. Higher ballistic coefficient translates into more available energy per unit area but is generally accompanied with a higher vehicle mass, making the required energy storage system a lower overall percent of the original entry vehicle mass.

Another way to examine the performance requirements for energy storage systems is to provide a fixed mass constraint, such as 5% entry mass for the energy storage system, and perform a parameter search across specific power and energy to find the minimum values required to store all available energy as in Figure 2.8. These values can be converted to the TRL of the required EES system, given as Table 2.10.

The results shown in Table 2.10 are indicative of the capability of the conceptual design methodology to determine the viability of MHD energy generation and storage for a variety of entry vehicles and trajectories. With the exception of the Mars sample return class entry

Table 2.9: Initial Conditions for Case Studies at 120 km Altitude

Vehicle Case	MSR		MRP		MHMN	
Trajectory Case	$E_{Total}$ $MJ/m^2$	$P_{Max}$ $kW/m^2$	$E_{Total}$ $MJ/m^2$	$P_{Max}$ $kW/m^2$	$E_{Total}$ $MJ/m^2$	$P_{Max}$ $kW/m^2$
5.5 km/s Mars	7.9	89.8	7.8	89.3	11.8	114.3
7 km/s Mars	39.5	596.0	39.2	594.6	60.7	694.5
8 km/s Earth	0.6	14.9	0.6	14.8	0.9	23.1
11.5 km/s Earth	13.0	406.1	12.9	404.7	18.1	516.4
13 km/s Earth	21.0	703.3	20.9	700.6	29.3	901.3

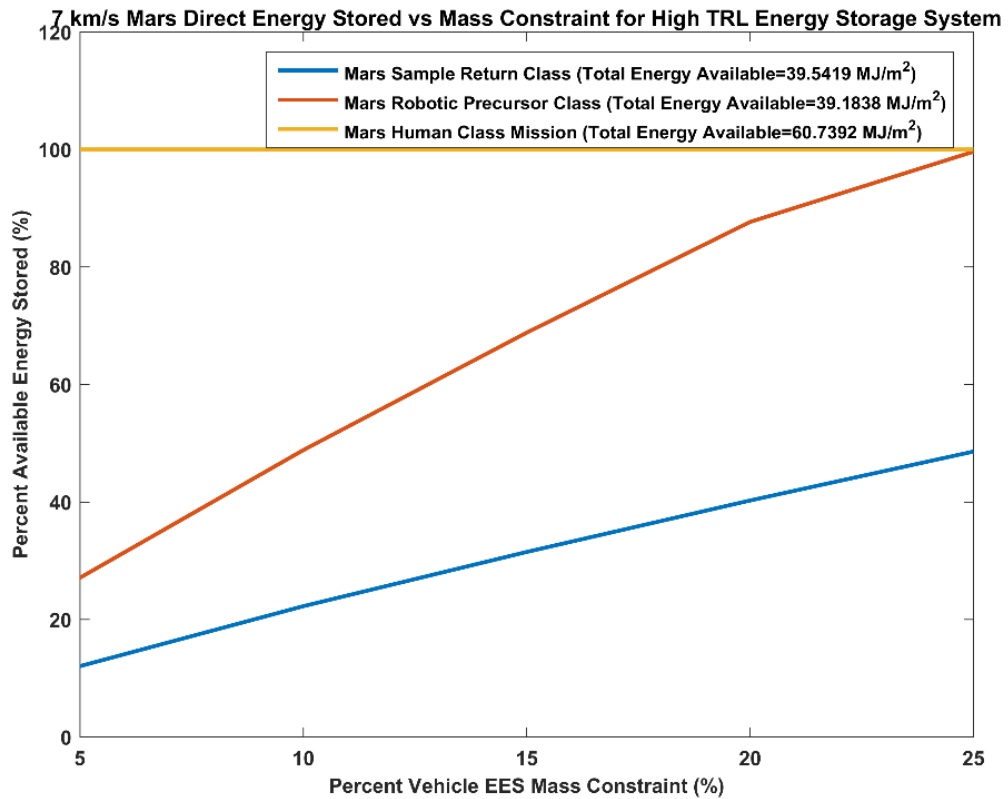


Figure 2.11: Sensitivity of percent energy stored to EES mass constraint for the 7 km/s Mars entry condition

vehicle, all cases could store the available energy with an EES system that had a medium or higher TRL. As such, MHD energy generation and storage could be a useful part of future planetary exploration missions.

The primary performance limitation identified is the specific power of the EES technologies, rather than the specific energy. As such, if not all the available energy generated can be stored, it would necessarily be dissipated as heat within the vehicle. To avoid this undesirable consequence, an approach could be to reduce the applied magnetic field value from the  $0.2 T$  assumed in these examples in order to match the energy generated with the capability of the EES system technology in use. This reduction in applied magnetic field would also likely reduce any drag generated as well, which would need to be updated in the simulation as well, highlighting the necessity and utility of the MHD and planetary entry integrated systems analysis capabilities presented in this thesis.

These results demonstrate the ability of the developed analysis methodology to perform comparisons of MHD energy generation across planetary bodies, trajectories, and entry vehicle configurations to inform trade studies for mission design.

### **2.3 Case Study for Impact of Magnetohydrodynamic Lorentz Force Drag Augmentation on Planetary Entry Systems**

Using the analysis techniques described in this thesis, a parameter study was conducted. There existed a total of four input parameters with the following levels: five potassium seed mass fractions, four vehicle configurations, one trajectory initial state, and six applied magnetic field magnitudes, summarized below as Table 2.11. The result was 120 unique parameter combinations. For each parameter combination, the resultant trajectory, deceleration profile, and electrical conductivity profile were stored and plotted. Example results from this study are presented in this section.

An example of this methodology applied to the Mars Pathfinder vehicle with entry mass of  $582 kg$ , ballistic coefficient of  $63.1 kg/m^2$ , and diameter of  $2.65 m$ , subject to modified

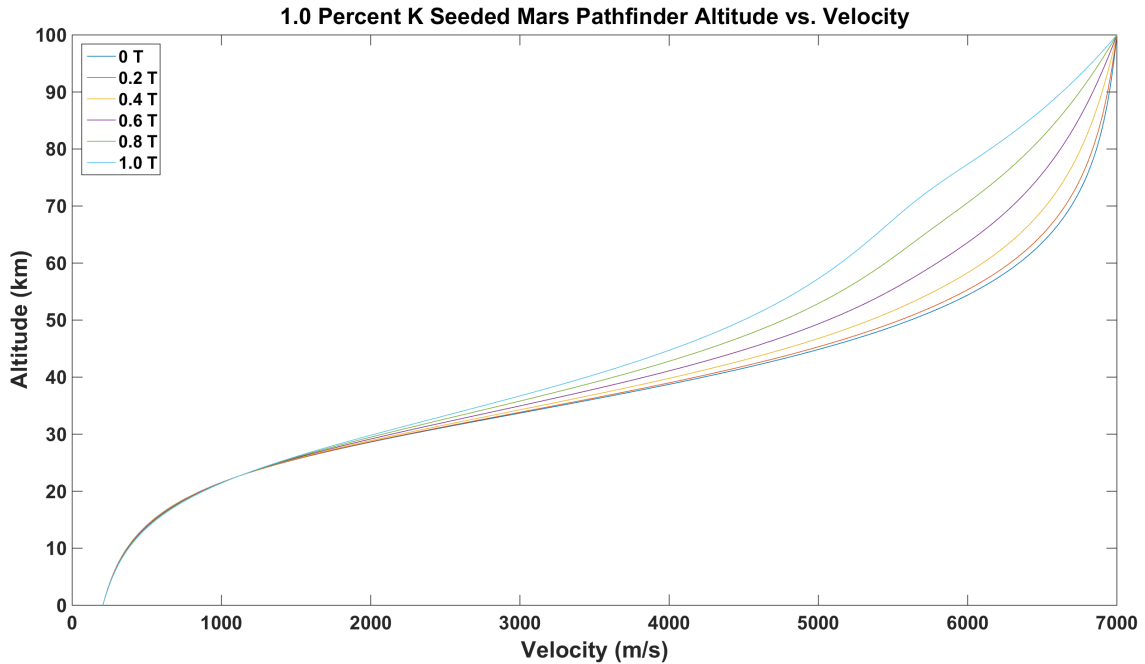


Figure 2.12: 1% K seed Mars Pathfinder altitude versus velocity curves for various B field magnitudes.

entry conditions of a flight path angle of 11 degrees and velocity of  $7 \text{ km/s}$  at an altitude of  $100 \text{ km}$  at Mars is shown in Figures 2.12 and 2.13.

The results presented in Figure 2.12 show that the trajectory is influenced by MHD flow interaction. It is also evident that the influence of MHD flow interaction on the vehicle altitude history is much more significant as the magnetic B-field strength is increased, causing the trajectory to mimic that of a vehicle with a lower ballistic coefficient. In addition, the higher imposed B-field reduced the peak deceleration and has a spreading effect on the deceleration history, causing deceleration to occur at a higher altitude than it otherwise would. This effect is most apparent in Figure 2.13, where there exist two deceleration peaks: one dominated by MHD flow interaction forces and the other dominated by aerodynamic forces. The results for the unseeded and 1% mass fraction K seed cases are presented numerically as Tables 2.12 and 2.13.

Table 2.10: TRL of EES System Required at 5% Mass Constraint for Each Case

	MSR	MRP	MHMN
Trajectory	EES TRL	EES TRL	EES TRL
5.5 km/s Mars	Medium	Medium	High
7 km/s Mars	Low	Medium	High
7.5 km/s Earth	High	High	High
11.5 km/s Earth	Medium	Medium	High
13 km/s Earth	Low	Medium	Medium

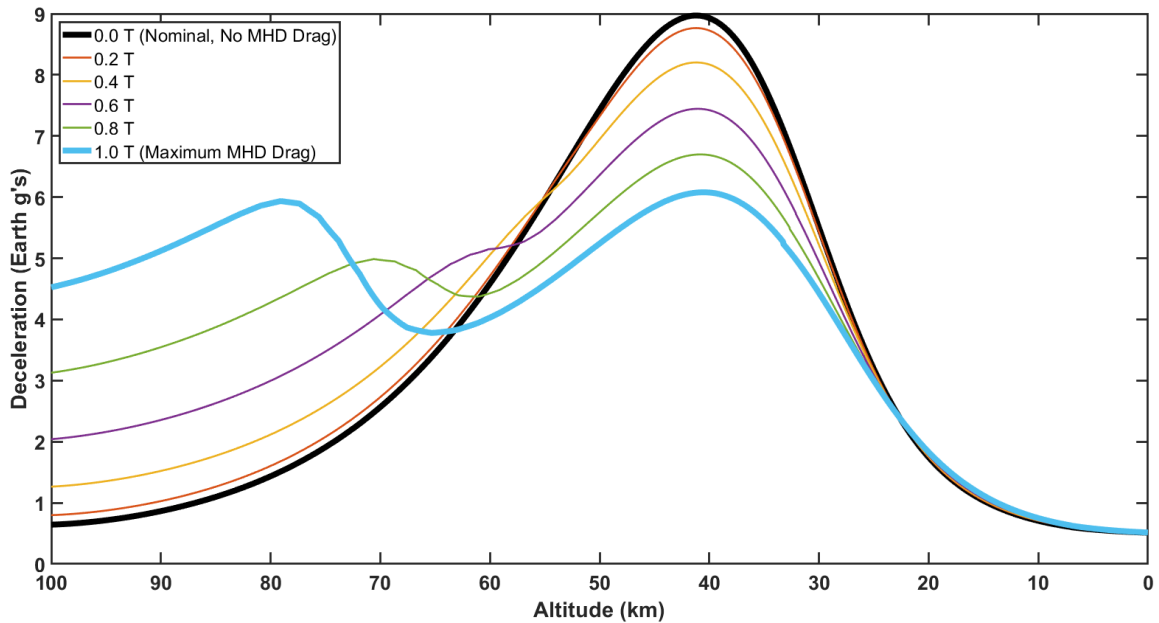


Figure 2.13: 1% K seed Mars Pathfinder total deceleration versus altitude for various B field magnitudes

Table 2.11: Lorentz Force MHD Drag Augmentation Parameter Study Names and Values

Seeding Levels	Vehicle Configurations	Trajectory Types	Applied B Field
Unseeded	Mars Pathfinder	7 km/s Direct Entry	0.0 T
0.25% K Mass Fraction	Mars Science Lab		0.2 T
0.50% K Mass Fraction	Moses Test Vehicle		0.4 T
0.75% K Mass Fraction	Mars Human Mission		0.6 T
1.00% K Mass Fraction			0.8 T
			1.0 T

Table 2.12: Unseeded Case Peak Decelerations as a Function of B-field and Vehicle Configuration

Vehicle	MPF	MSL	MOSES	MHMN
B Field	nMax (g's)	nMax (g's)	nMax (g's)	nMax (g's)
0 T	8.97	8.32	6.72	5.42
0.2 T	8.95	8.31	6.71	5.41
0.4 T	8.91	8.26	6.66	5.4
0.6 T	8.84	8.18	6.6	5.38
0.8 T	8.75	8.08	6.52	5.35
1.0 T	8.64	7.97	6.43	5.31
Ratio of 0T to 1.0T	1.04	1.04	1.05	1.02

Table 2.13: 1% K Seeded Case Peak Decelerations as a Function of B-field and Vehicle Configuration

Vehicle	MPF	MSL	MOSES	MHMN
B Field	nMax (g's)	nMax (g's)	nMax (g's)	nMax (g's)
0 T	8.97	8.32	6.72	5.42
0.2 T	8.76	8.11	6.54	5.36
0.4 T	8.2	7.54	6.07	5.2
0.6 T	7.44	6.79	5.48	4.96
0.8 T	6.7	6.09	5	4.69
1.0 T	6.08	5.55	4.65	4.45
Ratio of 0T to 1.0T	1.48	1.5	1.44	1.22

The numerical results in Tables 2.12 and 2.13 confirm the observations noted from Figure 2.13. For the unseeded case shown in Table 2.12, there is a reduction in overall peak deceleration when applying a 1 T magnetic field, but this reduction is only by a factor of 1.05. As an important note, the results presented by this model were computed assuming local thermodynamic equilibrium, and as a result, may have differing ionization values than more detailed simulations. Expected drag results for the unseeded cases computed using non-equilibrium simulations are expected to be higher, as shown in previous literature. [53].

However, in the 1% K seeded case shown in Table 2.13, this same reduction occurs at a factor of approximately 1.25 for the Mars Human Mission case, and 1.5 for the other three vehicle cases. These results demonstrate the ability of the developed analysis methodology to perform comparisons of MHD Lorentz drag forces using a non-vehicle specific framework for conceptual design applications.

**CHAPTER 3**  
**EXPERIMENTAL DESIGN FOR MAGNETOHYDRODYNAMIC ENERGY**  
**GENERATION IN CONDITIONS AND CONFIGURATIONS RELEVANT TO**  
**PLANETARY ENTRY**

As mentioned earlier, experimental data for MHD interaction relevant to planetary entry is limited. As a consequence, validation of numerical and analytical performance models for MHD and planetary entry is rendered difficult or impossible. Experimental data related to MHD energy generation for planetary entry vehicles is particularly limited.

Traditional MHD energy generator concepts consist of an open channel design through which plasma flows. For a planetary reentry vehicle, it is undesirable to have plasma flowing through the vehicle's heat-shield, due to the likelihood of damage or complete destruction of the spacecraft from the high-temperature entry plasma, as occurred in the Space Shuttle Columbia disaster in 2003.

In previous work, a non-channel type MHD energy generator concept was tested in an artificially ionized supersonic flow. [51][8] A supersonic flow was achieved through a converging-diverging nozzle, which when supplied with a vacuum pump system capable of achieving the proper pressure ratio and flow rate, produced a low-density supersonic gas flow with a freestream Mach number of approximately 2. This supersonic flow was then ionized within a cylindrical microwave resonance cavity operating around 2.4GHz. The result was a free-flowing supersonic plasma in which a representative MHD energy generator model was placed.

In this thesis, the goal of the experimental campaign is to demonstrate and characterize MHD energy generation in configurations and conditions relevant to planetary entry. To achieve the necessary environment, an artificially ionized supersonic plasma discharge is created in the laboratory, similar in part to that presented in [50][8]. Similar to the

previous experiment, a gas source is accelerated to supersonic speed using a converging-diverging nozzle and mechanical vacuum pumping system. However, unlike the previous experiment, the gas is instead artificially ionized with a radio-frequency (RF) antenna and automatic impedance matching network to create a repeatable, computer-controlled, supersonic plasma with rise times to steady state operations on the order of milliseconds. Various input gas mass flow rates and input RF antenna power levels are achieved via computer control, with error levels of less than 1%. The sections that follow present the design, implementation, and characterization of this supersonic plasma wind-tunnel.

### **3.1 Test Chamber Experimental Design**

For this experiment, the overall design goal is to create an artificially ionized, sustained low-density supersonic plasma flow. Due to its relatively simple ionization and facility safety characteristics, Argon gas is chosen as the test gas. The inlet test gas mass flow rate through the system is controlled through the use of a mass flow controller feedback loop, and flow is driven through the use of a large mechanical pumping system consisting of two pairs of rotary vane blowers and mechanical backing pumps connected to the test section exhaust. The test gas then is accelerated to supersonic speed through the use of a custom fused-quartz tube and converging-diverging nozzle. Prior to passing through the converging-diverging nozzle, the test gas is ionized with a radio-frequency (RF) antenna coil wrapped around the quartz tube and located just before the nozzle inlet.

A representative planetary entry system MHD energy generator model with embedded permanent magnets and electrodes is inserted into this ionized supersonic discharge, and the current collected through MHD energy generation is recorded. A notional schematic of the experimental design is given as Figure 3.1, and a solid model of the final experimental design is given as Figure 3.2. Finally, Figure 3.3 shows a photograph of the assembled experimental apparatus.

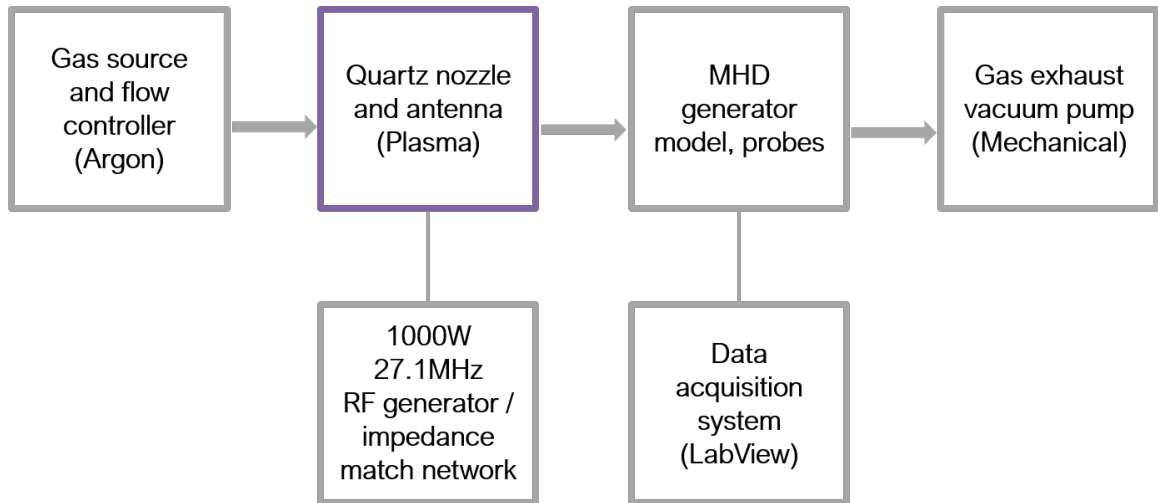


Figure 3.1: MHD energy generation for planetary entry vehicles experimental design schematic

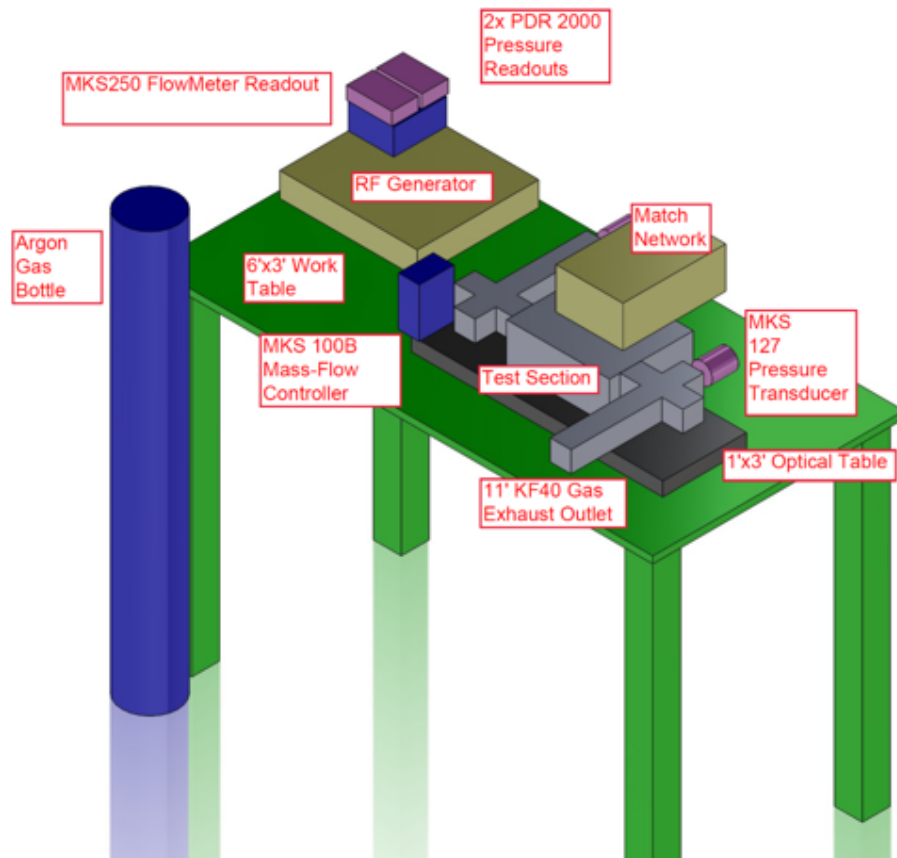


Figure 3.2: MHD energy generation for planetary entry vehicles solid model design implementation

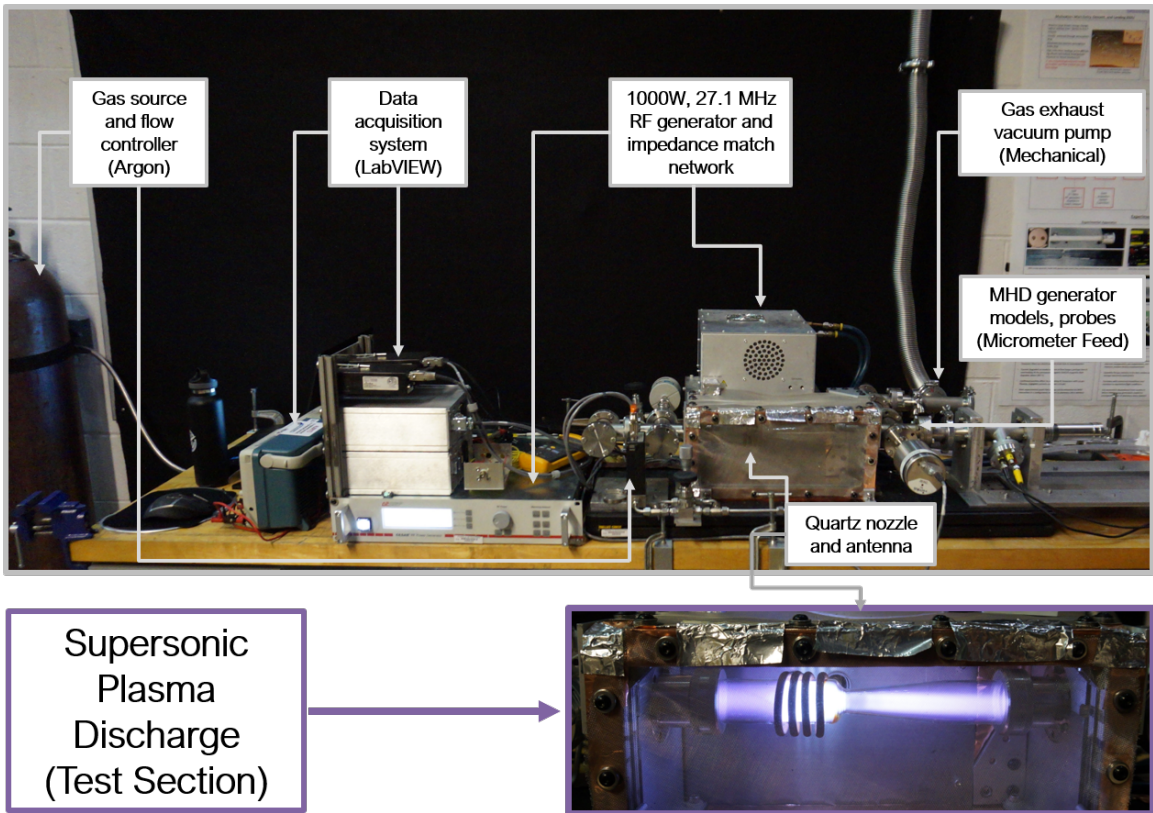


Figure 3.3: Actual final experimental assembly. Gas flow is from left to right as pictured.

### 3.1.1 Gas Exhaust System

In designing the experiment, the mechanical pumping system capacity is a key factor in determining the achievable test section size and flow rate. In the current configuration, the mechanical pumping system employed is that of the Vacuum Test Facility-1 (VTF-1) at the Georgia Institute of Technology High-Power Electric Propulsion Laboratory (HPEPL). A photograph of VTF-1 is given as figure 3.4. The VTF-1 mechanical pumping system consists of two 3800 CFM blowers and two 495 CFM rotary-vane pumps operating in a parallel configuration with a base pressure of 0.03 Torr. The two dual-stage VTF-1 mechanical pumping systems are connected to a pump manifold system located under the main chamber and are shown in Figure 3.5.



Figure 3.4: High-Power Electric Propulsion Laboratory Vacuum Test Facility-1.



Figure 3.5: HPEPL VTF-1 Twin dual-stage mechanical pumping systems.

The experimental design is a bench-top setup with a KF40 flange gas exhaust port connection and is coupled to the mechanical pumping system manifold. This coupling is achieved by a flexible 2-inch inner diameter stainless-steel vacuum hose connected to an end-point on the manifold. The VTF-1 manifold end connection terminates in an ISO-K 250 flange fitting and is adapted with a custom-made ISO-K 250 to Kwik-Flange™ ISO-KF (KF) KF40 flange adapter plate to facilitate a connection compatible with that used by the bench-top experiment exhaust port. Figure 3.6 shows the end-point of the VTF-1 manifold with the custom adapter plate.

An analysis was conducted of the estimated pumping speed including viscous conductance losses of the VTF-1 manifold experiment gas exhaust system according to a methodology given by [63]. The VTF-1 manifold is constructed of stainless-steel tubing of approximately 10.5 *in* (27.5 *cm*) inner-diameter. In conducting this nominal pumping-speed analysis, the first determination was whether the gas flow was in the continuum or molecu-



Figure 3.6: HPEPL VTF-1 pump manifold ISO-K 250 end flange with a custom adapter to KF40 flange installed.

lar flow regime. The flow regime is determined by calculating the Knudsen number,  $Kn$ , a non-dimensional ratio which compares the length scale of gas dynamic collisions to bulk-flow field length scales, defined in equation 3.1 as:

$$Kn = \frac{\lambda}{L} \quad (3.1)$$

where  $\lambda$  is the mean free path of gas dynamic collisions, that is, how far, on average, a gas molecule travels before colliding with another molecule within the gas, and  $L$  is a characteristic length scale of the flow system, for example the diameter of a pipe. For a gas to be considered in continuum, we must have  $Kn \ll 1$ . The mean free path is determined by a number of gas-dynamic parameters, including pressure, temperature, and kinetic collision-cross section area. However, practical simplifications can be made in its estimation if the gas pressure and composition are known [63]:

$$Kn = F_g \frac{0.066}{Pd} \quad (3.2)$$

where  $P$  is the gas pressure in  $mbar$ ,  $d$  is the flow system diameter in  $mm$ , and  $F_g$  is a constant for the type of gas, which has a value of 0.959 for Argon. Based on previous measurements using the experimental equipment with this type of vacuum technology, a line pressure of 100  $mTorr$  or 133.3  $mBar$ , is assumed. For the VTF-1 manifold piping diameter of approximately 275  $mm$ , the Knudsen number, calculated using equation 3.2, is  $1.7264 \times 10^{-6}$ . This puts the exhaust gas flow in the VTF-1 manifold firmly in the continuum flow regime, and subsequent pump speed calculations proceed accordingly.

Through calculations in line with methodologies presented in [63], the manifold gas flow is also determined to be laminar, with an expected turbulent to laminar transition pressure of 1.5  $Torr$ , approximately 15 times the design line pressure of 100  $mTorr$ . Using the laminar, continuum flow formulations for viscous flow conductance, and the measured distance from each mechanical pump package to the VTF-1 end flange of  $L_1 =$

267 in and  $L_2 = 511$  in respectively, an approximate overall VTF-1 mechanical volumetric pumping capacity of  $S_n = 2637$  l/S was determined within the manifold line.

It was also of interest to determine whether or not the gas flow in the line would be ‘choked’ at any point, so the critical volumetric flow rate  $S_{critical}$  for the manifold line was calculated using Argon gas properties and the manifold diameter. This critical flow rate was found as  $S_{critical,manifold} = 25,660$  l/s, which definitively indicates that the gas flow is not choked within the approximately 10.5 in diameter manifold line. However, repeating this calculation for the bench-top experiment’s KF40 exhaust port fitting, which had a diameter of 2 in or approximately 50 mm, resulted in a critical volumetric flow rate of  $S_{critical,KF40} = 848$  l/s. The choked volumetric flow rate in the KF40 experiment exhaust port is less than a third of available VTF-1 pumping capacity at the end of the pump manifold including viscous losses. Thus, it is concluded that the VTF-1 pump capacity is more than sufficient to not limit flow rate from the experiment as designed. Thus, the experiment exhaust port proceeded to be connected to the VTF-1 manifold using the custom flange at the designed location. A photograph of the assembled, secured, stainless steel experiment vacuum exhaust line connection and Varian right angle isolation valve is shown as Figure 3.7.



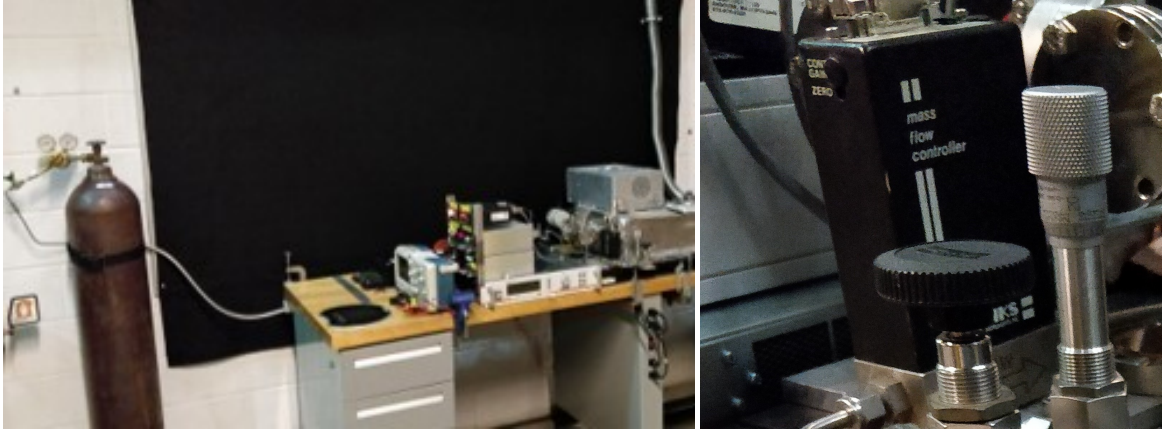
Figure 3.7: Experiment 2-inch stainless-steel vacuum gas exhaust line, with right angle isolation valve connection to VTF-1 manifold end-flange.

### 3.1.2 Gas Supply System

The experiment test gas supply was via Argon gas cylinders. For flow system diagnostics and experimental preliminary design testing, industrial purity (99.95% argon) gas was used. For experimental data acquisition, ultra-high purity (UHP, 99.999% argon) gas was employed. Gas cylinders were securely strapped to a wall cylinder support secured to the cinder-block wall using TapCon 5/16-inch concrete anchors. Gas cylinder output pressure is controlled using a Harris model 9296 dual-stage regulator set to 30 psi adapted to 1/4-in Swagelok compatible stainless steel tubing.

The experiment gas supply line is a 1/4-in inner diameter flexible stainless steel-jacketed industrially cleaned gas supply line, which connects to 1/4-in stainless steel tubing at the bench-top experiment gas inlet. The gas line is securely supported under the bench-top experiment with multiple strain-relief mechanisms to reduce the potential for mechanical failure and leaks. The gas supply system was stress-tested overnight at double the design pressure for the experiment, and found to have minimal leaks and no failure. Figure 3.8a shows a photograph of the experiment setup including gas bottle, regulator, and output gas supply line.

The experiment test gas inlet is 1/4 in Swagelok compatible tubing, coupled to the gas supply line with a small valve manifold consisting of a 1/4 in Swagelok ball valve, and micrometer needle valve. Experiment test-gas mass-flow control is provided by a MKS model 1162B mass flow controller (MFC) with integrated mass flow meter (MFM), the inlet of which is connected to the test gas inlet valve manifold. Figure 3.8b shows a photograph of experiment test gas inlet valve manifold and MFC connection. The input pressure to the MFC is the gas supply line output pressure of 30 psi as set by the regulator, and the gain of the controller is set such that gas flow is efficiently set to any set-point within the design range. For the MFC, the full-scale mass flow rate is set as 10,000 *sccm N<sub>2</sub>*, or approximately, 15,000 *sccm Ar*, corresponding to a full-scale voltage value of 5 *V*. When sent a set-point signal between 0 and 5 *V*, the MFC rapidly adjusts (within 1 - 2 *s*) to the



(a) MHD energy generation experiment test gas supply system. (b) MHD energy generation experiment test gas inlet valve manifold and MFC.

mass-flow rate to that corresponding to the set-point signal.

In addition, a true volumetric mass-flow rate calibration was performed for the MKS 1162B mass flow meter and mass-flow control system. The calibration was performed using a CalTrak 500, 0-500 *scm* true volumetric flow rate calibration system, with precise displacement measurements made from a moving piston in a cylinder with photo-gate technology. After being connected to a MKS type 250 mass flow controller for MFM/MFC power supply and readout voltage indication, the MFM was calibrated in an 'open' valve position for the MFC against various volumetric flow rates. The volumetric flow rate for Argon gas was also automatically corrected for measured differences in pressure and temperature from standard conditions (0 degrees Celsius and 1 atmosphere). The result of the calibration was that the MFM was found to be very linear and in good working order over a portion of the full-scale value, and extrapolation is used to determine mass-flow rates outside of the calibration range of 0-500 *scm*Ar. The same MKS Type 250 readout and power supply system was used in all the following experiments, and measurements of mass-flow rate are only taken after an at least 2-hour warm-up period to facilitate consistency between testing periods. The results of this calibration and corresponding linear fit are shown as Figure 3.9.

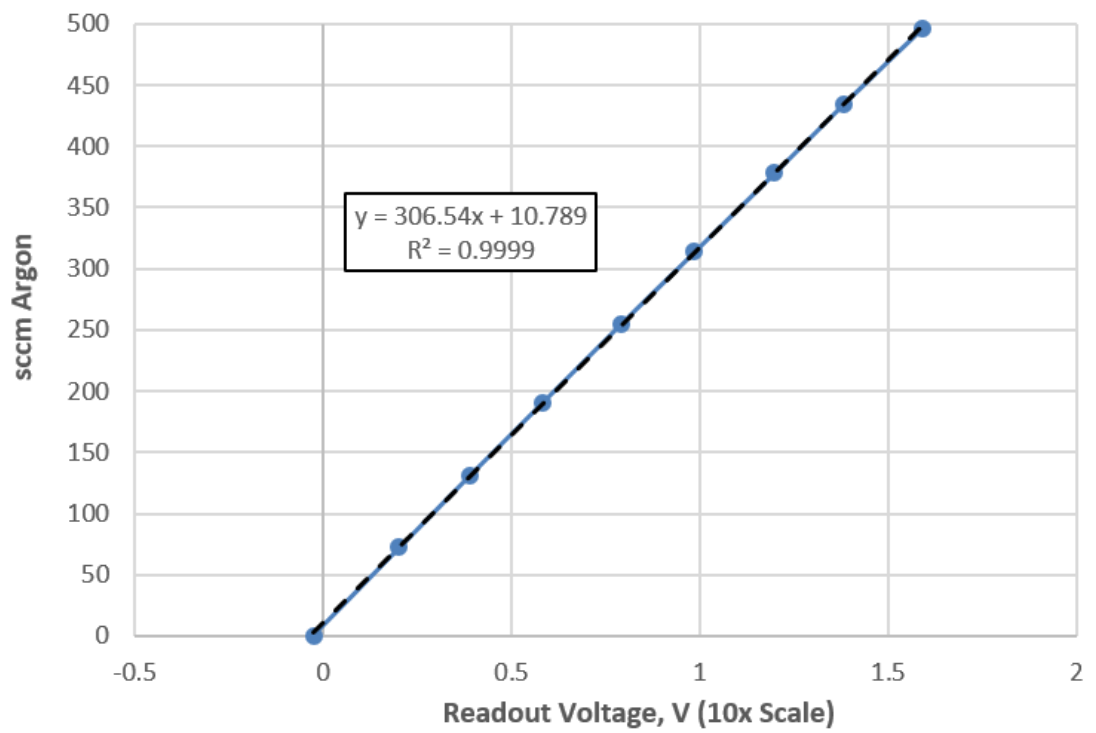


Figure 3.9: Experiment MKS 1162B MFM/MFC calibration. Calibration date is August 2016. Calibration range is 0 - 500 *sccm Ar*

### 3.1.3 Quartz Nozzle Design

In choosing a material for the converging-diverging nozzle necessary to achieve supersonic flow conditions, several considerations were important. Because of the radio-frequency (RF) ionization technique employed, it was necessary the tube carrying the gas be a strong dielectric, to avoid the RF current coupling to the tube itself and not the gas, thereby inhibiting signal transference. In addition, expected plasma temperatures on the order of thousands of degrees Kelvin necessitated high-temperature tolerant materials as well. These constraints limited material choices to heat-resistant, strong dielectrics such as machinable ceramics or quartz glass.

Previous experimental work [51][8], employed a machinable alumina ceramic nozzle, embedded within a quartz-glass tube with o-rings such that a visible test section could be created. This approach necessitated precise machining of ceramics, generally a brittle class of materials. In turn, this machining process required special, unfired ceramics that were not as robust to the extreme temperature and flow conditions present within the nozzle. Moreover, the use of ceramics blocked optical access into the nozzle itself and created an undesirable seam between the nozzle and test-section quartz tube.

For this experiment, the approach is to instead combine the quartz tube and nozzle concept, to create a singular quartz tube with embedded converging-diverging nozzle. This design decision gives consistent optical access throughout the entire assembly, enabling full flexibility in model placement at any point within the nozzle assembly to achieve desired flow conditions. In addition to this flexibility advantage, fused quartz tubes of the required structural integrity can be made with thinner wall thicknesses than machinable ceramics, which enables the RF antenna coil to be placed much closer to the test gas for ionization. Finally, using a singular fused quartz tube enables a seamless design between the quartz gas tube delivery fittings and converging-diverging nozzle, eliminating a potential source of flow quality degradation.

The converging-diverging nozzle was designed according to isentropic flow equations

using argon as the working gas. Design constraints included facility pumping speed, outer diameter specifications for the quartz tube compatible vacuum fittings, minimum safe exit pressure for the facility mechanical pumps, and the desired exit Mach number. The overall length of the quartz-tube nozzle assembly is fixed at 12 *in* to ensure compatibility with the existing optical table, quartz-tube vacuum fittings, and structural support system to limit torsion and shear loads on the glass. The overall length of the converging-diverging section was determined as 4 *in* to maximize nozzle expansion length while allowing sufficient room for a test-section aft of the nozzle throat. At both the entrance and exit to the nozzle, 4 *in* of straight quartz tubing is added to facilitate the placement of the RF antenna coil around either the nozzle exit or entrance tubing.

In order to calculate the desired nozzle throat diameter, an assumption was made for the quartz tube thickness such that the 1.5 *in* required outer-diameter for the quartz-tube vacuum fitting could be converted into the tube inner-diameter. Based on this fixed nozzle exit diameter and area,  $A$ , and desired exit Mach number,  $M$ , the area-Mach relation from compressible flow theory[64], equation 3.3, was used to calculate the nozzle throat diameter based on throat area,  $A^*$ .

$$\frac{A}{A^*} = \left(\frac{\gamma + 1}{2}\right)^{-\frac{\gamma+1}{2(\gamma+1)}} \frac{\left(1 + \frac{\gamma-1}{2}M^2\right)^{\frac{\gamma+1}{2(\gamma-1)}}}{M} \quad (3.3)$$

Once the required throat area,  $A^*$  was calculated, the next step in the process was to determine the choked mass-flow rate,  $\dot{m}_*$  given as equation 3.4.

$$\dot{m}_* = \frac{A^*P_t}{\sqrt{T_t}} \sqrt{\frac{\gamma}{R}} \left(\frac{\gamma + 1}{2}\right)^{-\frac{\gamma+1}{2(\gamma-1)}} \quad (3.4)$$

Based on an assumed minimum downstream pressure of 100 *mTorr* and a fixed upstream to downstream pressure ratio of 100:1 based on requirements for shock-free expansion, the upstream total pressure  $P_t$ , is estimated as approximately 1 *Torr*. This value was later updated to 5.6 *Torr* based on actual pumping system capability. Assuming the test

gas entered the nozzle at room temperature, with an approximate total temperature  $T_t$  of 300 K, an initial estimate of the required choked mass flow rate could be made, according to equation 3.4. This required mass-flow rate was converted to gas flow in *sccm Ar*, and compared with pump-speed specifications to determine at a preliminary level whether the gas-exhaust system could accommodate required flow rate. Through iterations in this manner, a feasible nozzle design was determined. This nozzle design and sizing process is summarized in Figure 3.10.

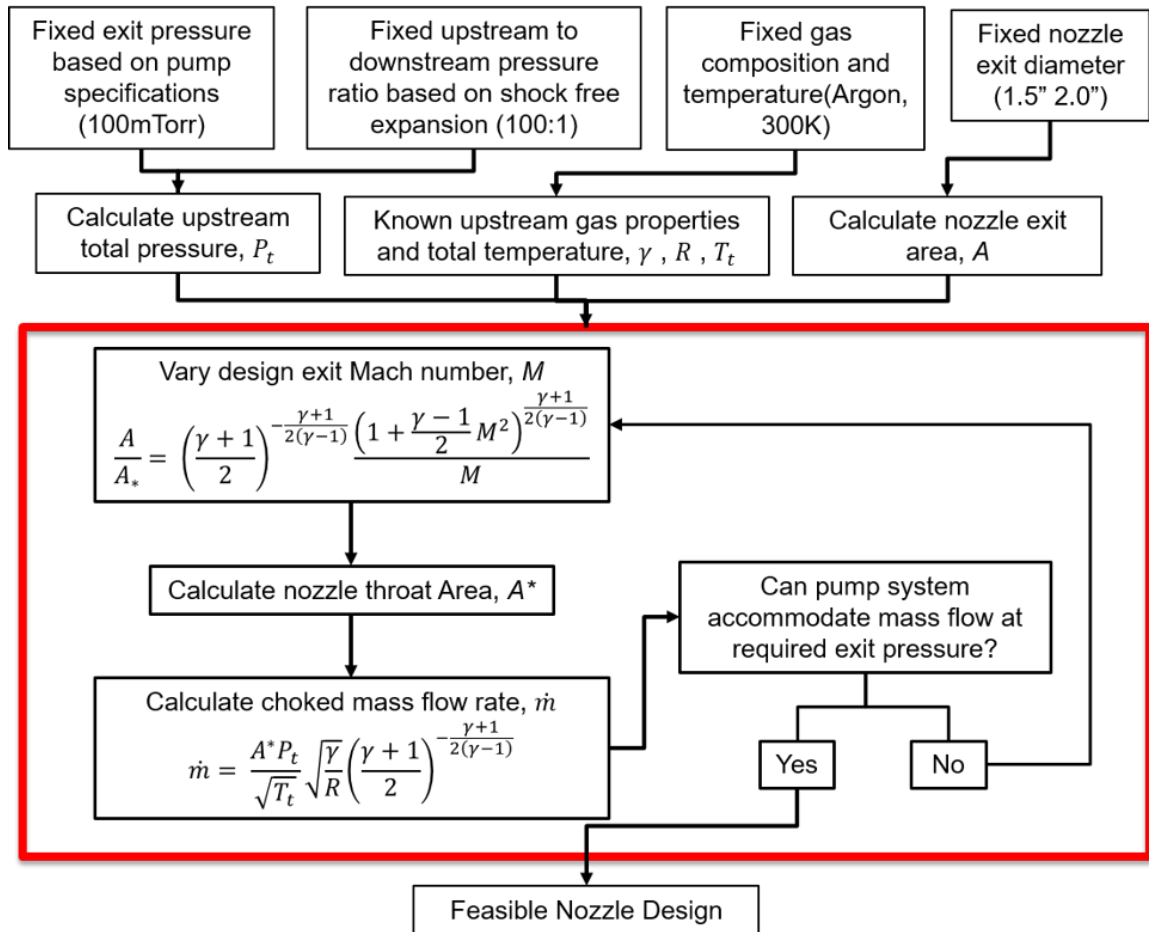


Figure 3.10: Experiment quartz converging-diverging nozzle sizing process

The results of this design iteration for exit Mach numbers between 2 and 5 are given as Figure 3.11. Additional calculations were performed to assess the influence of RF power addition aft of the nozzle throat on exit Mach number using quasi-one-dimensional flow with heat addition theory. Based on the overall Mach number reducing effect of the RF

antenna heating downstream of the throat, the design RF antenna placement was set to be upstream of the nozzle throat, where it served to increase the upstream total temperature and pressure, and by extension, the downstream Mach number should the actual gas exhaust system fail to provide a low enough nozzle back-pressure for shock-free expansion.

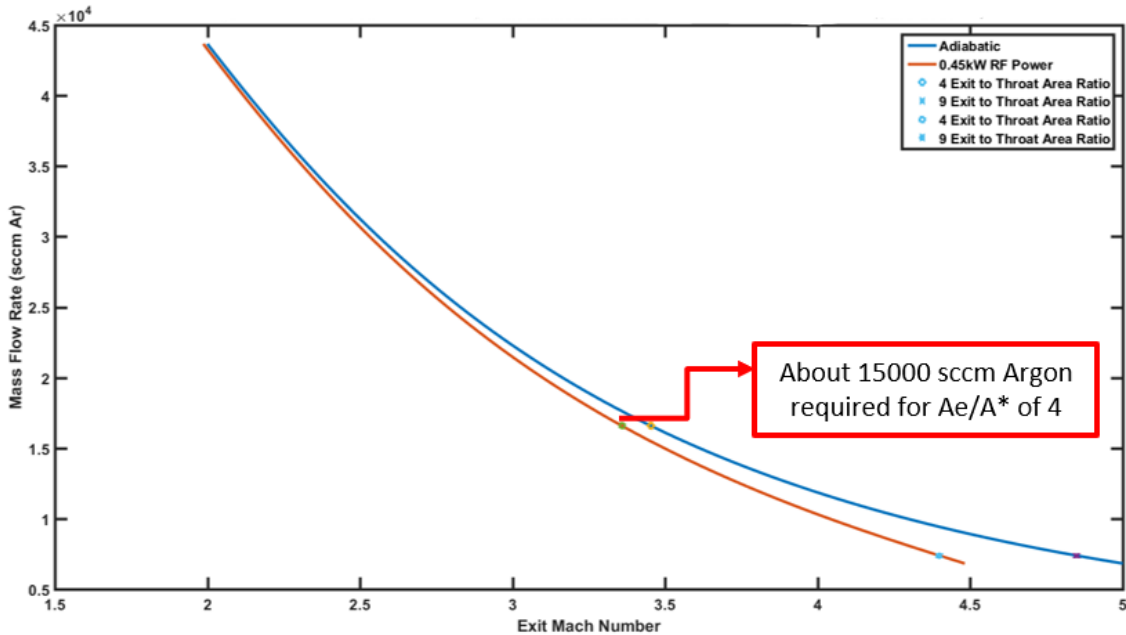


Figure 3.11: Required mass flow rate in *sccm Ar* vs. exit Mach number,  $M$ , for 34.1 mm exit diameter and 5.6 Torr upstream  $P_t$  at  $T_t = 300 K$

The design logic employed was that supersonic flow within the nozzle should be achieved at first without requiring RF power deposition upstream of the nozzle, such that the flow would be guaranteed to be supersonic when RF power is added. Thus, based on the approximately 15,000 *sccm Ar* regulation capability of the mass-flow controller available for this experiment, a nozzle exit area to throat area ratio  $\frac{A_e}{A^*}$  of 4.0 was chosen, corresponding to a design exit Mach number of approximately 3.5 and highlighted in Figure 3.11. The final design specification for nozzle throat diameter was thus 0.67 in, and the overall quartz tube-nozzle assembly design schematic chosen is given as Figure 3.12.

The nozzle designs shown in Figure 3.12 were manufactured from fused quartz via a custom precision scientific glassblowing manufacturer with tolerances of  $\pm 0.005$  in on



process, and prioritizing correct dimensions for the outer-diameter for a proper seal.

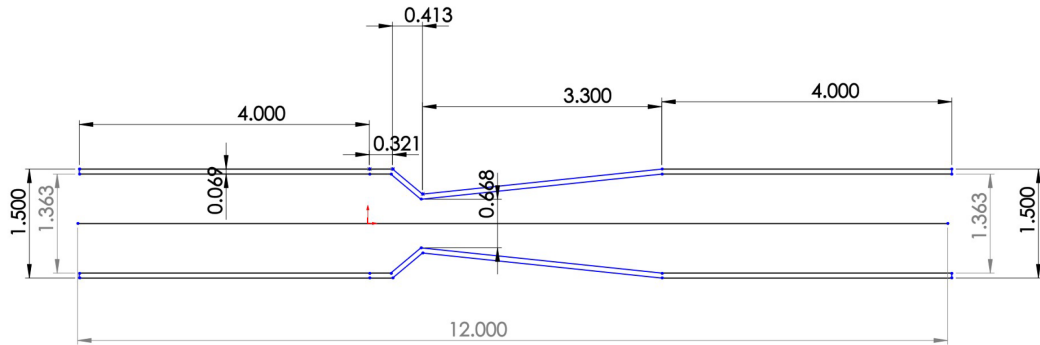


Figure 3.14: Schematic of final delivered quartz nozzle, updated with actual dimensions.

The final, delivered nozzle had an exit to throat area ratio of  $\frac{A_e}{A_*} = 4.16$ . This ratio corresponded to a calculated maximum exit Mach number of  $M = 3.5121$  in accordance with equation 3.3. This design choice facilitated low-density continuous supersonic gas flow while allowing for RF antenna coupling to the test gas, thereby creating a low-density supersonic flowing plasma in the nozzle expansion length and quartz-tube test section.

### 3.1.4 Radio-Frequency (RF) Ionization System

For the experimental design presented in this thesis, the energy source for ionization is a 27.1 MHz radio-frequency (RF) generator connected to a 4-turn copper coil and variable capacitance automated impedance matching network. The plasma created is termed a radio-frequency (RF) plasma, and power deposition levels of up to 1000 W as measured by the RF power meter on the generator are possible with the implemented equipment. The 4-turn copper coil is constructed from 1/4-inch copper tubing and is water cooled to protect from the extreme temperatures present in the discharge. The antenna is placed just before the nozzle inlet to aid in energy deposition for supersonic expansion. To shield the experimental equipment and operators from RF radiation and interference, a Faraday cage is placed around the coil, test-section, and impedance matching network. A photograph of

the implemented RF power delivery system and antenna are given as Figures 3.15 and 3.16.

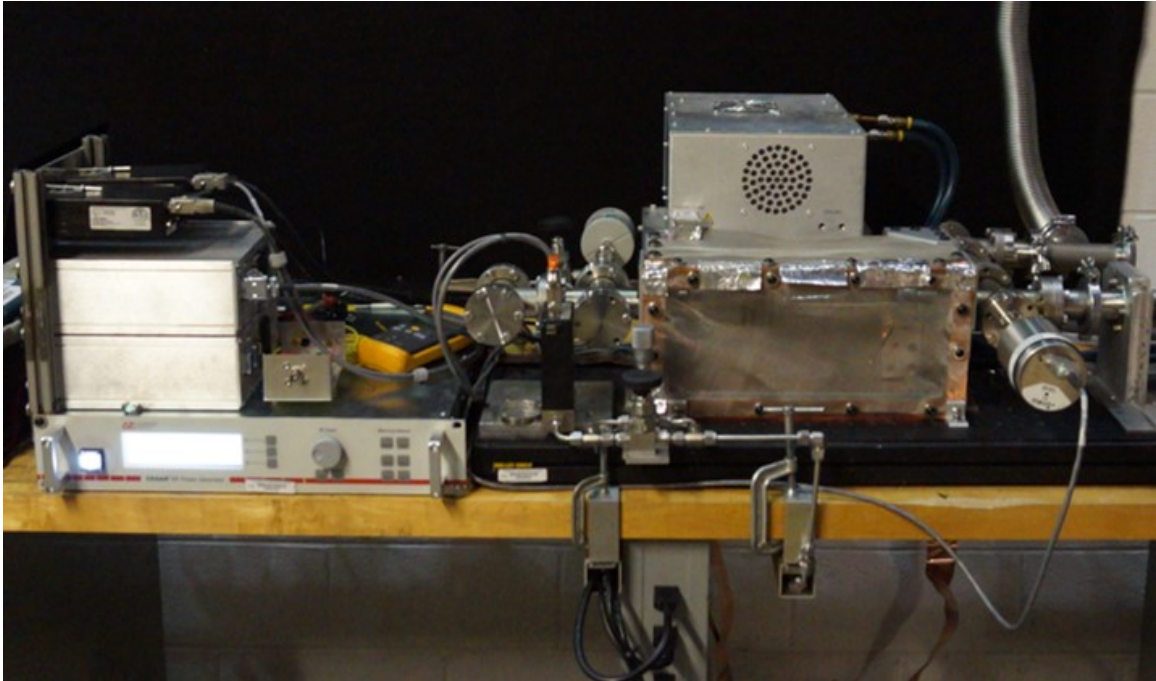


Figure 3.15: RF generator (left) and variable capacitance impedance matching network (right).

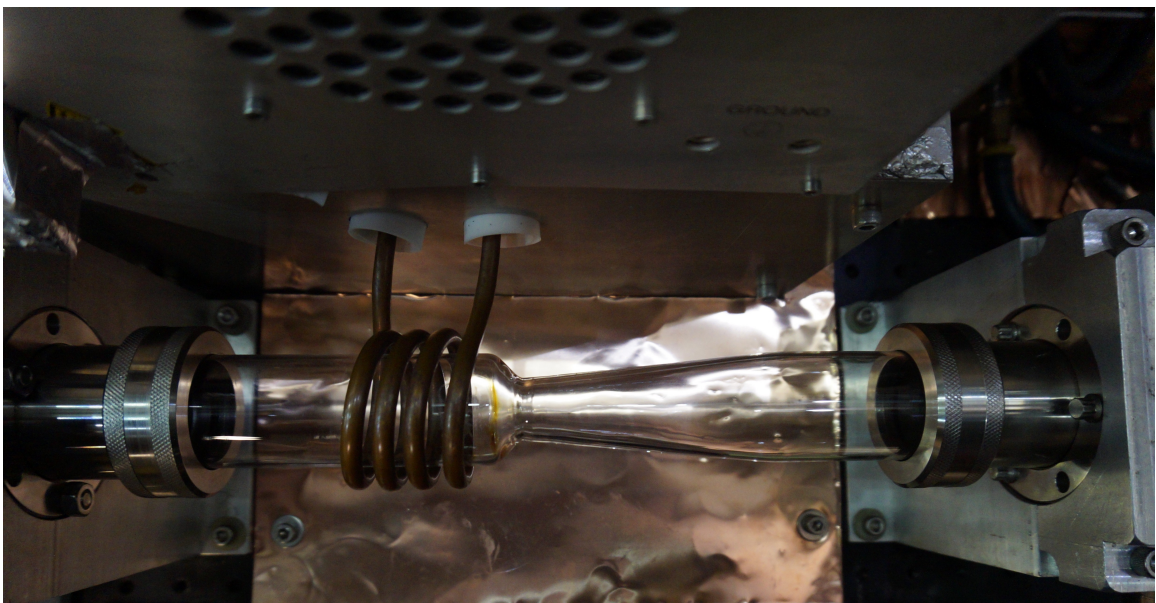


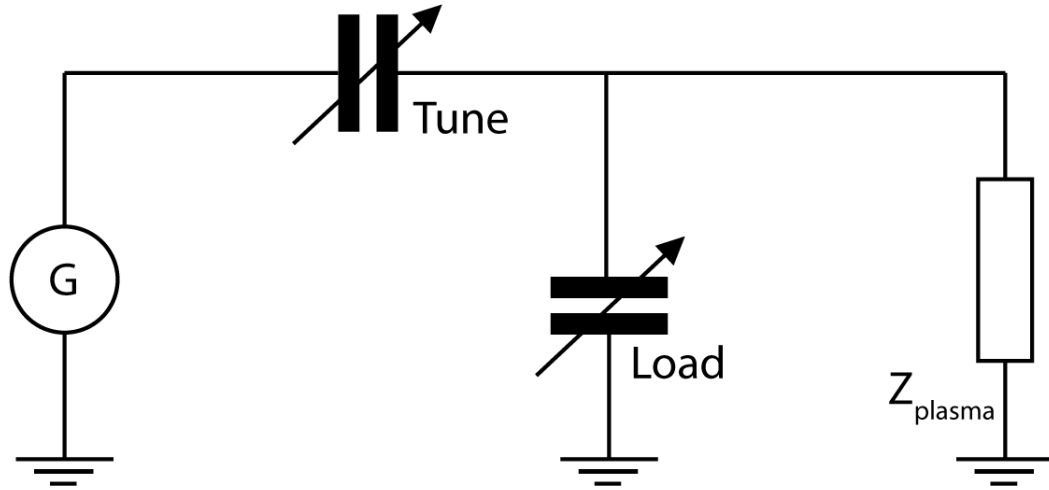
Figure 3.16: Top view of 4-turn coil constructed of 1/4-inch water-cooled copper tubing. Antenna placement is upstream of nozzle throat. Gas flow from left to right as pictured

The RF generator is a computer-controlled Advanced Energy CAESAR model 6140020

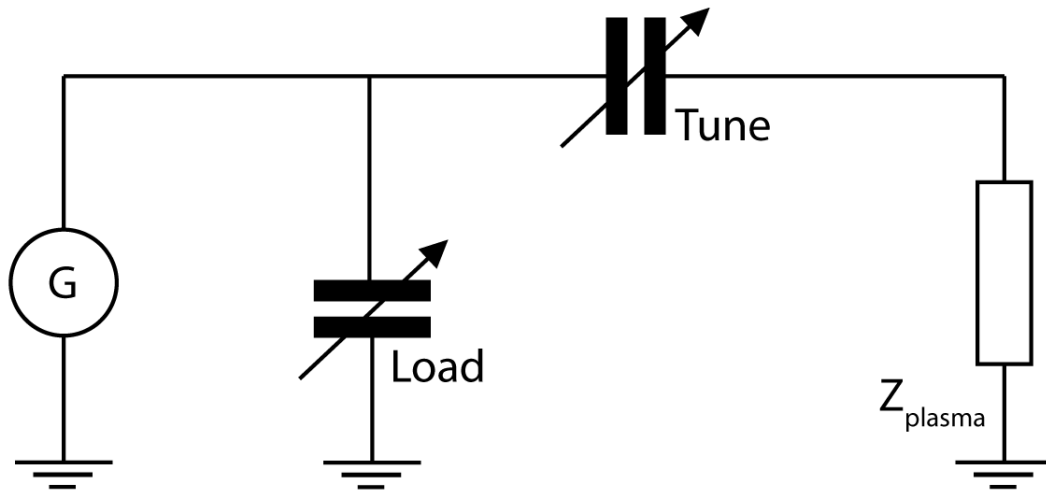
27.1 MHz RF generator, with a maximum forward RF power,  $P_F$ , of 1000 W delivered to the impedance matching network via a 50- $\Omega$  coaxial output. The automated impedance match network, an Advanced Energy model VM2715AW L-Match topology network, achieves efficient RF power delivery to the plasma load by attempting to match the overall plasma load-match network impedance to the 50- $\Omega$  output source impedance from the RF generator. This impedance match is made necessary by RF power transmission physics, as when the source and load impedances at the transmission frequency are mismatched, either all or some of the RF power output is reflected back to the source and not deposited into the load as desired.

In order to achieve this impedance match, the matching network implemented uses a system of two variable high-voltage capacitors driven by computer-controlled stepper motors, which in turn are controlled via an optimization algorithm that aims to minimize the reflected power,  $P_R$ , at the load while maximizing the portion of the forward generator power output,  $P_F$  absorbed by the load. The match network implemented places two variable capacitances between the generator and load, referred to as the ‘tune’ and ‘load’ capacitances respectively. The matching network as implemented uses an ‘L-Match’ topology, which determines the order of the two capacitors from the generator’s point of view. One of these capacitors, the ‘tune’ capacitance, is connected in series with the generator output and load, and the other capacitance, the ‘load’ capacitance is connected between the generator output and ground (shunt connection). For the ‘L-match’ topology, the tune (series) capacitance comes after the load (shunt) capacitance, forming an ‘L-like’ shape. The alternate ordering is termed a ‘Gamma’ topology, where the capacitance ordering has a ‘ $\Gamma$ -like’ shape. These two topologies are shown below as Figure 3.17.

The ‘L-Match’ topology is chosen due to the wide range of load impedances it can tune to, important in this case as the plasma load impedance is not known *a priori*. In practice, the ‘L-Match’ topology implemented is modified by the inclusion of a water-cooled ‘tune’ coil inductance connected in series with the load and tune capacitor. This



**A: Gamma topology**



**B: L match topology**

Figure 3.17: 'Gamma' and 'L' RF matching network topologies

6-turn coil is tapped at each turn to provide variable load inductance and thus transform the ‘effective’ tuning capacitance range. This water-cooled tune coil is responsible for absorbing up to 200  $W$  of reflected RF power safely without overheating, and forward RF generator power is automatically limited via a custom computer interface cable to ensure that this limit is met. The load capacitance appears first from the generator’s point of view, and has a range of 5-500  $pF$  and is rated for 4.2  $kV$ , while the tune capacitance has a range of 5-250  $pF$  and is rated for 9.0  $kV$ . The tune coil is electrically connected in-between the plasma load and tune capacitance via a high conductance copper strap. The tap point on the tuning coil set for maximum inductance, and was selected such that the tune capacitance for proper impedance match is between 20% and 80% of the capacitance range according to manufacturer specifications for avoiding RF stress. A photograph of the L-match impedance match network as implemented is given as Figure 3.18.

The physical connection between the tuning coil and RF antenna is considered part of the coil inductance, and for this reason, the connection between the matching network and RF antenna was made as short and low-impedance as possible. Due to the high frequency nature of RF currents, the ‘skin-effect’ conductance property of AC applies, wherein the vast majority of the current travels within a short distance from the surface of the conductor, termed the skin-depth,  $\delta$ , favoring larger surface area, low-inductance conductors for minimal impedance. This ‘skin-depth,’ for frequencies far below the conductor material’s plasma frequency is given by equation 3.5

$$\delta = \sqrt{\frac{2\rho}{\omega\mu}} \quad (3.5)$$

where  $\rho$  is the electrical resistivity of the conductor ( $1.68 \times 10^{-8} \Omega m$  for copper),  $\omega = 2\pi f$  is the angular frequency of the AC, and  $\mu = \mu_r \mu_0$ , where  $\mu_r$  is the relative permeability of the material (0.99991, or nearly 1 for copper) and  $\mu_0$  is the permeability of free-space. For an RF frequency of  $f = 27.1 \text{ MHz}$  and copper strap conductor, the calculated skin-depth,  $\delta$ , is approximately 12.5  $\mu m$ , effectively making the surface area of the conductor the



Figure 3.18: Advanced Energy model VM2715AW impedance matching network configuration with water-cooled 6-turn tune-coil connected for 6 active coils in L-match topology.

only relevant factor. As a result, RF connections to the load and ground are made through thin (0.002 in), wide (2.0 in) copper strap connectors of low-inductance and relatively high surface area for low RF impedance. A photograph of the Teflon-Kapton insulated custom copper-strap connection between the impedance match network tune coil output and RF antenna within its grounded aluminum enclosure is given as Figure 3.19.



Figure 3.19: Thin copper strap connection between the matching network output and water-cooled copper RF antenna coil.

Low-impedance RF grounding is achieved through the matching network body, RF generator, antenna enclosure, vacuum flanges, and Faraday cage through a 2-inch wide 0.002 in thick copper strap connected to each element and joined to a real-earth ground behind the bench-top experiment table.

Although RF radiation is considered non-ionizing, at the high power levels employed in this experimental design, there is still a risk of high-voltage arcs and burns to the sur-

rounding lab environment and equipment operators. To mitigate this risk, a Faraday cage designed to block RF radiation was constructed and placed around the RF antenna and plasma load. The Faraday cage implemented is constructed of a stainless-steel mesh bolted to an aluminum frame wrapped in grounded copper-foil to facilitate a continuous electrically conductive enclosure around the RF antenna and plasma test section while maintaining optical access. A common rule-of-thumb for Faraday cage design is that reasonable signal attenuation is achieved with mesh-gap sizes no greater than  $1/10$  the wavelength of the frequency corresponding to the signal shielding is intended from. For  $f = 27.1 \text{ Mhz}$ , the corresponding wavelength,  $\lambda = 11.035 \text{ m}$ , or approximately  $434 \text{ in}$ . The maximum gap size of the Faraday cage constructed is on the order of approximately  $0.1 \text{ in}$ , far below  $\lambda/10$ , and serves as an effective barrier between the RF radiation and external lab environment and experiment operators. The implemented design has been RF safety tested, and was found to have minimal signal leakage. A photograph of the implemented Faraday cage is given as Figure 3.20.

One of the key distinguishing factors of the computer-controlled RF generator and variable automated impedance matching network is precise, efficient, and rapid delivery of RF energy to the plasma load, achieving ignition and full-impedance match with minimal reflected power on the order of milliseconds across a variety of plasma densities. This property of the experimental design enables repeatable pulsing of the RF plasma with relatively short overall pulse widths on the order of less than  $1 \text{ s}$ , which significantly reduce the heating of models within the test section due to the high-temperature plasma. This capability is in contrast to a manually operated impedance match network, in which a human operator must turn variable capacitors to experimentally find the point for successful plasma ignition, then rapidly turn the dials to bring the reflected power to acceptable levels to prevent generator overheating. Furthermore, computer-control of the impedance match enables forward power outputs of up to  $P_F = 1000 \text{ W}$  with reflected power levels of  $P_R < 10 \text{ W}$ , at almost any possible test-section flow condition, essential to conducting the experiment in

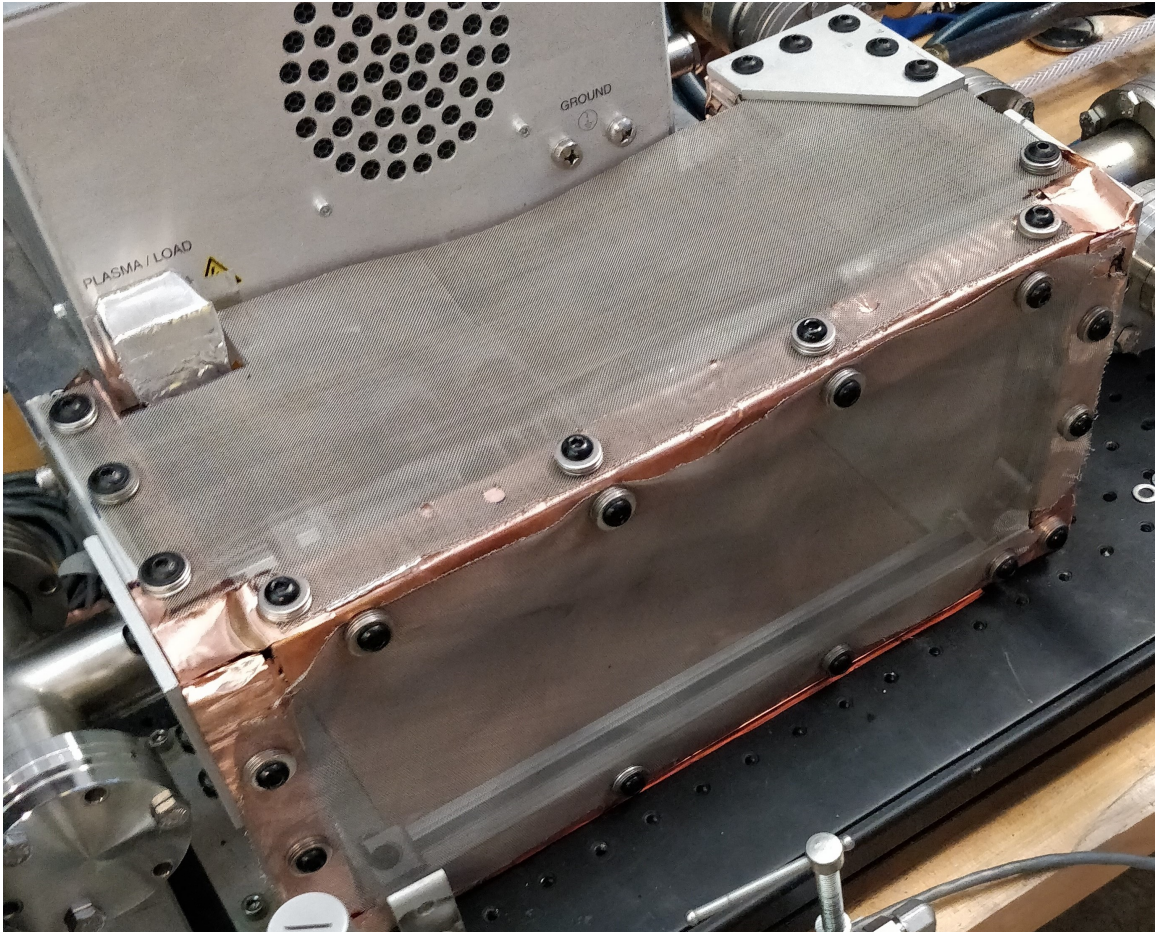


Figure 3.20: Stainless-steel mesh custom Faraday cage implementation surrounding RF antenna and experimental test-section.

a repeatable fashion across a variety of models and flow conditions without overheating of the models or excessive variability between pulses. The quality of the RF impedance match is captured in a parameter known as the standing wave ratio (SWR), defined in equation 3.6

$$SWR = \frac{1 + \sqrt{\frac{P_R}{P_F}}}{1 - \sqrt{\frac{P_R}{P_F}}} \geq 1 \quad (3.6)$$

For a perfect impedance match, all the forward power is delivered to the load, and  $SWR = 1.0$ . Experimentally determined SWR values for RF generator power levels, automated impedance match network, and antenna used in this experiment at full-scale mass flow rate are given in Table 3.1.

Table 3.1: RF Power System

Forward RF Power $P_F(W)$	Reflected RF Power $P_R(W)$	SWR
400	3	1.1896
800	2	1.1053

The SWR values given in table 3.1 correspond to greater than 99% power deposition in the plasma load and an effective impedance matching system.

Photographs of successful, impedance matched RF argon plasma ignition in the test section at 1/2 maximum power (500 W) and full-scale mass flow controller voltage (5 V) are shown as Figures 3.21 and 3.22.

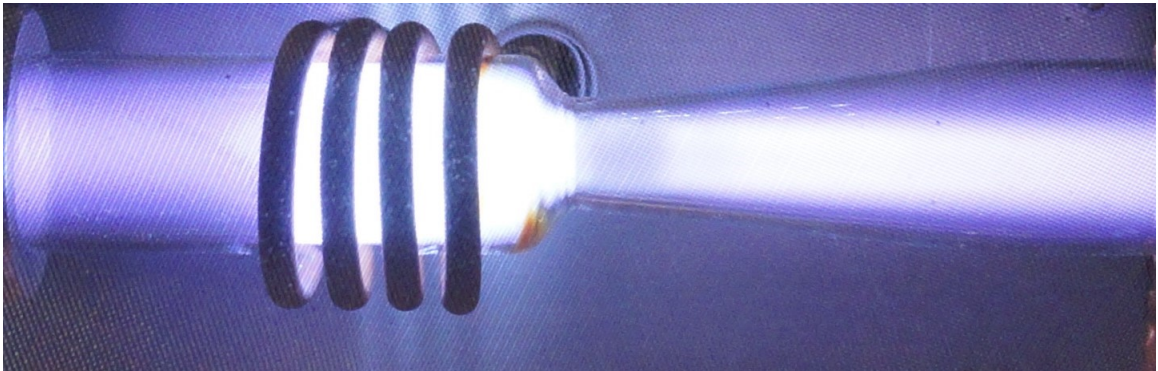


Figure 3.21: RF test pulse side view, gas flow from left to right.



Figure 3.22: RF test pulse top view

### 3.1.5 Experimental Instrumentation, Control, and Data Acquisition

The test chamber is instrumented for gas mass-flow measurements, upstream and downstream pressure measurements, as well as temperature measurements. Further RF power instrumentation is provided on the RF generator itself, which measures forward and reverse RF power. Control is via LabVIEW virtual instruments, which send signals and commands to the mass-flow controller and RF generator for flow-rate and plasma ignition control respectively. Data acquisition is via oscilloscope, thermocouple readout, photographs, videos, and instrumentation gauge panels.

The primary experiment test chamber instrumentation is shown in Figure 3.23.

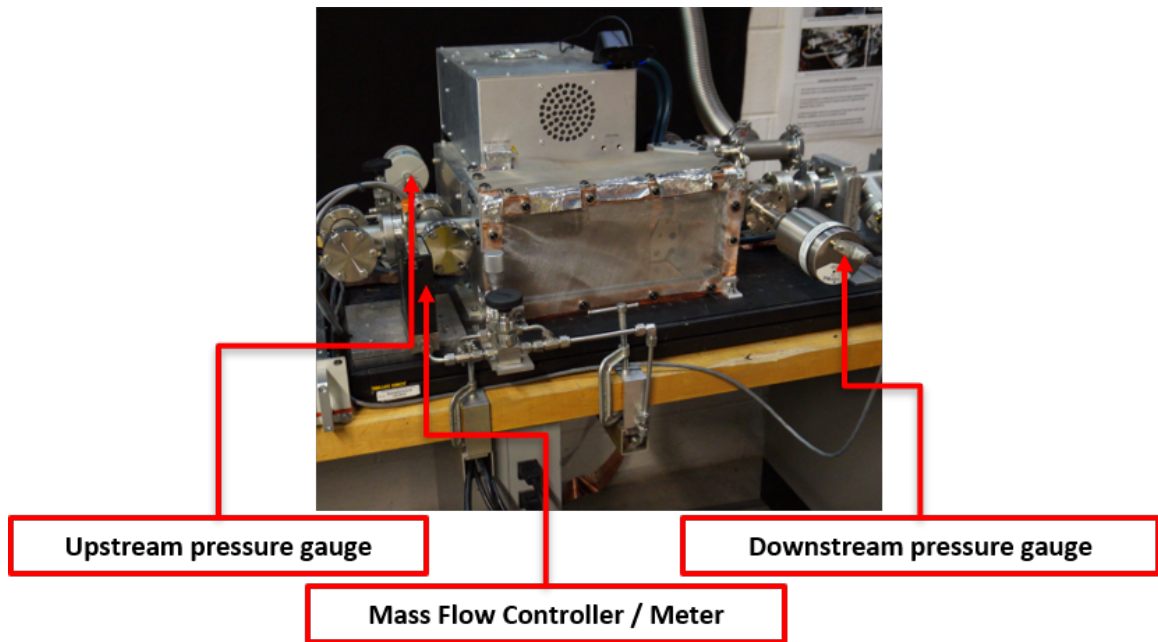


Figure 3.23: Test chamber instrumentation.

The upstream pressure gauge is a MKS Baratron<sup>®</sup> type 627A variable capacitance absolute pressure transducer, model 627A12TBC. This type of transducer consists of a permanently evacuated chamber ( $10^{-7}$  Torr) and a pressure inlet port, the interface of which is an elastic metal diaphragm. When the diaphragm is deflected by changes in absolute pressure, the capacitance to the diaphragm changes, which is measured and converted to a linear-scaled pressure value by electronics embedded within the sensor. The gauge has

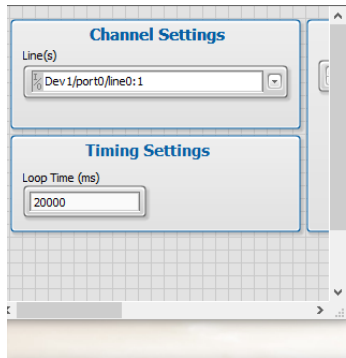
a full-scale pressure value of  $100 \text{ Torr}$ , corresponding to a full-scale voltage of  $10 \text{ V}$ , and is heated to  $45 \text{ }^\circ\text{C}$  to reduce the sensitivity of the internal zero to external temperature fluctuations by a factor of at least 35, with acceptable ambient operating temperatures between  $15$  and  $40 \text{ }^\circ\text{C}$ . The gauge output is readable (reliably different than zero) for pressures as low as  $5 \times 10^{-2} \text{ Torr}$ . For the MKS type 627 unit, combined accuracy is  $0.12\%$  of the reading with a measurement time constant of  $\approx 20 \text{ msec}$ . The downstream pressure gauge is also a MKS Baratron<sup>®</sup> type 627 variable capacitance absolute pressure transducer, model 627B21TDC1B, with a full-scale pressure reading of  $20 \text{ Torr}$ . The upstream and downstream pressure gauges are located outside of the RF antenna Faraday enclosure and upstream and downstream of the quartz tube-nozzle assembly respectively, as shown in Figure 3.23.

For both the upstream and downstream pressure gauges, readout and  $\pm 15 \text{ VDC}$  power supply is powered by two MKS PDR2000 dual capacitance diaphragm gauge controllers, shown in Figure 3.24. In addition to providing reliable power supply, these panels also provide a precise measurement of the  $0$  to  $10 \text{ VDC}$  analog signal output from the pressure gauges, and convert the value to a reading in  $\text{Torr}$ , with a variety of integrated signal zeroing and conditioning options to enable manual gauge calibration. For this experiment, the gauge calibration as set by the manufacturer is used, and the readouts are programmed to convert the voltages as sent by the gauges. In addition, as mentioned in section 3.1.2, the mass flow meter readout ( $5 \text{ VDC}$  full-scale) is provided by an MKS Type 250 controller, which was used in the calibration of the mass flow meter / controller. All readouts are mounted on the same aluminum strut assembly, and are grounded to the chassis of the RF generator, which is in turn connected to common chamber ground.

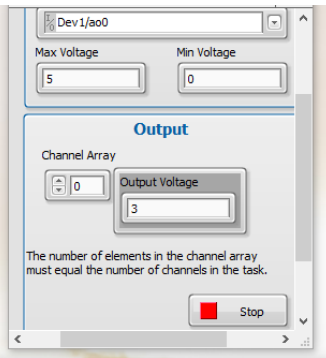
Experimental control is via the mass flow controller, described in section 3.1.2, and the RF generator forward power output, described in section 3.1.4. The mass flow controller set-point and RF generator on/off functionality are controlled via LabVIEW Virtual Instrument (VI) analog and digital output signals respectively. Mass flow controller set-points



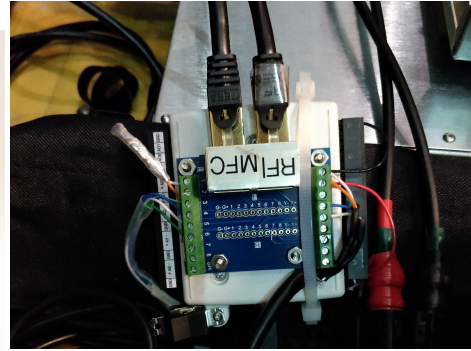
Figure 3.24: Test chamber gauge readouts. Upstream pressure is 0.75 Torr, downstream pressure is 0.518 Torr, and mass-flow rate readout is 0.241 V, as described in section 3.1.2.



(a) Experimental control LabVIEW VIs. Flow voltage set-



vice (white, bottom) and dual Ethernet point (right) is 3  $VDC$ , and RF generator single-shot pulse (top, blue) breakout board for experiment control.



(b) National Instruments USB6009 device (white, bottom) and dual Ethernet point (right) is 3  $VDC$ , and RF generator single-shot pulse (top, blue) breakout board for experiment control.

across the full 0-5  $VDC$  range are possible, and the RF on pulse-width time is controllable with  $ms$  precision, software timed. RF generator forward power output is set directly on the generator front panel in units of  $W$  with 1  $W$  precision via a dial setting. All signals to and from the mass-flow controller and RF generator are provided via individually foil-shielded twisted pair CAT7 grade Ethernet wiring to protect against electromagnetic interference. LabVIEW signal output is provided via a National Instruments USB6009 device, which is interfaced with the signal cabling via a dual-Ethernet breakout board. These LabVIEW control program and USB 6009 signal interface are shown as Figures 3.25a and 3.25b, respectively.

Primary data acquisition for the experiment is through a Tektronix brand 2 channel 100 MHz oscilloscope, model MSO2012B. Channel 1 is set as the MHD generator signal, while Channel 2 provides a real-time analog scaled output signal of the forward RF generator power (10  $VDC$  = 1  $kW$  RF forward power). The RF generator on/off signal serves as the oscilloscope data acquisition trigger input, and the resulting waveforms are captured and saved over a USB interface via a LabVIEW VI. The oscilloscope also includes a low-pass filter functionality with intelligent glitch detection that selectively filters noise without obscuring high-frequency anomalies. All captured waveforms are filtered to 5.50 MHz using this technology, removing the artifacts caused by the 27.1 MHz RF generator output.

Temperature data acquisition is made through a Fluke model 52B thermometer readout calibrated for use with Type-K thermocouples. The oscilloscope and thermometer readout are shown as Figure 3.26.

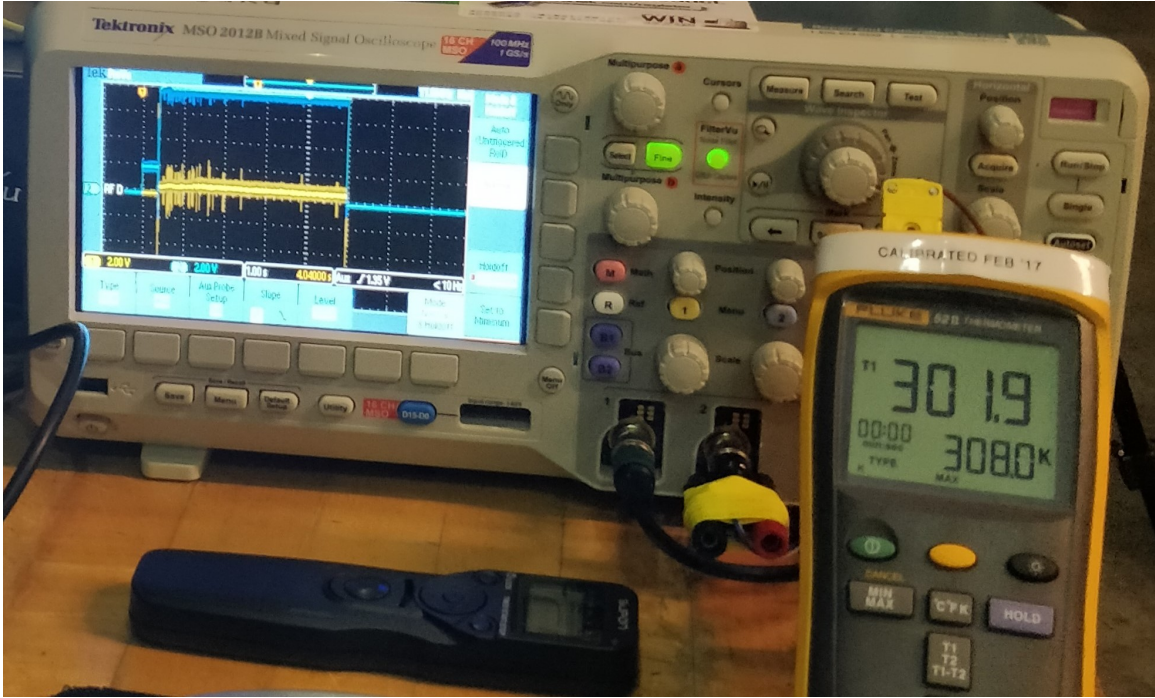
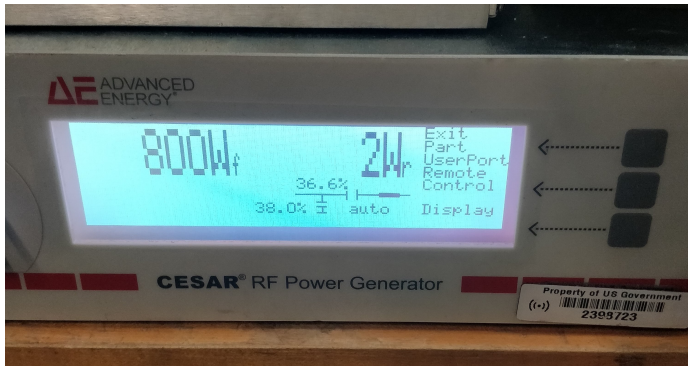


Figure 3.26: Oscilloscope data acquisition system. Channel 2 (blue) shows forward RF power 5000 *ms* pulse output with maximum of 8 *VDC* (800 *W*). Test-section thermocouple readout shown at right.

Test-section visual monitoring for remote operation and video data acquisition is provided by a Logitech C920 pro 1920x1080p resolution web camera positioned above the test-section. Additional high-resolution photography of the test-section is made with a Sony model NEX-3N digital camera, manually focused past the Faraday cage mesh and triggered using a remote shutter timer. The RF generator front panel provides additional feedback of reflected RF power as well as the positions of the tune and load match network capacitors as percentages of their respective full-scale values. The RF generator front-panel and test-section video monitoring system are shown as Figures 3.27a and 3.27b, respectively.

Overall, the instrumentation and data acquisition system were found to accurately and



(a) RF generator front panel with 800 W forward power, 2 W reflected power, with resultant capacitor positions for proper impedance match shown. (b) Logitech C920 webcam positioned over test-section.

repeatedly perform measurements with and without the presence of the RF discharge to within 1%, indicating minimal noise and systemic errors. These tests were repeated over a period of a few months in order to confirm consistency. Furthermore, there was no signal measured by the oscilloscope without electrodes connected directly in the test section, which confirms that the measured waveforms were not simply due to the presence of RF energy.

### 3.1.6 Test Section Model Mount Assembly

The model mount assembly (MMA) facilitates insertion and positioning of models in the experiment test-section. In addition, the MMA features a 4-port BNC electrical feedthrough system for extraction of data and diagnostics from models mounted in the test-section. The MMA is constructed from Conflat 2 3/4" flanges and tees, adapted to a KF40 flange interface for connection to the test-section outlet. The entire MMA is mounted on aluminum saddle supports to ensure alignment with the test-section and enable the model to be affixed to the experiment optical table. Side and top views of the MMA are given as Figures 3.28 and 3.29, respectively.

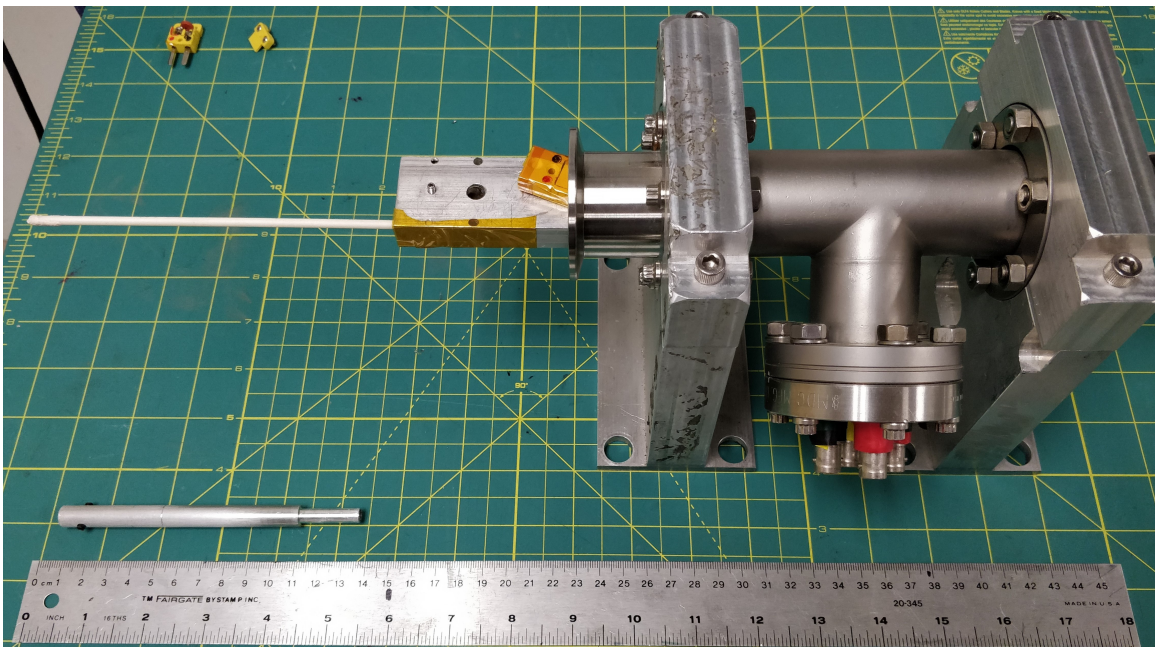


Figure 3.28: MMA Side view, with the thermocouple probe (white) installed in the model mount block. Also pictured is model mount extension tube (bottom left)

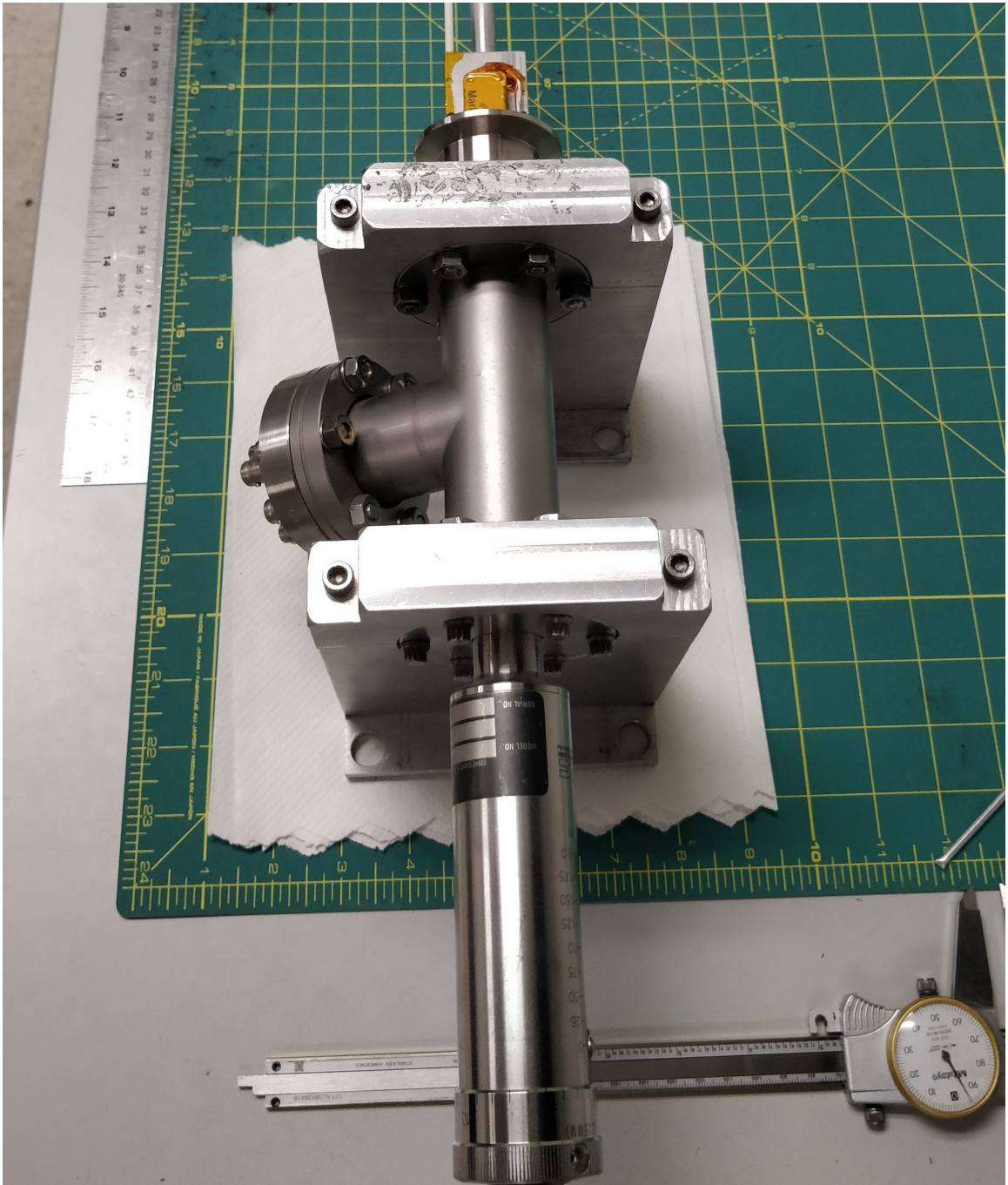


Figure 3.29: MMA top view with precision linear feedthrough adjustment (bottom cylinder).

The MMA positioning mechanism consists of a custom precision milled aluminum model mount block (MMB) and precision linear feedthrough. The aluminum MMB is rigidly affixed to a MDC linear micrometer adjustment feed-through, model MDC HTBLM-275-2, with range 0.000 - 2.000 *in* and precision 0.001 *in*. Figure 3.30 shows a close-up photograph of the MMB.

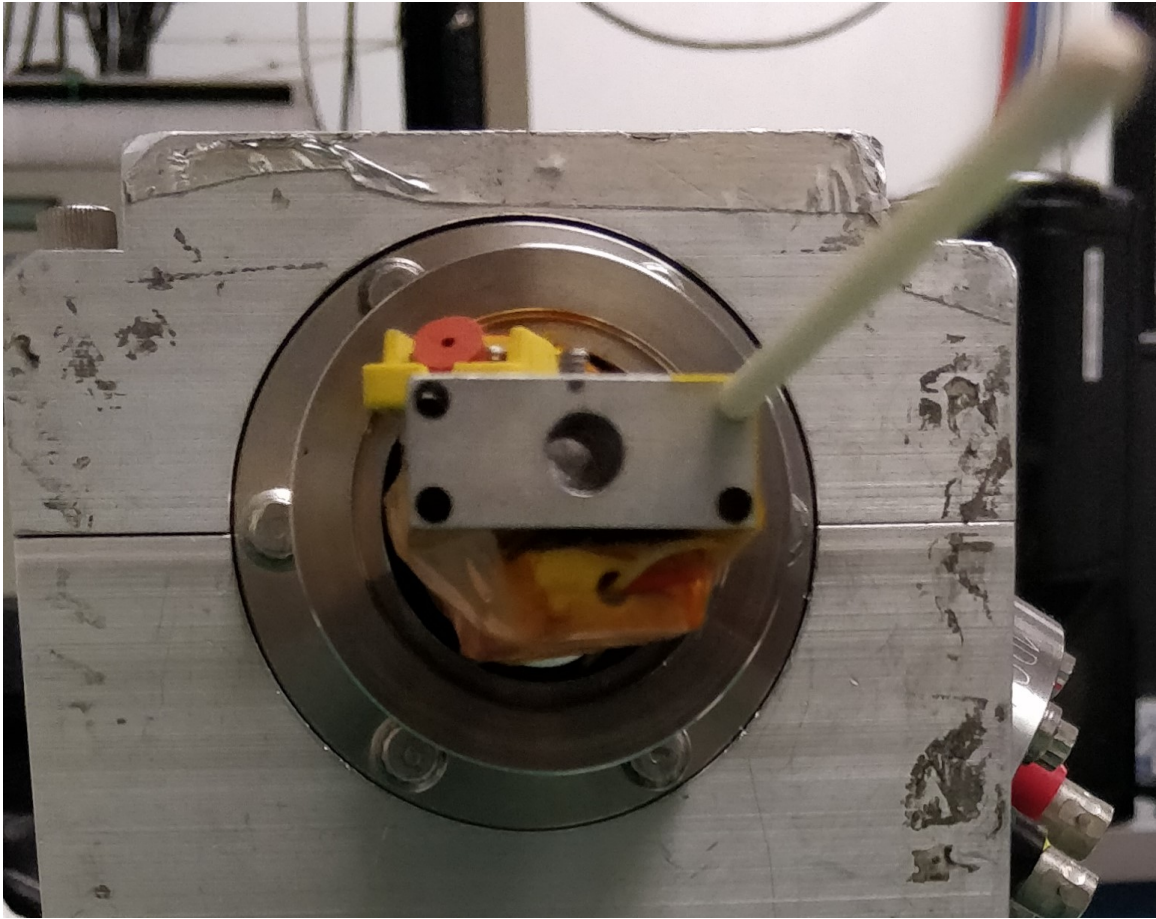


Figure 3.30: Model mount block front view. 0.257 *in* center model mount hole, and 0.128 *in* probe mount holes shown at each corner. Type0K thermocouple interface (bottom) and model electrode interface (top) connections shown

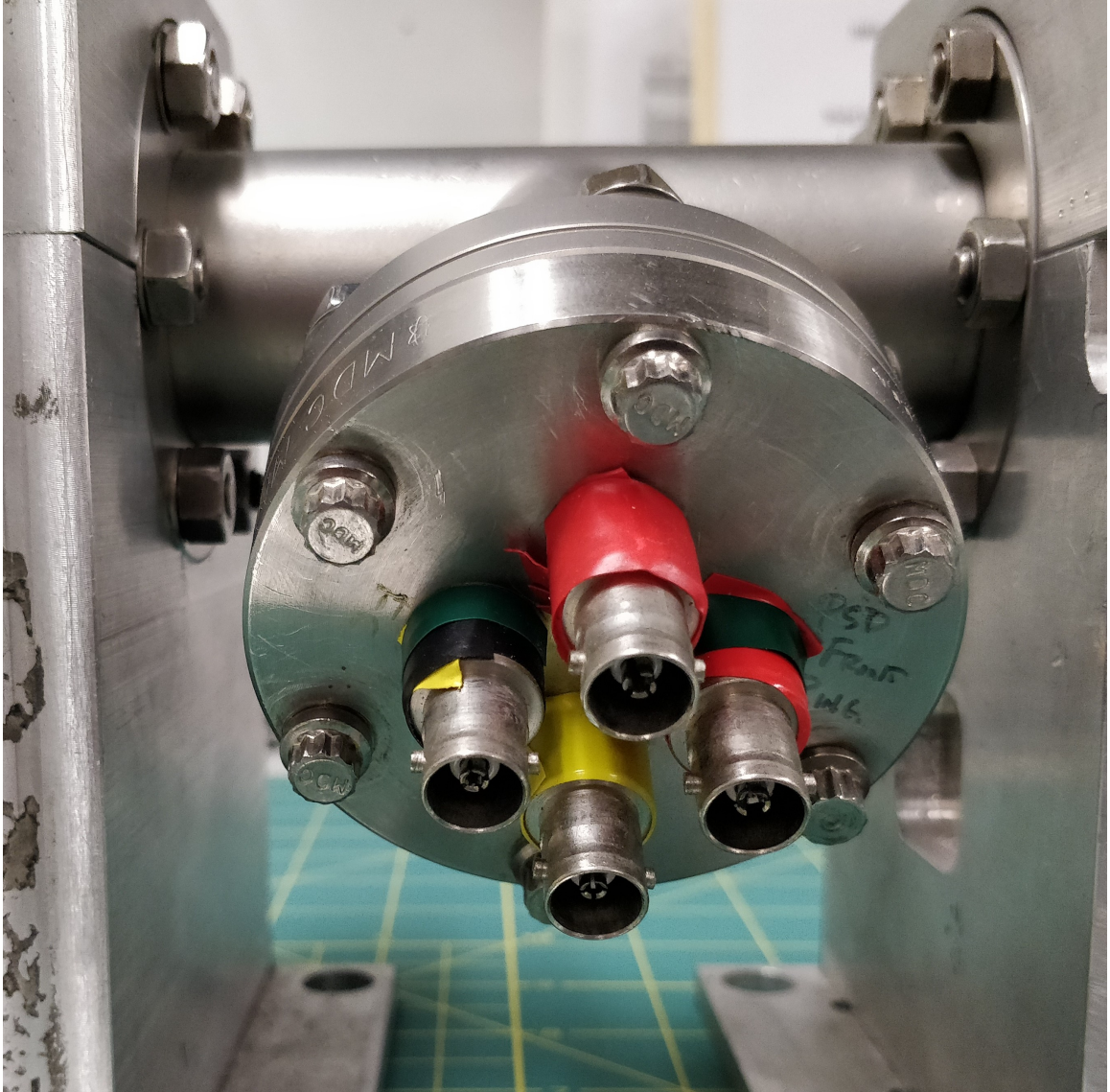


Figure 3.31: Model mount assembly BNC interface. Passes signal from model electrodes (red-green, black-green) and Type-K thermocouple (red, yellow) Only BNC center pins are used, as outer pins are chamber ground.

The MMB consists of a 1.2 *in* x 0.5 *in* rectangular milled block with a 0.257 *in* center hole into which 1/4" diameter model mount tubes or a precision machined model mount extension tube (MMT) is inserted. At each corner, and with a 0.080 *in* offset, there are 0.128 *in* holes for 1/8" diagnostic probes such as thermocouples. The precision machined aluminum MMT is approximately 5 *in* length and consists of a 3/8" outer diameter hollow tube and 0.257 *in* inner diameter and 3 1/4" depth, which facilitates flexible placement of models with respect to the MMB, effectively adding about 3 *in* of placement flexibility. In both the MMB and MMT, models are secured using set screws for secure, repeatable model placement in the test section.

Electrical interface connections from the MMA are made using a 4-port BNC Conflat 2 3/4" flange adapter plate shown in Figure 3.31. The four wires electrical interface wires for the model (+/-) electrodes and thermocouple (type K) as shown in Figure 3.30 are each connected to the center-pins of each BNC connector. The BNC connectors are color coded, and adapted such that the signal is transferred to the oscilloscope (model electrodes, red-green and black-green) or thermocouple readout (type K thermocouple interface, red and yellow).

The MMA is positioned aft of the test section in a precision ground and lubricated sliding track, which enables the MMA and model to slide into the test section without damage to the model while maintaining repeatable alignment. A photograph of this sliding track, the MMA, and an example test article are shown as Figure 3.32. After insertion the MMA is then laser-leveled by using an appropriately sized spacer underneath the MMB to mitigate beam deflection due to cantilever loading, shown as Figure 3.33.

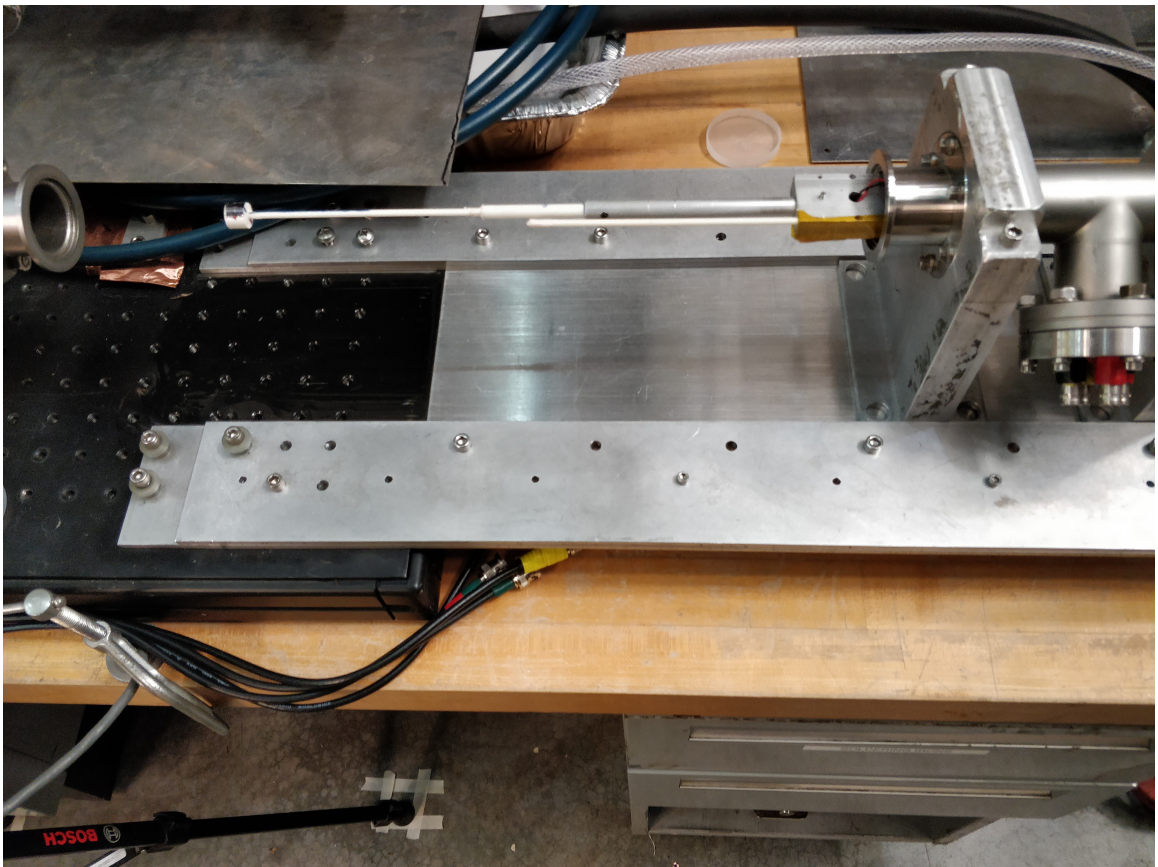


Figure 3.32: MMA in lubricated sliding track for test section insertion alignment.

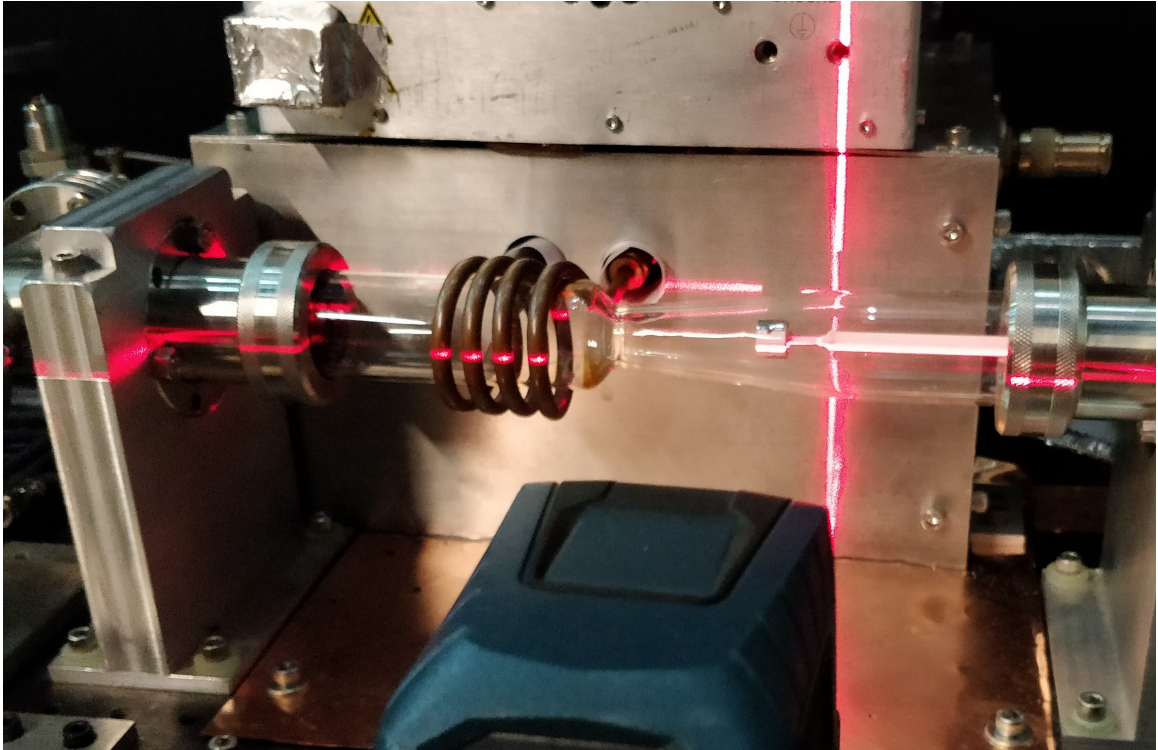


Figure 3.33: MMA laser-leveling process to ensure model centering in test-section.

Finally, the MHD model locations are experimentally positioned in such a way that at full (2.000 *in*) extension of the MMA positioning system, the front edge of the model is coincident with the quartz nozzle throat. For this condition to be true, the empirical requirement for the distance from the front of the model to the front of the MMB is found to be 11 3/16". All models utilized in this experiment are thus positioned in reference to the nozzle throat, with 0.001 *in* precision. The result of this positioning process, at full extension are illustrated as Figures 3.34 and 3.35.



Figure 3.34: Model fully extended, with front of model coincident with nozzle throat.



Figure 3.35: Linear micrometer feedthrough in fully extended position.

### 3.2 Test Section Demonstration of Supersonic Flowing Plasma

The experimental design, implementation, and potentially supersonic plasma discharge described in section 3.1 presents a unique opportunity: direct visual confirmation of shock waves through light emission from the ionized gas. As such, a brief experiment was devised to verify the presence of supersonic flow, should the experiment be capable of it in practice.

Based on preliminary experimental design iteration tests without RF ionization, it was found that the upstream and downstream pressure readings diverged significantly as test gas flow rate was increased. This divergence pointed to compressibility effects, and possibly supersonic flow within the nozzle; however, the downstream pressure did not necessarily have a low enough value to guarantee shock-free expansion of the test gas—there would likely be a standing normal shock wave within the nozzle at the location and Mach number necessary to equilibrate the nozzle pressure with the measured downstream backpressure.

Preliminary calculations based on the isentropic flow relations suggested that this normal shock wave, without added RF power deposition upstream of the nozzle throat, may be located around 1.0 *in* aft of the nozzle throat. As such, a 1/8” diameter cylindrical alumina ceramic ‘sting’ was constructed, and positioned in the flow using the model mount assembly such that it was located 1.000*in* from the throat, retractable up to 2.000*in* from the throat. The working hypothesis was that added RF power would serve to increase the energy upstream (total temperature and pressure) of the throat, and thus drive the standing normal shock much further downstream of the 1.0 *in* location, guaranteeing a supersonic free-stream flow condition ahead of the sting. A schematic of the test design is given as Figure 3.36, and a photograph of the completed test implementation (with Faraday cage removed for clarity), is shown as Figure 3.37.

Full-scale mass flow rate of 5 *V* was commanded to the mass flow controller, equivalent to an overall gas mass flow rate of approximately 15,380 *sccm Ar*, as per the aforementioned

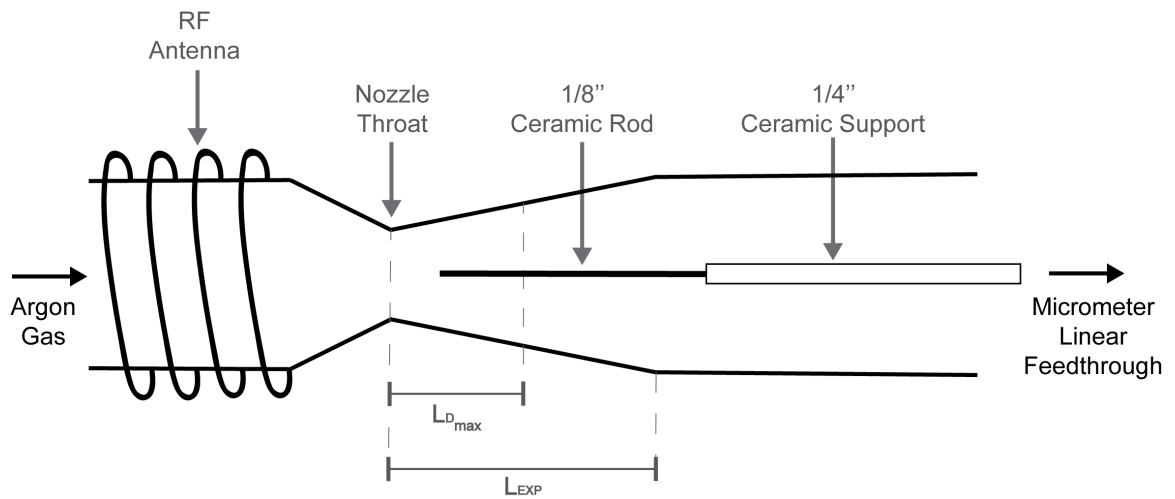


Figure 3.36: Test schematic to visualize and confirm supersonic flowing plasma shock wave.

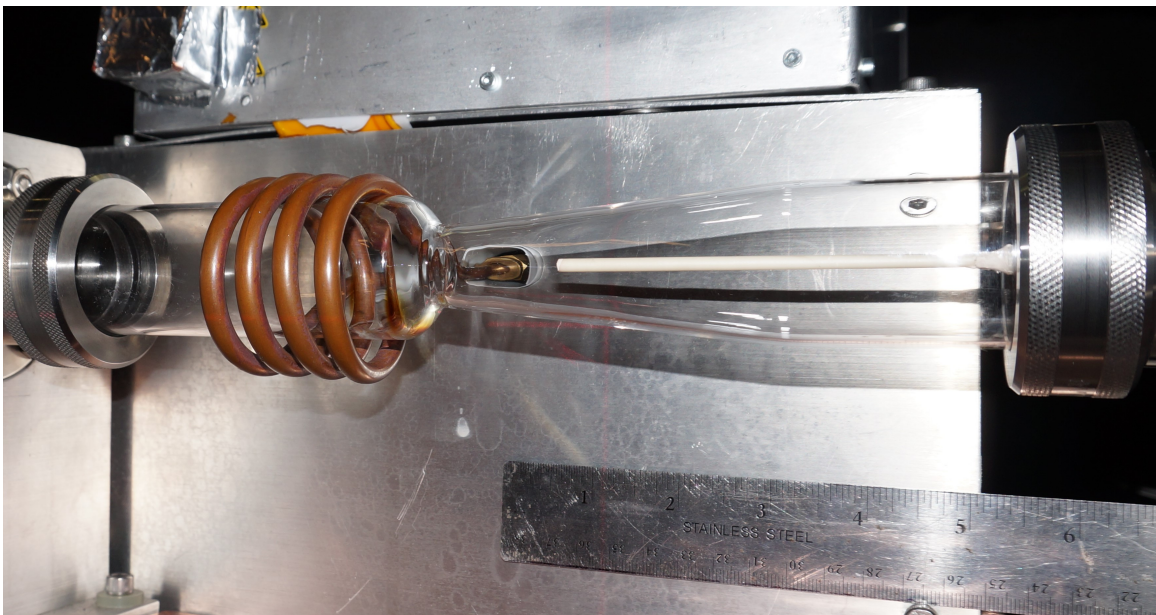


Figure 3.37: Test implementation to visualize and confirm supersonic flowing plasma shock wave.

gas mass flow meter calibration on Argon as described in section 3.1.2. A mid-range forward RF power level of  $600\text{ W}$  was chosen, and the discharge was allowed to run in a continuous fashion and visually inspected for the presence of shock waves. Photographs of the resulting shock wave are shown as Figures 3.38 and 3.39.

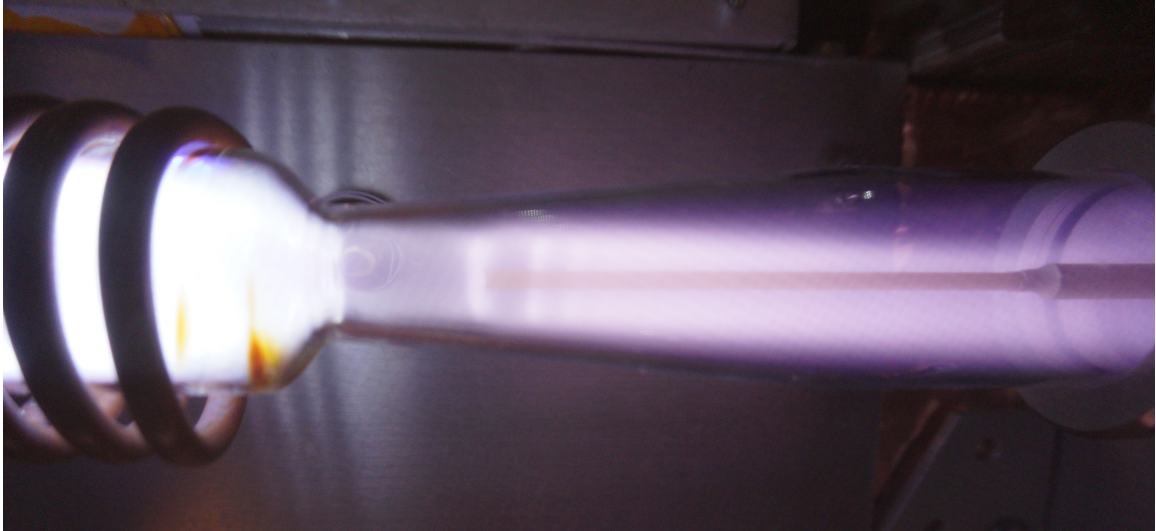


Figure 3.38: Shock wave for model located  $1.000\text{ in}$  from the throat,  $600\text{ W}$  forward RF power, and  $15,380\text{ sccm Ar}$  mass flow rate. Side view.

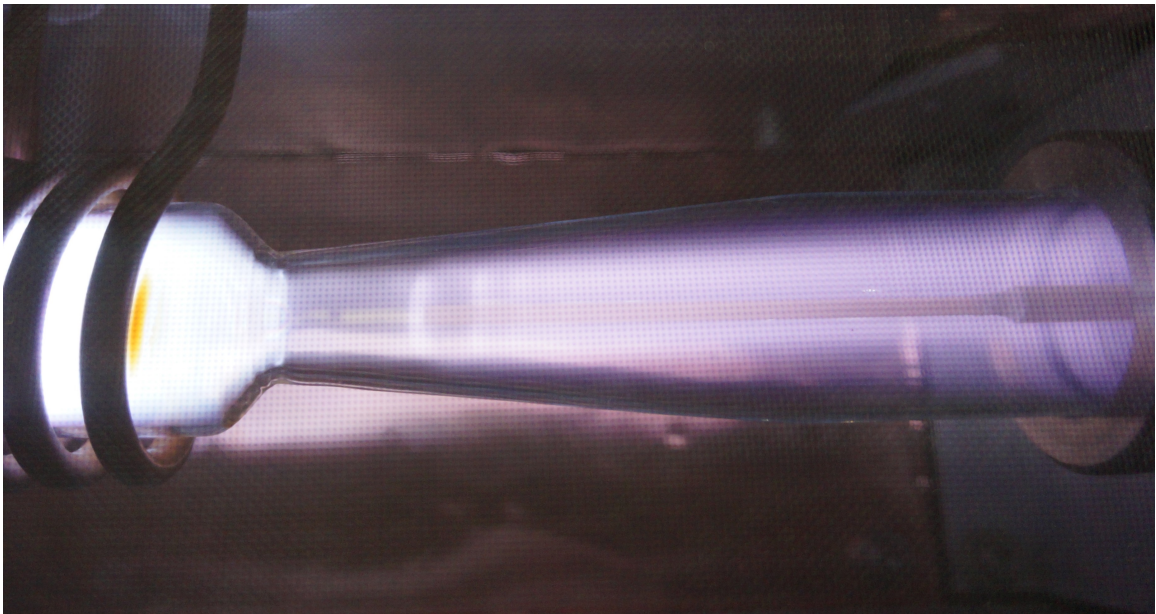


Figure 3.39: Shock wave for model located  $1.000\text{ in}$  from the throat,  $600\text{ W}$  forward RF power, and  $15,380\text{ sccm Ar}$  mass flow rate. Top view.

In addition to the shock wave found at the initial model location and test conditions, it was found that shock waves were present in the ionized discharge at forward RF power levels of 400 W and 800 W, flow-rates as low as 3 V (9300 *sccm Ar*), and model positions as far back as 2.000 *in* from the throat. Thus, it was concluded that the experimental design goal of creating a supersonic ionized discharge for simulating MHD energy generation during reentry had been achieved. An example photograph from these subsequent tests is shown as Figure .

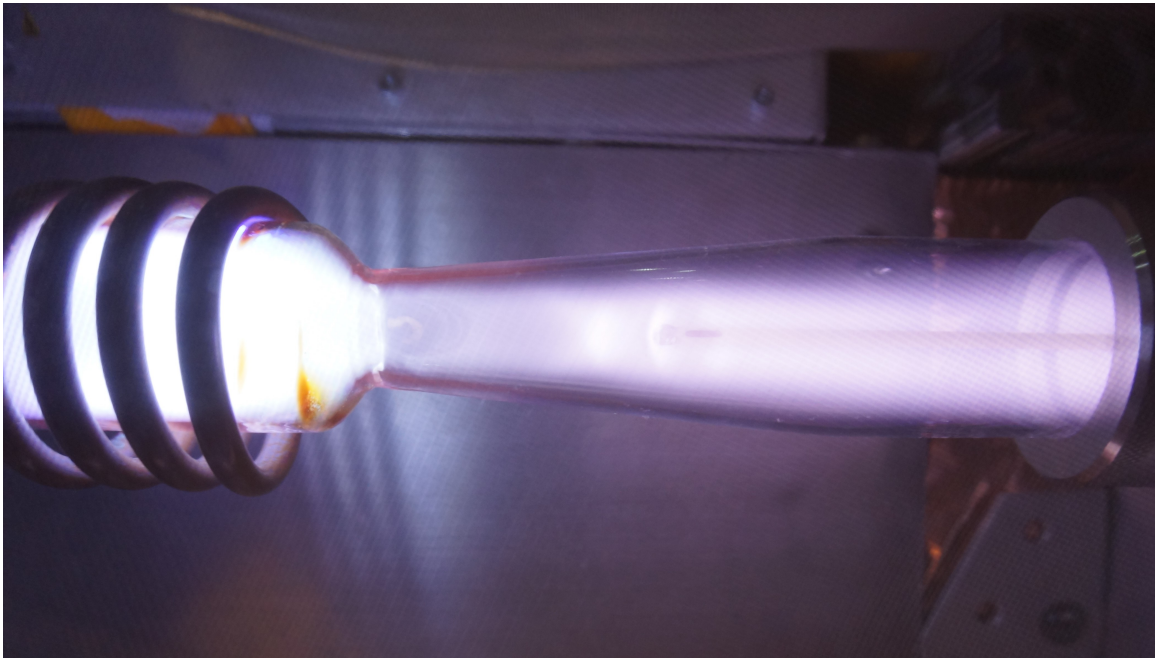


Figure 3.40: Shock wave for model located 2.000 *in* from the throat, 800 W forward RF power, and 9,300 *sccm Ar* mass flow rate. Side view.

### 3.3 Test Section Aerothermal Characterization

In addition to the visual verification of supersonic flow described in section 3.2, it was desirable to numerically quantify and characterize the test section aerothermal environment to check for choked flow at the nozzle throat and characterize the resulting supersonic expansion. For potentially supersonic flows, values of interest included the location and strength of the nozzle standing shock wave as well as the test section gas temperature to

calculate gas velocity and better inform model design.

A test plan to collect the necessary data was devised, shown as Figure 3.41. The framework of the test is similar to that of the shock verification test, except that the shock ‘sting’ model is replaced with a high-temperature, quick response thermocouple. The probe employed is a MEDTHERM Corporation Type K thermocouple, model 203-05K05, with 0.0005 *in* diameter wire for the thermocouple junction, resulting in a less than 5 *ms* thermal response time. The fast thermocouple response time more than sufficient for the 10 *s* and 20 *s* RF pulse times employed per test condition. Thermocouple readout is provided by the Fluke model 52B readout described in section 3.1.5.

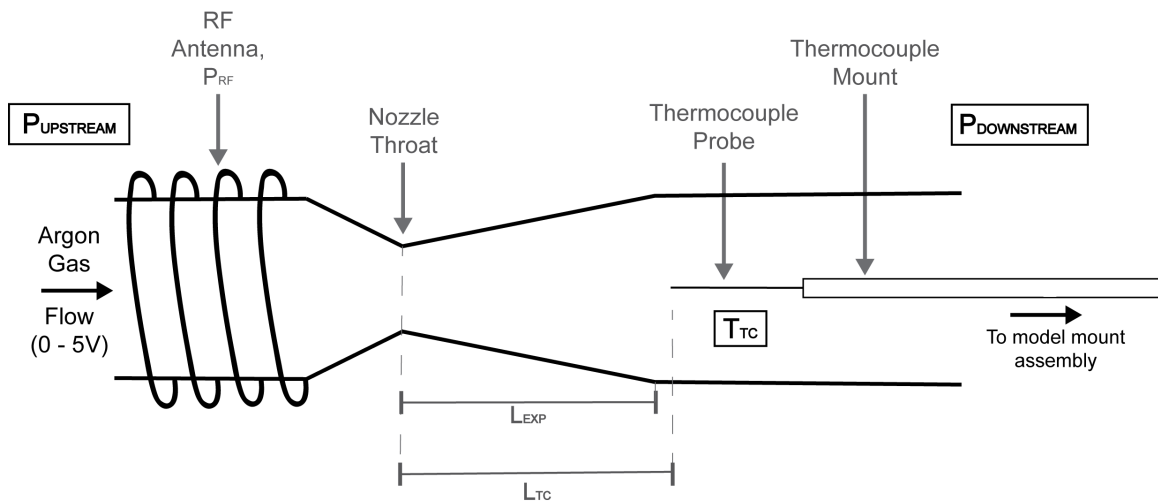
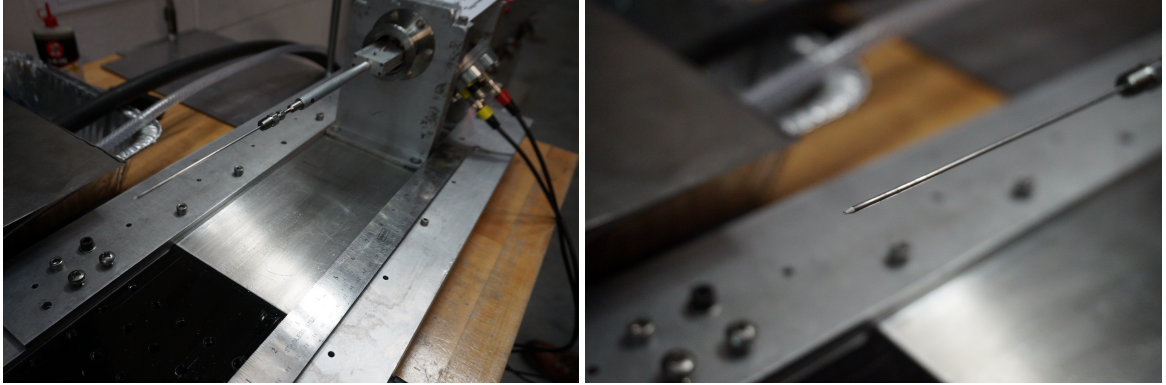


Figure 3.41: Experimental schematic to characterize test section aerothermal environment.

The probe temperature is taken at a location near the straight quartz tube at the nozzle exit (about 3 *in* from the nozzle throat), to capture the post-shock temperature. In addition to the probe temperature, upstream and downstream pressure measurements, with and without added RF power levels are recorded as a function of test gas mass flow rate and RF generator forward power outputs. Photographs of the thermocouple probe installed in the model mount assembly are shown as Figures 3.42a and 3.42b.



(a) Installed thermocouple.

(b) Insulated fine wire thermocouple tip.

Tests were run at forward RF power levels of  $0\text{ W}$ ,  $400\text{ W}$ ,  $600\text{ W}$ , and  $800\text{ W}$ , with flow rates set points ranging from  $0\text{ V}$  to  $5\text{ V}$  in  $0.25\text{ V}$  increments. The upstream pressure ( $Torr$ ), downstream pressure ( $Torr$ ), mass flow meter readout ( $V$ ), and thermocouple temperature ( $K$ ) were recorded at each test condition. These data were then used to first determine whether or not there existed a choked flow condition, and later, for those conditions found to be supersonic, what the flow properties were. A photograph of an example discharge with the installed thermocouple is shown as Figure 3.43.

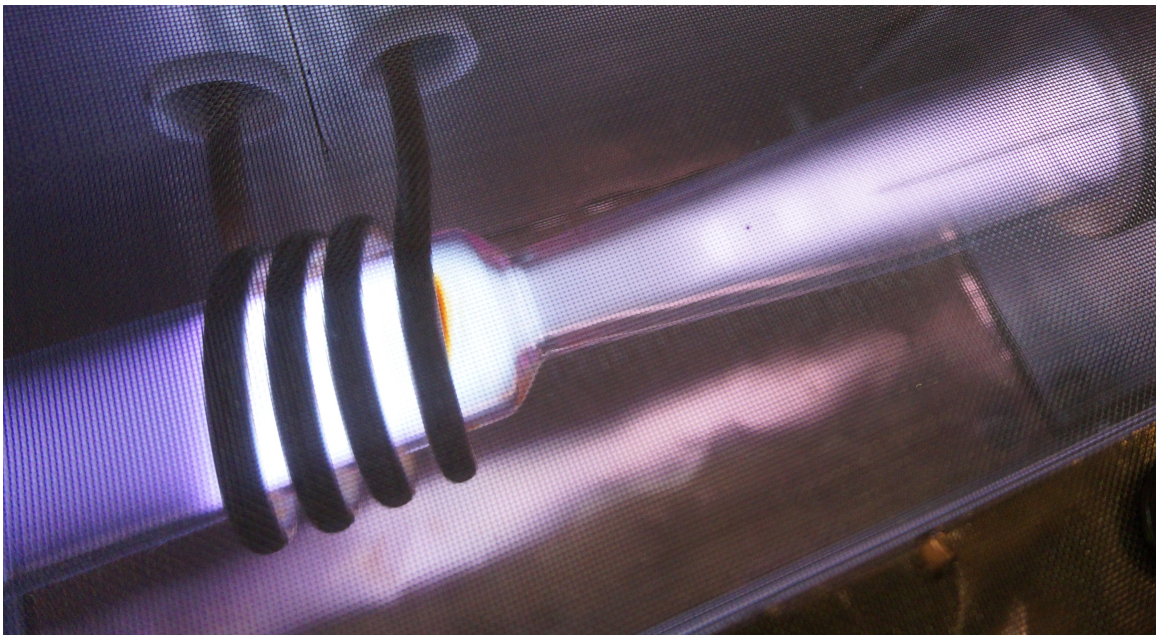


Figure 3.43: MEDTHERM thermocouple in supersonic plasma discharge.  $800\text{ W}$  forward RF power,  $9,300\text{ sccm Ar}$  ( $3\text{ V}$ ) gas mass flow rate. Measured temperature is approximately  $1215\text{ K}$ .

### 3.3.1 Choked Flow Testing

For an isentropic, compressible, one-dimensional gas flow, with total pressure  $P_t$  and total temperature  $T_t$ , the mass flow rate is defined as given by equation 3.7.

$$\dot{m} = \frac{AP_t}{\sqrt{T_t}} \sqrt{\frac{\gamma}{R}} M \left( \frac{\gamma + 1}{2} M^2 \right)^{-\frac{\gamma+1}{2(\gamma-1)}} \quad (3.7)$$

where  $M$  is the local Mach number and  $A$  is the cross-sectional area of the nozzle. If  $A$  is the nozzle throat area, and the Mach number is equal to one, then the flow is choked and equation 3.7 becomes 3.4. Indeed for a given nozzle geometry, the throat area,  $A^*$  is a constant, and if the Mach number is equal to one, then the mass flow rate becomes a sole function of the gas total temperature and pressure.

Without RF power deposition upstream of the nozzle throat, the gas total temperature can be said to be roughly constant over the entire testing mass flow rate range, which is confirmed upon thermocouple measurements. Thus, if the flow is choked at the nozzle throat *without upstream RF power deposition*, there will be a direct linear relationship between the measured upstream (stagnation) pressure,  $P_t$  and the mass flow rate  $\dot{m}$  as shown in equation 3.8.

$$\frac{\dot{m}_*}{P_t} = \frac{A}{\sqrt{T_t}} \sqrt{\frac{\gamma}{R}} \left( \frac{\gamma + 1}{2} \right)^{-\frac{\gamma+1}{2(\gamma-1)}} = Constant \quad (3.8)$$

Numerically,  $\frac{\dot{m}}{P_t}$  is a small number for common units and the test conditions under consideration, so the inverse is used instead. Thus, the condition that becomes true if the flow is choked at the nozzle throat (adiabatic, without RF power) is given as equation 3.9

$$\frac{dP_{t,measured}}{d\dot{m}_{measured}} \approx 0 \quad (3.9)$$

The condition given by equation 3.9 can be evaluated by measuring upstream pressure vs. mass flow rate and computing the ratio. Such a curve for this experiment without RF

power deposition, is shown as Figure 3.44.

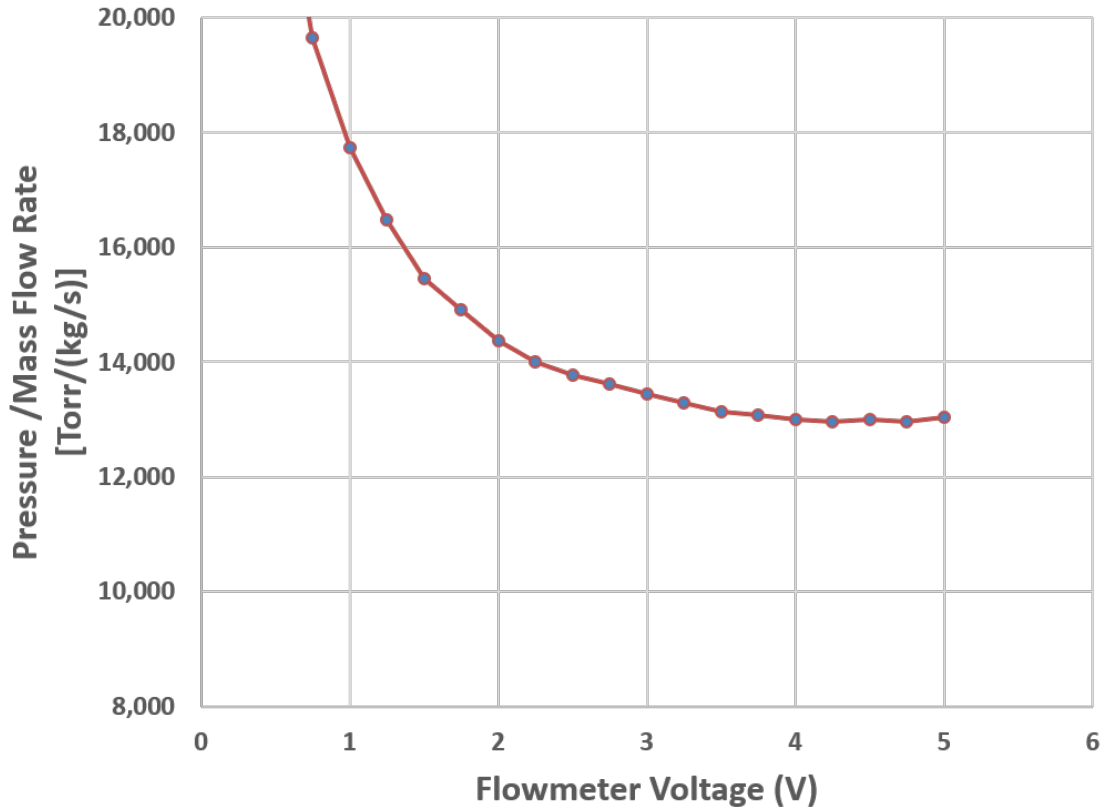


Figure 3.44: Adiabatic choked flow check value for test section, ratio of measured upstream pressure to mass flow rate. No added RF power upstream of nozzle throat.

In Figure 3.44, the flow appears to be choked for mass flow controller set-points between 4 V ( 12,280 *sccm Ar*) and 5 V ( 15,300 *sccm Ar*). Conducting the same measurements over multiple testing days, weeks, and even years yielded similar results for the experimental setup, and it is concluded that even without RF power deposition upstream of the nozzle, choked flow at the nozzle throat is achieved within a range controllable by the mass flow controller and within the capabilities of the gas exhaust system as implemented.

When RF power deposition upstream of the nozzle throat is considered, the total temperature,  $T_t$ , can no longer be considered constant, and must be measured. An estimate of the gas temperature is obtained using the aforementioned thermocouple probe, and the choked flow condition without RF is obtained in a similar fashion to that without RF and is

given as equation 3.10.

$$\frac{dP_{t,measured}}{d\dot{m}_{measured}\sqrt{T_t}} \approx 0 \quad (3.10)$$

Figures 3.45, 3.46, and 3.47 show this modified choked flow condition applied to 400 W, 600 W, and 800 W datasets respectively. The datasets appear to show, as expected, a leftward shift of the point at which the derivative becomes near-zero as compared to the dataset without RF power shown in Figure 3.44.

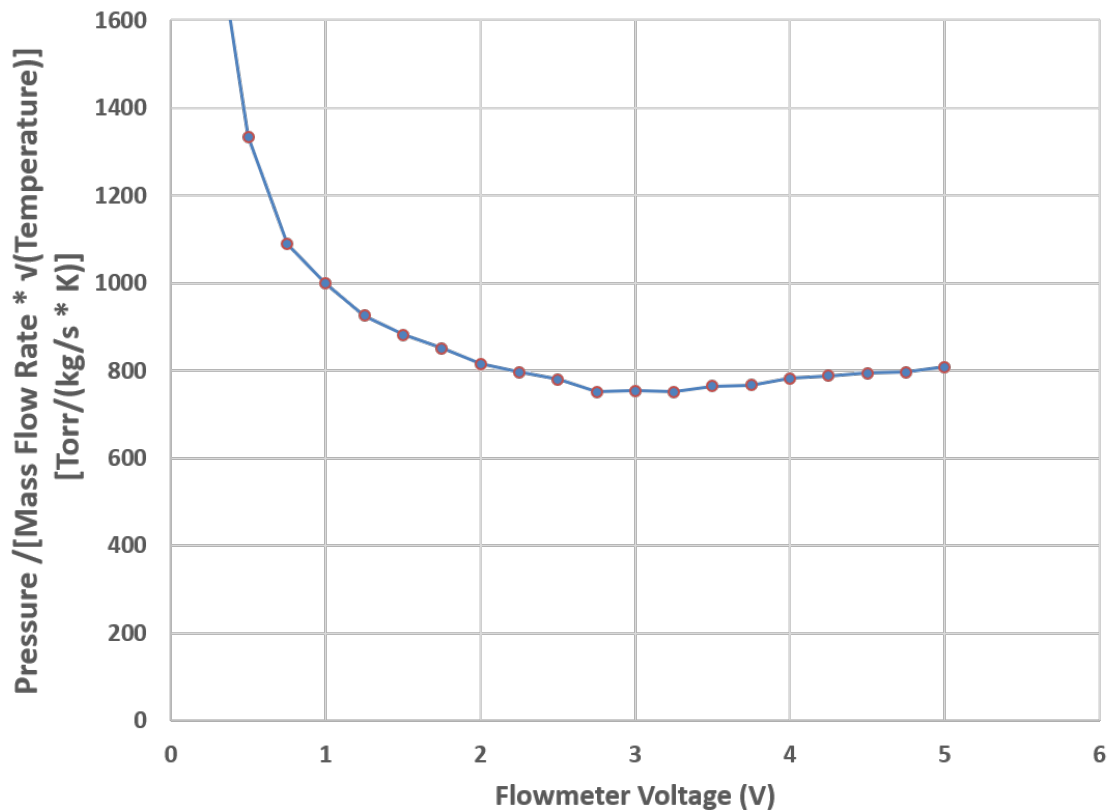


Figure 3.45: Choked flow check value for test section, ratio of measured upstream pressure to mass flow rate. RF power deposition of 400 W upstream of nozzle throat.

Based on these results, mass flow controller set points of 3 V and above are considered for further analysis, as they are the most likely to exhibit supersonic flow with RF power addition. These results provide concurring numerical evidence for prior visual observations of supersonic plasma discharge flow as described in section 3.2.

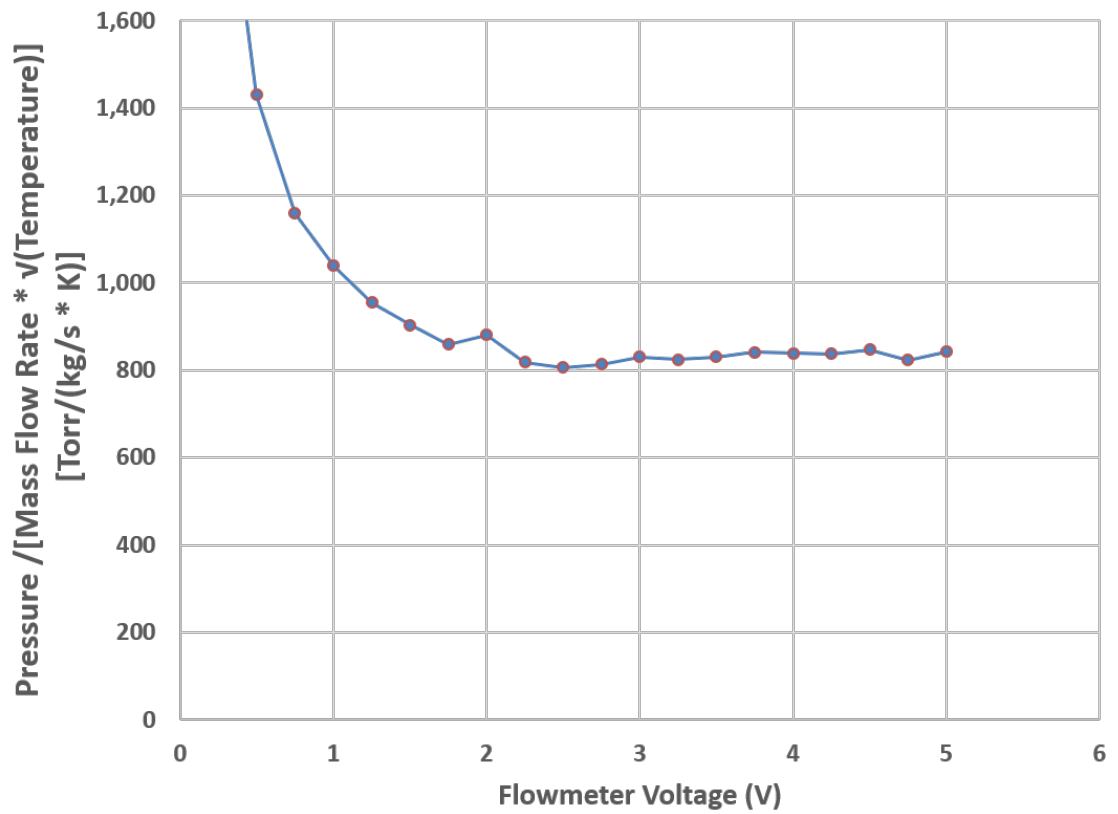


Figure 3.46: Choked flow check value for test section, ratio of measured upstream pressure to mass flow rate. RF power deposition of 600 W upstream of nozzle throat.

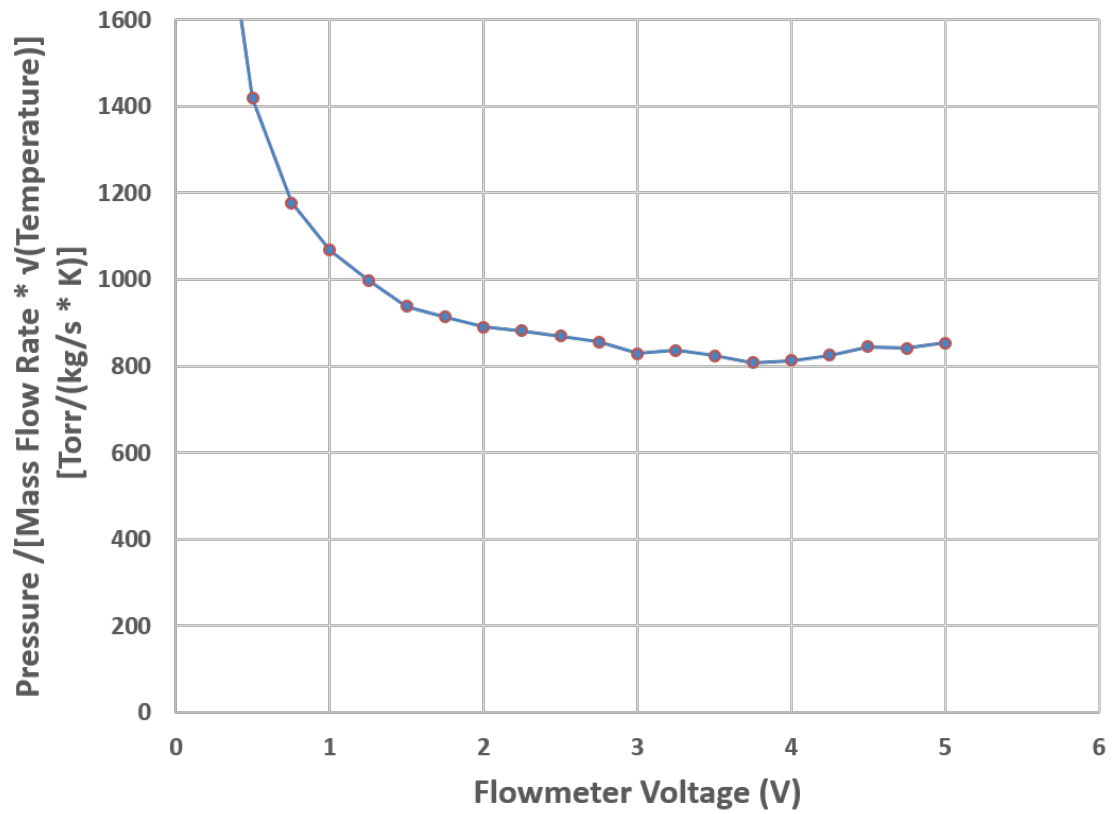


Figure 3.47: Choked flow check value for test section, ratio of measured upstream pressure to mass flow rate. RF power deposition of 800 W upstream of nozzle throat.

### 3.3.2 Supersonic Flow Characterization

With visual and quantitative data supporting the presence of supersonic plasma discharge in the nozzle test section, a characterization of the flow properties could follow. Although the supersonic flow was observed within the nozzle, and choked flow conditions determined present at the nozzle throat, upstream and downstream data supported the hypothesis that there must exist a shock wave somewhere along the nozzle expansion length as illustrated in Figure 3.41. Test section instrumentation measurements for a selection of conditions where flow is likely to be choked at the nozzle throat are shown as Table 3.2.

For these flow rates and RF power levels, measured pressures downstream of the quartz nozzle-tube assembly were much lower than those measured upstream of the quartz tube. However, the downstream pressure was still much higher than that expected for fully expanded flow, representing an elevated back pressure condition on the nozzle. From one-dimensional isentropic compressible flow theory, this condition requires that a normal shock wave exist in the nozzle, with Mach number (strength), such that the resulting stagnation pressure drop across the shock result in a local flow pressure approximately equal to the measured back-pressure condition from the downstream pressure gauge.

For a normal shock wave, the drop in stagnation pressure across the shock and resulting upstream to downstream stagnation pressure ratio,  $\frac{P_{t,d}}{P_{t,u}}$ , is given by equation 3.11, as derived from the normal shock relations. [64].

$$\frac{P_{t,d}}{P_{t,u}} = \left[ \frac{(\gamma + 1)M_\infty^2}{(\gamma - 1)M_\infty^2 + 2} \right]^{\frac{\gamma}{\gamma - 1}} \left[ \frac{(\gamma + 1)}{2\gamma M_\infty^2 - (\gamma - 1)} \right]^{\frac{1}{\gamma - 1}} \quad (3.11)$$

From equation 3.11, it is evident that for a given gas composition and specific heat ratio,  $\gamma$ , the stagnation pressure ratio across a normal shock is purely a function of Mach number,  $M$ . For the quartz-nozzle used in this experiment as described in section 3.1.3, the design exit Mach number is calculated as approximately  $M = 3.51$ , corresponding to an upstream to downstream stagnation pressure ratio of approximately  $\frac{P_{t,d}}{P_{t,u}} = 0.314$ , or,  $\frac{P_{t,u}}{P_{t,d}} = 3.18$ .

Table 3.2: Test Section Instrumentation Measurement Data

400W $P_{RF}$	(RF Off)	(RF Off)	(RF Off)	(RF On)	(RF On)	(RF On)
MFC Set Point	$P_u$	$P_d$	$T_d$	$P_u$	$P_d$	$T_d$
(V)	(Torr)	(Torr)	(K)	(Torr)	(Torr)	(K)
3	3.71	2.592	298.3	6.74	2.737	1020
4	4.76	3.227	298.3	8.22	3.41	810
5	5.96	3.904	298.3	9.59	4.139	690

600W $P_{RF}$	(RF Off)	(RF Off)	(RF Off)	(RF On)	(RF On)	(RF On)
MFC Set Point	$P_u$	$P_d$	$T_d$	$P_u$	$P_d$	$T_d$
(V)	(Torr)	(Torr)	(K)	(Torr)	(Torr)	(K)
3	3.66	2.564	297.6	7.45	2.727	1075
4	4.71	3.184	297.6	9.09	3.417	880
5	5.88	3.855	297.6	10.61	4.152	760

800W $P_{RF}$	(RF Off)	(RF Off)	(RF Off)	(RF On)	(RF On)	(RF On)
MFC Set Point	$P_u$	$P_d$ , no RF	$T_d$ , no RF	$P_u$ , RF	$P_d$ , RF	$T_d$ , RF
(V)	(Torr)	(Torr)	(K)	(Torr)	(Torr)	(K)
3	3.67	2.575	299.1	8.27	2.755	1320
4	4.74	3.199	299.1	10.12	3.535	1123
5	5.93	3.877	299.1	11.88	4.31	827

However, as mentioned earlier, for the flow conditions shown in Table 3.2, this condition is not quite met.

It is desirable to use stagnation pressures, rather than the local static pressures, as for an isentropic flow, the stagnation pressure only changes across a shock wave or with added heat (does not occur after that deposited by the RF antenna). Although the pressure and temperature measurements shown in Table 3.2 are technically static measurements, they can be assumed to be reasonable estimates of the true stagnation values.

Evidence for the validity of this assumption for the upstream is provided by calculated estimates of the upstream flow Mach number based on mass-flow rate measurements and nozzle dimensions, which resulted in a maximum calculated upstream Mach number of  $M \approx 0.1$ , which is less than the  $M < 0.3$  condition for which a flow can be considered incompressible. In this flow regime, the calculated stagnation pressure is in absolute terms relatively close to the measured static pressure. As an example, at full-scale mass flow rate set-point of  $5 V$ , the measured upstream static pressure is  $P_{u,m} = 5.88 \text{ Torr}$ , and the corresponding calculated upstream stagnation pressure is  $P_{t,u} = 5.95 \text{ Torr}$ , a difference of 1.17%. This example represented the most extreme case, and for the upstream pressure values, the difference is typically much smaller. Thus, to avoid additional uncertainties introduced by estimating the upstream Mach number, and noting that the numerical difference is small in practice, the final assumption is made that  $P_{t,u} \approx P_{u,m}$ .

For the downstream pressure static measurements,  $P_{d,m}$ , calculation of  $P_{t,d}$  is not possible directly, because the isentropic flow relations require the downstream post-shock Mach number, which although less than one can be greater than 0.3 and is not known *a priori*. In addition, even if a normal shock wave is not present in the nozzle due to a high back-pressure, the pressure measured by the downstream gauge would still represent the pressure after a shock-wave, due to the presence of gaskets and transitions from the quartz tube to vacuum flanges. From the normal shock relations[64], it is known that the Mach number after a normal shock is *always* subsonic, and for the maximum upstream Mach number of

$M_1 = 3.5$  possible with this configuration had a maximum value of  $M_2 \approx 0.50$ . For this maximum post-shock Mach number, the static to stagnation pressure ratio has a value of  $\frac{P}{P_t} \approx 0.85$ .

Given that all possible post-shock Mach numbers will be less severe than this calculated value, it can be reasonably assumed that the measured downstream static pressure will be within 15% or less of the post-shock stagnation pressure value. For simplicity, and to avoid the necessity of further estimations and assumptions, the final assumption is made to set the downstream stagnation pressure as roughly equivalent to the measured static pressure, or  $P_{t,d} \approx P_{d,m}$ .

Similarly for the temperature measurements downstream of the nozzle throat and aft of the nozzle exit plane, the measured temperature would closely approximate the stagnation temperature, with corresponding minimum static to stagnation temperature ratio of  $\frac{T}{T_t} \approx 0.92$ . Again for simplicity and to avoid the necessity of iteration for preliminary characterization data, the final assumption is made that  $T_{d,t} \approx T_{d,m}$ .

With these estimated stagnation pressure total temperature values, it becomes possible to quantify the free-stream Mach number, gas velocity, and location of the normal shock within in the nozzle at each test condition combination based on the normal shock and isentropic flow relations. Consider the schematic shown in Figure 3.48.

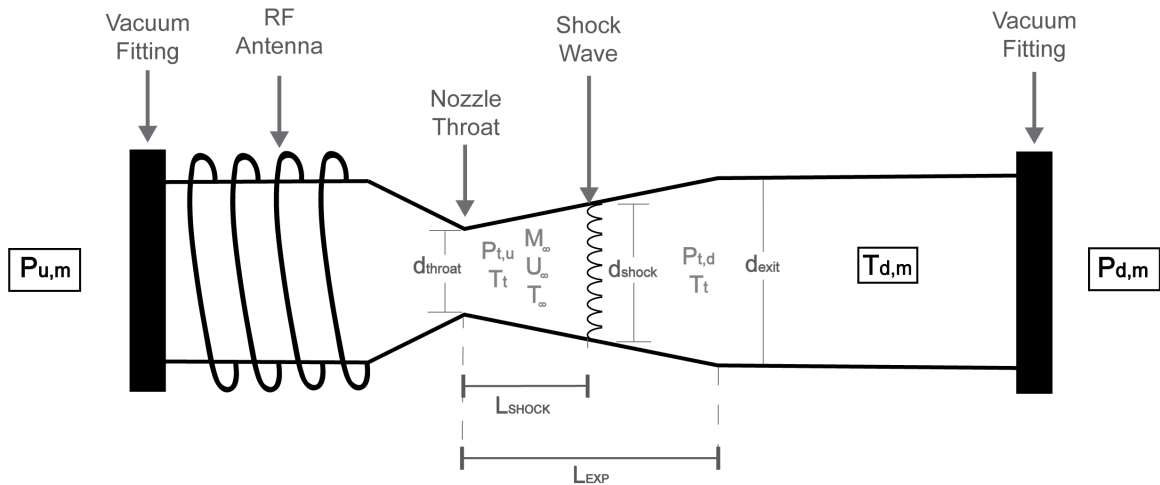


Figure 3.48: Nozzle shock location computation schematic.

For the quartz-tube nozzle assembly described in section 3.1.3, measured dimensions listed in Figure 3.48 are given as Table 3.3.

Table 3.3: Table of nozzle shock location dimensions

Nozzle Parameter	Value	Units
$L_{exp}$	3.30	<i>in</i>
$d_{throat}$	0.668	<i>in</i>
$d_{exit}$	1.366	<i>in</i>
$\frac{A_{exit}}{A_{throat}}$	4.16	—
$M_{d,exit}$	3.512	—

At each test condition, the process for performing the calculation is described as follows:

**Calculation of  $M_\infty$ :** First, the upstream and downstream pressure measurement values are used in conjunction with an inversion of equation 3.11 to determine a value for the freestream Mach number,  $M_\infty$ .

**Calculation of  $u_\infty$ :** Second, the downstream stagnation temperature measurement is used in conjunction with the computed freestream Mach number to calculate the freestream gas velocity,  $u_\infty$ . Because the total temperature is constant across a normal shock wave, the freestream Mach number and total temperature estimated from the downstream temperature measurement can be used to estimate the freestream static temperature,  $T_{inf}$ , in accordance with the isentropic relations, shown as equation 3.12.

$$\frac{T_t}{T_\infty} = \left(1 + \frac{\gamma - 1}{2} M_\infty^2\right) \quad (3.12)$$

Once the static temperature,  $T_\infty$ , is known, the freestream Mach number,  $M_\infty$ , is converted into the freestream gas velocity,  $u_\infty$  as shown by equation 3.13.

$$u_{\infty} = M_{\infty} \sqrt{\gamma R T_{\infty}} \quad (3.13)$$

**Calculation of  $L_{shock}$ :** Third, the ratio of the nozzle area at the shock,  $A_{shock}$ , to the nozzle throat area,  $A_{throat}$ , is computed by inverting the area Mach Relation, as shown in equation 3.14.

$$\frac{A_{shock}}{A_{throat}} = \left(\frac{\gamma + 1}{2}\right)^{-\frac{\gamma+1}{2(\gamma+1)}} \frac{\left(1 + \frac{\gamma-1}{2} M_{\infty}^2\right)^{\frac{\gamma+1}{2(\gamma-1)}}}{M_{\infty}} \quad (3.14)$$

The computed area ratio referenced to the nozzle throat from the Area Mach relation,  $\frac{A_{shock}}{A_{throat}}$ , is converted into a diameter ratio by taking the square-root,  $\frac{d_{shock}}{d_{throat}} = \sqrt{\frac{A_{shock}}{A_{throat}}}$ . Using this diameter ratio, a value for the diameter of the nozzle at the location of the shock,  $d_{shock}$  is computed. As the nozzle is radially symmetric, with a circular cross-section and linear diameter expansion, nozzle diameter is a simple function of distance from the throat along the expansion length. Thus, the location of the standing normal-shock wave in the nozzle,  $L_{shock}$ , can be computed and is given as equation 3.15.

$$L_{shock} = \frac{d_{shock}}{d_{exit} - d_{throat}} L_{exp} \quad (3.15)$$

The described calculation procedure is carried out on the test section instrumentation output data given previously as table 3.2. The results of these computations are given as Table 3.4.

The results without RF power deposition depicted in Table 3.4 show very consistent computed values across the three tests, highlighting the consistency and repeatability of the gas flow and pressure measurements. Without RF power deposition, the freestream Mach number reaches a maximum value of approximately  $M = 2.3$  at a location of around  $L_{shock} = 1$  in from the nozzle throat. Freestream gas velocities, based on the measured gas

Table 3.4: Test Section Flow Characterization Results

400W $P_{RF}$	(RF Off)	(RF Off)	(RF Off)	(RF On)	(RF On)	(RF On)
MFC Set Point (V)	$L_{shock}$ (in)	$M_\infty$	$u_\infty$ ( $\frac{m}{s}$ )	$L_{shock}$ (in)	$M_\infty$	$u_\infty$ ( $\frac{m}{s}$ )
3	1.00	2.19	447.17	2.50	3.10	889.15
4	1.07	2.24	451.46	2.43	3.07	790.12
5	1.16	2.30	455.92	2.31	3.00	725.37

600W $P_{RF}$	(RF Off)	(RF Off)	(RF Off)	(RF On)	(RF On)	(RF On)
MFC Set Point (V)	$L_{shock}$ (in)	$M_\infty$	$u_\infty$ ( $\frac{m}{s}$ )	$L_{shock}$ (in)	$M_\infty$	$u_\infty$ ( $\frac{m}{s}$ )
3	0.99	2.18	446.83	2.82	3.27	923.98
4	1.08	2.25	451.88	2.74	3.23	833.45
5	1.16	2.30	455.85	2.61	3.16	770.87

800W $P_{RF}$	(RF Off)	(RF Off)	(RF Off)	(RF On)	(RF On)	(RF On)
MFC Set Point (V)	$L_{shock}$ (in)	$M_\infty$	$u_\infty$ ( $\frac{m}{s}$ )	$L_{shock}$ (in)	$M_\infty$	$u_\infty$ ( $\frac{m}{s}$ )
3	0.99	2.18	446.60	3.13	3.43	1034.10
4	1.09	2.25	452.10	2.98	3.35	949.20
5	1.17	2.31	456.20	2.85	3.28	811.09

temperature (within 5 degrees Kelvin of room temperature at all times), were about 450  $m/s$ . These results support the existence of supersonic flow within a portion of the nozzle even without added RF power deposition for all three considered flow rates, and further guarantee the existence of supersonic flow once the RF power deposition is added.

The results with RF power deposition depicted in Table 3.4 show increased values for all three computed parameters, owing to the increased thermal and kinetic energy deposited into the test gas by the RF antenna. For all three RF power level tests, the shock location  $L_{shock}$  is furthest from the nozzle throat at the smallest MFC set point of 3 V, as compared to higher MFC set point voltages at a given power level. This asymmetry is most likely due to higher test-gas temperatures due to constant RF power deposition into a smaller test-gas densities at the lower MFC set point values. The minimum shock location with RF power on across all possible test conditions shown in Table 3.4 is approximately  $L_{shock} = 2.31$  in,

which occurs at 400 W  $P_{RF}$  and 5 V MFC set-point, as expected.

For a given MFC set point voltage,  $L_{shock}$ ,  $M_\infty$ , and  $u_\infty$  increased monotonically with increasing RF forward power,  $P_{RF}$ . This result indicates that increasing RF power deposition upstream of the throat effectively ‘blows’ the standing normal shock wave in the nozzle downstream, as expected. This effect is most visible at the 800 W  $P_{RF}$  and 3 V MFC set-point condition, where the test gas maximum freestream Mach number and velocity are highest at  $M_\infty = 3.43$  and  $u_\infty = 1034 \text{ m/s}$  respectively, which is 98% of the maximum theoretical Mach number of approximately  $M = 3.5$  as computed using the measured nozzle dimensions and area-Mach relation. This result indicates that the design Mach number is nearly achievable with maximum RF power deposition of 800 W. Unfortunately, it was not possible to safely test at the maximum RF power level of 1000 W, as there was a risk of high-voltage arcing that would damage the quartz nozzle-tube assembly. Total maximum expected uncertainty in these results is expected to be approximately 20%.

Overall, the test section plasma flow characterization results depicted in Table 3.4 show computed freestream ionized gas velocities greater than  $u_\infty = 720 \text{ m/s}$ , and freestream Mach numbers greater than  $M_\infty = 3$ . It is concluded that the test chamber experimental design and implementation described in this Chapter is capable of successfully creating and maintaining a repeatable, computer-controlled, supersonic plasma discharge.

### **3.4 Experimental Test Conditions and Relevance to Planetary Entry**

Forward RF power levels,  $P_{RF}$  of 400 W and 800 W are chosen as bounding cases for RF power deposition, and mass flow controller set-point voltages of 3 V (60% full-scale) and 5 V (100% full-scale) are chosen as bounding cases for test gas mass flow rate. The result is four total possible test condition combinations.

Based on the computed normal shock locations for the considered test conditions, model placement for guaranteed supersonic free-stream plasma flow is set as  $L_{model} = 2 \text{ in}$  from the throat for all subsequent testing.

For an actual planetary entry vehicle, un-ionized, cold gas is shocked and thermally ionized during the hypersonic entry phase. The result is shocked, subsonic, ionized gas impinging on the vehicle surface. The resulting entry plasma created has a relatively high density and temperature, while having a relatively low ionization fraction (less than 1%).

By contrast, the laboratory artificially ionized supersonic plasma discharge presented has relatively low density and velocity, a maximum of  $1000\text{ m/s}$  as shown in Table 3.4 vs.  $6000\text{ m/s}$  as might be encountered during Mars entry. However, the artificially ionized gas has a relatively high ionization fraction (on the order of 10%), due to non-equilibrium coupling of energy to the electrons in the plasma. The low-density nature of the discharge means that the electron-neutral collision frequency, which inhibits electron mobility and therefore electrical conductivity, is expected to be much lower than that for planetary entry.

In combination with the much higher ionization densities encountered in this experiment, the plasma electrical conductivity should be much higher than that encountered during planetary entry. This increased conductivity works to offset the reduction in velocity as compared with real planetary entry, for which holding all parameters constant would reduce generated energy by an order of magnitude. The exact degree to which the conductivity is enhanced requires additional plasma diagnostics and experiments, which due to the repeatable, computer-controlled nature of this experiment, can be left to future work. As a consequence of the artificial ionization mechanism and unknown electrical conductivity, the conditions of this experimental investigation are non-equilibrium and not directly computable by the methodologies presented as Contribution I in this thesis, requiring additional plasma diagnostics to correlate electrical conductivities.

Finally, though the laboratory discharge is ionized before passing through a shock wave, the result from the model's perspective is similar: a shocked, now subsonic, ionized gas is impinging on the surface, exactly as would occur during planetary entry.

As a note, though some photographs of the discharge initially appear as though the flow does not extend to the nozzle-wall, this is in part an artifact due to a lensing effect from the

curved glass wall as well as some plasma recombination due to collisions. This assertion is supported by the pressure measurements and flow calculations shown in Tables 3.2 and 3.4, in which the calculated exit area to throat area matched that measured for the nozzle in a machine shop-environment within approximately 2%. Furthermore, the plasma discharge appears slightly asymmetric in some photographs due to the off-axis gas exhaust location, with some turbulence induced by the sharp bends in the exhaust tubing. This design was necessary due to current facility capability limitations and could be addressed in the future by exhausting the gas into a ‘dump-tank’ before connection to the exhaust line, thereby limiting asymmetric pressure gradients and turbulence.

The subsequent sections describe the design, development, and execution of an experimental investigation of MHD energy generation during planetary entry using the supersonic plasma discharge test chamber capability described in this Chapter and the chosen test condition combinations.

**CHAPTER 4**  
**EXPERIMENTAL INVESTIGATION FOR MAGNETOHYDRODYNAMIC**  
**ENERGY GENERATION IN CONDITIONS AND CONFIGURATIONS**  
**RELEVANT TO PLANETARY ENTRY**

In previous work, a non-channel type MHD energy generator concept was tested in an artificially ionized flow. [51][8] A supersonic flow was achieved through a converging-diverging nozzle, which when supplied with a vacuum pump system capable of achieving the proper pressure ratio and flow rate, produced a low-density supersonic gas flow with a freestream Mach number of approximately 2. This supersonic flow was then ionized within a cylindrical microwave resonance cavity operating around 2.4GHz. The result was a free-flowing supersonic plasma in which a representative MHD energy generator model was placed. In this work, a measurable extracted MHD generated current was observed, indicating an initial positive result. However, this dataset was limited, and as presented did not fully characterize the plasma, vary the test conditions, or vary the model design.

Thus, there is a need for an experimental design that investigates MHD energy generation in both conditions and configurations relevant to planetary entry systems over a variety of test conditions and model geometries for which the plasma and models are well-characterized. This experimental design and initial dataset will allow for verification of the parametric dependence of the energy generated on various design parameters as well as extension to flight conditions relevant to planetary entry.

As stated previously, the goal of this experimental campaign is to demonstrate and characterize MHD energy generation in configurations and conditions relevant to planetary entry. The supersonic plasma wind tunnel facility described in Contribution II is used to conduct the experiment. In contrast to the previous experiment, multiple MHD generator model design configurations are developed and tested, through variation of magnet orienta-

tion and location relative to the electrodes and each other. Computer-aided manufacturing techniques are employed in order to improve repeatability between models, and multiple trials (N=3) of each design are tested in order to form a more complete data-set. Furthermore, voltage potentials across MHD generator model electrodes with and without a resistive load are tested, enabling estimation of the plasma electrical conductivity. The presented experiment furthers the ultimate goal of extending experimental results to expected performance at actual atmospheric entry flight conditions.

#### **4.1 Research Questions**

In order to achieve these goals, this experimental investigation aims to answer the following two research questions:

**Research Question 1:** *Can electrical energy be extracted during planetary entry using a non-flow through MHD energy generator?.*

**Research Question 2:** *If so, how does such an MHD energy generator perform for various design geometries and test conditions?*

#### **4.2 MHD Energy Generator Model Development**

The goal of this model development process is to design and manufacture MHD energy generator models representative of a blunt-body atmospheric entry vehicle, presented in the sections that follow.

##### 4.2.1 MHD Model Design: Theory

The principal design guideline is to avoid flow-through plasma channel designs such as those shown in section 1.6. The design presented in this thesis achieves this goal through a cylindrical dielectric ceramic body with embedded permanent magnets located just behind the model forebody, shown in sketch format as Figure 4.1. Two sheet metal electrodes are

affixed and conformed to the cylindrical side of the model body and oriented such that they take advantage of the electric field induced by the applied magnetic field and supersonic flowing plasma current. When a resistive load is placed across these two electrodes, a current flow is induced, and electrical energy is extracted via MHD energy generation.

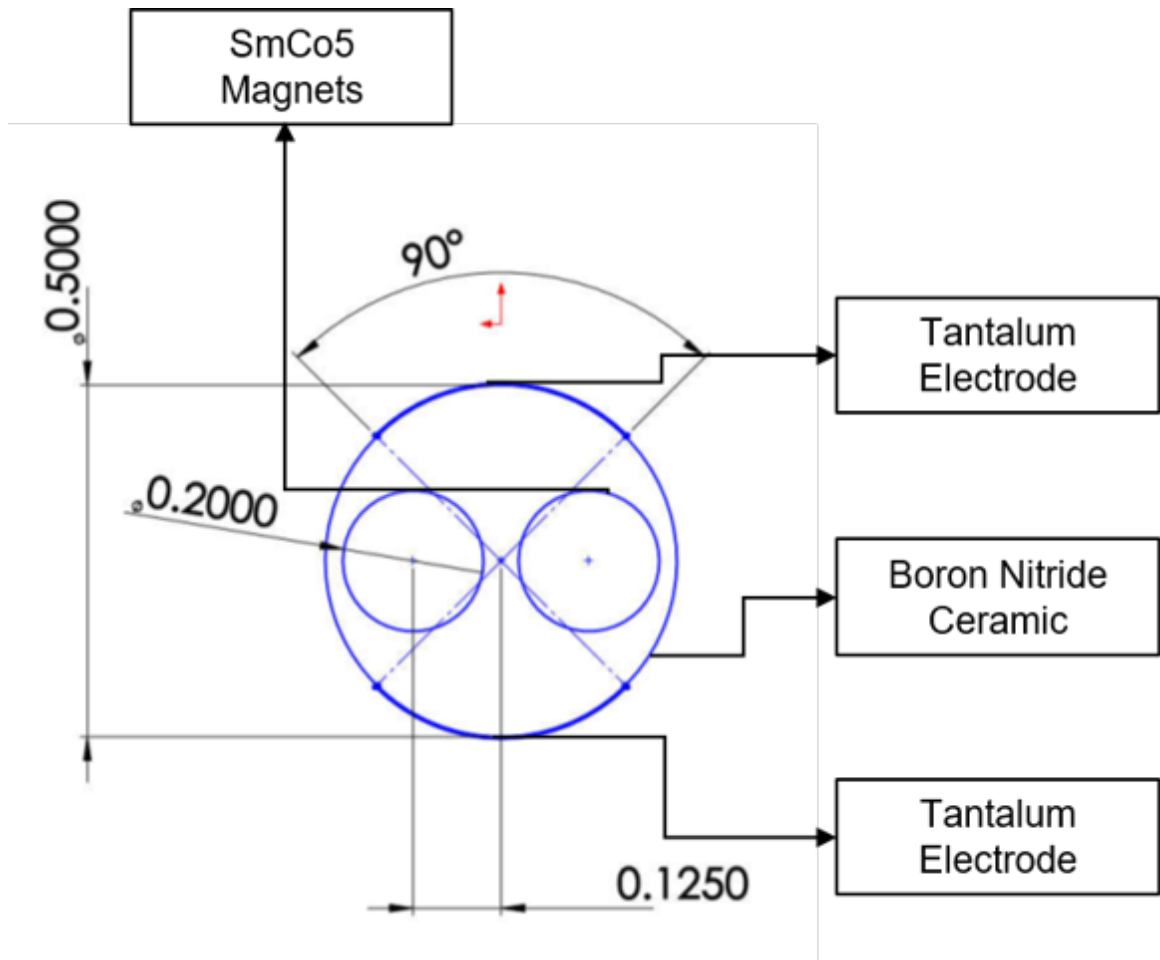


Figure 4.1: Representative blunt-body MHD energy generator model design, dimensions in inches (front view). Cylindrical ceramic model body with rare-earth permanent magnets and 90-degree arc length sheet metal electrodes.

The two embedded permanent magnets have their magnetic dipole moments (N-S) vectors oriented normal to the model forebody surface depicted in Figure 4.1. However, there are two possible orientations of the dipole moments relative to one another, illustrated as Figure 4.2.

The resulting combined magnetic field lines are distinct, with the key feature being the

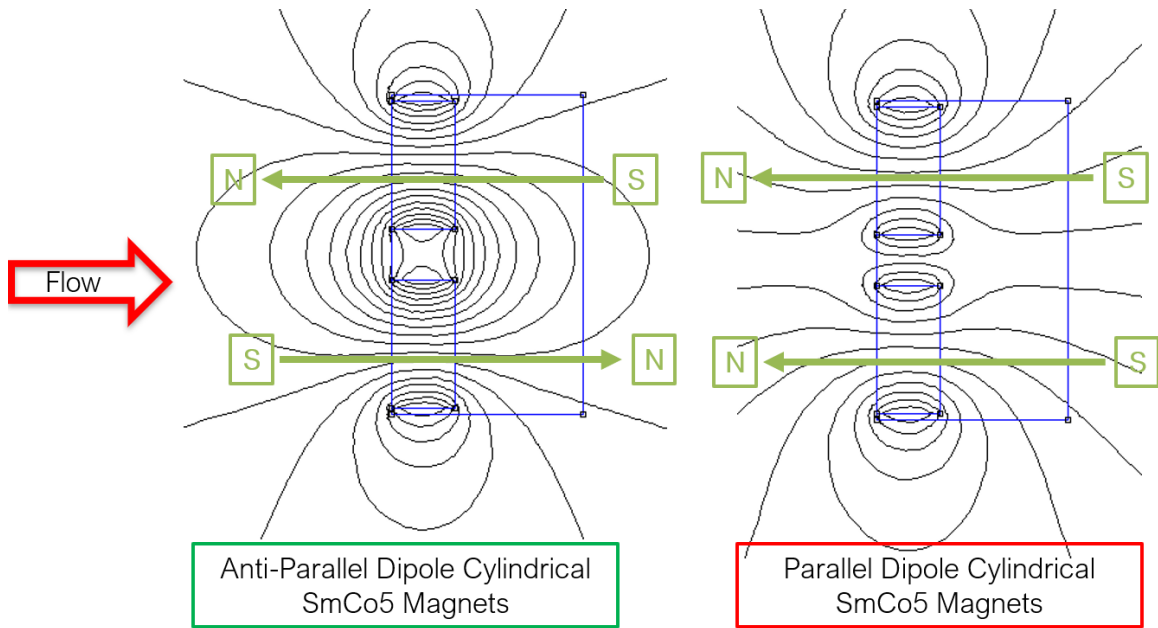


Figure 4.2: Finite element simulation results of parallel (left) and Anti-parallel (right) magnetic dipole orientations. Top view.

orientation of the field lines relative to the vehicle forebody and plasma discharge flow. In section 1.5.2, the magnetic force described by equation 1.8 states that charged particles moving through a magnetic field experience a force with magnitude and direction determined by the cross-product of the particle velocity and magnetic field vector. Referencing the field lines shown in Figure 4.2, it is clear that the cross-product of flow velocity and magnetic field orientation differs significantly between the parallel and anti-parallel dipole orientations. Specifically, the cross product of the magnetic field and plasma flow (current) direction should be higher for the anti-parallel dipole orientation due to the mutually perpendicular vector directions.

In accordance with the generalized Ohm's law from the MHD equations, equation 1.20, there should therefore be an induced electric field in a direction mutually perpendicular to both the magnetic field and plasma flow directions. For the model geometry under consideration, this induced electric field vector is expected to exist a plane coincident with the vehicle forebody and perpendicular to the axis connecting the two magnets within that plane. The electrodes shown in Figure 4.1 are aligned with this electric field to facilitate

maximum MHD voltage potential for current extraction.

#### 4.2.2 MHD Model Design: Sizing

The MHD model dimensions are sized beginning with the model diameter. The model cross-section shown in Figure 4.1 is circular, and must be large enough to reasonably accommodate two permanent magnets a model mounting rod attachment point for suspension in the test-section. Larger model diameters allow for inclusion of more powerful magnets and a larger model forebody surface area,  $A_{model} = \frac{\pi}{4}d_{model}^2$ , which serves magnetohydrodynamic interaction surface area,  $A$ , as described in section 1.6 by equation 1.36.

However, there is a maximum size constraint on the model diameter, which must not be so large as to completely obstruct the test-section flow by creating a ‘second throat’ choke point in the annular area between the nozzle walls and model. Based on the previously presented test-section characterization data and selected model position of  $L_{test} = 2.000$  *in* from the nozzle throat, the computed nozzle wall inner-diameter is  $d_{nozzle} = 1.091$  *in*. Applying a minimum annular area to nozzle throat area constraint of 2.0, the largest possible model diameter is approximately  $d_{model} = 0.546$  *in*. As a result, a final MHD model diameter of  $d_{model} = 0.500$  *in* is selected. Computed geometric values based on this chosen model diameter for the nozzle dimensions in Table 3.3 are shown below as Table 4.1.

Table 4.1: Table of nozzle shock location dimensions

Parameter	Value	Units
$L_{test}$	2.000	<i>in</i>
$d_{nozzle}$	1.091	<i>in</i>
$d_{model}$	0.500	<i>in</i>
$A_{throat}$	0.351	<i>in</i> <sup>2</sup>
$A_{annular}$	0.739	<i>in</i> <sup>2</sup>
$\frac{A_{annular}}{A_{throat}}$	2.109	—

The electrodes for the MHD energy generator model prototype are metal sheet electrodes conformed to the model outer-diameter. The model forebody is divided into 90-degree arc quadrants, as shown in Figure 4.1. Each electrode is sized to be close to this 90-degree arc length while remaining entirely within the quadrant. For the selected model diameter of 0.5 *in*, this 90-degree arc length is approximately 0.393 *in*. Thus, a metal sheet electrode length of 3/8" or 0.375 *in* is selected. For manufacturing consistency, a square electrode sheet cutout geometry is chosen, which drives the electrode height and model thickness to 3/8" as well.

The permanent magnets are embedded beneath the MHD model forebody surface. From electromagnetism, it is known that the magnetic field strength scales as  $\frac{1}{R^3}$ , where  $R$  is the radial distance from the dipole. For this reason, it is desirable to embed the magnets as close to the MHD forebody surface as possible while leaving sufficient ceramic material for structural integrity and electrical and thermal insulation. Based on these guidelines, a forebody surface to magnet offset of 0.40 *in* is chosen, illustrated by Figure 4.3. Magnets are inserted from the back of the model to facilitate consistent placement and a smooth, unblemished forebody surface.

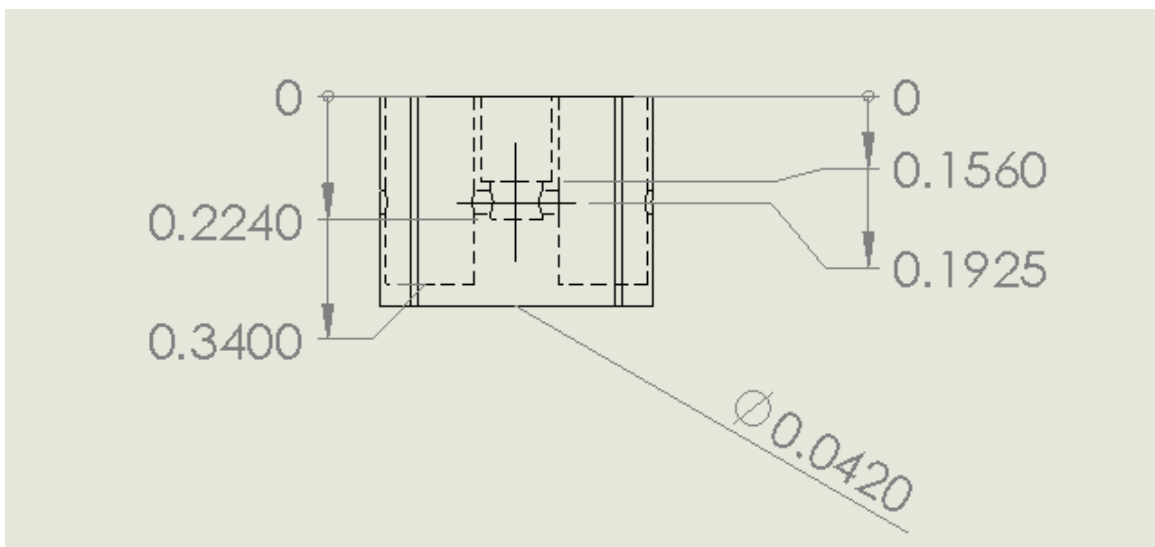


Figure 4.3: Side view of MHD energy generator model design, showing dimensions in inches and magnet offset from forebody surface

Cylindrical permanent magnet geometry with axis-aligned magnetic dipole directions are chosen. The diameter of each permanent magnet is set such that both magnets can be reasonably accommodated within the MHD energy generator model prototype diameter while leaving room for a ceramic mounting rod attachment point for suspension in the test-section. For structural integrity, a 1/8" diameter mounting rod is chosen, which attaches at the center of the model. Based on the required mount hole size, and leaving sufficient material between all three holes, the maximum magnet diameter that can be accommodated is 0.161 *in.* From this constraint, 0.157 *in* (4 *mm*) diameter cylindrical permanent magnets are chosen. A drawing of the two magnet holes and model mount center attachment point hole is shown as Figure 4.4. The magnet length is chosen such that the magnets, when placed within the model as shown in Figure 4.3 do not intersect the blind hole drilled through the model for the electrode wires, which decouples the magnet and electrode wire insertion process during manufacturing for consistency. From this requirement, the maximum feasible magnet length is 3 *mm*, or approximately 0.118 *in.* Final magnet dimensions are therefore a 4 *mm* diameter x 3 *mm* length cylindrical geometry with an axis aligned magnetic dipole moment. A diagram of the chosen magnets is given as Figure 4.5.

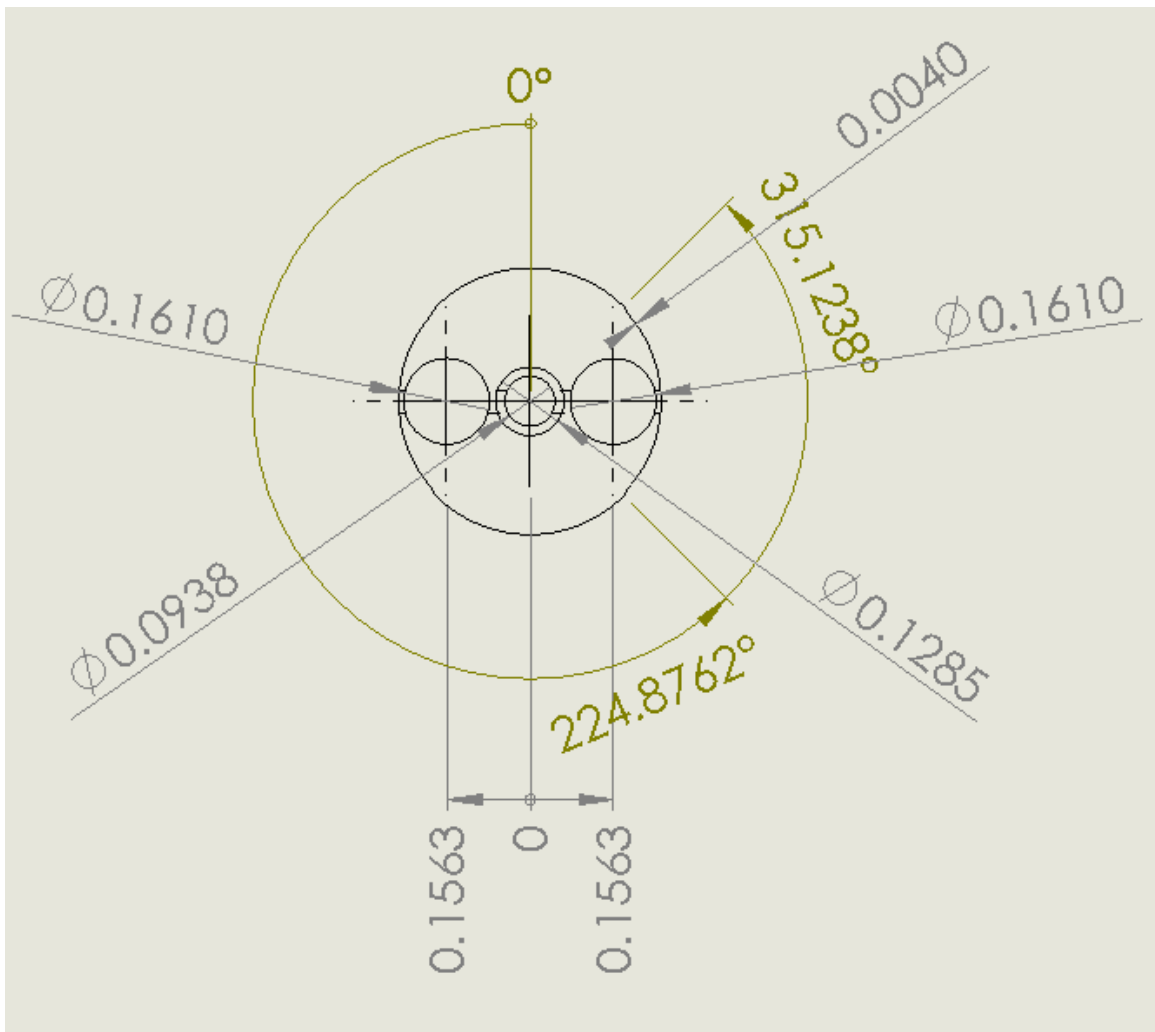


Figure 4.4: Back view of MHD energy generator model design, showing dimensions in inches and locations of the magnet and mounting holes

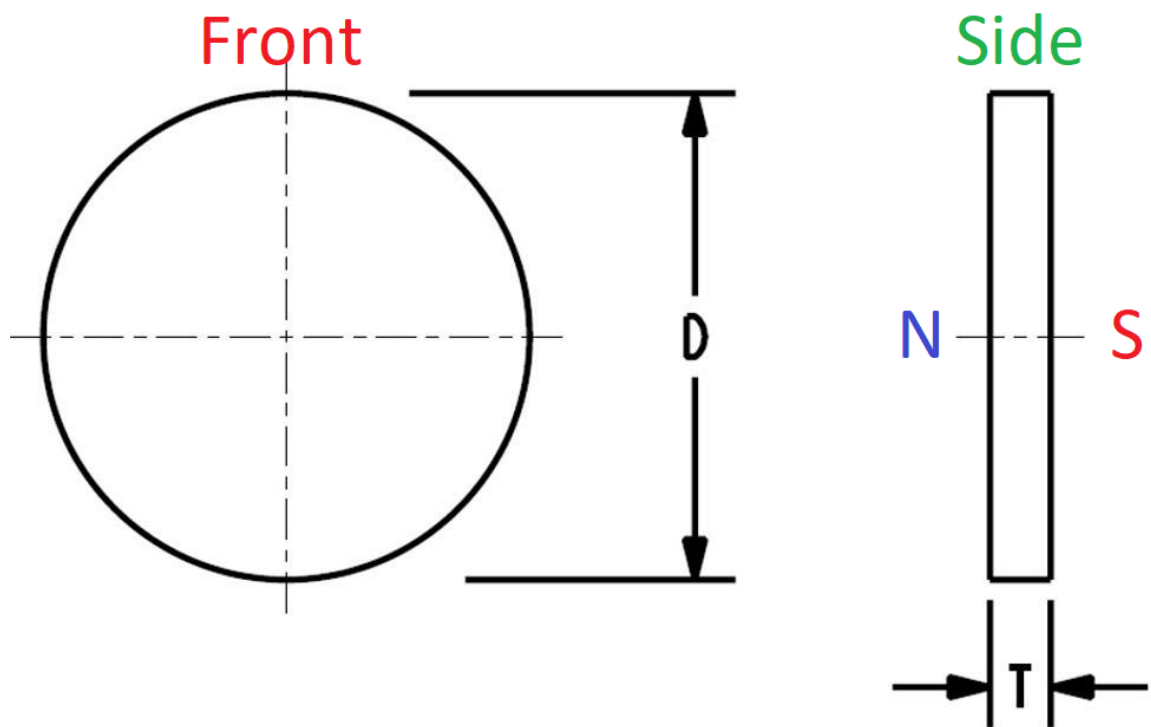


Figure 4.5: Selected model permanent magnet geometry front(left) and side(right views). Diameter dimension  $D = 4 \text{ mm}$  ( $0.158 \text{ in}$ ), thickness dimension  $T = 3 \text{ mm}$  ( $0.118 \text{ in}$ ). Magnetic dipole moment aligned with the cylinder axis.

### 4.2.3 MHD Model Design: Design Variations and Final Drawings

Additional variations of the initial MHD energy generator model design geometry are possible by changing the orientation of the magnets with respect to the electrodes. This orientation is characterized by an angle in degrees, and the three variations chosen are 90(original), 45, and 0 degrees. Final drawings for all three model variations are included as Figures 4.6 ,4.7 and 4.8 for the 90, 45 and 0-degree models respectively.

90 Degree Electrode Orientation Relative to Magnet Axis

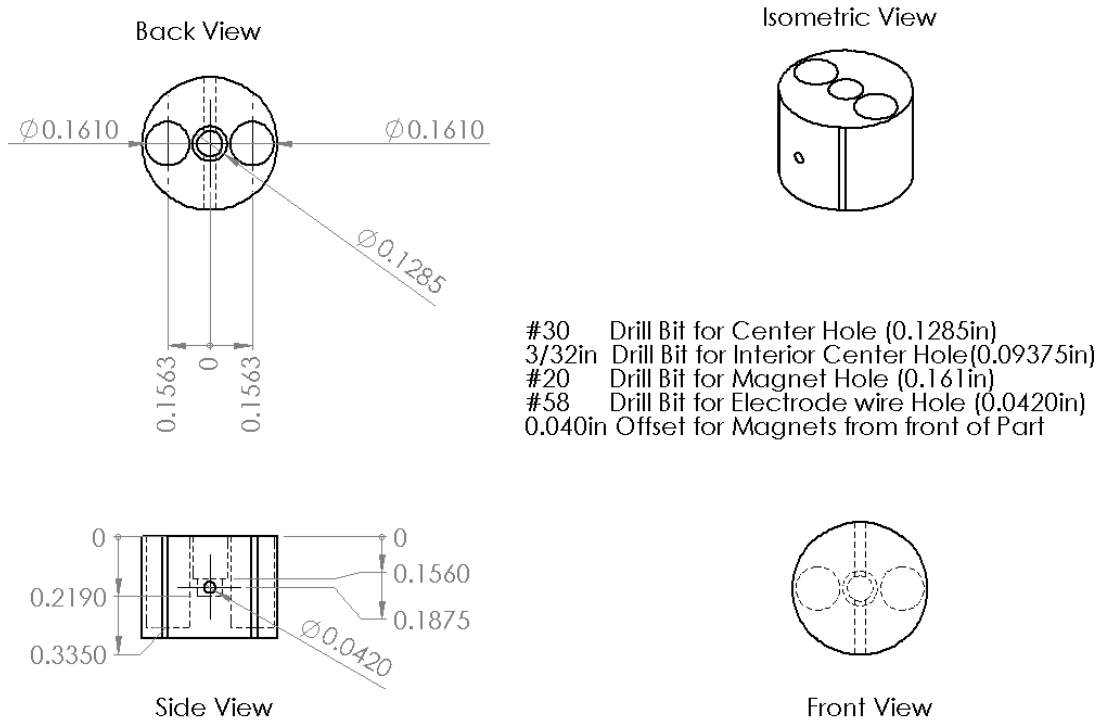


Figure 4.6: 90 Degree final MHD energy generator model drawing for manufacturing. All dimensions in inches.

45 Degree Electrode Orientation Relative to Magnet Axis

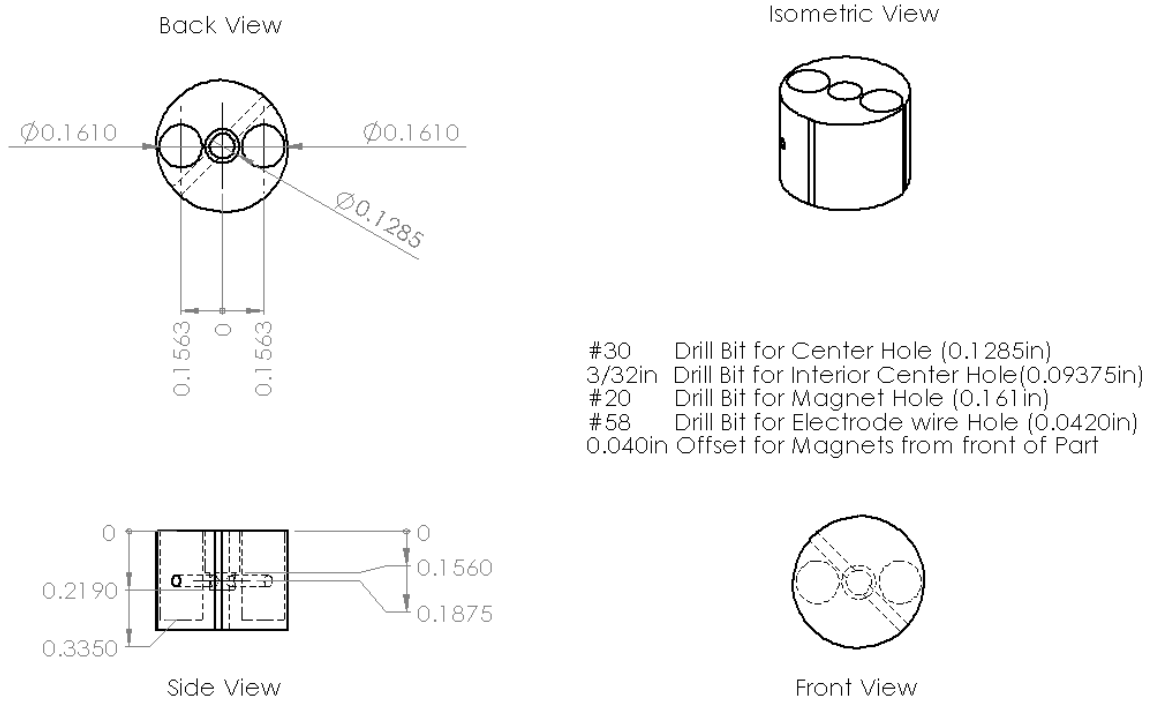


Figure 4.7: 45 Degree final MHD energy generator model drawing for manufacturing. All dimensions in inches.

0 Degree Electrode Orientation Relative to Magnet Axis

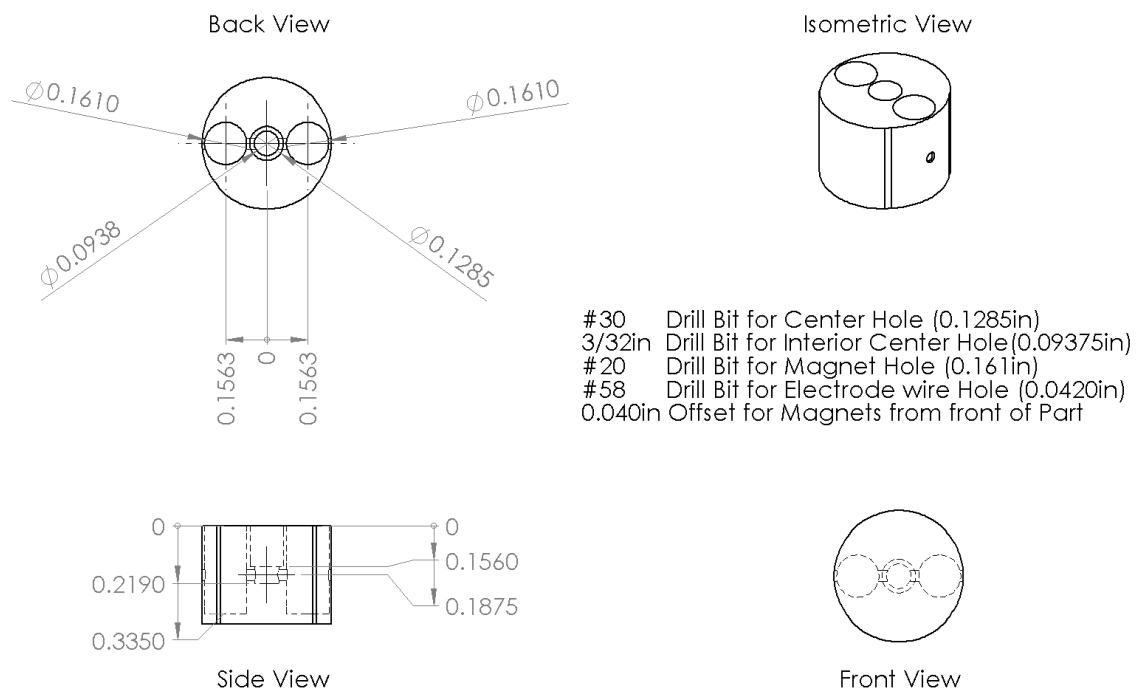


Figure 4.8: 0 Degree final MHD energy generator model drawing for manufacturing. All dimensions in inches.

#### 4.2.4 MHD Model Manufacturing: Materials and Process

The main MHD model body must be constructed from a machinable, high temperature safe, dielectric material. Sintered Boron-Nitride machinable ceramic stock is selected, which is soft enough to be machined using conventional mill tooling while remaining tolerant to high temperatures and an excellent dielectric. All models are machined on a computer numerical-control (CNC) 3 axis mill from a 0.375 *in* ceramic plate, as shown in Figure 4.9. The computer-aided manufacturing technique results in dimensional accuracy of +/- 0.0001 *in*.

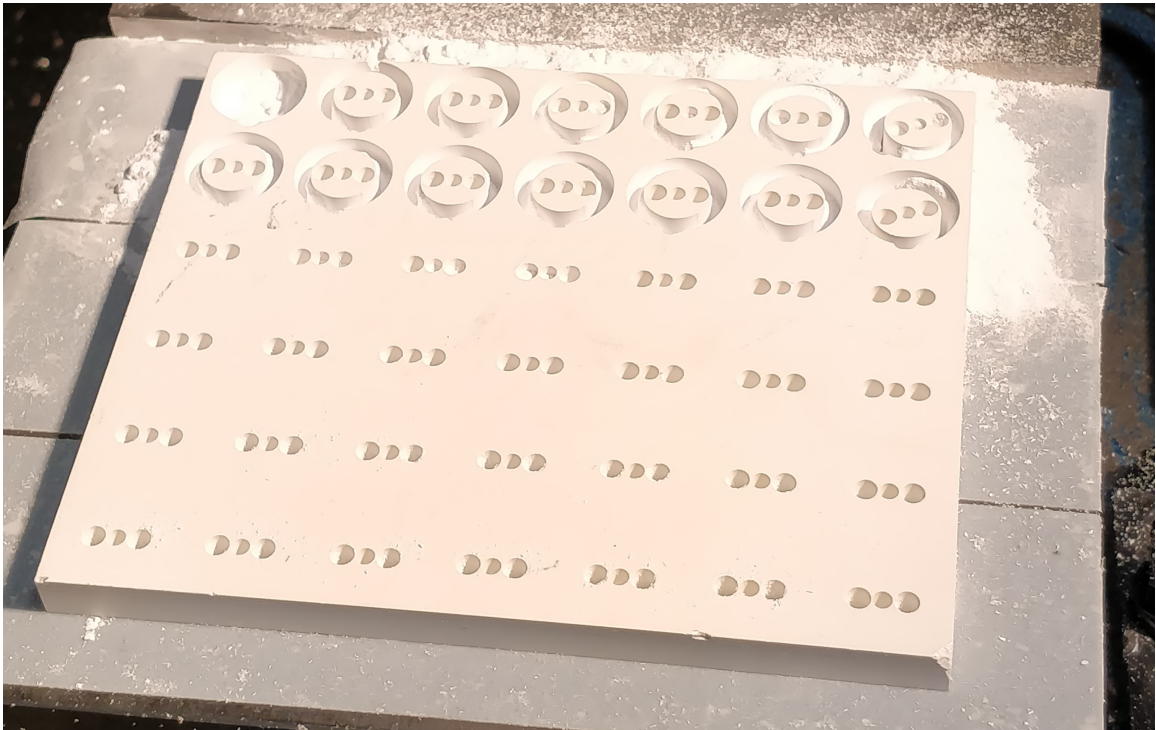


Figure 4.9: CNC milling process for MHD energy generator models. Material is 0.375 *in* thick Boron-Nitride ceramic plate.

In each model, two 0.004 *in* slots for the electrodes corresponding to a 90-degree arc lengths is milled, and a 0.0420 *in* blind hole is drilled through the center of this slot and the MHD model itself for the electrode signal wires to pass through. An example photograph of an MHD energy generator model after final machining is shown as Figure 4.10

Electrode material must be vacuum safe, tolerant of high temperatures, corrosion resis-

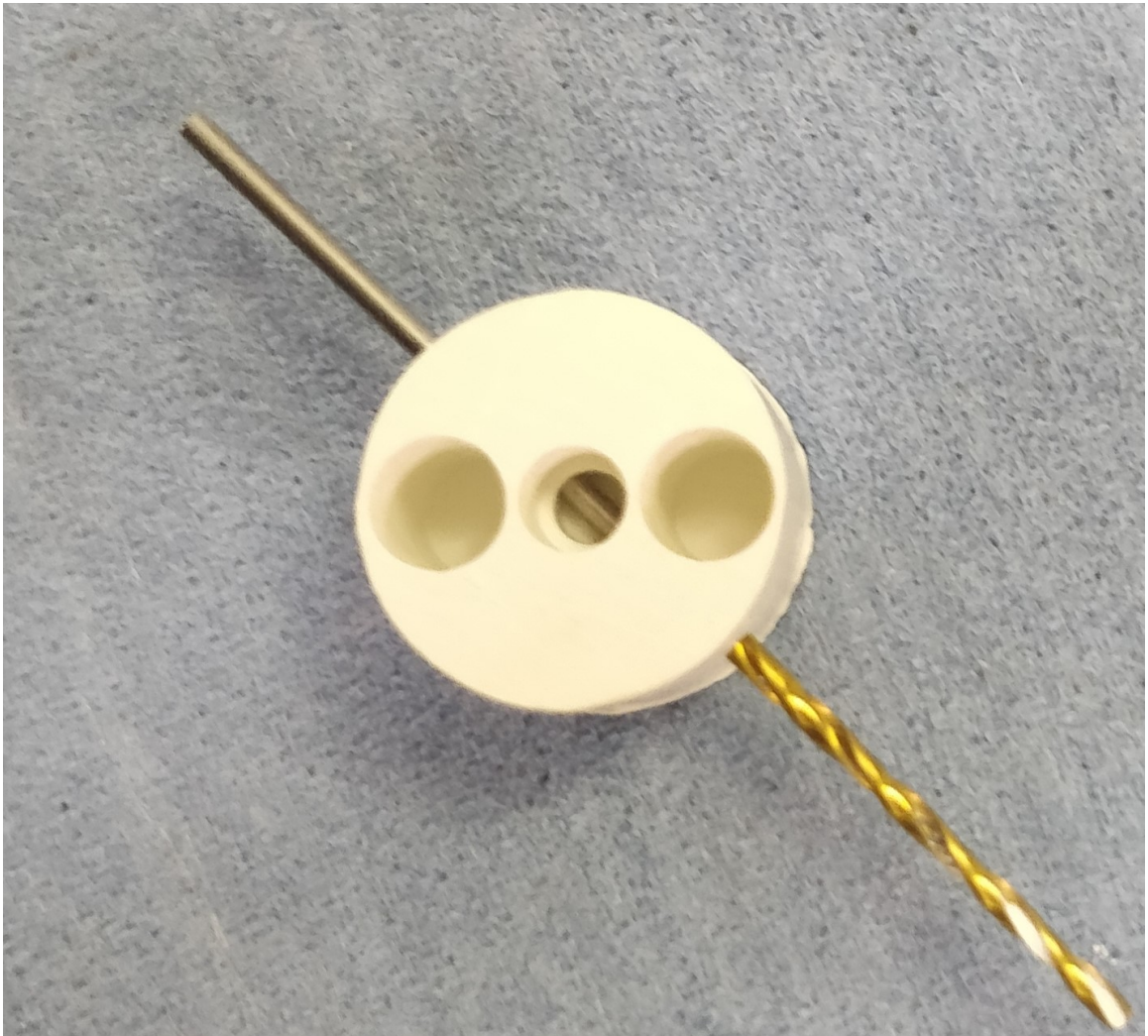


Figure 4.10: Example MHD model after machining with hole for electrode wire. 45 Degree variation, as shown in Figure 4.7, back view.

tant, and flexible enough to conform to the cylindrical model body. Tantalum foil is chosen for its high melting temperature, corrosion resistance, and spot-weld compatibility with high-temperature Nickel-Chromium alloy lead wire.

Electrodes were cut from a 0.002 *in* thick sheet of 99.9% pure Tantalum foil using a water-jet process. The foil was wrapped and sandwiched between two 1/8" thick aluminum plates, which served as structural support for cutting in the water-jet machine, shown as Figure 4.11. The water-jet process allowed for enhanced repeatability and speed of manufacturing, leading to the production of over 90 electrodes with average 0.001 *in* variance from the design dimensions of 0.375 *in* x 0.375 *in*.



Figure 4.11: Tantalum foil electrode water-jet process. Design dimensions of 0.375 *in* x 0.375 *in* manufactured to a tolerance of 0.001 *in*

The square electrodes were each spot-welded to 0.010 *in* diameter solid core Nickel-Chromium 80/20 alloy wire. The wire material and resulting electrode junction technique were both chosen for their tolerance to the high temperatures of the supersonic plasma discharge. A small sparkle jewelry type-welder was used, and the spot weld was repeated

multiple times to ensure good electrical contact and structural integrity. The thin Nickel-Chromium wire is placed between the outer electrode surface and ceramic model body, leaving only the Tantalum foil directly exposed to the flowing plasma. A photograph of this spot-welding process is shown as Figure 4.12.

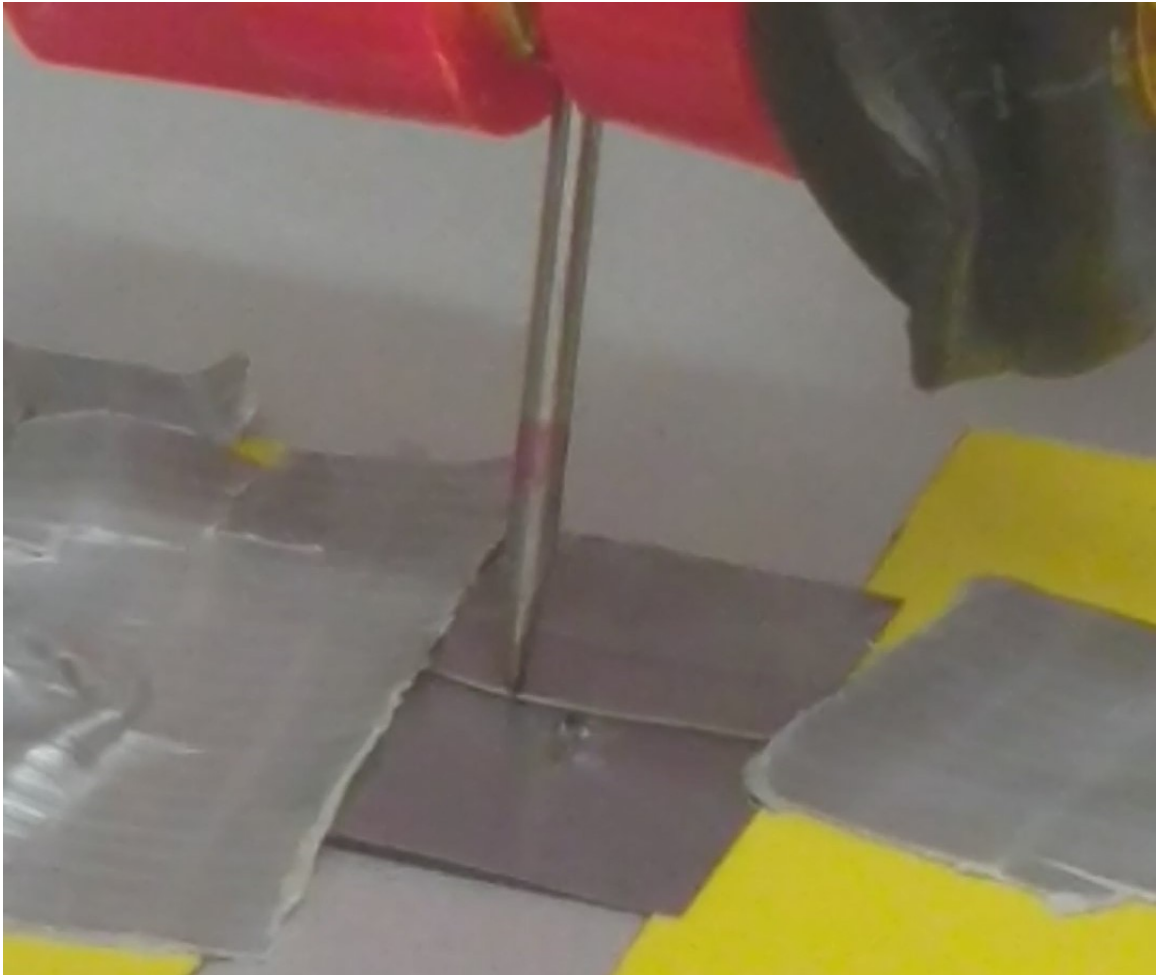


Figure 4.12: Tantalum foil electrode spot-welding to 0.010 *in* diameter Nickel-Chromium wire.

The supersonic plasma discharge has the potential to significantly heat the MHD energy generator model, and the permanent magnets embedded within it. When the magnet approaches the Curie temperature of the material, magnetization is inhibited or even permanently lost. For this reason, permanent magnet materials compatible with high temperatures are necessary. Samarium cobalt ( $SmCo_5$ ) rare earth magnets are chosen in this design.

Samarium cobalt magnets rival the strength of neodymium permanent magnets, while able to operate at high temperatures. Samarium Cobalt grade 18 magnets are sourced, which are temperature stabilized up to  $250\text{ }^{\circ}\text{C}$ , enabling longer continuous plasma discharge testing times for each model without degradation of magnetic field strength.

#### 4.2.5 MHD Model Manufacturing: Assembly

After manufacturing, the MHD model components, which include: cylindrical ceramic model body, square sheet metal electrodes, cylindrical permanent magnets, and cylindrical ceramic mount and support tubes are assembled. Model assembly is set in high-temperature OMEGA ceramic paste, and fully cured at  $85\text{ }^{\circ}\text{C}$  before testing. A complete set of MHD model components is shown as Figure 4.13.

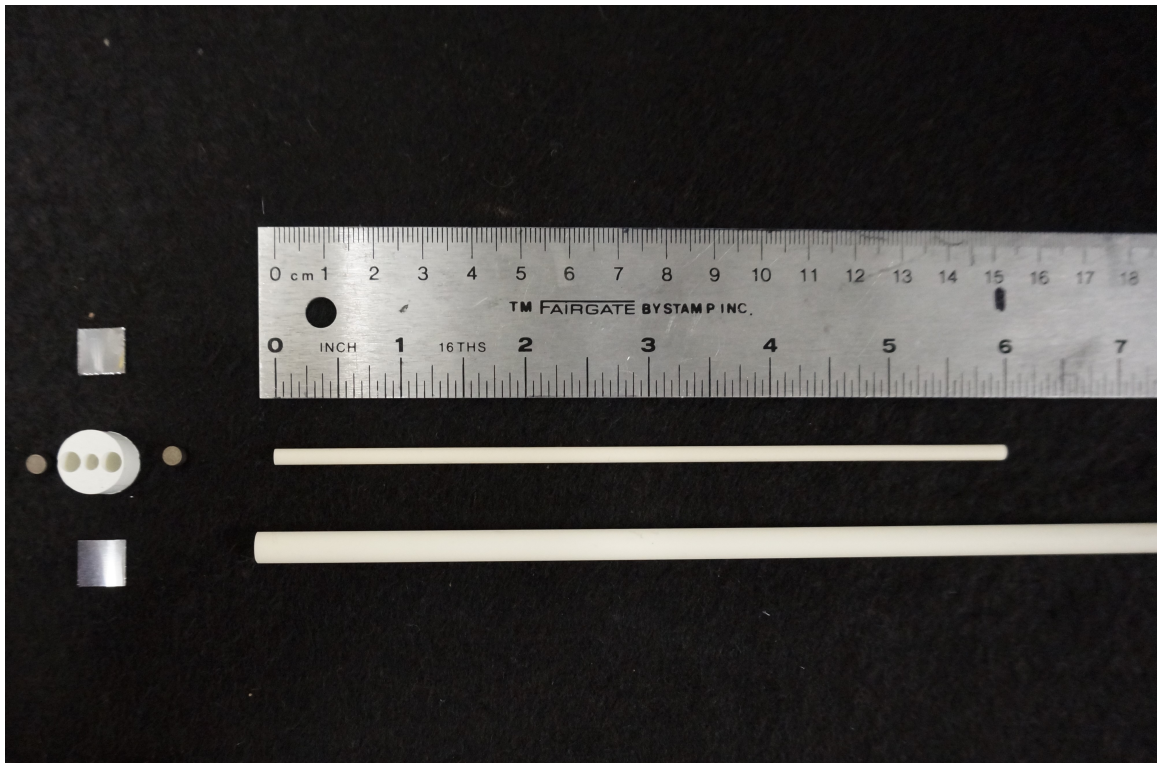


Figure 4.13: MHD model components. MHD model body, electrodes, and permanent magnets shown at left, and 6 in length 1/8 in diameter double-bore ceramic model mount tube shown at right. Also pictured is 1/4" model mount structural support tube, right.

First, the permanent magnets are inserted into the model body from the rear, with mag-

netic dipoles aligned either parallel or anti-parallel. Once inserted and set, magnets are cemented with high-temperature ceramic paste. In addition, control model variations with no magnets are assembled as well.

Second, after magnet insertion, the Tantalum foil electrodes with spot-welded Nickel-Chromium wire leads are threaded through the electrode wire holes on the side of the model and the model mount support point in the center of the model. The model mount tube is a 1/8" (0.125 *in*) diameter double-bored alumina ceramic insulator tube with 0.020 *in* diameter holes for wires. Each electrode wire is threaded through a separate hole in the tube, and the tube is inserted into the model attachment point with the wires under tension, ensuring that electrode wires are not shorted within the model. The Tantalum foil electrodes and the model mount tube are then cemented to the model with ceramic paste. The resulting model sub-assemblies, shown as Figure 4.14, are then oven-cured at 85 degrees Celsius.

In order to connect the MHD energy generator model electrodes to the test section electrical feedthroughs, the solid 0.010 *in* Nickel-Chromium wire used is soldered to 24-*AWG* vacuum safe Teflon insulated hookup wire at the 6 *in* model mount tube exit. This design decision dramatically reduces the electrode lead resistance, while enhancing model placement flexibility and wire length, as the thin, high-temperature tolerant Nickel-Chromium wire has a resistance of nearly 1  $\Omega$  per linear inch. After soldering, the entire model sub-assembly is inserted into a 1/4" outer-diameter, 1/8" inner-diameter alumina ceramic model support tube for rigidity, length for proper test-section positioning, and mating to the test-section model mount assembly. An example of this soldered connection and a completed MHD model assembly is shown as Figures 4.15 and 4.16, respectively.

In addition to the primary MHD model assemblies, MHD model bodies without electrodes and an embedded thermocouple junction are assembled for thermal response characterization, shown as Figure 4.17. 24-*AWG* solid-core Type-K thermocouple wire is passed through the double bore ceramic insulator model mount tubes, and spot welded at the termination point. This junction is then coated in ceramic paste and inserted into the main



Figure 4.14: MHD model sub-assemblies on a plate for oven-curing.



Figure 4.15: MHD model electrode wire solder extension to sliver-coated, Teflon insulated 24-AWG hookup wire for reduced lead resistance and model placement flexibility.

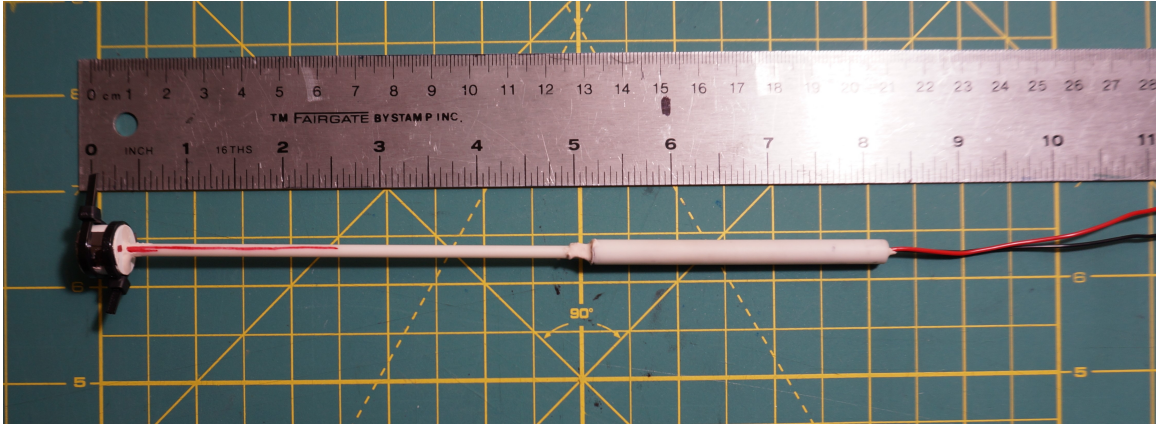


Figure 4.16: Example fully-assembled MHD model. 90-degree model type, parallel magnetic dipole alignment.

ceramic MHD model body without electrodes or magnets. All voids are filled and coated with ceramic paste for electrical insulation from the supersonic plasma discharge.

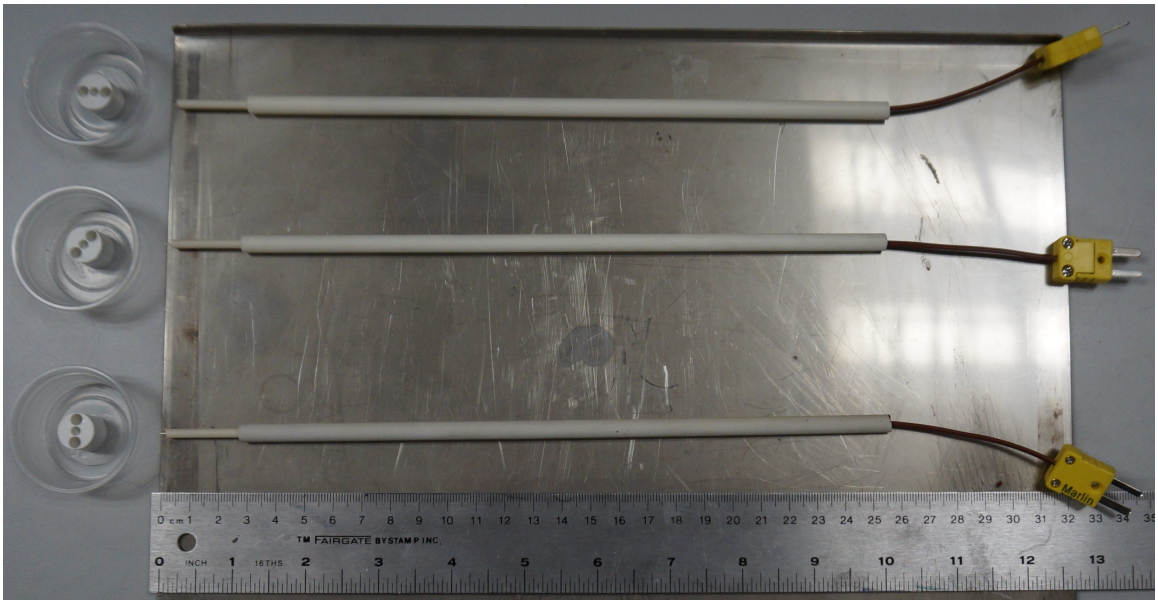


Figure 4.17: Type-K spot-welded thermocouple junctions and 90, 45, and 0-degree MHD model variations sub-assemblies. Assembled and cemented with ceramic paste to facilitate MHD model thermal response characterization

This model design variation provides a reference inert model with similar thermal mass to the primary MHD models. The primary purpose is to enable empirical determination of appropriate supersonic plasma discharge pulse times to keep the model temperature below the maximum recommended Samarium Cobalt magnet operating temperature of  $250\text{ }^{\circ}\text{C}$ .

A secondary benefit is an inert model with no electrodes or magnets of similar dimensions for plasma flow investigation without additional potential interactions from flowing MHD generated current.

#### 4.2.6 MHD Model Manufacturing: Completed Models

The manufacturing and assembly processes described in sections 4.2.4 and 4.2.5 respectively are repeated for a number of MHD model variations, documented in Table 4.2 .

Table 4.2: Completed MHD Energy Generator Model Inventory

Ceramic Model Body Angle	Relative Magnet Orientation	Number Manufactured
90 Degrees	Parallel Dipoles	3
90 Degrees	Anti-Parallel Dipoles	3
90 Degrees	No Magnets, Control	1
0 Degrees	Parallel Dipoles	3
0 Degrees	Anti-Parallel Dipoles	3
0 Degrees	No Magnets, Control	1
45 Degrees	Parallel Dipoles	1
45 Degrees	Anti-Parallel Dipoles	1
45 Degrees	No Magnets, Control	1

For this initial experimental investigation, full-sets ( $N = 3$ ) of only the 90 degree and 0 degree MHD model body design variations are manufactured, including two controls, for a total of 14 models. Of these, five are selected for testing (each possible variation and one control), with the others available for redundancy in case of premature failure. These 14 assembled models are securely stored in a humidity controlled container in preparation for testing, shown as Figure 4.18, as the Boron-Nitride ceramic material has a non-zero porosity of approximately 7%.

As discussed in section 4.2.5, thermocouple embedded (thermal response) MHD models are constructed from the 90, 45, and 0-degree ceramic model bodies respectively, shown as Figure 4.19.



Figure 4.18: Full set of assembled 0 degree and 90 degree MHD energy generator model variations.  $N = 3$  each for versions with embedded magnets and two control models without magnets. Total of 14 assembled models.

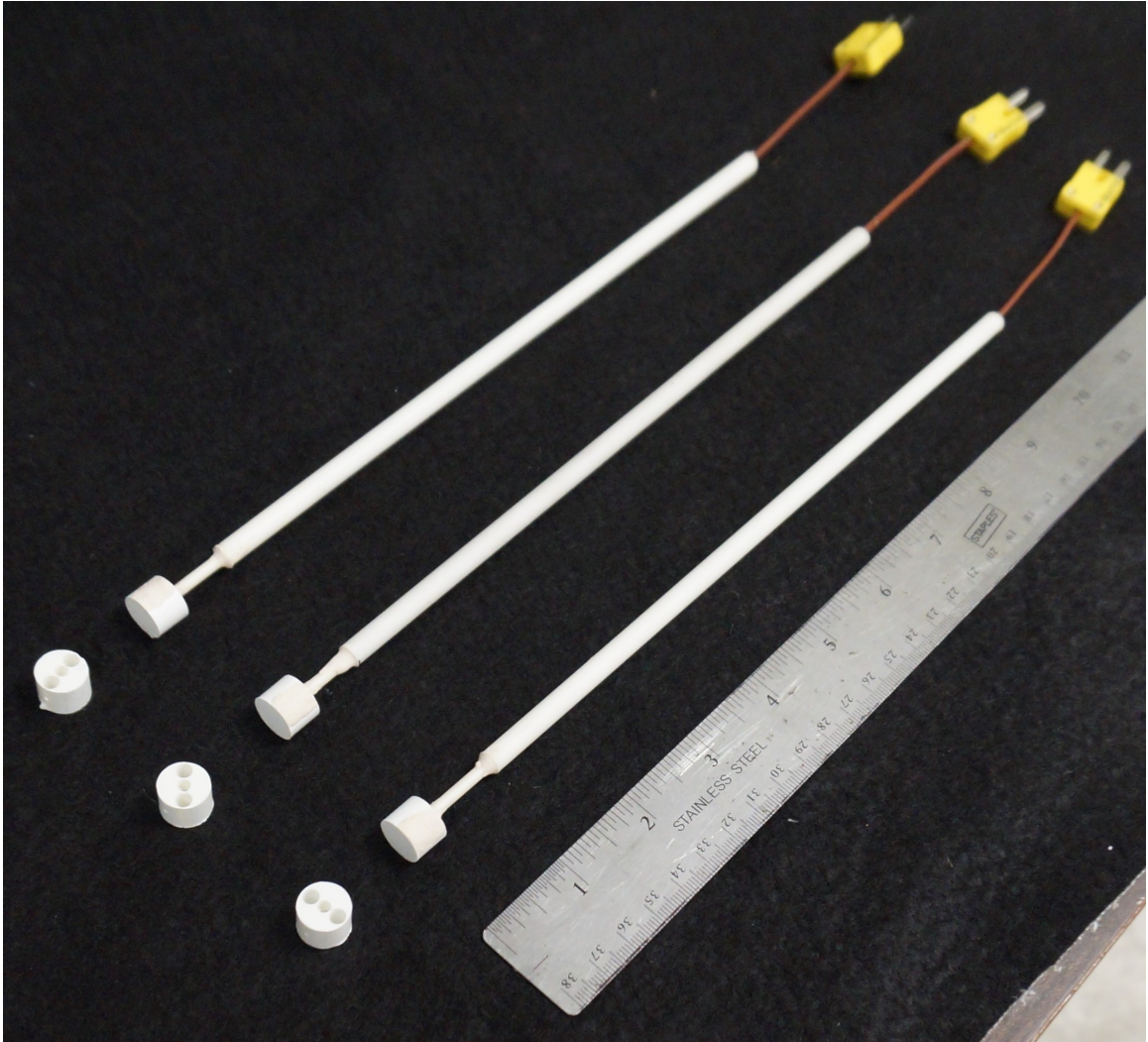


Figure 4.19: Thermocouple embedded inert MHD model bodies for thermal response characterization. One of each of 90, 45, and 0-degree model variations respectively.

### 4.3 Experimental Design

As stated previously, the goal of this experimental investigation is an assessment of MHD energy generation in conditions and configurations relevant to planetary entry. Specifically, the aim is to answer the research questions stated in section 4.1. These questions are addressed by an experimental design in which the prototype MHD energy generator models described in section 4.2 are placed in the supersonic plasma discharge chamber discussed in Chapter 3 and tested for MHD energy extraction. This experimental design is shown in schematic form as Figure 4.20.

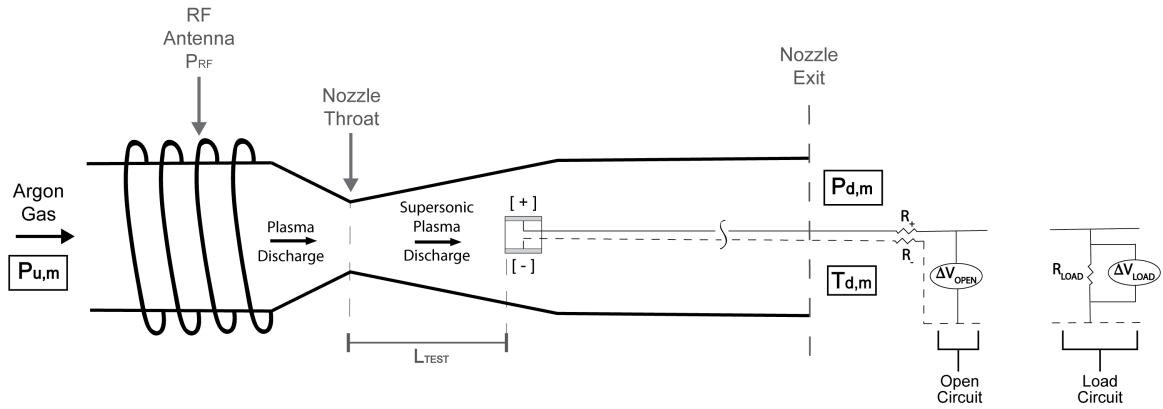


Figure 4.20: MHD energy generation for planetary entry experimental schematic.

#### 4.3.1 Experimental Design: Theory and Measurement Objectives

As mentioned in section 1.6, MHD power output for a Faraday type MHD energy generator, given by equation 1.33, is parametrically dependent on the load factor,  $K$ , electrical conductivity,  $\sigma_e$ , applied magnetic field,  $B$ , and plasma flow velocity,  $u$ , multiplied by the product of interaction area,  $A$ , and generator interaction length  $L$ . For a non-flow through type MHD energy generator model design in this thesis, the same performance scaling equation law is shown to apply in [43], applied as equation 4.1

$$P_{MHD,model} = \sigma_e u^2 B^2 K(1 - K) A_{model} L_{model} \quad (4.1)$$

Because the MHD energy generator model prototype designs discussed in section 4.2 have permanent magnets and fixed dimensions, applied magnetic field  $B$ , interaction area  $A = \frac{\pi}{4}d_{model}^2$ , and generator interaction length  $L = L_{Model}$  can be said to be fixed parameters for a given MHD model.

The plasma flow velocity,  $u$ , and electrical conductivity,  $\sigma_e$ , are expected to be functions of the test conditions: uniquely specified by combinations of the test gas input mass flow rate and RF generator output power, as described in section 3.3.

The load factor,  $K$ , is determined by the ratio of voltage potential across the generator electrodes with and without an electrical load, respectively. Using a purely resistive load, with resistance  $R_{Load}$ , and referencing the experimental schematic in Figure 4.20, two measurements are collected at each test condition: the voltage potential across the load,  $\Delta V_{Load}$ , and the open circuit voltage potential without the load,  $\Delta V_{Open}$ .

From these two measurements two calculations are made. First, the voltage potential across the purely resistive load can be directly converted to a measurement of the extracted MHD power by application of Ohm's law, shown as equation 4.2

$$P_{MHD,Exp} = \frac{\Delta V_{Load}^2}{R_{Load}} \quad (4.2)$$

Second, the load factor  $K$  is experimentally determined by as shown by equation 4.3

$$K_{MHD,Exp} = \frac{\Delta V_{Load}}{\Delta V_{Open}} \quad (4.3)$$

For the exploratory experimental investigation presented in this thesis, measured values of  $\Delta V_{Load}$ ,  $\Delta V_{Open}$  and calculated values of  $P_{MHD}$  and  $K_{MHD}$  are presented, with additional analysis of the exact model magnetic field values and extrapolation of experimental results to relevant flight conditions left to future work.

### 4.3.2 Experimental Design: Test Matrix and Methodology

As mentioned in section 3.4, bounding case test conditions for input test gas mass flow rate and plasma discharge power are selected, for a total of four possible unique test condition combinations. The specific conditions are shown as Table 4.3.

Table 4.3: MHD Energy Generation Experiment Plasma Discharge Test Conditions

Test Condition Label <i>Condition # (Value, Value)</i>	MFC Set Point (V)	Forward RF Power, $P_{RF}$ (W)
Condition 1 (Low , Low)	3	400
Condition 2 (High, Low)	5	400
Condition 3 (Low , High)	3	800
Condition 4 (High, High)	5	800

The MHD model geometries selected are the bounding 0 and 90-degree variants, as described in section 4.2.6. In addition to the two possible relative magnetic dipole orientations each for the two model body design variants, a control model with electrodes, but not embedded magnets is also tested, for a total of five models. The properties of these five models are listed in Table 4.4.

Table 4.4: Summary of MHD Energy Generator Model Designs for Testing

Model Number	Ceramic Model Body Angle	Relative Magnet Orientation
Model 1	90 Degrees	Parallel Dipoles
Model 2	90 Degrees	Anti-Parallel Dipoles
Model 3	0 Degrees	Parallel Dipoles
Model 4	0 Degrees	Anti-Parallel Dipoles
Model 5	0 Degrees	No Magnets, Control

At each test condition, values for the voltage difference across the electrodes with a purely resistive load, with load resistance,  $R_{Load} = 121 \Omega$  and the open circuit MHD voltage are measured, as shown by Figure 4.20. A total of  $N = 8$  unique test matrix

points per model are tested, and  $N = 3$  trials are conducted for each point, for a total  $N = 24$  plasma pulses overall per model. These pulses are spread over two tests of 12 pulses each, one with the load connected between the two electrodes, and the other without. The experimental test matrix and parameters are given as Tables 4.5 and 4.6, respectively.

Table 4.5: MHD Energy Generation for Planetary Entry Experimental Test Matrix,  $N = 3$  Trials at Each Test Point

Model #	Test Condition #	$\Delta V$ Measured
Model 1	Condition 1	$\Delta V_{Load}$
Model 2	Condition 2	$\Delta V_{Open}$
Model 3	Condition 3	-
Model 4	Condition 4	-
Model 5	-	-

Table 4.6: MHD Energy Generation for Planetary Entry Experimental Test Parameters, Schematic Shown as Figure 4.20.

Parameter	Value	Description
$L_{Test}$	2.000 in	Location of model from nozzle throat
$R_{Load}$	121.2 $\Omega$	Pure resistive load resistance
$R_+$	4.5 $\Omega$	(+) Electrode lead resistance
$R_-$	4.5 $\Omega$	(-) Electrode lead resistance

A minimum RF on pulse time of  $\tau_{pulse} = 1.0$  s is employed, based on the empirically determined time of approximately 0.5 s for steady-state impedance matched RF power deposition at the possible test conditions. For each test condition and model combination, the RF generator is pulsed for an amount of time  $\tau_{pulse}$  that is sufficient for steady-state power deposition into the test gas, but not so long that the model temperature rises above the maximum magnet operating temperature of 250 °C. This pulse time is empirically determined by placing the MHD model bodies with embedded thermocouples at the  $L_{Test}$  location for each of the four conditions, and continuously running the plasma discharge

while monitoring the model temperature as a function of time. When the temperature reached  $250\text{ }^{\circ}\text{C}$ , the plasma discharge was cycled off, and the final time recorded. The thermal response was found to be roughly linear, and as a result test time per pulse is determined by using a weighted average across all four test conditions, given as equation 4.4.

$$\tau_{pulse} = \frac{1}{3\left(\frac{1}{\tau_1} + \frac{1}{\tau_2} + \frac{1}{\tau_2} + \frac{1}{\tau_4}\right)} \quad (4.4)$$

where  $\tau_1$ ,  $\tau_2$ ,  $\tau_3$ , and  $\tau_4$ , are the continuous plasma run-times necessary to reach 250 degrees Celsius for test conditions 1, 2, 3, and 4, respectively, as defined in Table 4.3.

Sample photographs from the test are shown as Figures 4.21 and 4.22, and the recorded values for the 90 degree and 0 degree model geometries are shown as Table 4.7.



Figure 4.21: Model thermal response characterization test. Condition 1,  $P_{RF} = 400\text{ W}$ , MFC set-point voltage of  $3\text{ V}$  or approximately  $9,300\text{ sccm Ar}$  test gas mass flow rate. 0-degree based MHD model body variation with embedded thermocouple.

Based on the approximately  $8\text{ s}$  maximum pulse width shown in Table 4.7, a final pulse time for the 12 RF pulses per model and load condition of  $\tau_{pulse} = 5\text{ s}$  is selected. This pulse time allows for the most testing time at steady-state conditions without overheating the embedded permanent magnets.

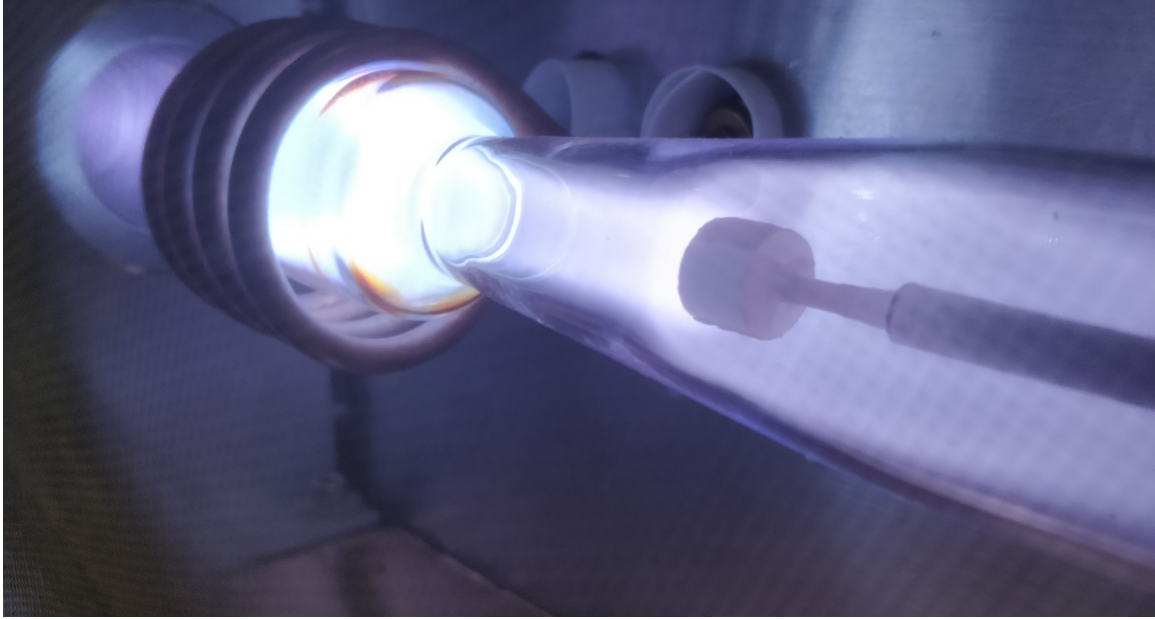


Figure 4.22: Model thermal response characterization test. Condition 4,  $P_{RF} = 800 W$ , MFC set-point voltage of  $5 V$  or approximately  $15,300 sccm Ar$  test gas mass flow rate. 90-degree based MHD model body variation with embedded thermocouple.

Table 4.7: MHD Energy Generator Ceramic Model Thermal Response Testing

Test Condition #	90 Degree TC Embedded Model Time (s) to $250^{\circ}C$	0 Degree TC Embedded Model Time (s) to $250^{\circ}C$
Condition 1	97.0	117
Condition 2	421	423
Condition 3	52.0	49.0
Condition 4	121	100.0
$\tau_{pulse,max}$	8.30	8.06
$\tau_{pulse,selected}$	5 s	

### 4.3.3 Experimental Design: Testing Protocol

Prior to testing, each MHD energy generator model was baked at  $85^{\circ}C$  for two hours in order to drive away any trapped water vapor prior to being placed in the test chamber. Models were installed and set to  $L_{test} = 2.000 in$  using the micrometer linear feedthrough adjustment on the model mount assembly, as described in section 3.1.6. In line with the schematic shown in Figure 4.20, the electrode corresponding to the (+) wire of the oscillo-

scope voltage measurement system is rotated such that it is facing up, for consistency.

For each test condition and model, the testing protocol was to first record the upstream and downstream pressures,  $P_{u,m}$  and  $P_{d,m}$  respectively. A 24-AWG type-K spot-welded thermocouple insulated with ceramic cement is located about 5 inches downstream of the model, and gathers diagnostic data on downstream temperature  $T_{d,m}$ . Measurements from these sensors are recorded with and without added RF power for each pulse in order to verify consistent plasma discharge properties from shot to shot.

The RF generator is triggered using a digital output signal from a LabVIEW program, which also triggers a digital oscilloscope data acquisition system, as described in section 3.1.5. The RF generator power output is recorded in real-time on one oscilloscope channel, with the voltage potential across the MHD generator electrodes in either a loaded or unloaded circuit configuration recorded on another oscilloscope channel. Waveforms for both signals are captured from the oscilloscope after each pulse and saved for analysis. The average steady-state value for MHD generator electrode voltage as determined from the RF power deposition signal is recorded as the final value, and this process is repeated three times for each possible test condition and model. Sample acquired waveforms for the loaded and unloaded voltage potential cases are presented as Figures 4.23 and 4.23, respectively.

In addition to the experiment instrumentation output and oscilloscope waveforms, high-resolution photographs and videos of each test are taken and recorded, which serve as visual indications of the flow-field while allowing the experiment operator to remain a safe distance from the test chamber during operation.

Results of this experimental investigation and the corresponding discussion are presented in section 4.4

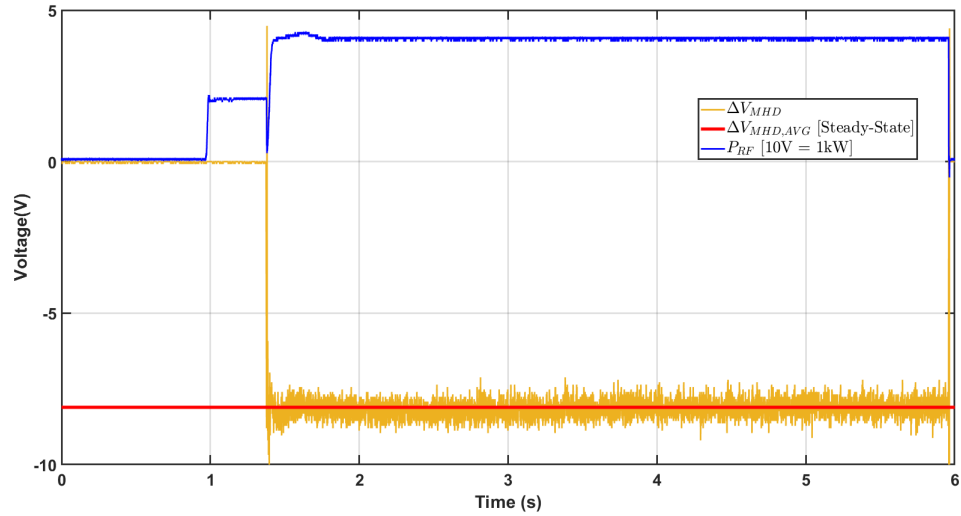


Figure 4.23: Condition 2, trial 2 voltage across model 1 electrodes with no load (open) circuit configuration and average steady-state value. Also shown is generator RF power output reaching steady-state of 400 W in less than 1 s.

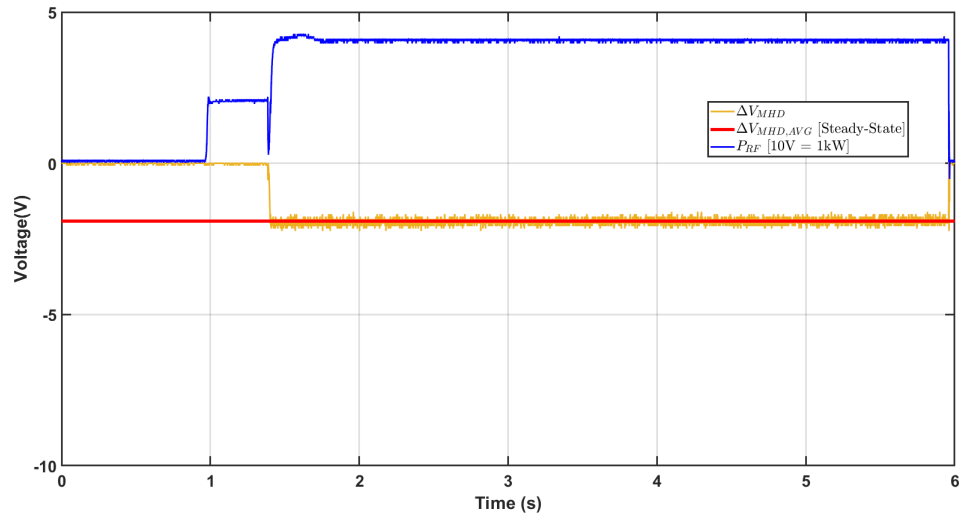


Figure 4.24: Condition 2, trial 2 voltage across model 1 electrodes with load circuit configuration and average steady-state value. Also shown is generator RF power output reaching steady-state of 400 W in less than 1 s.

#### 4.4 Experimental Results

Selected high-resolution photographs of each of the four test condition combinations for the control MHD model with no magnets (Model 5) are shown as Figures 4.25, 4.26, 4.27, and 4.28. Similar photographs were captured for each MHD energy generator model tested, and all flow fields were found to be visually comparable, observations that support the consistency and repeatability of the plasma discharge test chamber conditions across the various models tested.

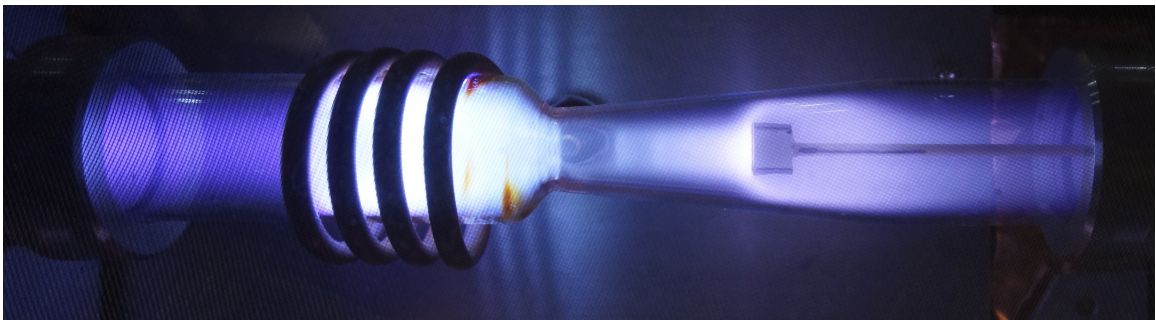


Figure 4.25: Test condition 1 photo, test gas mass flow rate set-point of 3  $V$  and forward RF power level of 400  $W$ . Model 5, open circuit configuration.

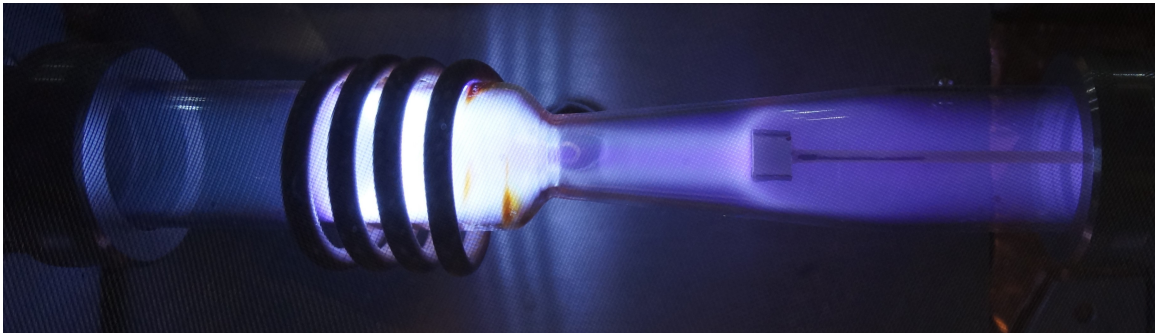


Figure 4.26: Test condition 2 photo, test gas mass flow rate set-point of 5  $V$  and forward RF power level of 400  $W$ . Model 5, open circuit configuration.

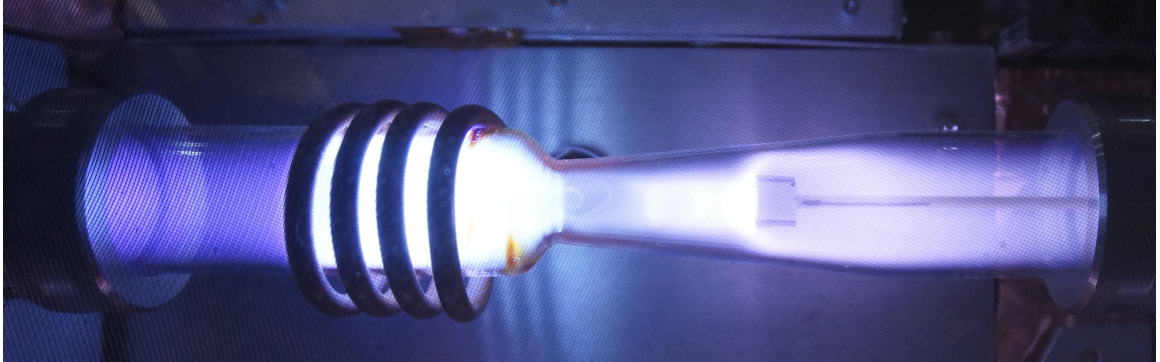


Figure 4.27: Test condition 3 photo, test gas mass flow rate set-point of 3  $V$  and forward RF power level of 800  $W$ . Model 5, open circuit configuration.

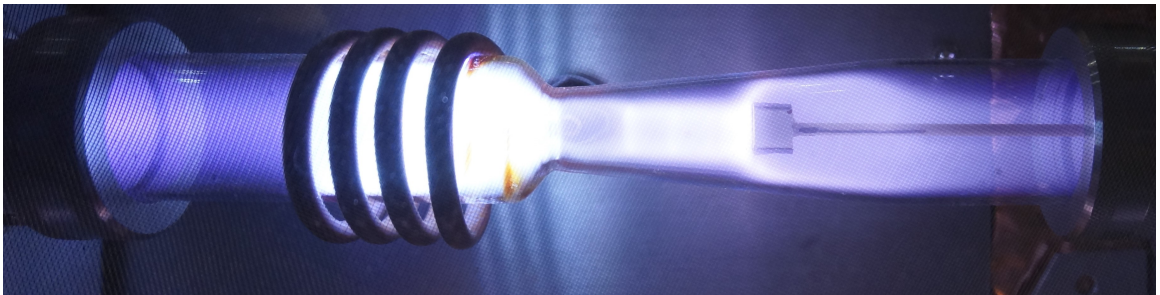


Figure 4.28: Test condition 4 photo, test gas mass flow rate set-point of 5  $V$  and forward RF power level of 800  $W$ . Model 5, open circuit configuration.

For each test condition and trial, the average measured steady-state open circuit and load voltage is computed as shown by Figures 4.23 and 4.24. The mean and standard deviation across all three trials for each steady-state electrode voltage potential are computed. Tables of the mean and standard deviation for all steady-state open circuit and load voltage recordings are shown as Tables 4.8 and 4.9.

These electrode voltage potential measurements in both Tables 4.8 and 4.9 exhibit consistent measured values across all three trials, evidenced by the standard deviation values. Derived values for MHD power dissipated in the resistive load,  $P_{MHD}$ , and load factor,  $K_{MHD}$ , are computed in the manner described in section 4.3.1. These values, along with standard error bars, are plotted and shown as Figures 4.29 and 4.30, respectively.

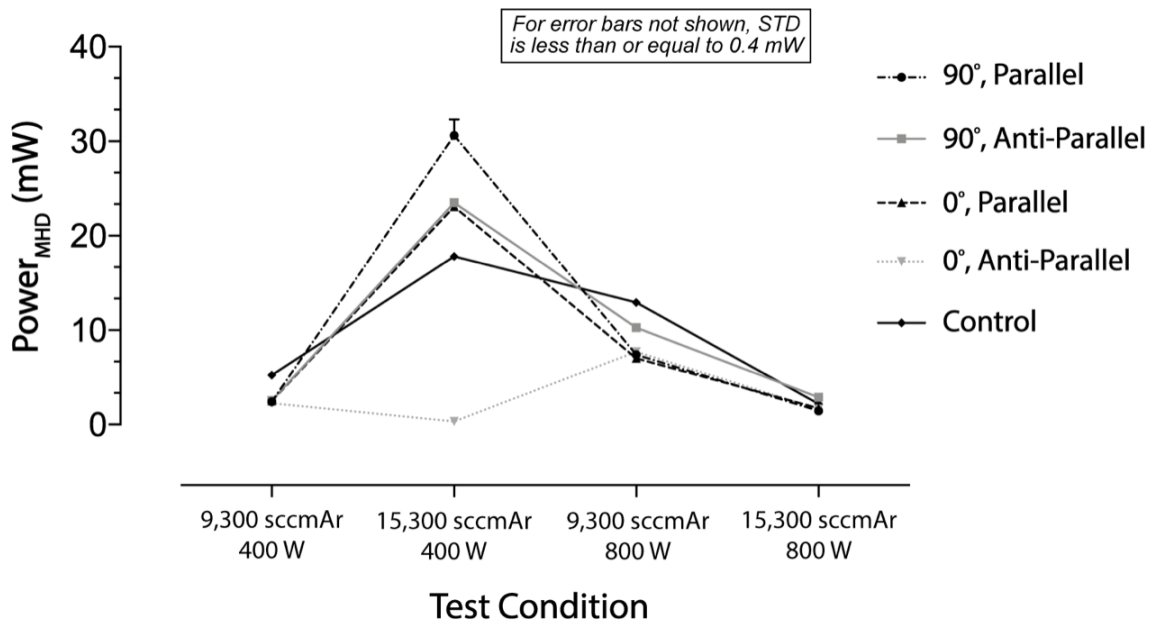


Figure 4.29: Calculated resistive load dissipated power,  $P_{MHD}$ , for all models and test conditions.

Table 4.8: Measured Electrode Voltage Potentials. Open Circuit Configuration.

<i>Model</i>	<i>1</i>		<i>2</i>		<i>3</i>		<i>4</i>		<i>5</i>	
	$\mu$ (V)	$\sigma$ (V)								
3V 400W	3.61	0.094	2.10	0.291	3.76	0.344	5.31	0.374	4.87	0.068
5V 400W	8.08	0.061	7.24	0.002	8.19	0.405	6.61	2.701	6.78	0.017
3V 800W	9.94	0.078	10.13	0.155	12.32	0.737	13.54	0.113	11.95	0.126
5V 800W	8.10	0.069	6.09	0.030	12.66	0.108	11.42	0.403	8.67	0.043

Table 4.9: Measured Electrode Voltage Potentials. Load Circuit Configuration.

<i>Model</i>	<i>1</i>		<i>2</i>		<i>3</i>		<i>4</i>		<i>5</i>	
	$\mu$ (V)	$\sigma$ (V)								
3V 400W	0.543	0.004	0.555	0.006	0.550	0.008	0.524	0.002	0.797	0.014
5V 400W	1.926	0.053	1.687	0.012	1.672	0.014	0.197	0.004	1.470	0.006
3V 800W	0.947	0.001	1.116	0.009	0.924	0.011	0.968	0.003	1.253	0.009
5V 800W	0.418	0.001	0.588	0.041	0.457	0.003	0.447	0.005	0.513	0.005

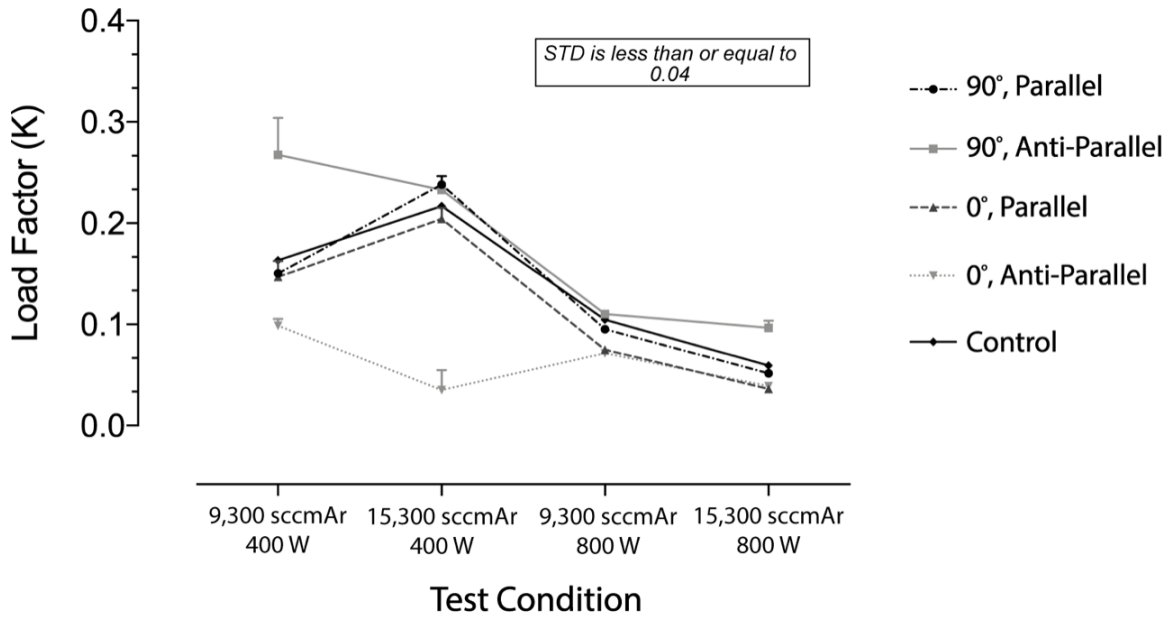


Figure 4.30: Calculated generator load factor,  $K_{MHD}$ , for all models and test conditions.

The experimental results displayed in Figures 4.29 and 4.30 demonstrated, significant difference in parameters for models with embedded magnets (Models 1 - 4) vs. the control model without. These results suggest an initial positive results for the presence of a magneto-hydrodynamic interaction effect on measured values of power dissipated in the resistive load,  $P_{MHD}$  and generator load factor  $K$ . In particular, test condition 2, corresponding to a 5 V MFC set-point and 400 W, generator power level exhibits the largest difference for this effect. This effect is followed in significance by test condition 3. At other test conditions, differences between models with magnets embedded and the control were not as pronounced, but still distinct. Bar charts at each of these conditions are given as Figures 4.31, 4.32, 4.33, and 4.34.

Generator load factors,  $K_{MHD}$ , varied between 0.1 and 0.3 overall, indicating sub maximal MHD energy generator power output, as discussed in section 1.6. In Figure 4.30, all models, including the control follow a similar trend, with the exception of model 4, the 0-degree, anti-parallel magnet model variant at condition 2. It is likely that this departure from the prevailing trend was due to an experimental anomaly, as it should be noted that for that particular model and test condition, a slight shift was observed in the RF generator

### Test Condition: 5V, 400W

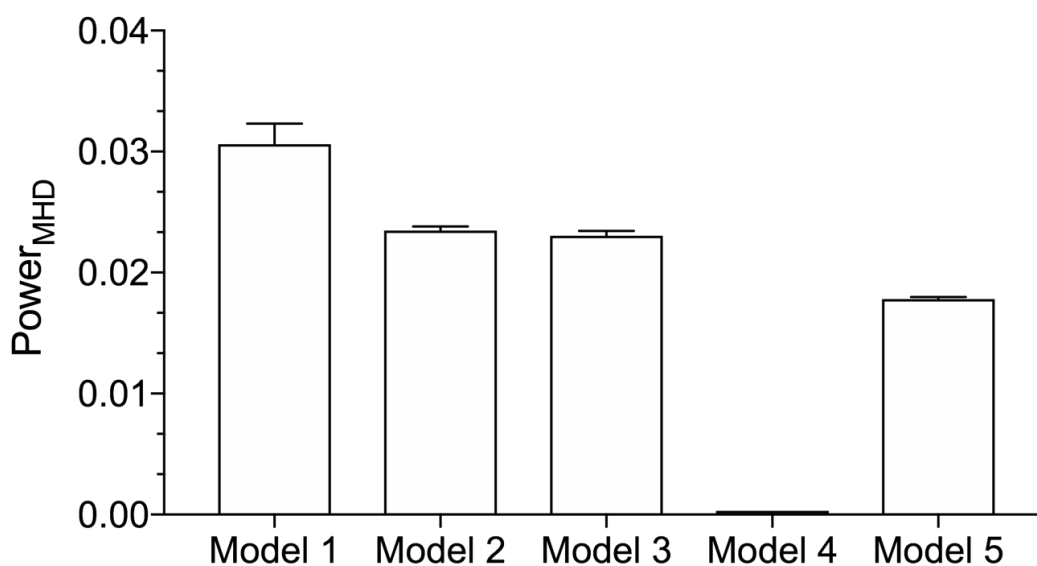


Figure 4.31: Calculated dissipated power in resistive load,  $P_{MHD}$ , for test condition 2. 5 V ( 15,300 *sccm* Ar mass-flow rate set-point, 400 W RF power)

### Test Condition: 3V, 800W

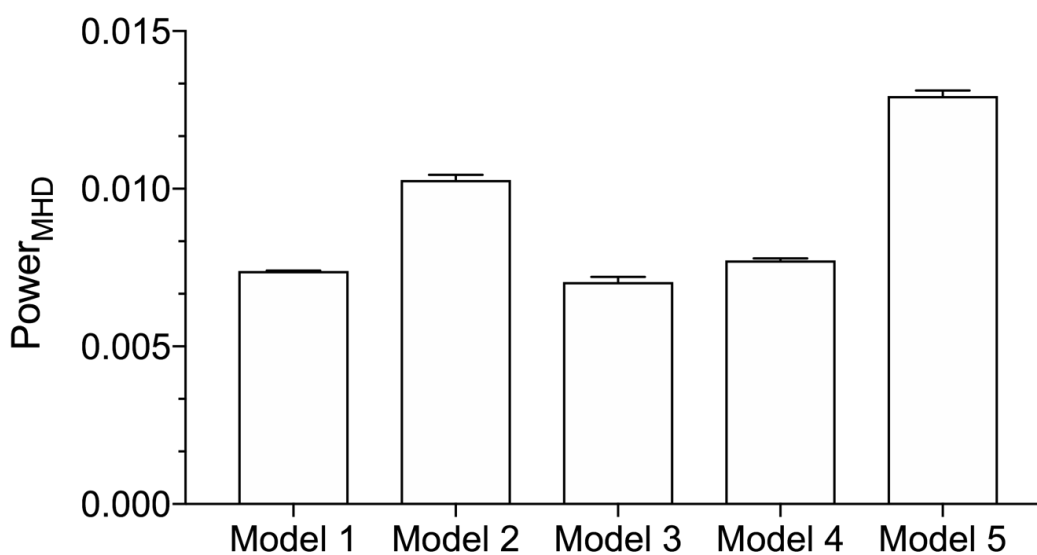


Figure 4.32: Calculated dissipated power in resistive load,  $P_{MHD}$ , for test condition 3. 3 V ( 9,300 *sccm* Ar mass-flow rate set-point, 800 W RF power)

### Test Condition: 5V, 400W

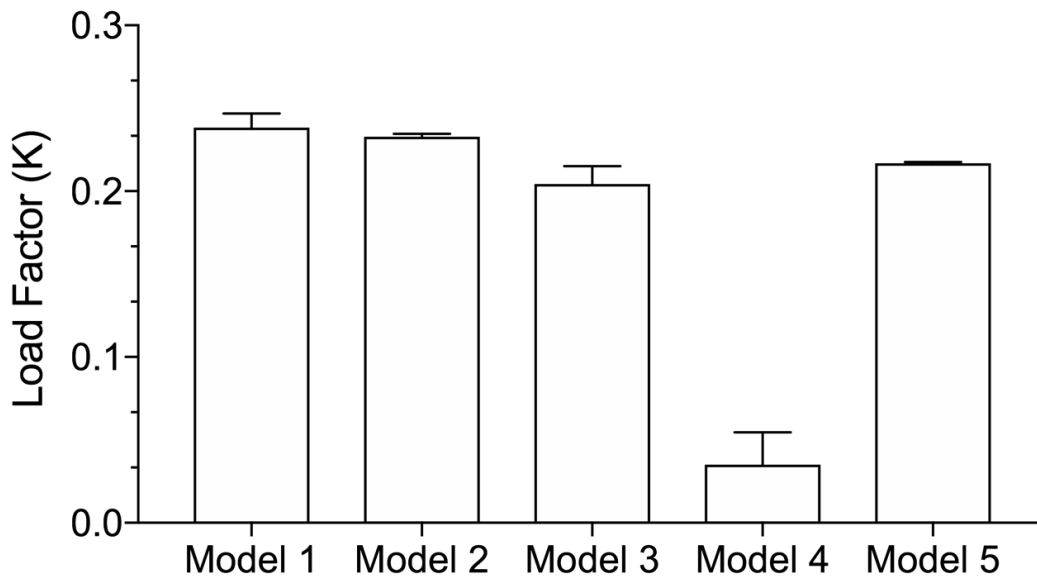


Figure 4.33: Calculated generator load factor,  $K_{MHD}$ , for test condition 2. 5 V ( 15,300 sccm Ar mass-flow rate set-point, 400 W RF power)

### Test Condition: 3V, 800W

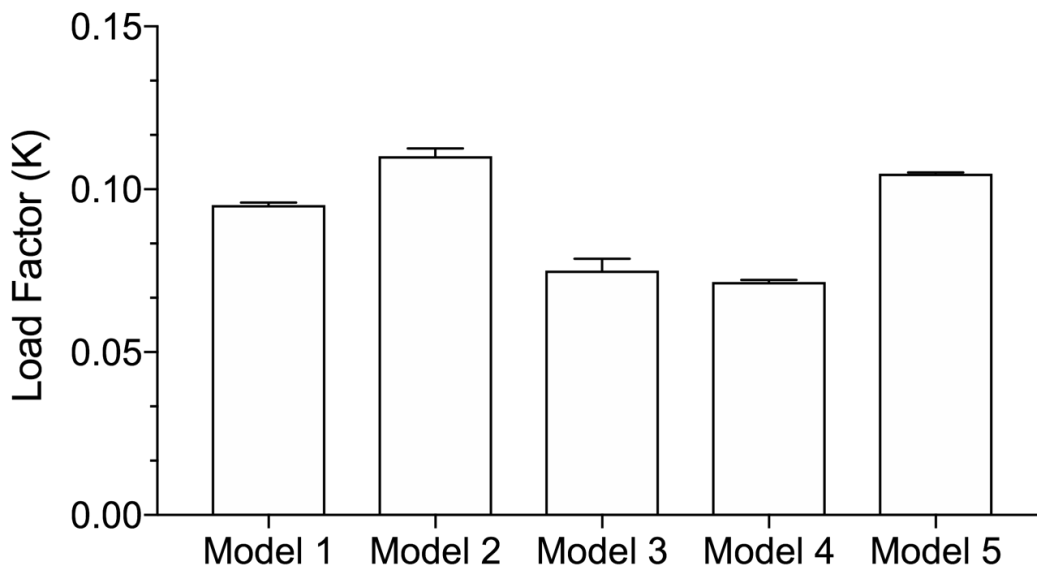


Figure 4.34: Calculated generator load factor,  $K_{MHD}$ , for test condition 3. 3 V ( 9,300 sccm Ar mass-flow rate set-point, 800 W RF power)

power output, followed by a return to normal operation at the subsequent conditions. It is as of yet unclear exactly why this anomaly occurred, but it was not observed again at other conditions. This is likely due to a transient issue with the equipment as opposed to a real effect of that particular model.

For both power and load factor, there was an observed non-monotonic trend as power level and flow rate were increased. This trend could be potentially be explained by a combination of a change in ionization physics and RF coupling methods. Decreased flow rates have lower densities, and depositing the same amount of RF power could result in higher-order ionization, without increasing the temperature proportionally. This assertion is supported by the downstream gas temperature measurements in Table 3.2. Furthermore, as the power level is increased, the type of RF discharge could have switched from a capacitive to an inductive mode. Determining which of these factors had the most influence quantitatively would require additional plasma diagnostics not taken during this experiment, though those diagnostics could be part of future work due to the repeatable nature of the discharge.

Interestingly, the control model (model 5) with no magnets embedded shows non-zero potential difference across the electrodes at all test conditions. Additional diagnostic testing on the instrumentation was conducted to verify that this potential difference was not simply induced by the RF antenna, and the conclusion is that the supersonic plasma discharge is non-axisymmetric, and the electrodes are measuring a difference in plasma potential. The control model potential difference appears higher than that for non-control models in some cases, which could be explained due to the asymmetric nature. If the asymmetry bias is against that induced by the magnets, then the measured potential difference would appear to be lower.

This control model electrode potential difference is separate from any potential difference induced by the permanent magnets in the non-control models and suggests that in future work the experiment flow quality and plasma symmetry should be improved. Another possibility would be to increase the magnetic field strength to compensate, or simply

subtract the control result from other non-control models.

Overall, the results for the models with permanent magnets embedded indicate that there is likely a measurable MHD interaction effect present for the prototype blunt-body non flow through MHD energy generator models developed in this thesis. In particular at test condition 2, corresponding to a 5 V test gas mass flow rate set point ( 15,300 *sccm Ar*) and 400 W generator power, models, 1, 2, and 3 exhibited significant measured power dissipation in the attached resistive load as compared with control model 5. From the results shown, there is not a clear in power or load factor due to magnetic orientation, possibly due to plasma potential asymmetry obscuring slight changes in electrode potential difference. AS a result, these experimental results are more consistent with an expanded feasibility study, as opposed to a broad presentation of parametric variance. To conclude, this experimental investigation demonstrates that there is an initial positive result for the feasibility of MHD energy generation and interaction in conditions (supersonic plasma discharge) and configurations (blunt-body non flow through MHD generator) relevant to planetary entry vehicles.

## **CHAPTER 5**

### **SUMMARY, CONCLUSIONS, AND FUTURE WORK**

In this investigation, the state of the art for planetary entry systems equipped with magnetohydrodynamic interaction devices has been advanced. Primary conclusions find that MHD energy generation and drag augmentation for planetary entry systems has been demonstrated, with potential to significantly benefit planetary entry system performance. In parallel, a preliminary experimental investigation to confirm feasibility was designed and executed, finding an initial positive result. The sections that follow summarize contributions to the state of the art. Suggestions for future work with regards to MHD and planetary entry are also provided.

#### **5.1 Summary of Contributions**

The state of the art for planetary entry systems equipped with magnetohydrodynamic interaction devices has been advanced through two primary contributions. A detailed summary of these contributions is provided in the sections that follow.

##### 5.1.1 Magnetohydrodynamic Energy Generation and Lorentz Force Drag Augmentation Performance Characterization and Impact on Planetary Entry Architectures

In this contribution, upper-bound, best case estimate methodologies are developed by which the energy available for extraction through MHD energy generation and additional drag due to the Lorentz force can be calculated in a manner suitable for conceptual design. The analytic, one-dimensional, non-vehicle specific models developed require inputs of only altitude, velocity, and basic entry vehicle sizing parameters, enabling rapid trade space exploration and determination of feasibility for MHD interaction to occur early in conceptual design.

An example integrated systems analysis case study was designed and conducted for MHD energy generation during planetary entry. For the energy generation case study, a performance and mass model for the required electrical energy storage system is developed. The integrated systems analysis enabled by the MHD energy generation performance model found that for typical atmospheric entry conditions at both Earth and Mars, a significant amount of electrical energy is available for extraction via MHD energy generation. Energy storage system performance and mass constraints were identified as key performance drivers, in particular energy storage system specific power, with technology development requirements increasing as available mass for the energy storage system decreased.

An example exploratory systems analysis case study for Lorentz drag force augmentation during planetary entry is also conducted. Results similar to those generated using full-field, computationally expensive, numerical simulation were obtained for the Lorentz drag force potential across the entire trajectory. The addition of the MHD Lorentz force drag to the trajectory dynamics lead to deceleration higher in the atmosphere, with peak, primarily MHD Lorentz force driven decelerations at this higher altitude similar in magnitude to the peak, primarily aerodynamic decelerations encounters lower in the atmosphere. The overall effect of this ‘magnetoaerodynamic decelerator’ is to reduce overall peak deceleration by ‘spreading’ through the trajectory, similar to that of reducing the vehicle ballistic coefficient,  $\beta$ , by increasing the drag area. However, with this technology, a benefit is that this effect is achieved while maintaining the original physical dimensions, mitigating launch fairing and mass constraints on entry vehicle diameter. The integrated systems study also included the effects of various magnetic field strengths, and reveals a potential for in-situ drag augmentation by employing a variable on-board electromagnet.

For both exploratory systems analysis case studies conducted, the results demonstrate the ability of the developed MHD interaction performance models for planetary entry to provide computational trade space exploration and novel insights during conceptual de-

sign. These frameworks allow for identification of system conditions and configurations that can significantly benefit from the inclusion of MHD interaction devices, for further study through detailed numerical or experimental investigations. The results of these higher fidelity, vehicle configuration specific studies can also feedback into the one-dimensional analytic models via the presented calibration coefficients, improving design tool accuracy for future use.

### 5.1.2 Experimental Design and Investigation for Magnetohydrodynamic Energy Generation in Conditions and Configurations Relevant to Planetary Entry

In this contribution, a successful experimental design and implementation of a supersonic plasma discharge for simulation of atmospheric entry plasma conditions is discussed. In combination with precise control of the test-gas input mass flow rate, a computer-controlled 27.1 MHz 1000W RF generator and automated impedance matching network will be used, allowing for measurement and control of the RF coil current and dissipated power in real-time. In combination with a novel quartz tube-nozzle assembly design and implementation, high volume mechanical vacuum pumping system, a low-density supersonic plasma wind tunnel is created. The end result is a highly repeatable supersonic plasma discharge that can be pulsed for shorter test durations. These shorter test durations are key to enable successful demonstration of MHD energy generator concepts with permanent magnets and small models, as permanent magnets are subject to demagnetization at elevated temperatures.

An initial characterization effort is conducted for the plasma discharge chamber by varying the input test gas mass flow rate and RF generator power output conditions. Pressure and temperature measurements in the test chamber indicated that supersonic flow is likely to be present for several conditions, with minimum freestream Mach numbers on the order of  $M = 3$  and test gas velocities of  $u_\infty = 700 \text{ m/s}$ . These observations and results support the successful design and implementation of a supersonic plasma discharge in the test chamber, informed model placement for exposure to supersonic free-stream flow in the

subsequent experimental investigation.

To summarize earlier discussion, the principal contribution of this thesis related to this area is the design and execution of an experimental campaign to demonstrate MHD energy generation for a non-channel type MHD energy generator on a simulated blunt-body reentry vehicle.

The design and subsequent precise, repeatable manufacturing and assembly of such a non-channel type MHD energy generator prototype is presented, with several variations of model magnetic field and electrode orientation constructed. In addition, several thermocouple embedded models are created in order to characterize the thermal response of models to the high-temperature supersonic plasma discharge. These tests help to ensure that the field strength of the embedded magnets is maintained throughout the entire discharge test duration, helping ensure validity and consistency in the experimental results.

In the presented exploratory experiment, a positive result for MHD energy generation in the supersonic laboratory discharge was observed. The MHD energy generator open and voltage traces across the two electrodes are recorded using a high-resolution oscilloscope data acquisition system for a variety of plasma discharge test conditions and MHD energy generator model configurations. Measurable differences are observed across the experimental test matrix, suggesting that there is indeed some MHD interaction effect present. Calculations of the MHD power dissipated in the load,  $P_{MHD}$ , and the generator load factor,  $K_{MHD}$ , are made, forming a data-set with the necessary values for future extrapolation of experimental results to relevant atmospheric entry flight conditions.

As mentioned previously, due to the artificial ionization mechanism and unknown electrical conductivity, the conditions of this experimental investigation are non-equilibrium and not directly computable by the methodologies presented as Contribution I in this thesis, requiring additional plasma diagnostics to correlate electrical conductivities.

## 5.2 Suggestions for Future Work

Suggestions for future work regarding each of the three presented contributions are discussed in the sections that follow.

### 5.2.1 Suggested future work: Magnetohydrodynamic Energy Generation and Lorentz Force Drag Augmentation Performance Characterization

As stated earlier, this contribution represents methodologies by which the energy available for extraction through MHD energy generation and additional drag due to the Lorentz force can be calculated in a manner suitable for conceptual design. Though these simple models are largely complete from a conceptual point of view, the constants used in equations 2.7 and 2.15 can be updated through an expanded numerical simulation effort or new experimental results. It is planned to compare at least one run of the design tool to the output of a full-field numerical simulation for a single case, and calibrate the constants as necessary to achieve a good match. Additional future work in this area could include the potential system impacts and benefits of drag modulation along the trajectory for applications such as downrange distance targeting and control. In addition, similar analyses are expected to be conducted for lift to drag ratio modulation for non-axisymmetric magnetic field configurations.

For this exploratory study, and in line with previous work on MHD Lorentz drag augmentation, the mass of the required electromagnet system is not considered, owing to the significant design complexities and challenges for superconducting magnet systems in general, and the lack of available performance and flight heritage data for such systems. Such a design undertaking, along with supporting validation data, could be of tremendous potential benefit to the technology readiness level and subsequent integration of MHD interaction devices on planetary entry vehicles.

## 5.2.2 Suggested Future Work: Experimental Design and Investigation for MHD Energy Generation in Conditions and Configurations Relevant to Planetary Entry

Currently, the test chamber experimental design allows for the installation of Langmuir probes for measurement of the electron temperature and density. In addition, the same probes can be offset in the axial direction to allow for velocity approximations via time of-flight diagnostic techniques. A key challenge for implementing this Langmuir probe technique will be probe mechanical strength and measurement accuracy within a high-velocity supersonic plasma discharge. In future work, fully instrumented tests for a variety of input power levels and flow velocities can be conducted. The goal of this investigation would be to directly measure the electrical conductivity and flow velocity of the plasma in the test chamber.

Furthermore, additional quartz-nozzle tube geometries are possible. Based on the quartz nozzle tube assembly examined in the experiment, combinations of test gas mass flow rates and RF input power that result in fully expanded flow are limited. Reducing the nozzle throat and exit area to create a smaller supersonic plasma discharge jet could create similar free-stream conditions while reducing the test-gas mass flow rate requirements and associated demands on the mechanical vacuum pumping system.

As mentioned in section 4.3.1, extrapolation of experimental test conditions and results to relevant atmospheric entry flight conditions is suggested for future work. In conjunction with the measured values of  $\Delta V_{Load}$ ,  $\Delta V_{Open}$ , calculated values of  $P_{MHD}$  and  $K_{MHD}$  are presented. Calculation of these two parameters, along with measurement of the model magnetic field intensity,  $B$ , and calculation of the freestream flow velocity,  $u_{\infty}$ , as described in section 3.3, leaves only the plasma electrical conductivity  $\sigma_e$  undetermined, allowing for a potentially experimentally determined value. The product of this experimentally determined electrical conductivity  $\sigma_e$  and freestream velocity squared,  $u_{\infty}^2$ , could in theory be translated to the output one-dimensional analytic model presented in section 2.1, and therefore provide correlation of test chamber supersonic plasma discharge conditions to relevant

atmospheric entry flight conditions of altitude and velocity.

Finally, and as an addendum to the energy generation aspect of the presented experimental work, it is likely that MHD Lorentz drag augmentation forces are present and acting on the models. Placing the entire experiment within a vacuum chamber and mounting the model assembly on a suitable thrust-stand would facilitate measurement of these forces. Furthermore, the effects of asymmetric magnetic fields, both on MHD energy generation and drag augmentation, could be assessed by simply removing one of the permanent magnets embedded within the models, potentially enabling estimation of MHD lift and control moments as well.

# Appendices

**APPENDIX A**  
**LIST OF PUBLICATIONS BY THE AUTHOR**

**Thesis-relevant publications**

●Ali H.K., and Braun R.D., “*Modeling Magnetohydrodynamic Energy Generation and Storage in Planetary Entry System Conceptual Design*, AIAA Journal of Spacecraft and Rockets, Vol. 55, No. 2, pp. 356-364, 2018.

●Ali H.K., and Braun R.D., “*Effects of Magnetohydrodynamic Energy Generation on Planetary Entry Vehicle Flight Dynamics*,” in 2015 AIAA Propulsion and Energy Forum, Orlando, Florida July 2015.

●Ali H.K., and Braun R.D., “*In Situ Magnetohydrodynamic Energy Generation for Planetary Entry systems*,” Georgia Institute of Technology Master’s Special Project Report, July 2015.

●Ali, H.K. and Braun R.D., “*Application of Magnetohydrodynamic Energy Generation to Planetary Entry Vehicles*,” in 2014 AIAA Propulsion and Energy Forum, Cleveland, Ohio, July 2014.

**Non-thesis-relevant publications**

●Mueller, R.P., Braun, R.D., Sforzo B., Sibille, L., Gonyea, K., and Ali H. K., “*Mars Molniya Orbit Atmospheric Resource Mining*, in 68th International Astronautical Congress, Adelaide, Australia, September 2017.

●Ali H.K., Hanson V.S., Polzin, K.A., and Pearson, J.B., “*Proof of Concept Experiments on a Gallium Based Ignitron for Pulsed Power Applications*, NASA TM-2015-218202, April 2015.

## REFERENCES

- [1] NASA, “2015 NASA Technology Roadmaps - TA 9: Entry, Descent, and Landing Systems,” National Aeronautics and Space Administration, Tech. Rep. July, 2015, p. 167.
- [2] R. D. Braun and R. M. Manning, “Mars Exploration Entry, Descent, and Landing Challenges,” *Journal of Spacecraft and Rockets*, vol. 44, no. 2, pp. 310–323, 2007.
- [3] P. R. Mahaffy, C. Webster, and E. Al., “Abundance and Isotopic Composition of Gases in the Martian Atmosphere from the Curiosity Rover,” *Science*, vol. 341, no. 6143, pp. 263–266, 2013.
- [4] D. W. Way, R. W. Powell, A. Chen, A. D. Steltzner, a. M. S. Martin, P. D. Burkhart, and G. F. Mendeck, “Mars Science Laboratory: Entry , Descent , and Landing System Performance,” *IEEE Aerospace Conference*, No. 1467, 2006.
- [5] A. D. Steltzner, A. M. S. Martin, T. P. Rivellini, A. Chen, and D. Kipp, “Mars Science Laboratory Entry, Descent, and Landing System Development Challenges,” *AIAA Journal of Spacecraft and Rockets*, vol. 51, no. 4, 2014.
- [6] D. A. Spencer, R. C. Blanchard, R. D. Braun, P. H. Kallemeyn, and S. W. Thurman, “Mars Pathfinder Entry, Descent, and Landing Reconstruction,” *Journal of Spacecraft and Rockets*, vol. 36, no. 3, pp. 357–366, 1999.
- [7] R. P. Mueller, R. D. Braun, B. Sforzo, L. Sibille, and H. Ali, “Mars Molniya Orbit Atmospheric Resource Mining,” in *68th International Astronautical Congress*, Adelaide, Australia, 2017.
- [8] S. Popović, R. W. Moses, and L. Vuskovic, “System Development for Mars Entry in Situ Resource Utilization,” in *Proceedings of the 8th International Planetary Probe Workshop*, Portsmouth, VA, 2011.
- [9] K. Goneya, “Use of the Mars Atmosphere to Improve the Performance of Supersonic Retropropulsion,” PhD Thesis, Georgia Institute of Technology, 2017.
- [10] I. Langmuir, “Oscillations in Ionized Gases,” *Proceedings of the National Academy of Sciences*, vol. 14, no. 8, pp. 627–637, 1928.
- [11] F. Chen, *Introduction to Plasma Physics and Controlled Fusion*. 1984. arXiv: arXiv:1011.1669v3.

- [12] K. Thorne and R. Blandford, “Part VI Plasma Physics,” in *Applications of Classical Physics*, Pasadena, California: CalTech, 2012.
- [13] W. M. Stacey, *Fusion Plasma Physics*, 2nd. Weinheim, Germany: Wiley-VCH, 2012, p. 666.
- [14] W. F. Bergerson, C. B. Forest, G. Fiksel, D. A. Hannum, R. Kendrick, J. S. Sarff, and S. Stambler, “Onset and Saturation of the Kink Instability in a Current-Carrying Line-Tied Plasma,” *Physical Review Letters*, vol. 96, no. 1, pp. 1–4, 2006.
- [15] W. Baumjohann and R. A. Treumann, *Basic Space Plasma Physics*. London: Imperial College Press, 1997.
- [16] R. J. Rosa, “Physical Principles of Magnetohydrodynamic Power Generation,” *Physics of Fluids*, vol. 4, no. 2, pp. 182–194, 1961.
- [17] B. Karlovitz, *Process for the Conversion of Energy*, 1940.
- [18] R. J. Rosa, *Magnetohydrodynamic Energy Conversion*, Revised Pr. New York: Hemisphere Publishing Corporation, 1987.
- [19] G. W. Sutton, “The Theory of Magnetohydrodynamic Power Generators,” Space Sciences Laboratory Aerophysics Section, General Electric Company, Philadelphia, PA, Tech. Rep., 1962.
- [20] J. Chapman, H. Schmidt, R. Ruoff, V. Chandrasekhar, D. Dikin, and R. Litchford, “Flightweight Carbon Nanotube Magnet Technology,” NASA, NASA Technical Publication 2003-212342, Tech. Rep. NASA/TP-2003-212342, 2003, p. 45.
- [21] E. L. Resler and W. R. Sears, “The Prospects for Magneto-Aerodynamics,” *Journal of the Aerospace Sciences*, vol. 25, no. 4, pp. 235–245, 1958.
- [22] W. B. Bush, “Magnetohydrodynamic-Hypersonic Flow Past a Blunt Body,” *Journal of the Aerospace Sciences*, vol. 25, no. 11, pp. 685–690, 1958.
- [23] W. B. Bush, “On the Viscous Hypersonic Blunt-Body Problem,” Doctoral Thesis, California Institute of Technology, 1964.
- [24] P. J. Gierasch, D. B. Henderson, and R. H. Levy, “Hypersonic Magnetohydrodynamics With or Without a Blunt Body.,” *AIAA Journal*, vol. 2, no. 12, pp. 2091–2099, 1964.
- [25] P. O. Jarvinen, “On The Use of Magnetohydrodynamics During High Speed Re-Entry,” Avco-Everett Research Laboratory, AVCO-Everett Research Note 463, Tech. Rep., 1964, p. 62.

- [26] M. Smith, C. Wu, and H. Scwhimmer, “Magnetohydrodynamic Hypersonic Viscous and Inviscid Flow Near the Stagnation Point of a Blunt Body,” Rand Corporation, Santa Monica, California, Tech. Rep., 1965.
- [27] R. J. U. Nowak, R. W. U. Porter, M. C.N. U. Yuen, and A. B.N. U. Cambel, “Magnetoaderodynamic Re-Entry,” in *AIAA Plasmadynamics Conference*, Monterey, CA: AIAA, 1966.
- [28] S. Y. Chen, “Magnetic Hypersonic Flow Near the Stagnation Point at Low Reynolds Number.,” *Journal of Spacecraft and Rockets*, vol. 6, no. 8, pp. 872–877, 1969.
- [29] R. W. Ziemer and W. B. Bush, “Magnetic Field Effects on Bow Shock Stand-Off Distance,” *Physical Review Letters*, vol. 1, no. 2, pp. 58–59, 1958.
- [30] K. R. Lobb, “Experimental Measurement of Shock Detachment Distance on Spheres Fired in Air at Hypervelocities,” *High Temperature Aspects of Hypersonic Flows*, vol. 14, no. 5, pp. 519–527, 1964.
- [31] E. Locke, H. E. Petschek, and P. H. Rose, “Experiments with Magnetohydrodynamically Supported Shock Layers,” Avco-Everett Resaerch Laboratory, Everett Massachusetts, Tech. Rep., 1964, p. 36.
- [32] G. R. Seemann and A. B. Cambel, “Observations Concerning Magnetoaderodynamic Drag and Shock Standoff Distance,” *Proceedings of the National Academy of Sciences of the United States of America*, vol. 55, no. 3, pp. 457–465, 1966.
- [33] S. Kranc, M. C. Yuen, and A. Cambel, “Experimental Investigation of Magnetoaderodynamic Flow Around Blunt Bodies,” Northwestern University, Evanston, IL, Tech. Rep., 1969, p. 71.
- [34] J. Poggie and D. V. Gaitonde, “Magnetic control of flow past a blunt body: Numerical validation and exploration,” *Physics of Fluids*, vol. 14, no. 5, pp. 1720–1731, 2002.
- [35] T. Fujino, T. Yoshino, and M. Ishikawa, “Numerical Analysis of Reentry Trajectory Coupled with Magnetohydrodynamics Flow Control,” *Journal of Spacecraft and Rockets*, vol. 45, no. 5, pp. 911–920, 2008.
- [36] S. O. Macheret, M. N. Shneider, and G. V. Candler, “Magnetohydrodynamic Energy Generation for Planetary Entry Vehicles,” in *35th AIAA Plasmadynamics and Lasers Conference*, Portland, Oregon: AIAA, 2004.
- [37] H. Katsurayama, M. Kawamura, A. Matsuda, and T. Abe, “Kinetic and Continuum Simulations of Electromagnetic Control of a Simulated Reentry Flow,” *Journal of Spacecraft and Rockets*, vol. 45, no. 2, pp. 248–254, 2008.

- [38] M. K. Kim, “Electromagnetic Manipulation of Plasma Layer for Re-Entry Blackout Mitigation,” PhD Dissertation, University of Michigan, 2009.
- [39] N. Bisek, I. Boyd, and J Poggie, “Three Dimensional Simulations of Hypersonic MHD Flow Control,” in *40th AIAA Plasmadynamics and Lasers Conference*, 2009.
- [40] N. J. Bisek, I. D. Boyd, and J. Poggie, “Numerical Study of Magnetoaerodynamic Flow Around a Hemisphere,” *Journal of Spacecraft and Rockets*, vol. 47, no. 5, pp. 816–827, 2010.
- [41] N. Bisek, I. Boyd, and J. Poggie, “Numerical Study of a MHD-Heat Shield,” *41st Plasmadynamics and Lasers Conference*, no. July, pp. 1–19, 2010.
- [42] S. Kranc, A. B. Cambel, and R. W. Porter, “Electrodeless Magnetogasdynamic Power During Entry,” *Journal of Spacecraft*, vol. 4, no. 6, pp. 813–815, 1967.
- [43] C. A. Steeves, H. N. G. Wadley, R. B. Miles, and A. G. Evans, “A Magneto-hydrodynamic Power Panel for Space Reentry Vehicles,” *Journal of Applied Mechanics*, vol. 74, no. 1, p. 57, 2007.
- [44] A. Gülhan, B. Esser, U. Koch, F. Siebe, J. Riehmer, D. Giordano, and D. Konigorski, “Experimental Verification of Heat-Flux Mitigation by Electromagnetic Fields in Partially-Ionized-Argon Flows,” *Journal of Spacecraft and Rockets*, vol. 46, no. 2, pp. 274–283, 2009.
- [45] M. Kawamura, A. Matsuda, H. Katsurayama, H. Otsu, D. Konigorski, S. Sato, and T. Abe, “Experiment on Drag Enhancement for a Blunt Body with Electrodynamical Heat Shield,” *Journal of Spacecraft and Rockets*, vol. 46, no. 6, pp. 1171–1177, 2009.
- [46] M Kawamura, Y Nagata, H Katsurayama, H Otsu, K Yamada, and T Abe, “Magnetoaerodynamic Force on a Magnetized Body in a Partially Ionized Flow,” *Journal of Spacecraft and Rockets*, vol. 50, no. 2, pp. 347–351, 2013.
- [47] D. E. Gildfind, D. Smith, S. W. Lewis, R. Kelly, C. M. James, H. Wei, and T. J. McIntyre, “Expansion Tube Magneto-hydrodynamic Experiments with Argon Test Gas,” in *2018 Flow Control Conference*, Atlanta, GA, 2018.
- [48] D. R. Smith, D. E. Gildfind, C. M. James, T. McIntyre, and V. Wheatley, “Magneto-hydrodynamic Drag Force Measurements in an Expansion Tube,” *2018 Flow Control Conference*, 2018.
- [49] L Vuškovi, S Popovi, J Drake, and R. W. Moses, “Magneto-hydrodynamic Power Generation in the Laboratory Simulated Martian Entry Plasma,” Old Dominion University, Norfolk, VA, Tech. Rep., 2005.

- [50] D. J. Drake, S Popović, L Vušković, D. J. Drake, S Popovi, and L Vuškovi, “Characterization of a supersonic microwave discharge in Ar / H<sub>2</sub> / Air mixtures,” *Journal of Applied Physics*, vol. 063305, no. 2008, 2008.
- [51] D. J. Drake and S Popović, “Kinetic Description of Martian Atmospheric Entry Plasma,” *IEEE Transactions on Plasma Science*, vol. 37, no. 8, pp. 1646–1655, 2009.
- [52] G. Candler, “Computation of Thermo-Chemical Nonequilibrium Martian Atmospheric Entry Flows,” in *Proceedings of the AIAA/ASME 5th Joint Thermophysics and Heat Transfer Conference*, Seattle, WA, 1990.
- [53] M. Kim and I. D. Boyd, “Effectiveness of a Magnetohydrodynamics System for Mars Entry,” *Journal of Spacecraft and Rockets*, vol. 49, no. 6, pp. 1141–1149, 2012.
- [54] R. W. Moses, “Regenerative aerobraking,” in *AIP Conference Proceedings*, vol. 746, 2005, pp. 1361–1370.
- [55] R. W. Moses, C. A. Kuhl, and J. D. Templeton, “Plasma Assisted ISRU At Mars,” in *15th International Conference on MHD Energy Conversion*, NASA Langley Research Center, Portland, Oregon, 2005.
- [56] H. K. Ali and R. D. Braun, “In Situ Magnetohydrodynamic Energy Generation for Planetary Entry Systems,” Masters Special Project, Georgia Institute of Technology, 2015.
- [57] H. K. Ali and R. D. Braun, “Modeling Magnetohydrodynamic Energy Generation and Storage in Planetary Entry System Conceptual Design,” *AIAA Journal of Spacecraft and Rockets*, vol. 55, no. 2, pp. 356–364, 2018.
- [58] H. K. Ali and R. D. Braun, “Effects of Magnetohydrodynamic Energy Generation on Planetary Entry Vehicle Flight Dynamics,” in *2015 AIAA Propulsion and Energy Forum 13th International Energy Conversion Engineering Conference*, 2015, pp. 1–14.
- [59] T. Fujino and T. Takahashi, “Numerical Simulation of Mars Entry Flight using Magnetohydrodynamic Parachute Effect,” *47th AIAA Plasmadynamics and Lasers Conference*, no. June, pp. 1–9, 2016.
- [60] A. R. Sparacino, G. F. Reed, R. J. Kerestes, B. M. Grainger, and Z. T. Smith, “Survey of Battery Energy Storage Systems and Modeling Techniques,” *2012 IEEE Power and Energy Society General Meeting*, 2012.
- [61] S. Gordon and B. J. McBride, “Computer Program for Calculation of Complex Chemical Equilibrium Compositions and Applications,” NASA Reference Publication 1311, Tech. Rep., 1994.

- [62] H. Chen, T. N. Cong, W. Yang, C. Tan, Y. Li, and Y. Ding, “Progress in electrical energy storage system: A critical review,” *Progress in Natural Science*, vol. 19, no. 3, pp. 291–312, 2009.
- [63] J. M. Lafferty, *Foundations of Vacuum Science and Technology*. New York, NY: Wiley-Interscience, 1998.
- [64] J. N. Mueller, “NACA Technical Note 4063,” NACA Langley Aeronautical Laboratory, Langley Field, VA, Tech. Rep., 1957.

## VITA

Hisham K. Ali is a graduate research assistant and NASA Space Technology Research Fellow in the Daniel Guggenheim School of Aerospace Engineering at the Georgia Institute of Technology. As a NASA Space Technology Research Fellow, his research has focused on magnetohydrodynamic energy generation and flow control for planetary entry and in-situ resource utilization applications. Since arriving at Georgia Tech in 2013, he has developed performance modeling tools for magnetohydrodynamics and planetary entry systems suitable for conceptual design while working to advance the state of the art for magnetohydrodynamics and planetary entry at NASA Marshall Spaceflight Center, Langley Research Center, and Jet Propulsion Laboratory. In addition, he has designed and created an experimental testing platform for magnetohydrodynamic energy generation in conditions and configurations relevant to planetary entry. The term of this fellowship funding is from August 2013 August 2017.

Hisham earned a Bachelor of Science in Aerospace Engineering with minors in Mathematics and Computer Based Honors from the University of Alabama in 2013. In 2015, he earned a Master of Science in Aerospace Engineering from the Georgia Institute of Technology. He is currently a Doctoral Candidate in the Daniel Guggenheim School of Aerospace Engineering at the Georgia Institute of Technology and is the recipient of numerous academic scholarships and awards in addition to the NASA Space Technology Research Fellowship, including but not limited to the Barry M. Goldwater Scholarship, the Alfred P. Sloan Minority Ph.D. Fellowship, and the Georgia Institute of Technology Presidential Fellowship.

During his undergraduate studies, Hisham conducted research in luminescent photoelastic coating stress analysis with Dr. James P. Hubner through the University of Alabama Computer Based Honors Program. Furthermore, he was employed as the lead rapid pro-

totyping lab manager in the Computer Based honors program, overseeing the purchase, installation, and use of the first rapid prototyping machine available for interdisciplinary undergraduate research at The University of Alabama. He also worked with NASA's Marshall Space Flight Center to identify, design, and test candidate parts for rapid prototyping in microgravity as part of NASA's effort to demonstrate rapid prototyping on-board the International Space Station. During this project, he utilized previous experience in experimental stress analysis techniques such as photoelastic stress analysis to inform design modifications necessary for manufacturing of tools in microgravity. Finally, he is the original founder of the University of Alabama hovercraft team, overseeing an interdisciplinary student design team that created a human-scale hovercraft powered by a light aircraft engine and organizing a competition against a similar team at Auburn University.

Hisham's current research interests are in magnetohydrodynamics, hypersonics, plasma physics, space systems, and planetary entry systems. He hopes to continue pursuing these research interests through a career in spaceflight research in academia, government, or private industry.